McDermott Technology, Inc.
a McDermott company

Contract Research Division
2016 Mt. Athos Road
Lynchburg, VA 25404-5447
(434) 522-5165
Fax: (434) 522-6933

October 7, 2002

Investigation of Low Temperature
Time Dependent Cracking
DOE: DE-FG02-97ER14809
MTI: CRD 1373

Mr. Terry L. Vlasich, Contract Specialist
Office of Acquisitions and Assistance
U.S. Department of Energy
Chicago Operations Office
9800 South Cass Avenue
Argonne, IL 60439

Dear Mr. Vlasich:

Subject: Final Technical Report

In accordance with your letter dated July 25, 2002, enclosed are three (3) copies of the Final Technical Report, DOE F 241.1 Announcement of U.S. Department of Energy (DOE) Scientific and Technical Information (STI), and the Final Financial Status Report (Standard Form 269A) for the close-out of the referenced grant. A CD containing the entire final technical report has also been included. The cost figures presented in the Final Financial Status Report do not include any adjustments for approved final rates. Government approval of rates can be 1-2 years after the rates are submitted. An invoice will be submitted for costs incurred during September, 2002. McDermott has enjoyed working with the Chicago Operations Office in the administration of this grant. If there are any questions or comments concerning this submittal, please contact me at (434) 522-5710.

Sincerely,

McDERMOTT TECHNOLOGY INC.
a McDermott company

J.P. Doran
Senior Contract Manager

Enclosures

DISCLAIMER

DISCLAIMER

Portions of this document may be illegible in electronic image products. Images are produced from the best available original document.

DOE/ER/14809-1

INVESTIGATIONS OF LOW TEMPERATURE TIME DEPENDENT CRACKING

Final Report

J. Bloom, E.S. Robitz, B.A. Young
and W.A. VanDerSluys

McDermott Technology, Inc.
Alliance, Ohio 44601

September 2002

Prepared for

THE U.S. DEPARTMENT OF ENERGY
AWARD NO. DE-FG02-97ER14809

Summary

Over the past 30 years, fossil boilers have been shown to be susceptible to a failure mechanism that results in a sudden and unexpected window blow-out at carbon-manganese steel pipe bends which have seem service at a nominal 650 F for approximately 10,000 hours. These failures have had a substantial financial impact both in the U.S. and abroad, and perhaps more importantly, they present a safety issue, potentially resulting in the loss of life.

Earlier work by other investigators has shown that these cold bent pipes are failing due to a low temperature creep crack growth mechanism. Cracking by this mechanism apparently initiates at otherwise innocuous imperfections at the extrados of the bend. This earlier work also suggested that, among other things, susceptibility to this damage mechanism is related to the levels of free nitrogen and tramp elements in these steels. The level of strain in the cold bend and the amount of cross section deformation also are known contributing factors. In spite of the knowledge gained in earlier investigations, cold bent pipes have continued to fail, so additional work was needed to better understand contributing factors and to identify palliative measures.

In the work described herein a test method and specimen are developed which are able to reproduce low temperature creep crack growth in commercially available heats of SA-106, Grade C carbon-manganese steel. This method then was used to evaluate a matrix of heats representing high and low levels of tramp elements and free nitrogen. The matrix addressed these heats at a level of cold work typical of that anticipated in pipe bends. It also explored the beneficial influences of post bend heat treatment, and for one case evaluated the impact of reducing the amount of strain initially imparted to the starting material.

This work confirmed the influence of steel cleanliness and free nitrogen on performance. It also suggested that marginal heats of material may benefit from post-bend heat treatment, but that these provide little, if any, benefit to those heats that are truly susceptible. The results of this work also successfully were integrated with previously available life prediction tools. Lastly, recommendations are offered as to additional work that would build upon the foundation laid by this effort.

Introduction

Over the past 30 years, fossil boilers have been shown to be susceptible to a failure mechanism that results in a sudden and unexpected catastrophic at the extrados of carbon steel pipe cold bends. These failures have had a substantial failure impact, and perhaps more importantly, they present a safety issue, potentially resulting in the loss of life.

Such failures have occurred in boilers for both domestic and European utilities, and have given rise to numerous investigations worldwide to better understand the failure mechanism, and how it might be avoided. The work to date has concluded that these window failures initiate and propagate due to a time dependent cracking mechanism that has come to be described as low-temperature creep crack growth (CCG). This designation comes about because the service temperature is below the temperature range at which creep mechanisms normally operate.

Studies have suggested that the factors that contribute to creep brittleness, also influence susceptibility to CCG. Materials composition issues were identified, such as the level of residual elements, tramp elements and free nitrogen content. Materials condition issues were identified, such as microstructure, hardness, and strength. Pipe bend conditions also were identified as potential contributors, such as bend radius, pipe ovality, and surface condition.

Consideration of the potential contributing factors led to a number of suggested approaches and attempts to mitigate the failure mechanism. However, the fact that cold bent pipes continue to fail suggests that the understanding of this mechanism and how to avoid it is incomplete. The work described herein makes progress toward a fuller the understanding of this failure phenomenon, and the factors that contribute to its' occurrence.

The details of this work are provided herein in a series of six annexes. These mirror the structure of the program itself.

- Annex A: Materials Issues – describes considerations that led to the selection of four (4) candidate heats for testing. The heats were chosen to explore some of the materials-related theories regarding which heats are more susceptible. Based on these and other issues a full test matrix was developed.
- Annex B: Test Design - describes development of a test specimen design that could be used to induce low-temperature CCG in susceptible materials. This annex describes the preparation of test specimens from the candidate heats. Lastly, it describes the testing methodology.
- Annex C: Creep Crack Growth Test Results – this annex provides the results of the CCG testing performed in this program.
- Annex D: C* Analysis - provides a more detailed description of the theoretical underpinnings of the testing methodology.
- Annex E: Examination of Test Specimens – this annex provides the results of the detailed metallurgical examination to confirm the physical crack length

measurements inferred from the CCG test technique. Also provided are a correlation between the pipe metal microstructure and test results.

- Annex F: Application of Findings – uses life prediction methodology and the results of this testing to estimate service life in an actual application.

Each of the annexes has a separate numbering system for the figures and tables contained therein. The references for each annex are included at the end of the annex.

The main body of this report provides a summary that ties together the main points of the annexes. It begins by providing some additional background information regarding earlier investigations. It goes on to provide an overview of the results of this program. It then concludes with recommendations for future efforts.

Background

In the early 1970's, time dependent cracking at the extrados of cold bent elbows resulted in unexpected, catastrophic failures in the piping systems of a number of fossil power utilities around the world. Failures occurred within the plants of at least five U.S. utilities and it has been reported that failures have occurred within at least twelve European utilities[1]. These failures typically caused significant damage to the boiler facility.[2] Most importantly, cracking often culminated in 'blow-outs' of sections of the elbows, producing a serious threat to human safety.

Significant resources have been dedicated to characterizing the problem and defining economic means for eliminating this problem. Investigations were independently performed within the U.S. and Europe, but there was no common resolution to this problem. However, the studies in Europe did reveal a number of distinct features that were common to most failures[3]: (1.) Cracking failures occurred in cold-formed material manufactured from common grades of boiler pipe, e.g. SA-106, Grade C and SA-210, Grade C. (2.) The operating temperature of the failed components was in the range of 572F to 788F. (3.) Failures usually occurred before 10,000 hours of operation, but several were noted at times up to 100,000 hours of operation. Usually the longer lives were attributed to straight pipe sections while the shorter lives were elbows. (4.) Cracking always occurred at the extrados of the bends initiating at the OD surface. (5.) Cracking was typically associated with the presence of small surface defects that were within the limits of the inspection criteria - i.e., laps, seams, hammer marks, gouges, etc. (6.) Stable cracking occurred by an intragranular mode before transitioning to a transgranular mode during final fracture.

Most of the failures, which have occurred in the United States, occurred in the early 1970's. In the U.S., steps were taken in the mid 1970's to limit the stress on the elbows, eliminate defects, and to improve the uniformity of the steels used to fabricate the elbows. This appeared to have eliminated the problems. In Europe failures continued and a large research project was performed in Europe that identified the failure mechanisms identified below. In Europe most of the failures have been eliminated by reducing the stress, eliminating the defects and eliminating the high free nitrogen in the steel. The elimination of elbows with

high free nitrogen in the steel is quite costly. Free nitrogen is difficult to measure reliably, and there are very few laboratories in the world that can perform the analysis.

More recently, it has been reported that Indian boiler tube failures account for a power generator loss equivalent to power generated on one 500 MW Unit at a 70% power loading for one year. On eight separate occasions riser tube failures resulted in forced shut down of the power grid. Their study showed the mechanism to be creep crack growth. Temporary fixes, reflecting European research studies, were adopted and included stress relief, improved NDE, and control of the base metal specification.

In the U.S., there were two failures in the early 1990's. These failures were slightly different from the others. The elbows had high residual and tramp element contents. The steel used to fabricate these elbows had been manufactured in Europe, and although the steel met the U.S. code requirements for this grade of steel, the failed elbows contained much higher levels of residual and tramp elements than is typically found in steel manufactured in the U.S. These recent failures raised the concern that a better understanding of the physical metallurgy and mechanical aspects of these failures is needed. In addition, these recent failures raise concerns about the adequacy of U.S. boiler material specifications when the materials are manufactured overseas where the manufacturing practices are substantially different from those in the U.S.

Mechanisms:

Research on this issue demonstrated that metallurgical conditions which produce good creep rupture strength in carbon-manganese piping steels also typically produce poor creep crack growth resistance[5,6,7,8]. The cause is believed to be related to the relative strength of the matrix and grain boundaries in the temperature range of 572 F to 788 F. When a crack is introduced into a material, the high strain fields ahead of the crack tip cannot be easily accommodated, if the material matrix has high creep strength. As a result, weakening of the grain boundaries by any mechanism can produce cavitation and cracking along the boundaries. This material model agrees well with the observation that these types of failures occur only over a limited temperature range. At lower temperatures, creep mechanisms on the grain boundaries are not operable so cracking does not occur. At higher temperatures, the strength of the matrix is sufficiently reduced to allow accommodation of the crack tip strains. This is also consistent with the relatively small numbers of failures for the large numbers of carbon steel cold bent elbows that are in service. Failures may require both a matrix strengthening and a grain boundary weakening mechanism to exist at the service temperature.

There are a variety of phenomena that can contribute to either strengthening of the matrix or weakening of grain boundaries. For example, free nitrogen, residual alloying elements, and austenitizing temperatures can strongly impact the matrix strength. Tramp element levels, grain size, and unfavorable distributions of microstructural phases can each influence the propensity for grain boundary cracking and decohesion to occur. These parameters comprise the primary metallurgical factors that will impact the creep crack growth resistance of a C-Mn steel. However, according to Gooch et al.[9], there are a number of engineering factors

that will also have an impact on the probability for failure, such as the constraint of the material at a crack tip. It has been observed that constraint influences the materials resistance to creep crack growth (i.e., specimen geometry, specimen size, crack depth, etc.). All of the parameters cited above must be considered when developing a test program to evaluate the propensity for cracking in the field.

A considerable amount of research has been performed on this topic. Still, the amount of creep crack growth data on these materials is limited[7]. Consequently, a number of unresolved issues remain that demonstrate that a more fundamental understanding of the problem must be obtained to assure elimination of this problem from in field. These are enumerated in the Technical Rationale section of this report.

Testing Methodology:

It has been demonstrated on a limited basis that creep crack growth rate test data can be used to reasonably predict the life of low carbon steel elbows[9]. However, the data from conventional, deeply cracked (a/W>0.4) compact specimens produce results that under-predict the observed failure lives of carbon steel elbows, sometimes by as much as a factor of 10. Deeply notched specimens can produce highly conservative creep crack growth rate data due to the high crack tip constraint associated with the deep notch. This has a direct influence on the damage mechanism and therefore, will influence the crack tip parameter C*, which characterizes the creep crack growth behavior. In fact, some tests using deeply notched specimens have shown that creep crack growth rates can be better correlated to the linear elastic stress intensity factor, K_I. Using such crack growth rates predicts overly conservative remaining life estimates.

It appears that this relates to whether a material is behaving in a creep-brittle or creep-ductile manor. In creep-ductile materials, the creep rate displacement is large compared to the total displacement rate. In creep-brittle materials, the creep rate displacement is small compared to the total displacement rates. There is little work on the effect of constraint on the creep-brittle versus creep-ductile behavior. However, the state of stress present in laboratory specimens typically used to study creep crack failures is not representative of the stresses that will exist in the field, at least in the early stages of crack growth.

Failure of the pipe elbows in the field has typically been associated with the existence of shallow longitudinal flaws on the pipe extrados that had been acceptable to the material inspection criteria imposed prior to service. The flaws range from seams or laps from the pipe manufacturing process to relatively blunt mechanical gouges or hammer marks. Studies of field failures indicate that the stresses on the pipe extrados are sufficiently high that any type of measurable flaw produces enough stress concentration to initiate creep crack growth early in the life of a susceptible elbow.

ASTM E 1457-98 recommends the use of the compact (CT) specimen under constant load to determining creep crack growth for both creep-ductile and creep-brittle materials. However,

it is suggested that constant displacement or displacement rate testing may be more suitable for creep-brittle materials. It is also thought that the single edge cracked specimen in tension with a shallow flaw will best simulate the cold bent pipe constraint. For this reason the shallow cracked single edge notched under displacement control was used in the program.

Work to date has demonstrated that classical creep is operative in C-Mn piping steels in the temperature range of 620°F to 680°F; which was previously thought to be too low for creep to occur[4,6,8]. Moreover, widespread creep damage such as that observed in rupture tests is not responsible for the time dependent cracking failures of C-Mn steels observed in the field. The generally accepted mechanism for these failures is believed to be related to a critical combination of creep strength of the metal matrix, decohesion strength of the grain boundaries, and level of constraint at the crack tip. When the critical combination occurs, high levels of crack tip constraint inhibit creep relaxation of the large strains ahead of a crack tip and these crack tip strains encourage separation along prior austenite grain boundaries.

Although a failure mechanism has been defined for the pipe elbow failures, a fundamental understanding of the critical metallurgical/mechanical factors required to produce field failures has not been completely determined. Thus, the purpose of this project was to conduct experimental studies of common grades of piping steels that are designed to elucidate the metallurgical phenomena that contribute to time dependent cracking failures. The goal of this project is to define mechanical and metallurgical conditions associated with creep crack growth in these types of steels.

Materials Issues:

This section of the report provides an overview of the materials selected for testing in this program. Annex A provides a more detailed review.

The rate of occurrence of field failures indicates that a critical combination of conditions must exist in a pipe bend for time dependent cracking to occur. Supporting this, previous experimental work has shown that different heats of the same steel grade have different susceptibilities to this type of cracking[5]. Considering that the manufacturing methods were similar between the heats studied in reference 5, and the global properties such as microstructure and hardness were nearly identical, the difference is postulated to lie in compositional differences between the heats - specifically in the free nitrogen, residual alloying element and tramp elements. Thus, materials were required which possess sufficient variations in composition to allow testing of the relative impact of these elements on creep crack growth susceptibility.

Pipe samples of SA106 Grade C or SA210 Grade C were obtained from various sources. Sufficient materials representing significant compositional variations were obtained for testing. The target test matrix is shown below. Note that "clean" steels were defined as those having low tramp element contents. Note also that in selecting steels having either high or low free nitrogen, the free nitrogen content was deduced based on the aluminum-to-nitrogen

ratio. High ratios were taken to indicate low levels of free nitrogen, so, aluminum-killed steels were favored in this regard.

Table 1: Target Test Matrix

	Clean	Dirty
Low Free Nitrogen	X	X
High Free Nitrogen	X	X

The following steps were followed to find samples of pipe to fill-out this matrix.

1. Contacted U.S. boiler manufactures looking for compositions desired and examples of failed pipe.
2. Performed a survey of B&W R&D archives looking for samples of failed pipe
3. Searched the inventory of pipe available at B&W manufacturing sites
4. Contacted Italian and Spanish boiler manufactures for samples of failed pipe
5. Contacted the European program for failed samples
6. Checked with tube vendor on available piping with desired compositions

The results of this effort were that there were no offers of pipe from other manufacturers either in the U.S. or overseas were received. An offer was received from the chairman of the European program of (4) samples of pipe material. Five candidate materials in R&D Division storage and four candidate materials from B&W manufacturing sites were located. However, only one of these samples was from a heat of pipe that had failed in service.

The compositions of these nine materials and the four materials offered from Europe were then reviewed and four materials were selected for the test matrix.The candidate heats were identified by the designations: Heats O, M, P, and D. The table below shows how these heats were intended to fill-out the test matrix. Note that the Heat D sample was extracted from the pipe which failed in service at a U.S. utility.

Table 2: Initial Placement of the Candidate Heats Within The Target Test Matrix

Condition:	Low Free Nitrogen	High Free Nitrogen
Clean	Heat O	Meat M
Dirty	Heat P	Heat D

Placement of the heats within the matrix was based on the mill certificates. Detailed chemical analysis of the pipe samples led to further refinement of the matrix, as is explained below. The results of the detailed analyses are provided in Table A-1, in Annex A.

Cleanliness Assessment:

The expressions which quantify tendencies toward temper embrittlement and stress relief cracking were used to provide guidance in identifying clean and dirty heats of steel. This was

appropriate in that it was understood that the same constituents that gave rise to these damage mechanisms also give rise to the creep embrittlement and notch sensitivity which would engender creep crack growth. The expressions are as follows:

Temper Embrittlement (TE) = 6.1 Sb + 13.8 Sn + 12.6 P + 10.5 As + 8.8 S [10]

Stress Relief Cracking (SRC) = 2.7 Sb + 1.9 Sn + 1.0 P + 1.8 As + 0.44 S + 0.2 Cu [11]

While, these expressions provide a way of ranking these alloys relative to one another in terms of cleanliness, the reader is cautioned that the expressions were not developed to quantify tendencies toward low temperature creep cracking. Rather, what is suggested here is that low temperature creep is influenced by the same objectionable elements that have been demonstrated to weaken grain boundaries during temper embrittlement and stress relief cracking, both of which involve exposure at higher temperatures for shorter time periods. Nonetheless, as a first approximation, it is postulated that the relative contribution of each of the objectionable elements to the tendency toward low temperature creep may be roughly proportional to their influence in either or both of these other mechanisms.

The table below provides the results of applying these expressions for the four candidate heats.

Table 3: Candidate Heats Ranked Based on Cleanliness

Heat	Aim Cleanliness	SRC Ranking	TE Ranking	Actual Condition
O	Good	0.019	0.186	Clean
M	Good	0.053	0.444	Intermediate
P	Poor	0.085	0.452	Intermediate
D	Poor	0.123	0.618	Dirty

Note from the above that Heats O and D are clearly distinguished as cleanest and dirtiest heats respectively. Heat M and P are intermediate.

Free nitrogen analyses were performed to complete the test matrix. A description of these tests and the results of the various approaches are provided in Annex A. The results of these tests suggested that the aluminum-to-total nitrogen ratio is not a consistent indicator of the amount of free nitrogen. They further indicate that heat treatment reduces the free nitrogen level for some heats, but not for others. A fuller understanding of the differences in response was beyond the scope of this effort.

The following free nitrogen determination results are offered as representative:

Table 4: Ranking of Heats Based on Free Nitrogen

Heat	Aim Free Nitrogen	Reported Al:N Ratio	Free Nitrogen Content, ppm	Actual Condition
O	Low	4.75	35	Intermediate Free N
M	High	1.95	18	Low Free N
P	Low	3.67	24	Intermediate Free N
D	High	0.46	67	High Free N

As one can see from the table above, one heat was clearly low in free nitrogen, one was high, and the other two were intermediate, but toward the low side. Based on this and the steel cleanliness analysis above, it was determined that the four (4) heats would more properly be characterized by the following matrix.

Table 5: Material Test Matrix Based on Cleanliness and Free Nitrogen

Condition:	Low Free Nitrogen	Intermediate Free Nitrogen	High Free Nitrogen
Clean	--	Heat O	--
Intermediate Cleanliness	Heat M	Heat P	--
Dirty	--	--	Heat D

CCG Testing

This section of the report provides an overview the CCG test set-up. It also provides a description of how samples were further prepared for testing and the test matrix filled-out. Annex B provides a more detailed review of these.

This section then goes on to provide a summary of the CCG test results. These are given in more detail in Annex C

Lastly, while it is not addressed in the body of this report, it should be noted here that Annex D provides a detailed explanation of the rationale for the testing methodology and the sample design employed.

Sample Preparation:

With the test heats selected, and pipe procured, it was then necessary to manufacture the samples needed to fill-out the final test matrix. In order to simulate the material condition in

service, it was necessary to pre-strain the test material to the relatively high plastic strains typical of the extrados of the as-bent pipe, i.e. roughly 20 to 25%. It was not possible to strain the pipe material in a uniaxial tension to achieve a uniform strain at this level. This is due to the fact that tension specimens would experience necking as the material achieved its' uniform strain limit at strain levels of 15 to 16%. Use of actual cold bent pipe to supply strained test samples would require an excessive amount of pipe, which was not available for all of the heats. Therefore, it was decided to design a special ("dog bone") specimen capable of developing biaxial constraint to achieve the desired uniform strain levels.

Development of the dog bone specimen design started with tension tests on one of the candidate heats. The stress strain curve from these tests was used in an elastic plastic finite element model of a flat plate tension specimen in order to optimize the proportions of the specimen. Three specimens were then machined based on the results of the finite element analysis. One specimen had optimal proportions per the finite element analysis. The second had a slightly longer gage length, and the third had an even longer gage length. These specimens were then loaded with a superimposed grid pattern and the strain distribution determined. The middle specimen of the three possessed an acceptable strain magnitude and distribution. Four tension or creep specimens or one creep crack growth specimen can be machined from each of the cold strained specimen.

Two levels of pre-strain were needed. For most samples the target pre-strain was 20%, as discussed above. It was further decided that specimens from Heat D would also be tested at a pre-strain of 10%. The rationale was to use the most susceptible heat to determine if there is a lower threshold of cold strain below which cracking will not occur. Each dog bone sample was mapped to ensure that the desired level of pre-strain was achieved. The records of these are provided in Annex B. CCG test samples later would be extracted from this region of the dog bone.

Once pre-straining was accomplished, additional test samples were needed to investigate whether there was a benefit to stress relieving or normalizing cold bent pipe. The intent was to provide test materials to fill-out the final test matrix.

Table 6: Test Matrix Finalized

Heat	AM + 10% Strain	AM + 20% Strain	AM + 20% Strain + Stress Relieved	AM + 20% Strain + Normalized
O	-	X	*	*
M	-	X	X	X
P	-	X	X	X
D	X	X	X	X

Note: "AM" = As-Manufactured

It should be noted that there was insufficient material from Heat O to test to the full matrix. So, Heat D only was tested in the as-cold worked condition. This was rationalized based on

the fact that it was anticipated that this heat would not be susceptible to CCG. Thus, the anticipated a lack of cracking in the worst-case as-cold worked condition would obviate the need for testing in the less severe, stress relieved and normalized conditions.

Stress relief and normalization were carried out by heating the dog bones at 1250 F and 1600 F respectively. Specimens were at temperature for one-half hour, then they were removed from the furnace and air cooled. These then were ready for machining into the final single-edge-notch (SEN(t)) specimen geometry. This is shown in Figure B-3 of Annex B. Tensile specimens and creep specimens also were machined at this time.

Table B-1, in Annex B, provides the full list of test specimens that were machined. Review of this list will show that three CCG test specimens were provided for each material condition. Three specimens were required because the ideal displacement rate was not known at the outset of testing, and multiple specimens were prepared in advance to allow the displacement rate to be selected in an iterative approach. The tensile specimens for each condition were needed for data analysis and modeling. Initially, it was thought that creep specimens also would be needed to assist in modeling. However, it was decided that data from the open literature would suffice, and creep tests were not performed.

Test Technique:

CCG tests were performed by mounting the SEN(t) specimen into place into an MTS test system. The specimen was encapsulated within a furnace, and was instrumented with a thermocouple to control to the desired temperature (650 F +/-5 F). The specimen then was loaded at a constant displacement rate, while monitoring displacement on the specimen (using a dc/dt transducer), and while monitoring crack advance (using the potential drop technique). Testing progressed until crack advance (or plastic deformation) was indicated. Samples then were removed from the test system, and subjected to visual and metallographic examination to confirm cracking and to measure the actual crack length. These examinations are detailed in Annex E.

As was mentioned above, an adequate number of specimens were provided to test at three displacement rates for each material condition. The initial displacement rate (0.016 in. per day) was selected based on a target anticipated time to failure. When tests at this rate proved successful, tests were performed at a slower rate (0.0016 in. per day) in order to provide the data needed to develop the test result curve which shows crack advancement rate (da/dt) as a function of creep crack driving force (C*). Since two points were needed to establish the curve, testing at a third displacement rate was not required, and these additional SEN(t) specimens were archived.

CCG Test Results:

Annex C of this report provides the details of the test results. They are summarized in the table below.

Table 7: Results Matrix

Material	Specimen ID	Condition	Cleanliness	Free Nitrogen	Displacement Rate (in./day)	Test Result
Heat M	M-2	ACW20	Intermediate	Low	0.0016	Blunting
	M-3	ACW20	Intermediate	Low	0.016	Tearing/Creep
	M-6	ACW20+SR	Intermediate	Low	0.0016	Blunting
	M-7	ACW20+SR	Intermediate	Low	0.016	Blunting
	M-10	ACW20+N	Intermediate	Low	0.0016	Blunting
	M-11	ACW20+N	Intermediate	Low	0.016	Blunting
Heat O	O-2	ACW20	Best	Intermediate	0.0016	Blunting
	O-3	ACW20	Best	Intermediate	0.016	Blunting
Heat P	P-2	ACW20	Intermediate	Intermediate	0.0016	Creep
	P-3	ACW20	Intermediate	Intermediate	0.016	Creep
Heat P	P-6	ACW20+SR	Intermediate	Intermediate	0.0016	Incipient Creep
	P-7	ACW20+SR	Intermediate	Intermediate	0.016	Blunting
Heat P	P-10	ACW20+N	Intermediate	Intermediate	0.0016	Blunting
	P-11	ACW20+N	Intermediate	Intermediate	0.016	Blunting
Heat D	K-2	ACW20	Worst	High	0.0016	Creep
	K-3	ACW20	Worst	High	0.016	Creep
	K-6	ACW20+SR	Worst	High	0.0016	Creep
	K-7	ACW20+SR	Worst	High	0.016	Creep
	K-11	ACW20+N	Worst	High	0.0016	Creep
	K-12	ACW20+N	Worst	High	0.016	Creep
	K-19	ACW10	Worst	High	0.0016	Creep
	K-21	ACW10	Worst	High	0.016	Creep

Note: ACW20 = As-cold worked at a pre-strain of 20%.
ACW10 = As-cold worked at a pre-strain of 10%.
ACW20+SR = As-cold worked at a pre-strain of 20% followed by stress relief.
ACW20+N = As-cold worked at a pre-strain of 20% followed by normalization.

The first result of this testing is the fact that the test specimen design and testing methodology were proven successful. The CCG testing as described above successfully generated creep crack growth in susceptible heats of material in an abbreviated test period. This claim is further substantiated by the metallographic examination of these specimens, as discussed later in this report, and provided in detail in Annex E. While it may be possible to further refine the testing methodology, this program has developed and demonstrated a testing tool that is able to rank the creep crack growth resistance of various candidate heats. Thus, it is available for use in any expanded test program. For the four heats tested to date, review of the table above, suggests the following observations:

- Heat O, having the best cleanliness, did not experience creep crack growth in spite of the fact that it had an intermediate level of free nitrogen.

- Heat D (the heat that had already failed in service), having the worst cleanliness and high levels of free nitrogen cracked in every condition tested. Neither stress relief (at 1250F) nor normalization (at 1600 F) had any apparent benefit.

    - It is interesting to note that the as-cold worked condition cracked even at the lower pre-strain level (10%). Thus, if there is a threshold pre-strain for this susceptible material, then it falls below this level.

- The two heats with intermediate cleanliness, Heats M and P, both experienced creep crack growth in at least one as-cold worked specimen.

    - Heat M, having intermediate cleanliness and low free nitrogen, was not consistent in this regard in that only the as-cold worked specimen tested at the higher displacement rate showed evidence of creep crack growth. This result is unexpected and worthy of additional confirmation.

    - Heat P, having intermediate cleanliness and intermediate free nitrogen, consistently cracked in the as-cold worked condition. It also showed evidence of incipient cracking in the stress relieved specimen that was tested at the lower displacement rate.

These results are strongly suggestive that both cleanliness and free nitrogen strongly influence susceptibility to CCG. The fact that a clean heat, Heat O, having intermediate free nitrogen level did not crack suggests that the role of cleanliness appears to be greater than that of free nitrogen. This is good news, in that cleanliness appears to be easier to determine and control than free nitrogen. Limits have not been set in either case, but the temper embrittlement and stress relief cracking expressions appear to provide a means for ranking heats and eventually setting limits on allowable alloying element levels.

During the course of this investigation, the question arose as to how such an expression might be modified to provide an improved tool for pre-sorting prospective heats with respect to their ability to resist CCG. The results of this work suggest that such a predictive expression would need to take into account the influence of tramp elements, free nitrogen, (and perhaps residual elements). Obviously, for the case at hand, four heats is far to few to develop a statistically supported relationship, but it would be possible, given the test methodology developed in this work, to quickly develop the relatively large data base of results needed to support development of such an expression, provided test materials are made available.

Crack Growth Rate Versus C*:

The test results for those specimens that experience CCG are plotted below as crack growth rate versus C*.

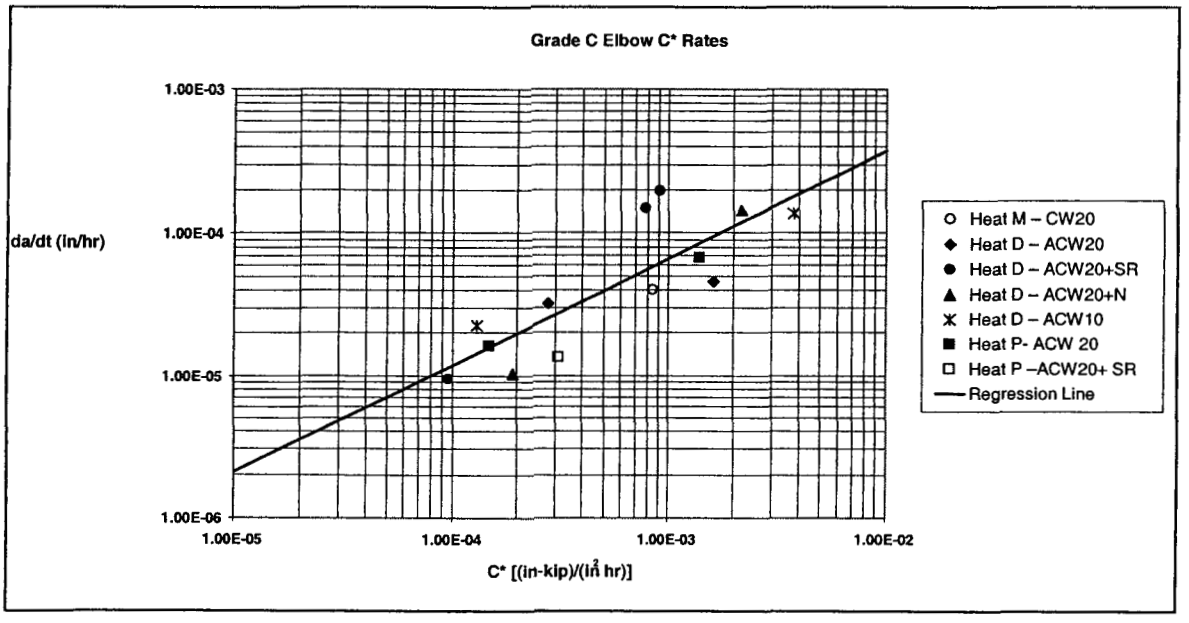

Figure 1: Creep Crack Growth Rate as a Function of C*

Also shown on the graph is a linear regression fit to the data (in log-log space).
One of the implications of these data and the curve is that, given a susceptible material, the crack growth rate can be controlled by controlling those factors that influence C*. Recall that C* (from Annex B) is a function of crack length, the applied load, the creep properties of the material and the specimen geometry. Annex F makes the argument that, implicit in the C* expression are the yield strength properties of the materials, and that all things being equal, materials having lower yield strengths can be expected to demonstrate lower C* values, and therefore experience lower creep crack growth rates.

Earlier it was stated that, for the case of a very susceptible material, such as Heat D, the reported CCG test results seemed to show no apparent benefit in performing the normalization heat treatment. The basis for this was that the post-bend heat treatment did not inhibit crack initiation in any of the test samples from the most susceptible heat, i.e. for Heat D. Further analysis, however, suggests that post-bend heat treatment may be beneficial due to the fact that it reduces the yield strength of the material, and thus reduces the applied C*. A lower C* value implies a lower crack growth rate. This can be inferred from Figure 1, but it is elaborated in detail in Annex F. So, given the lower yield strength for Heat D after stress relief or normalization (Annex B), it can be rationalized that this material might well have experienced a longer service life had it been heat treated after bending.

One area worthy of further consideration in this regard is that tests results seem to indicate that borderline heats (Heat M and Heat P) tend to benefit from the stress relief and normalization heat treatments. These heat treatments can have a beneficial influence on a number of the proposed contributing factors, i.e. residual stress, hardness, strength, free nitrogen content, microstructure, etc. Further testing would be needed to confirm the benefit and to understand the reason(s) for it.

Metallurgical Evaluations

Metallurgical evaluations were undertaken to characterize and hopefully correlate the pipe metal microstructure with performance in the tests. The details of these are provided in Annex E.

After CCG testing was completed, each of the (22) test specimens listed in the Results Matrix (Table 7) was examined using low power optics to confirm the presence or lack of cracking. On completion of the visual examination, the samples were sectioned into two pieces along the center-line of the specimen in the direction of crack extension. One of these two halves was prepared as a metallographic specimen. This specimen permitted an accurate physical measurement of the crack length at the mid-point in the crack front. The metallographic specimen also was used to examine the microstructure, in an attempt to correlate it with the performance of the material. This examination also confirmed the crack path and lack of ductility associated with crack extension during testing. This evidence was further confirmation that these test method did indeed generate cracking by the desired low temperature creep mechanism.

In some cases, the half of the test specimen that was not used in the metallographic examination was carefully broken open to allow an examination of the fracture surface. The fracture surface also provided further confirmation of the mode of crack extension during test. It also was used to correlate fracture features with the underlying microstructure.

Examination of the microstructure revealed tight, oxide-lined, intergranular cracks to be associated with the region of the fracture surface associated with creep crack growth. For the particularly susceptible heat, Heat D, grain boundary separations were noted adjacent to, but away from, the fracture surface, (see Figure E-17c in Annex E). These also are consistent with creep and/or embrittled grain boundaries. Of particular note is that, in at least one case, Heat D exhibited out-of-plane cracking (see Figures E-34, E-35, and E-43 through E-45). This specimen cracked along a plane that was parallel to the load axis. The crack path in this case was predominantly intergranular and suggests that these locations were very weak. This evidence further supports the negative influence of tramp elements in that Heat D was the dirtiest heat. It also supports the role of free nitrogen in that Heat D had the highest levels of this potential bad actor. Unfortunately, energy dispersive analyses were not adequate to conclusively confirm enrichment at, or near, to these affected boundaries. Further work with more sensitive tools, such as Auger electron spectrometry, would be needed to investigate this more fully.

A preliminary assessment suggested that some of the heats had a banded microstructure which may have contributed to test performance; however, no firm conclusions could be drawn in this regard. It should be noted that the normalization heat treatment appeared to diminish the appearance of banding, as might be expected.

It should lastly be pointed out that bulk hardness tests were performed on all (22) samples. While these showed the expected trends with regard to heat treatment and otherwise, no correlations could be made between hardness and material performance.

Application of Findings

One benefit of this work is that the results have been used in conjunction with the PCCREEP life prediction computer code developed earlier. This was confirmed by employing this computer code to calculate the life of the service-failed heat. The excellent life prediction in this regard further substantiates the power of the PCCREEP computer code life prediction methodology, and demonstrate that it can be adapted to the case at hand. The details of this work are provided in Annex F.

Conclusions

This work led to the following conclusions:

1. A valid test specimen and test technique were developed which can be used to identify heats and material conditions that are susceptible to low-temperature creep crack growth.

2. Difficulties in obtaining material resulted in a test matrix that fell short of the original plan; however, a number of significant findings could be deduced from this work, including:

    a. Steel cleanliness appears to strongly influence sensitivity to CCG.
    b. The same statistically-based equations that predict sensitivity to temper embrittlement and stress relief crack, also appear to predict the relative sensitivity to CCG for candidate heats.
    c. Free nitrogen appears also to be influential, however, the limited data available suggests that this influence is somewhat less than that of material cleanliness.
    d. The influence of residual alloying elements could not be conclusively determined based on this work. The fact that the tramp elements and residual elements followed the same trends may well have masked interactions and/or contributions.
    e. The aluminum-to-nitrogen ratio is not a reliable indicator of the amount of free nitrogen in the material.

3. Stress relief and normalization heat treatments appeared to have a beneficial effect on the test performance of marginal heats. These however were not able to improve the performance of an extremely susceptible heat.

4. Analysis suggests that the reduction in yield strength associated with post-bend heat treatment may result in an increase in service life for those materials that are crack susceptible.

5. Post-bend heat treatment does not appear consistently to reduce the level of free nitrogen in the material.

Recommendations

The work described herein lays a solid foundation for understanding and correcting problems associated with low temperature time-dependent cracking. However, a significant amount of work remains before this fully can be resolved.

The following recommendations are offered for follow-on work:

1. Further refinements to the test method – there would be some benefit in separating this work into two separate investigations, one addressing crack initiation, and the other crack propagation. The benefits and drawbacks of pre-cracking should fully be explored.
2. Further refinements to the specimen design – this would address the orientation of the specimen relative to the crack propagation path in service. The implication of corner cracking should fully be explored and addressed.
3. Determine conclusively the mechanism and contributing factors – this likely would involve comparative Auger and/or microprobe analysis of grain boundaries from good and bad heats of material. It likely also would involve employing more sensitive analytical tools to confirm the role of free nitrogen and perhaps the residual elements.
4. Increase the statistical base and develop predictive expressions for selecting heats for materials – it is envisioned that expressions such as those developed for temper embrittlement and stress relief cracking might also be developed for predicting sensitivity to low temperature CCG.
5. Provide further confirmation that the life prediction model relative to this damage mechanism – this work likely would involve application of the model to additional case studies.

Submitted by:

Joe Bloom/EDR

J. Bloom, Consultant

Ed Robitz

E. S. Robitz, Senior Principal Engineer

Bruce A Young

B. A. Young, Research Engineer II

W A VanderSluys/EDR

W. A. VanDerSluys, Consultant

Approved by:

D F LaCount

D. F. LaCount, Manager

References

1. W. R. Apblett, Jr., "Reasons For and Prevention of Riser and Feeder Failures in Large Utility Type Boilers", Foster Wheeler Report FWC/RN-247, May 1981.

2. "B&W Asks Customers to Inspect Boiler Tubing After Series of Failures", Electrical World Week, December 28, 1970.

3. M. Prager, Minutes of Materials Property Council Workshop on "Mechanisms and Causes of Cracking in Carbon and Low Alloy Steel Boiler Piping at Intermediate Temperatures", held in conjunction with the ASME Pressure Vessel and Piping Conference, June 1991.

4. I. A. Shibli, "Investigation of a Failure Problem in Cold-Bent Boiler Riser and Supply Pipes", International Journal & Pressure Vessel and Piping, 24, 1986, pp. 303-336.

5. I. A. Shibli, "Creep Crack Growth Characteristics of Pre-Strained C-Mn Steels at 360 C", Materials Science and Technology, 3, February 1987, pp. 110-117.

6. D. J. Gooch, "The Effect of Cold Work on Low Temperature ($0.35T_m$) Creep Crack Growth in C-Mn Steels", Materials Science and Engineering, 64, 1984, pp. 183-196.

7. D. J. Gooch, "The Effect of Microstructure on Creep Crack Growth in a C-Mn Steel at 360 C", Materials Science and Engineering, 83, 1986, pp. 17-27.

8. G. J. Neate, "Creep Crack Growth in Cold Formed C-Mn Steel at 360 C", Materials Science and Technology, 3, 1987, pp. 14-22.

9. D. J. Gooch, J. R. Haigh and B. Liking, "Relationship Between Engineering and Metallurgical Factors in Creep Crack Growth", Metal Science, November, 1977, pp. 545-550.

10. Roan, D.F., and Seth, B.B., "Metallographic and Fractographic Study of he Creep Cavitation and Fracture Behavior of 1Cr1Mo0.25V Rotor Steels with Controlled Residual Impurities", *Ductility and Toughness Considerations in Elevated Temperature Service*, MPC 8, ASME, NY, 1978.

11. Brear, J.M., and King, B.L., "Proceeding of the Conference on Grain Boundaries", The Metals Society, London, 1976.

Annex A – Materials Issues

The material test matrix was defined based on input from domestic and European experience.

It is well understood that those factors that lead to reduced creep ductility also lead to a notch sensitivity that results in an increase in susceptibility to creep crack growth.

However, in sorting this out for the case at hand, it is appropriate, first, to start by considering the factors common to this type of service failure. This evidence is summarized as follows:

- Crack initiation occurs at the O.D. surface of the pipe along the extrados of a cold bend.
- These cracks initiate at relatively minor surface imperfections, perhaps, pipe-making laps or seams that are aligned with the axis of the pipe.
- Evidence suggests that the surface imperfection(s) that are associated with initiation serve as a region of local stress concentration.
- Cracks form at grain boundaries in this region, and propagate intergranularly in a radial direction toward the I.D. surface of the pipe.
- As the crack grows it transitions to a tearing mode and ultimately terminates in a shear lip when the remaining ligament separates due to tensile overload.
- The crack is driven under the influence of a circumferential stress that is induced by internal pressurization of the pipe.
- Flattening (ovaling) of the pipe will increase the magnitude of the circumferential stress that drives the crack.
- The fact that the pipe was cold bent will negatively influence the stress field in the vicinity of the imperfection due to the residual stresses inherent in the bending operation.
- Installation fit-up issues also contribute to increased residual stresses in pipe.
- The cold bending operation also will negatively affect the susceptibility of the pipe material to creep crack growth due to the influence of strain hardening on the properties of the pipe material.
- Two types of carbon-manganese steel pipe are of concern SA 210, Grade C and SA 106 Grade C.
- Some heats of pipe perform better than others. The following have been identified as potential contributing factors:
    - Free nitrogen content.
    - Cleanliness.
    - Alloy content.
    - Microstructure, including grain size.
    - Hardness.
    - Strength.

With the above in mind the following approaches have been proposed as having the potential to mitigate the problem. This summarizes the results of a Materials Properties Council workshop to survey the problem (3).

Problem:	**Approach:**	**Reported Experience:**	**Drawback:**
Surface imperfections act as initiation site.	Tighten requirements on pipe making.	This approach has been taken by one manufacturer who reported favorable results when the bending operation is followed by stress relief.	Increased costs for pipe.
Pipe bending and/or pipe installation residual stresses assist in driving the crack.	Perform stress relief or normalization heat treatment after bending.	See above.	Increased processing costs.
Pipe flattening and/or ovaling increases circumferential stress.	Limit bend ratio.	One manufacturer reports good results when the minimum bend ratio is 4:1	Limits design options.
Some steel microsturctures are more susceptible than others.	This should not be a problem in that these pipes typically have a ferrite-pearlite microstructure. However, some may be more banded than others.	Not addressed in literature or otherwise.	
Minimize free nitrogen.	Use aluminum-killed steel with an adequate total Al: total N ratio to ensure that all of the nitrogen is combined.	European experience suggests good results with using aluminum-killed steels.	Aluminum becomes ineffective when it combines with other constituents in the steel, particularly oxygen.
High levels of tramp elements.	Specify cleaner steel.	Some investigators show a benefit while others do not.	Potentially increased cost for pipe.
Alloy content exacerbates impact of tramp elements.	These can be specified once allowable limits are defined.	No experience.	Not clear.
Hardness / strength.	These can be specified once allowable limits are defined.		These may require post-bend heat treatment to re-establish allowable levels.

The goal of the testing described herein was to provide additional data that further would shed light on both the mechanism of cracking and the benefits of the various palliative approaches prescribed above.

The approach taken was to select steels that satisfied a material matrix of good and bad conditions. It was desired to take these steels from the general population of commercially available pipe material. Based on this, and due to the reported European and domestic experience, it was decided that steel cleanliness and the availability of free nitrogen would likely present first order effects, in that, both of these are known to affect the creep ductility and notch sensitivity of steel.

It also was understood that the levels of residual alloying elements such as nickel, chromium, molybdenum, manganese, titanium, silicon, aluminum, boron etc. can affect creep ductility through a variety of proposed mechanisms. It has been postulated that some of these alloying elements can affect partitioning of tramp elements to the boundaries. They also can affect strengthening within the grain matrix itself. Others also may participate in processes that lead to a "denuded" zone adjacent to grain boundaries. While these are real concerns, for the purpose of this work these were assumed to have only second order effects, and therefore were only somewhat taken into consideration in selecting the heats for test. It is believed that this assumption was well borne out for the purposes of this investigation. Nonetheless, offered for consideration is the following expression (per Ito and Nakanishi (12)) that has been proposed to describe the sensitivity of candidate steels to strengthening of the grain matrix, and perhaps weakening of the boundary based on carbide-forming and solid solution strengthening tendencies.

$$I_i = Cr + (2.0)Mo + 10(V) + 7(Nb) + 5(Ti) + Cu - 2$$

In a similar manner the grain size (in particular the prior austenite grain size) of the pipe material is known to have an effect, with smaller grain sizes being preferred. The rationale for this is that smaller grain sizes provide for more surface area per unit volume over which to distribute tramp elements and other bad actors. While the grain sizes for these samples were recorded, the grain size was not a variable that was taken into account in selecting the heats of material for test. Nonetheless, it later will be shown (in Appendix E) that these were fairly consistent from heat to heat.

Material hardness and strength also may have had a first order effect; however, for the sake of limiting the initial number of variables it was assumed that these would be fairly consistent for the grade of steel under consideration. As will be shown later (in Appendix E), this assumption was fairly well borne out. Also, well borne out was the assumption that the microstructure of these steels would be consistently ferrite-pearlite; however, microstructural variability in terms of the extent of banding was not controlled in the as-received pipe specimens.

Based on the above, materials were sought to fill out the desired test matrix.

Amount of Free Nitrogen

Cleanliness	**Low Free Nitrogen**	**High Free Nitrogen**
Clean	**X**	**X**
Dirty	**X**	**X**

With the target matrix established, the next step is to decide how to define "cleanliness" and, how "high and low" free nitrogen. However, as will be shown, due to practical considerations, even this simplified matrix was difficult to fill using commercially available materials.

"Cleanliness": It is well established that the elemental constituents that give rise to temper embrittlement and stress relief cracking also reduce the creep ductility (and increase the notch sensitivity) of a material. These constituents are not intentionally added to steel and their presence comes about due to impurities that were introduced, and not removed, during the steelmaking process. These typically are termed "tramp" elements, and those steels with high levels of tramp elements are termed "dirty". The specific elements of concern are antimony, tin, phosphorous, arsenic, sulfur, (and copper) in anticipated descending order of impact. Note that the magnitude of impact has been correlated with the level of atomic radius mismatch between the tramp element and the matrix. Various authors have performed statistical analyses to derive mathematical expressions that can be used to predict the sensitivity of steel to temper embrittlement and/or stress relief cracking.

Roan and Seth (13) have developed an expression wherein temper embrittlement sensitivity is predicted by an effective impurity content factor (I_s), where:

$$I_s = 16.1(Sb) + 13.8(Sn) + 12.6(P) + 10.5(As) + 8.8(S)$$

The values in parentheses are the percentage by weight of the various objectionable tramp element constituents. Accordingly, steels having a high effective impurity content would be prone to temper embrittlement (and presumably creep crack growth).

In a similar manner, Brear and King (14) have developed an expression wherein stress relief cracking sensitivity is predicted by an impurity parameter (I_b), where:

$$I_b = 2.7(Sb) + 1.9(Sn) + 1.0(P) + 1.8(As) + 0.44(S) + 0.20Cu$$

Industry was approached to identify a pool of candidate heats. Then, these expressions were employed to rank the heats in terms of cleanliness. In the end, four candidate heats were identified based on mill certified compositions. These were reconfirmed upon receipt of materials. Table A-1 provides the composition of the four candidate heats per the confirmatory analyses. Table A-2 provides the results of the sensitivity calculations which were recalculated based on the confirmatory analyses.

Review of the results of the sensitivity calculations shows that Heat D is the dirtiest steel by either means of calculation. Heat O is the cleanest, and Heats M and P are intermediate with Heat M being slightly cleaner than Heat P. Originally, it was intended, as per the matrix described above, to use heats of material that clearly fell into "clean" and "dirty" categories. However, the sensitivity calculations reveal that two of the heats are intermediate. Since there is no reference value that delineates clean from dirty, it was decided to use three categories to describe these four heats: clean, dirty, and intermediate.

As an aside, Table A-3 shows the results when the same four heats are evaluated to assess the residual alloying element impact according to the Ito and Nakanishi expression. As can be seen this expression ranks the heats in the exact same order as either of the expressions that attempt to characterize the tramp element contribution, (compare Table A-2 with Table A-3). Based on this, these heats cannot be used definitively to determine the relative impact of tramp and residual elements. Nonetheless, literature seems to lend greater confirmation to the role of tramp elements.

Free Nitrogen:

The theoretical impact of the tramp elements is that they weaken grain boundaries relative to the grain matrix causing creep strains to be localized into these narrow regions, and effectively act as embrittling agents. Free nitrogen also is postulated to affect strain localization at grain boundaries. However, in this case rather than by weakening grain boundaries, nitrogen is postulated to act by strengthening the grain matrix relative to the boundaries. This is thought to occur through a "strain aging"-type mechanism. The mechanism requires the availability of the elemental nitrogen that is free to diffuse through the matrix to high dislocation density sites where it congregates and acts to inhibit further dislocation movement, thus, strengthen the material locally in that region.

It is important to understand the distinction between the elemental ("free") nitrogen, and the total nitrogen content of the steel. Nitrogen has a tendency to combine with certain constituents in steel, such as aluminum, and when the combined form is stable the nitrogen is not free and able to diffuse through the matrix. As an approximation, it is assumed that the driving force for aluminum and nitrogen to combine is compelling, and a that this reaction will occur to the extent that the stoichiometric ratio is met. In other words, the first-cut assumption is that, if there is enough uncombined aluminum available, then, all of the nitrogen will be combined with the aluminum, and therefore not free to diffuse through the matrix.

Based on this understanding, and due to the desire to identify heats having both low and high free nitrogen in order to complete the test matrix, the approach was taken to assume that aluminum-killed heats would have low free nitrogen. Heats that were silicon-killed, or otherwise, were assumed to have high free nitrogen.

As was mentioned earlier, four candidate heats were identified based on their impurity levels. The intent was to have two high-impurity heats, one with high and one with low free nitrogen. These were selected based on the chemical analyses reported on the mill

certificates, one heat was aluminum-killed, the other not. Likewise, two low-impurity heats similarly were selected. As was discussed earlier, when in-house analyses were performed to confirm composition, it was decided that, from a cleanliness point of view, rather than having two heats with high impurity levels and two with low levels, the projects had one heat high, one heat low, and two with intermediate levels of impurities. Knowing this, analyses were undertaken to verify the free nitrogen content.

Table A-4 shows the aluminum to nitrogen ratio based on the in-house analyses. Table A-5 shows a further refinement of this wherein the fact that some of the aluminum in the steel is combined with oxygen, and therefore is not free to combine with nitrogen. To address this, the ratio of soluble aluminum to total nitrogen was calculated. Review of this suggests that the heats would be predicted to be ranked as follows in terms of free nitrogen content, as ranked from low to high: Heat O, M, and P, then D.

Due to the emphasis placed on free nitrogen content by the European experience, further testing was undertaken to confirm conclusively that the free nitrogen rankings inferred from the aluminum to nitrogen ratio were valid. To do this, the free nitrogen content was measured directly by two separate laboratories.

The Sheffield Hallam University employed the Hedridge & Long method wherein the sample is heated at 450 °C and the hydrogen that out-gasses is captured and measured after it is combined with nitrogen. Sheffield Hallam indicated that the nitrogen content provided by this method would include the nitrogen in pores and that which resides uncombined at grain boundaries and other positions within the lattice. Sheffield Halllam indicates that their experience suggests that 60 ppm of nitrogen by this method equates to roughly 20 ppm nitrogen by the internal friction method. Thus, they are implying that only about one-third of the free nitrogen would be involved in strengthening the matrix. The results of their testing are provided in Table A-6.

Also note from this table, that the free nitrogen content was measured for the different material conditions that each heat experienced (more about these material conditions later). In this table, the as-cold worked condition would be expected to reflect as-received free nitrogen content. The other tests would show the effect of stress relief and normalization heat treatments on free nitrogen content.

Comparison of the results in Table A-6 with those predicted from the aluminum to nitrogen ratio (Table A-5) reveals that the aluminum to nitrogen ratio predicts general trends, but a high aluminum to nitrogen ratio cannot be used as conclusive evidence of low free nitrogen. This is of particular importance because this ratio is relatively easy to control and is easy to determine using standard chemical analysis. Thus, it would be the preferred approach to ensuring low susceptibility to strain aging. On the other hand, free nitrogen determinations are more involved and subject to error for a number of reasons including the fact that there are no reliable reference standards available to verify the accuracy of a test. Based on this, confirmation of the free nitrogen content was sought through testing at another laboratory.

Free nitrogen contents were also determined at the The Welding Institute (TWI). TWI used a somewhat different approach. First, they determined the total nitrogen content via the Leco fusion method. Then, they out-gassed the "soluble" nitrogen at 450 °C for one hour. TWI indicated that this "soluble" nitrogen would include any nitrogen that was free in the lattice, along with nitrogen bound as the less stable iron and manganese nitrides. Inclusion of these nitrides suggest the possibility that these analyses might over-predict the amount of free nitrogen. TWI further indicated that the out-gassing would likely extract only about 80 to 90 % of the soluble nitrogen. This obviously would lead to an under-prediction of free nitrogen. The relative effects of these somewhat offsetting influences is not clear. In any case, it seems that these same influences also would affect the results reported by Sheffield Hallam University in that there approach employs a similar out-gassing technique.

Per TWI, after the soluble nitrogen has been out-gassed at 450 °C for one hour, the nitrogen that remains in the sample is in the form of stable nitrides, such as those involving: titanium, boron, niobium, and vanadium. TWI terms this "residual" nitrogen. The residual nitrogen content then is determined via the Leco fusion method (same technique as for total nitrogen, only after out-gassing). Then, the residual nitrogen content is subtracted from the total nitrogen value to determine the amount free (soluble) nitrogen. The results of the TWI testing are provided in Table A-7. Review of this table reveals that, while the TWI analysis does not yield exactly the same free nitrogen content as reported by Sheffield Hallam University, nonetheless, the two techniques rank the heats in exactly the same order. The fact that these two direct analyses are not consistently in line with the ranking of these heats based on the aluminum to nitrogen ratio brings into question the validity of using this approach for selecting future heats.

Revised Test Matrix:

Based on the above, and considering the analysis results for the four test heats, the material test matrix can best be described per below:

Amount of Free Nitrogen

Cleanliness	**Low Free Nitrogen**	**Intermediate Free Nitrogen**	**High Free Nitrogen**
Clean	--	Heat O	--
Intermediate	Heat M	Heat P	--
Dirty	--	--	Heat D

Again, as a reminder, the "intermediate" designation for both cleanliness and for the amount of free nitrogen comes about because the test results did not yield two heats for each of the extreme cases. Rather, one heat clearly represented the low extreme, and one heat the high extreme, and the other two heats fell between them. This further was complicated by the fact that there is, at this point, no clear definition as to what level of, for instance, free nitrogen would be considered "high". Thus, it was necessary to use comparative terms such as "best" or "worst", or "highest" and "lowest", and to allow the testing to further discriminate between the qualities of these candidate heats.

Free Nitrogen as a Function of Heat Treatment:

Review of Tables A-6 and A-7 suggests that heat treatment does not consistently reduce the amount of free nitrogen in a given heat of steel. In some cases, it holds that increased heat treatment temperatures result in a reduction in free nitrogen (e.g. Heat P). In the worst case (e.g. Heat D), it clearly does not. Additional work would be needed to verify the repeatability of these results, and if valid, to understand the response of these materials.

Final Test Matrix:

With the four candidate heats selected and characterized, the test matrix was finalized by introducing and controlling variables that addressed the level of cold work in the material. Analyses were undertaken to develop a method for introducing a controlled level of plastic strain into specimens prior to test. The resultant technique is described elsewhere (Annex B). The 20% strain level was selected as being typical of service. A 10% strain level was also investigated (for Heat D, the worst case material) to gain insight as to whether there was a threshold strain for cracking.

With the prestraining technique developed and employed, it finally was necessary to address the question as to whether subsequent heat treatment would mitigate the cracking problem. To this end, specimens that had been previously strained (20%) were either stress relieved (at 1250 °F for 1 hour) or normalized (at 1600 °F for 1 hour). The final test matrix is as follows:

Heat	Condition	Free Nitrogen	Cleanliness
0	ACW20	Intermediate	Good
M	ACW20	Low	Intermediate
M	ACW20 + SR	Low	Intermediate
M	ACW20 + N	Low	Intermediate
P	ACW20	Intermediate	Intermediate
P	ACW20 + SR	Intermediate	Intermediate
P	ACW20 + N	Intermediate	Intermediate
D	ACW10	High	Poor
D	ACW20	High	Poor
D	ACW20 + SR	High	Poor
D	ACW20 + N	High	Poor

Where:
ACW20 = As-cold worked (20%)
ACW10 = As-cold worked (10%)
SR = Stress relieved.
N = Normalized

References

1. Prager, M., Minutes of Materials Property Council Workshop on "Mechanisms and Causes of Cracking in Carbon and Low Alloy Steel Boiler Piping at Intermediate Temperatures", held in conjunction with the ASME Pressure Vessel and Piping Conference, June 1991.

2. Ito, Y. and Nakanishi, M., ITW Document Y-668-72, 1972.

3. Roan, D.F., and Seth, B.B., "Metallographic and Fractographic Study of he Creep Cavitation and Fracture Behavior of 1Cr1Mo0.25V Rotor Steels with Controlled Residual Impurities", *Ductility and Toughness Considerations in Elevated Temperature Service*, MPC 8, ASME, NY, 1978.

4. Brear, J.M., and King, B.L., "Proceeding of the Conference on Grain Boundaries", The Metals Society,

Table A-1: Composition of Candidate Heats (wt.%)

	C	Mn	S	P	Si	Cr	Ni	Mo	Cu	Al	Al(sol)	V	Nb	Co	Sn
SA106, Gr. C	0.35 max	0.29 – 1.06	0.058 max	0.048 max	0.10 min	--	--	--	--	--	--	--	--	--	
SA 210, Gr. C	0.35 max	0.29 – 1.06	0.035 max	0.035 max	0.10 min	--	--	--	--	--	--	--	--	--	
Heat M	0.25	0.46	0.021	0.007	0.18	0.10	0.10	0.04	0.05	0.011	0.0078	0.001	0.001	0.007	0.005
Heat O	0.18	1.05	0.007	0.006	0.23	0.05	0.02	0.02	0.01	0.021	0.0163	0.001	0.001	0.003	0.001
Heat P	0.20	0.82	0.008	0.006	0.33	0.05	0.06	0.02	0.14	0.026	0.019	0.001	0.002	0.009	0.011
Heat D	0.26	0.68	0.01	0.008	0.24	0.15	0.11	0.02	0.22	0.004	--	0.001	0.001	0.011	0.015

	Ca	Ti	B	As	Pb	Sb	O	Zn	W	N(total)
SA106, Gr. C	--	--	--	--	--	--	--	--	--	--
SA 210, Gr. C	--	--	--	--	--	--	--	--	--	--
HeatM	--	0.002	0.0001	0.007	0.001	0.0018	0.0044	--	--	0.0055
Heat O	0.0013	0.001	0.0003	0.0024	0.0017	0.0006	0.006	--	--	0.0047
Heat P	0.0021	0.003	0.0001	0.0087	0.0029	0.0039	0.0048	0.001	--	0.0079
Heat D	0.0015	0.001	0.0001	0.013	<0.001	0.004	--	--	0.003	0.011

Table A-2: Sensitivity Calculation Results

Test Material	Temper Embrittlement Sensitivity, (I_s)	Stress Relief Cracking Sensitivity, (I_b)	Rank
Heat M	0.44	0.053	Intermediate
Heat O	0.19	0.019	Best
Heat P	0.45	0.085	Intermediate
Heat D	0.60	0.119	Worst

Table A-3 Alloying Element Contribution Calculation Results

Heat	I_i	Rank
M	0.26	Intermediate
O	0.12	Best
P	0.27	Intermediate
D	0.43	Worst

Table A-4 Aluminum (Total) / (Total) Nitrogen Ratio

Heat	Cleanliness	Al, (total) (wt.%)	N(total) (wt%)	Al (tot) : N (tot) (wt.%)
O	Clean	0.021	0.0047	4.47
M	Intermediate	0.011	0.0055	2.00
P	Intermediate	0.026	0.0079	3.29
D	Dirty	0.004	0.0110	0.36

Table A-5 Aluminum (Soluble) / (Total) Nitrogen Ratio

Heat	Cleanliness	Al, (soluble) (wt.%)	N(total) (wt%)	Al (sol) : N (tot) (wt.%)	Predicted Free Nitrogen Level
O	Clean	0.0163	0.0047	3.47	Lowest
M	Intermediate	0.0078	0.0055	1.42	Low Intermediate
P	Intermediate	0.019	0.0079	2.40	High Intermediate
D	Dirty	0.004	0.0110	0.36*	Highest

- Soluble aluminum was below the detection limit so this value represents the greatest possible ratio.

Table A-6 Nitrogen Determination Results per Sheffield Hallam University

Heat	Condition	Total Nitrogen Per Leco Method, (ppm)	Free Nitrogen, (ppm) Per Hedridge & Long Technique	Ranking of Heats Based on Free Nitrogen (As-Received)
M	As-Cold Worked	40	12	Best
	Stress Relieved	50	9	
	Normalized	50	5	
O	As-Cold Worked	40	30	Intermediate
P	As-Cold Worked	60	32	Intermediate
	Stress Relieved	60	12	
	Normalized	60	5	
D	As-Cold Worked	110	60	Worst
	Stress Relieved	110	30	
	Normalized	110	62	

Table A-7 Nitrogen Determination Results per TWI

Heat	Condition	Total Nitrogen, (ppm)	Resitual Nitrogen, (ppm)	Soluble (Free) Nitrogen, (ppm)	Ranking of Heats Based on Free Nitrogen (As-Received)
M	As-Cold Worked	55	36	19	Best
	Stress Relieved	45	34	11	
	Normalized	53	29	24	
O	As-Cold Worked	59	25	34	Intermediate
P	As-Cold Worked	66	36	30	Intermediate
	Stress Relieved	58	56	2	
	Normalized	64	61	3	
D	As-Cold Worked	114	67	47	Worst
	Stress Relieved	126	64	62	
	Normalized	123	32	91	

Annex B – Test Design

Material Pre-Straining:

Recall that it was desired that test materials be pre-strained to a level typical of service (20%). A lower level of pre-strain (10%) also was required to test the threshold limits for this influential factor. One way to achieve this might have been to extract the test specimens from cold-bent pipe; however, only limited amounts of pipe material were available from the four test heats. To conserve this material an alternate route was devised wherein, finite element analysis (FEA) was used to develop a specimen design which would allow the pipe material to be plastically pre-strained in tension. The FEA identified a geometry in which there was enough constraint to obtain the desired strain levels. This is in the form of a "dog bone" specimen, see Figure B-1. A few specimens were fabricated for the purpose of verifying the FEA model.[1]

Once the FEA model was verified, the additional specimens were machined. Prior to pre-straining, a pre-measured grid was marked onto the samples using a hardness indentations. Hardness marks were placed on each sample which included eleven rows with five columns in each row. This grid allowed the relative strain to be measured after the dog bone was loaded in tension. The grid configuration allowed for the measurement of the applied plastic strain gradient in the axial direction. The measured strain profiles for each dog bone specimen can be found in Appendix B-1.

In most cases, CCG test specimens were extracted from the dog bone such that the test region in the center of the CCG test specimen corresponded to the 20 to 25% strain region in the dog bone. Recall however that similar specimens were needed to test the 10% strain level, and these were generated in a similar fashion.

Material Conditioning via Heat Treatment:

Recall from the test matrix, that three specimen conditions were required to complete the test matrix: as-cold worked, stress relieved, and normalized. The as-cold worked were extracted directly from the pre-strained dog bones as described above. The other specimens were extracted from the pre-strained dog bones (20%) after these had been exposed to a subsequent stress relief or normalizing heat treatment: The conditions for these are as follows:

Stress Relief (SR):	1125 ± 25°F ½ hour
Normalization (N):	1600 ± 25°F ½ hour

Samples were air-cooled after heat treatment. These then were machined into test specimens, with care taken to preserve material properties. The test specimen geometry is discussed later in this annex. The machining sequence involved rough machining to establish the specimen outer dimensions. The EDM notch was then machined at mid-section, followed by

machining of the side grooves. Care was taken at each step to ensure the proper geometry and to minimize the influence of machining on the material properties.

A number of specimens were needed to fulfill the desired test matrix and to provide supportive tensile data. The following table shows the specimen designations, the heat-treatment subset, and the specimen configuration removed from the base sample.

TableB-1 – Sample Conditions and Specimen Types

Sample Number	Specimen Type	Condition		Sample Number	Specimen Type	Condition
M-1	Tensile	ACW20		O-1	Tensile	ACW20
M-2	CCG	ACW20		O-2	CCG	ACW20
M-3	CCG	ACW20		O-3	CCG	ACW20
M-4	CCG	ACW20		O-4	CCG	ACW20
M-5	Tensile	ACW20+ SR		O-5	Creep	ACW20
M-6	CCG	ACW20+ SR				
M-7	CCG	ACW20+ SR		P-1	Tensile	ACW20
M-8	CCG	ACW20+ SR		P-2	CCG	ACW20
M-9	Tensile	ACW20+ N		P-3	CCG	ACW20
M-10	CCG	ACW20+ N		P-4	CCG	ACW20
M-11	CCG	ACW20+ N		P-5	Tensile	ACW20+ SR
M-12	CCG	ACW20+ N		P-6	CCG	ACW20+ SR
				P-7	CCG	ACW20+ SR
K-1	Tensile	ACW20		P-8	CCG	ACW20+ SR
K-2	CCG	ACW20		P-9	Tensile	ACW20+ N
K-3	CCG	ACW20		P-10	CCG	ACW20+ N
K-4	CCG	ACW20		P-11	CCG	ACW20+ N
K-5	Tensile	ACW20+ SR		P-12	CCG	ACW20+ N
K-6	CCG	ACW20+ SR		P-13	Creep	ACW20
K-7	CCG	ACW20+ SR		P-14	Creep	ACW20+ SR
K-8	CCG	ACW20+ SR		P-15	Creep	ACW20+ N
K-9	n/a	---		P-16		ACW20
K-10	Tensile	ACW20+ N				
K-11	CCG	ACW20+ N				
K-12	CCG	ACW20+ N				
K-13	CCG	ACW20+ N				
K-14	Creep	ACW20				
K-15	Creep	ACW20+ SR				
K-16	Creep	ACW20+ N				
K-17		ACW20				
K-18	Tensile	ACW10				
K-19	CCG	ACW10				
K-20	CCG	ACW10				
K-21	CCG	ACW10				
K-22	Creep	ACW10				

Where: ACW20 = As-cold worked, with 20% pre-strain.
ACW10 = As-cold worked, with 10% pre-strain.
ACW20 + SR = As-cold worked, with 20% pre-strain, followed by stress relief.
ACW20 + N = As-cold worked, with 20% pre-strain, followed by normalization.

Tensile Tests:

Room and elevated temperature (650 F) tensile test data were needed as input to perform the calculations needed in assessing CCG. To conserve test materials, sub-sized tensile test specimens were used. Testing was conducted in accordance with ASTM E8 and ASTM E21. The test specimen geometry is shown in Figure B-2, (with 0.160 in. gage diameter).

Tensile data was obtained for the anticipated use in data analysis and data modeling. Details of the data model may be reviewed in Annex F. The following table summarizes the average tensile results for each subgroup at each temperature. Detailed data for each tensile test can be found in Appendix B-2.

Table B-2 – Summary of Tensile Tests

Heat	Condition	Nominal Test Temp. (°F)	R.A (%)	Elong. (%)	0.2% Y.S. (ksi)	UTS (ksi)	Strain Hardening Exponent (n)	Strength Coef. (a)
M	H / A	73	46.7	12.5	87.0	88.4	n/a	n/a
M	H / S	73	57.2	22.7	66.0	83.5	8.0	5.1
M	H / N	73	66.3	33.6	47.0	72.5	4.6	2.1
M	H / A	650	54.9	19.6	75.9	85.6	29.0	0.04
M	H / S	650	58.9	25.8	56.1	77.8	9.0	4.1
M	H / N	650	69.4	35.2	27.3	73.3	3.8	3.2
K	H / A	73	38.7	6.3	103.1	105.1	n/a	n/a
K	H / S	73	43.3	16.4	81.2	100.2	n/a	n/a
K	H / N	73	63.2	28.9	53.0	87.0	5.3	3.0
K	M / A	73	51.9	14.1	104.7	105.5	n/a	n/a
K	H / A	650	32.6	12.5	90.1	101.9	15.2	1.63
K	H / S	650	35.3	18.0	71.3	93.1	9.9	1.7
K	H / N	650	57.4	30.5	38.4	92.6	3.8	2.8
K	M / A	650	46.5	21.9	83.5	95.6	15.0	1.7
O	H / A	73	62.5	15.6	97.7	98.2	n/a	n/a
O	H / A	650	58.9	21.9	83.4	95.6	15.0	1.7
P	H / A	73	57.8	14.9	93.6	94.3	n/a	n/a
P	H / S	73	59.8	21.1	68.8	85.8	10.75	0.9
P	H / N	73	72.8	36.7	48.7	72.0	2.65	7.3
P	H / A	650	43.6	18.8	80.5	91.6	13.82	0.8
P	H / S	650	58.4	21.9	60.5	77.0	9.98	2.2
P	H / N	650	71.7	34.4	27.8	69.1	4.24	7.8

Condition H - High Pre-strain, M – Medium Pre-Strain, A – As Pre-strained, S – Stress Relieved, N – Normalized.

See Appendix B2 for Detailed Tensile Results.

CCG Specimens:

As previously discussed, during the course of the investigations into the field failures, investigations have shown that the cracking tends to initiate at an external imperfection at the extrados of the pipe and propagate inward. At the extrados of the pipe during the bending process a stress field is setup such that the imperfection can be modeled like a surface crack in tension. Since there are no standards for creep crack growth rate testing of a surface crack, an attempt to look at constraint for this condition was undertaken.

Since cracking occurs at these small imperfections, the ratio of the initial crack length to the wall thickness of the pipe is very small. The stress field at the extrados of the pipe near the surface is predominately a tensile stress field. For a short surface crack in tension stress field, the normalized T-stress is highly negative[2]. Since the normalized T-stress is negative, and the normalizing parameter is a positive stress, the T-stress is negative.

Since the T-stress for a short surface crack in a tensile stress field is negative; the biaxial stress ratio B is negative. For a laboratory specimen with these T-stress and biaxial stress characteristics and valid crack length to width ratio, the SEN(t) specimen was selected[3], see Figure B-3.

Since the specimens were long in comparison to the curvature of the pipe, the specimens were extracted from the pipe wall with the stress axis in the longitudinal orientation. The EDM notch was then oriented in the circumferential orientation. The goal of the project was to determine the material characteristics that would be contributors to creep crack growth. The described orientation does not align with the service failures, but early in this investigation, the test specimen orientation was not considered a primary effect as the material was believed to be homogeneous.

Once the specimen design was determined, an experimental approach was developed.

CCG Test Set-Up:

Although ASTM E1457[4] was used for guidance in the experimental approach, the test method chosen was a rising load, constant displacement rate test. The methodology and the idea for this approach were based upon rising load tests conducted in stress corrosion cracking (SCC) experiments. (Reference 4a)

The major advantage of testing the specimens under displacement rate control was the ability to stop the test prior to the specimen tearing apart. This was important to investigate the stress field in front of the crack tip. Another advantage (or disadvantage) is the stress is rising until cracking occurs. The disadvantage occurs when the displacement rate is too high.

Assuming the specimen will experience creep cracking, then cracking will be time dependent. If the displacement rate is too high, the stress field goes into a tearing mode

rather than a creep crack growth mode.[5] To try to avoid this, the experiments were run at slower and faster rates. The faster rate (0.016 in. per day) was tested initially.

Experiments were conducted using the initial rate. Some of the materials showed creep cracking while others did not. Since increasing the displacement rate would increase the stress rate, the decision was made to run a second set of tests at a lower displacement rate. The second displacement rate chosen was ten time slower or 0.0016 inches per day. Details of the experimental results can be found in Annex C.

The test is controlled using a linear variable-displacement transducer (LVDT) on the actuator of a servo-hydraulic test frame. The displacement rate of actuator rate was to a constant value. Two direct current displacement transducers (DCDT) were used to measure the displacement rates of the actual specimen.

During the experiments, data was collected using a data acquisition system. The data obtained during the experiments was data, time, load, DCDT voltages, potential drop voltage, and predicted crack length.

To comply with the ASTM standard, the specimens were side-grooved. The side-grooving was completed for two purposes. The first was to ensure a straight crack front. The second was to try to maintain in-plane constraint.

To pre-crack or not pre-crack:

Another important issue was discussed prior to running the experiments. The discussion topic was whether to pre-crack the specimens prior to CCG testing. Several factors entered into consideration. The following are the factors that lead to the discussion not to pre-crack.

1. While test preparations were being complete for these experiments, a new draft of ASTM E1457 was being prepared. The new version of ASTM E1457 was published in 2000. The new version allows EDM notches without pre-cracking.

2. The configuration of these specimens would require pre-cracking in bending. The stress field in the plastic zone at the tip of the crack would be wrong. This would have introduced a variable in testing.

3. The stress at which creep cracking occurs was unknown. Since this was the case, a final pre-crack stress would be difficult to determine.

4. Since the lap or fold at which the actual service failures occur are not sharp cracks, the phenomenon was know to occur from blunt stress risers.

After the experiments were complete, post-mortem analysis was conducted. Details of the post-mortem analysis can be found in Annex E. The post-mortem analysis has shown some compelling reasons that pre-cracking should have been completed.

1. Cracks were observed where the crack did not join to the EDM notch.

2. Corner cracks developed at the interface between the side-groove and EDM notch due to the higher stress concentration at the corner than at the EDM notch tip.

3. Once the new ASTM E1457[6] standard was adopted, the EDM notch height was limited to 0.004 inches. The EDM slot height for the experiments completed under this project was on the order of 0.010 inches.

4. The experiments may have lasted longer than necessary because of the blunt EDM notch. The experiment turned out to be an initiation plus growth experiment rather than just a growth experiment.

5. The side-grooves did not align with EDM notch. This caused a complex stress region at the tip of the notch which may have been alleviated if pre-cracking would have been performed.

Although there are still mixed opinions on whether or not to pre-crack, in light of the evidence during post-mortem analysis, some procedural changes may be necessary to comply with the current standards.

Once the experiment was designed, the pertinent formulas needed to be investigated for data analysis. Methods and formulas for calculating crack length, compliance, K, J, and C* were obtained. The following formulas were used in data reduction.

CCG Equations:

Crack Length

The recommend practice for obtaining crack length in the standard is the use of direct current electric potential drop (EPD)[4]. Although the standard does not give any guidance on the use of this method for other specimen geometries, the SEN(t) specimen has been used in conjunction with EPD by other investigators. The following formulas were used during the test to convert potential drop voltages to crack lengths.[7]

$$T_1 = \frac{2W}{\pi}$$

$$T_2 = \cosh\left(\frac{y\pi}{2W}\right)$$

$$T_3 = \cos\left(\frac{\pi a_0}{2W}\right)$$

$$a = T_1 \cos^{-1}\left(\frac{T_2}{\cosh\left(\frac{U}{U_0}\cosh^{-1}\left(\frac{T_2}{T_3}\right)\right)}\right)$$

W - specimen width

y - half the potential voltage probe distance

a_0 - initial crack length

U - potential voltage reading

U_0 - initial potential voltage reading at a_0

One of the issues with the using the Johnson equation has been found to be an over estimate of the crack length. This over estimation is due to the existence of plasticity in the test specimen. This plasticity changes the electrical characteristics (i.e. the resistance) of the specimen. This change in resistance is manifested in the Johnson equation by a longer predicted crack length.

During post test analysis, the specimens were broke apart to determine the actual final physical crack length. Once the final physical crack length was known, a post-test correction to the data was conducted. The following formula was used to post-test correct the data.[4]

$$a = \left[\frac{(a_f - a_0)}{(a_{pf} - a_0)}(a_p - a_0)\right] + a_0$$

a_f - final physical crack length

a_0 - initial physical crack length

a_{pf} - final physical crack length predicted from EPD

a_p - predicted crack length

Compliance

Although the crack length of the specimen would be determined through electric potential drop methods not through compliance measurements, the compliance of the specimen was needed to separate the elastic area from the plastic area for the determination of the creep displacement rate.[4] The following compliance expression was obtained for the SEN(t) specimen.[8]

$$Z = \frac{qBE'}{P}$$

$$Z = \frac{D}{W(1-\upsilon^2)} + F(\alpha)$$

$$F(\alpha) = 4.0(\alpha^2) - 1.1(\alpha^3) + 37.3(\alpha^4) - 67.4(\alpha^5) + 198.5(\alpha^6) - 423.8(\alpha^7) + 873.7(\alpha^8) - 921.0(\alpha^9) + 580.0(\alpha^{10})$$

$$\alpha = \frac{a}{W}$$

$$\frac{q}{P} = \frac{1}{BE'}\left[\frac{D}{W(1-\upsilon^2)} + F(\alpha)\right]$$

D = gage length

E - modulus of the material

W - specimen width

P - load on the specimen

q - displacement

υ - Poisson's Ratio

Linear Elastic Crack Tip Parameter – K

The linear elastic crack tip parameter K is required in the calculation of the creep displacement rate.[4] K is also useful if the material does not creep at the initial stages; if this occurs there may be a correlation of the crack growth rate to K. The following equation was used to calculate K.[9]

$$K_I = \sigma\sqrt{\pi a}\, F(\alpha)$$

$$\sigma = \frac{P}{BW}$$

$$\alpha = \frac{a}{W}$$

$$F\left(\frac{a}{W}\right) = 1.122 - .231(\alpha) + 10.550(\alpha^2) - 21.710(\alpha^3) + 30.382(\alpha^4)$$

Elastic-Plastic Crack Tip Parameter – J

The elastic-plastic crack tip parameter J needed to be developed for the determination of the creep displacement rate.[4] The following calculations were used in determining the elastic-plastic crack tip parameter J.[10]

$$J_{pl} = \frac{\eta_p A_{pl}}{B_N (W - a)}$$

A_{pl} - plastic area from the load displacement curve

B_N - net thickness of the specimen

W - Width of the specimen

a - crack length

η_p - plastic eta factor defined in Annex D

$$J_{el} = \frac{K^2}{E(1 - \upsilon^2)}$$

K - linear elastic stress intensity factor

E - material modulus

υ - Poisson's Ratio

Creep Displacement Rate - $\dot{v}_c$

In the analysis of the raw data, the total displacement rate must be broken into a mechanically driven rate and a rate due to creep. The following formula was used to determine the displacement rate due to creep.[4]

$$\dot{v}_c = \dot{v} - \frac{\dot{a} B_N}{P}\left(\frac{2K^2}{E'} + (m+1)J_{pl}\right)$$

$\dot{v}$ - total load - line displacement rate of the specimen

$\dot{a}$ - crack growth rate

B_N - net thickness of specimen

P - applied load on the specimen

$E' = \frac{E}{1 - \upsilon^2}$ where E is modulus and υ is Poisson's Ratio

m - stress exponent from the tensile tests

K and Jpl are the crack tip stress parameters defined above.

Creep Crack Tip Parameter - C*

The approach and the details of obtaining the C* expression for the SEN(t) specimen can be found in Annex D. This expression would be the basis of the crack tip field for the SEN(t) specimen under stable creep crack growth rate conditions.

$$C^*(t) = \frac{P\dot{v}_c}{B_N(W - a)}\frac{n}{n+1}\eta_p$$

P - aload on the specimen

$\dot{v}_c$ – displaceme nt rate due to creep [4]

B_N - net thickn ess of the specimen

W - Width of the specimen

a - crack length

n - creep exponent

η_p - plastic eta factor defined in Annex D

References:

1. Doran, J. P., "Investigation of Low Time Dependent Cracking – Progress Report", DOE: DE-FG02-97ER14809, MTI: CRD 1373, June 11, 1999.

2. Wang, Y. Y. "On the Two-Parameter Characterization of Elastic-Plastic Crack-Front Fields in Surface Cracked Plates," *Constraint Effects in Fracture, ASTM STP 1171*, E. M. Hackett, K. –H, Schwalble, and R. H. Dodds, Eds. American Society for Testing and Materials, 1993, pp. 120-138.

3. Anderson, T. L ., Fracture Mechanics – Fundamentals and Applications, 2nd ed., 1995 CRC Press LLC. pp. 160-162.

4. ASTM E1457-92, "Standard Test Method for Measurement of Creep Crack Growth Rates in Metals", American Society for Testing and Materials, West Conshohocken, PA, April 1992.

4a. Saxena, A., Ernst, H.A., Landes, J. D., "Creep Crack Growth Behavior in 316 Stainless Steel", International Journal of Fracture,Vol. 23, No. 4, December 1983.

5. Riedel, H., Fracture at High Temperatures, Springer-Verlag Berlin, Heidelberg, 1987, pp. 336-337.

6. ASTM E1457-00, "Standard Test Method for Measurement of Creep Crack Growth Rates in Metals", American Society for Testing and Materials, West Conshohocken, PA, November 2000.

7. Schwalbe, K. –H. and Hellmann, D, "Application of the Electric Potential Method to Crack Length Measurements Using Johnson's Formula," Journal of Testing and Evaluation, JTEV, Vol. 9, No. 3, May 1981, pp. 218 - 221.

8. Towers, O. L., "Tests for Fracture Toughness and Fatigue Assessment: A Compilation of Stress Intensity, Compliance and N Factors", Edison Welding Institute, Columbus, OH, 1985

9. Tada, H., Paris, P., and Irwin, G., "The Stress Analysis of Cracks Handbook," Paris Productions, Inc. and Del Research Corporation, St. Louis, MS, 1995, pp 2.10-2.11.

10. ASTM E1820-99a, "Standard Test Method for Measurement of Fracture Toughness", American Society for Testing and Materials, West Conshohocken, PA, April 2000.

Figure B-1 – Dog-bone Specimen

CUT SPECIMEN BLANK 1.75 INCHES WIDE. THE BLANK WILL BE FLATTENED FOR FINAL MACHINING

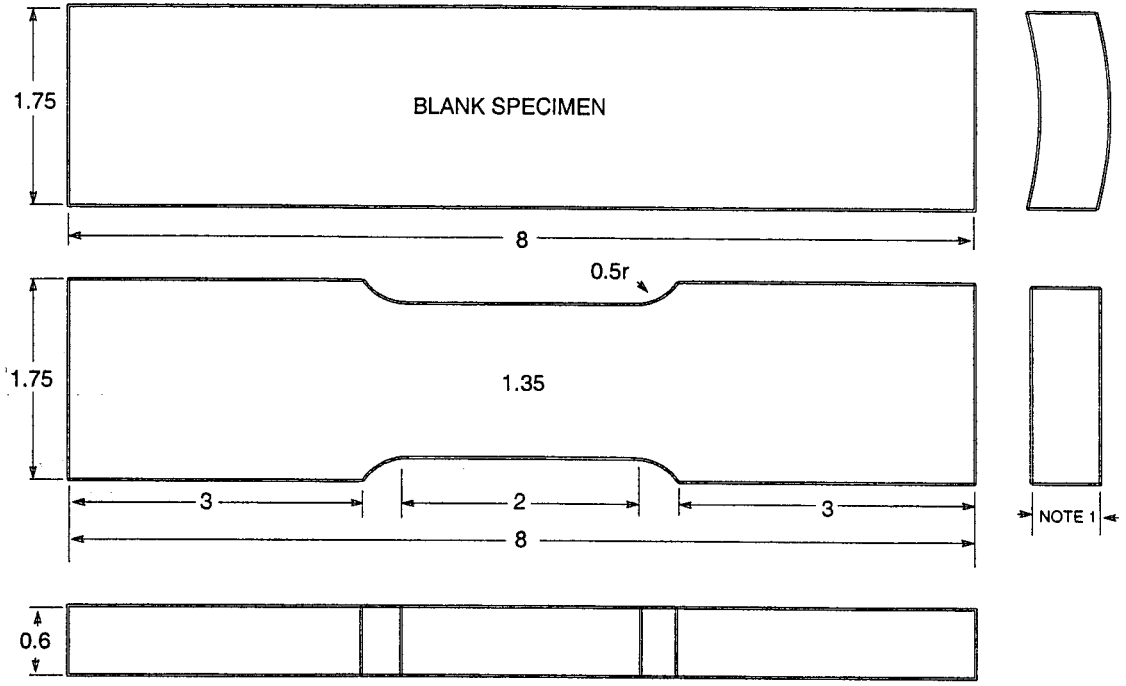

NOTE 1: MAKE SPECIMEN AS THICK AS POSSIBLE DEPENDING ON WALL THICKNESS

SKETCH 43638-1
CHARGE 43638-001
DWN. BY EA DeStephen
June 10, 1999

Figure B-2 – Tensile Specimen

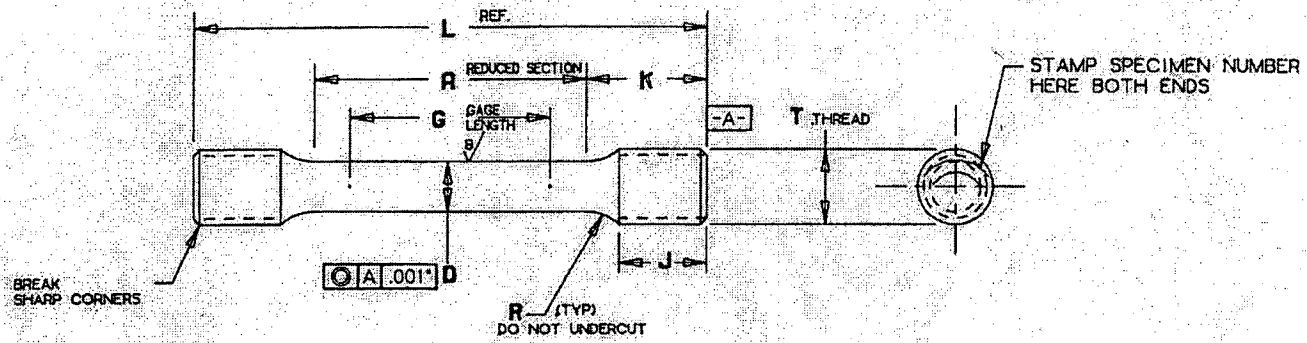

NOTE:
THE REDUCED SECTION MUST HAVE A GRADUAL TAPER FROM THE ENDS TOWARD THE CENTER WITH THE ENDS NOT MORE THAN 1% LARGER THAN THE CENTER

DIMENSIONS

SPECIMEN TYPE	REDUCED SECTION R ± 1/2	DIA D	GAGE LENGTH G	THREAD LENGTH J	DIM K ± 1/16	OVERALL LENGTH L	RADIUS (MINIMUM) R	THREAD SIZE T	
.500	2 1/4	.500±.010"	2.00±.005	1.00"	1 3/8"	5.00"	1/2"	3/4 -10UNC	
.350	1 3/4"	.350±.007"	1.40±.005	13/16"	1 3/8"	4 1/2"	1/4"	1/2 -13UNC	
.250	1 1/4"	.250±.005"	1.00±.005	13/16"	1 1/8"	3 1/2"	1/4"	1/2 -13UNC	
.160	3/4"	.160±.003"	.640±.005	1/2	5/8"	2	5/32"	1/4 -28UNF	

RELEASED FOR FABRICATION

REV NO	REV BY / DATE	CHK'D BY / APP'D BY	REVISION
1	APK 4/13/95	[illegible]	CHANGED .XXX & T DIMENSION FOR .160 DIMENSION

REFERENCE DRAWINGS

THIS DRAWING IS THE PROPERTY OF BABCOCK & WILCOX RESEARCH & DEVELOPMENT DIVISION AND IS LOANED UPON CONDITION THAT IT IS NOT TO BE REPRODUCED OR COPIED, IN WHOLE OR IN PART, OR USED FOR FURNISHING INFORMATION TO OTHERS OR FOR ANY OTHER PURPOSE DETRIMENTAL TO THE INTEREST OF BABCOCK & WILCOX AND IS TO BE RETURNED UPON REQUEST.

DWN BY A KISH	STANDARD TENSILE SPECIMEN	SCALE NONE	DRG NO 5294-70
DATE 3-MAR-94	.500 .350 .250 .160	SHT NO	CONT ON
CHK'D BY T DAVIS		DRG NO 11808-B	REV 1
APP'D BY R H E			

THIS IS A CAD DRAWING - DO NOT REVISE MANUALLY

Figure B-3 – SEN(t) Specimen

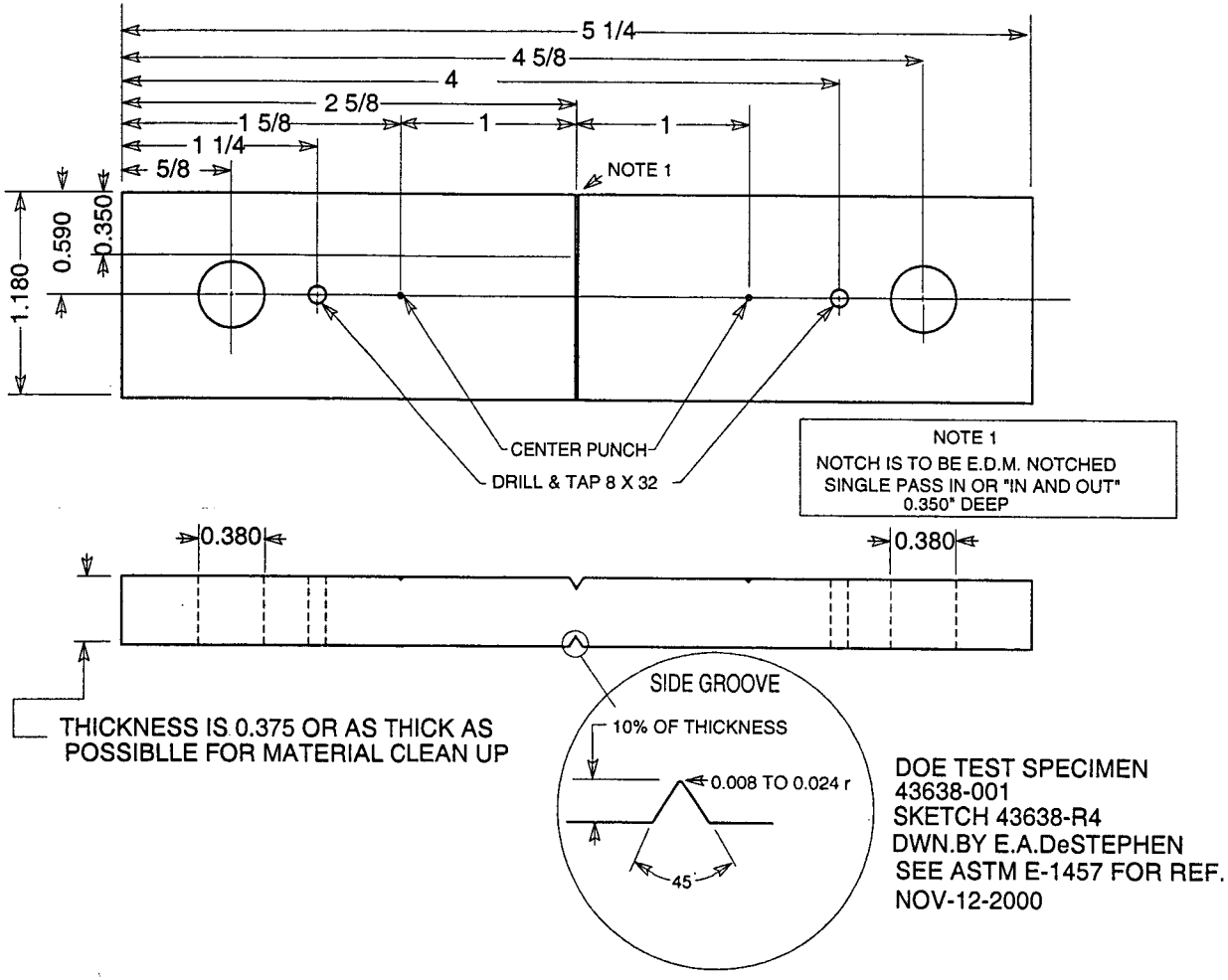

Appendix B-1 – Strain Profiles

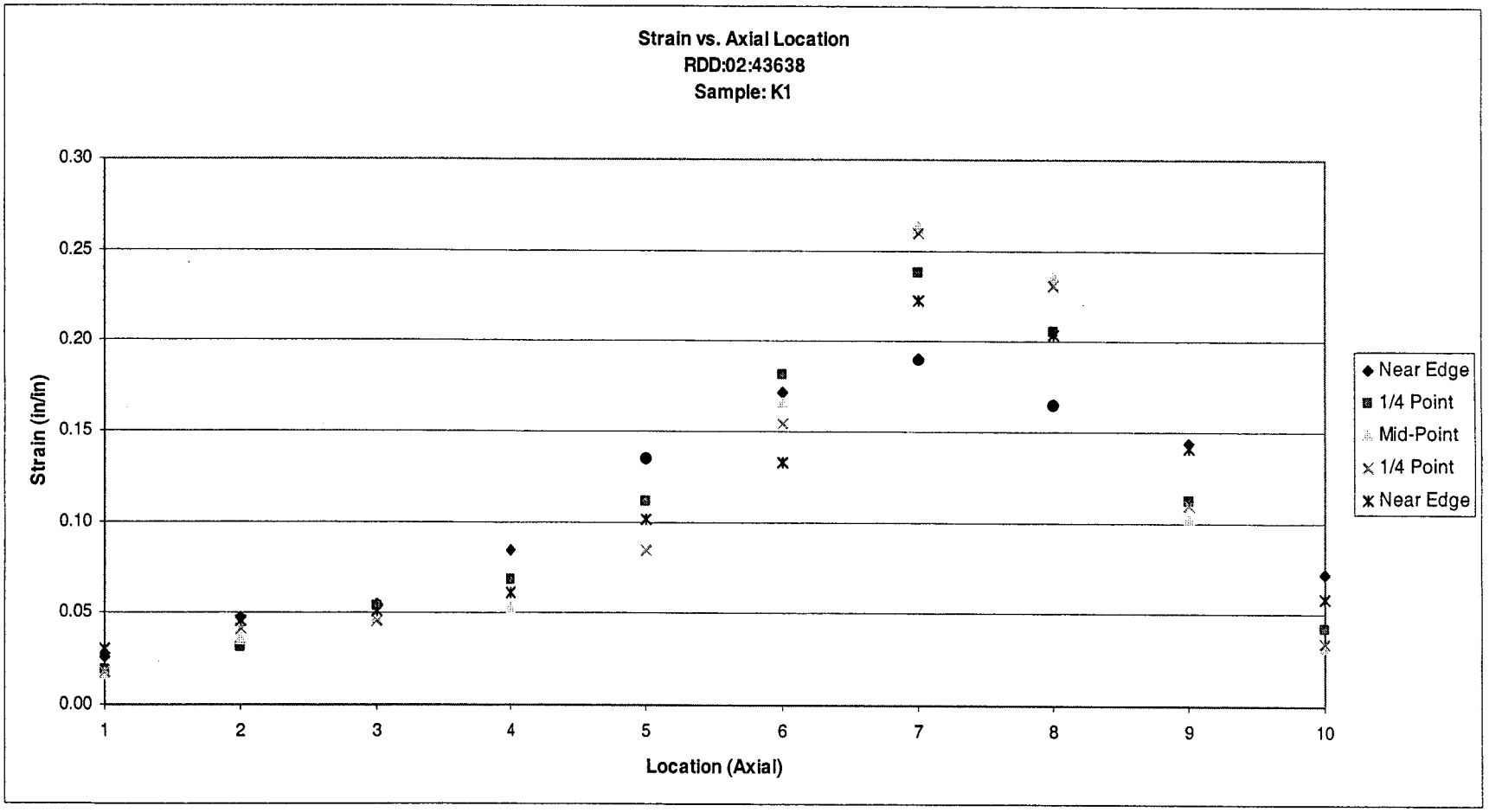
Strain vs. Axial Location
RDD:02:43638
Sample: K1
Strain (in/in)
0.30
0.25
0.20
0.15
0.10
0.05
0.00
1
2
3
4
5
6
7
8
9
10
Location (Axial)
Near Edge
1/4 Point
Mid-Point
1/4 Point
Near Edge

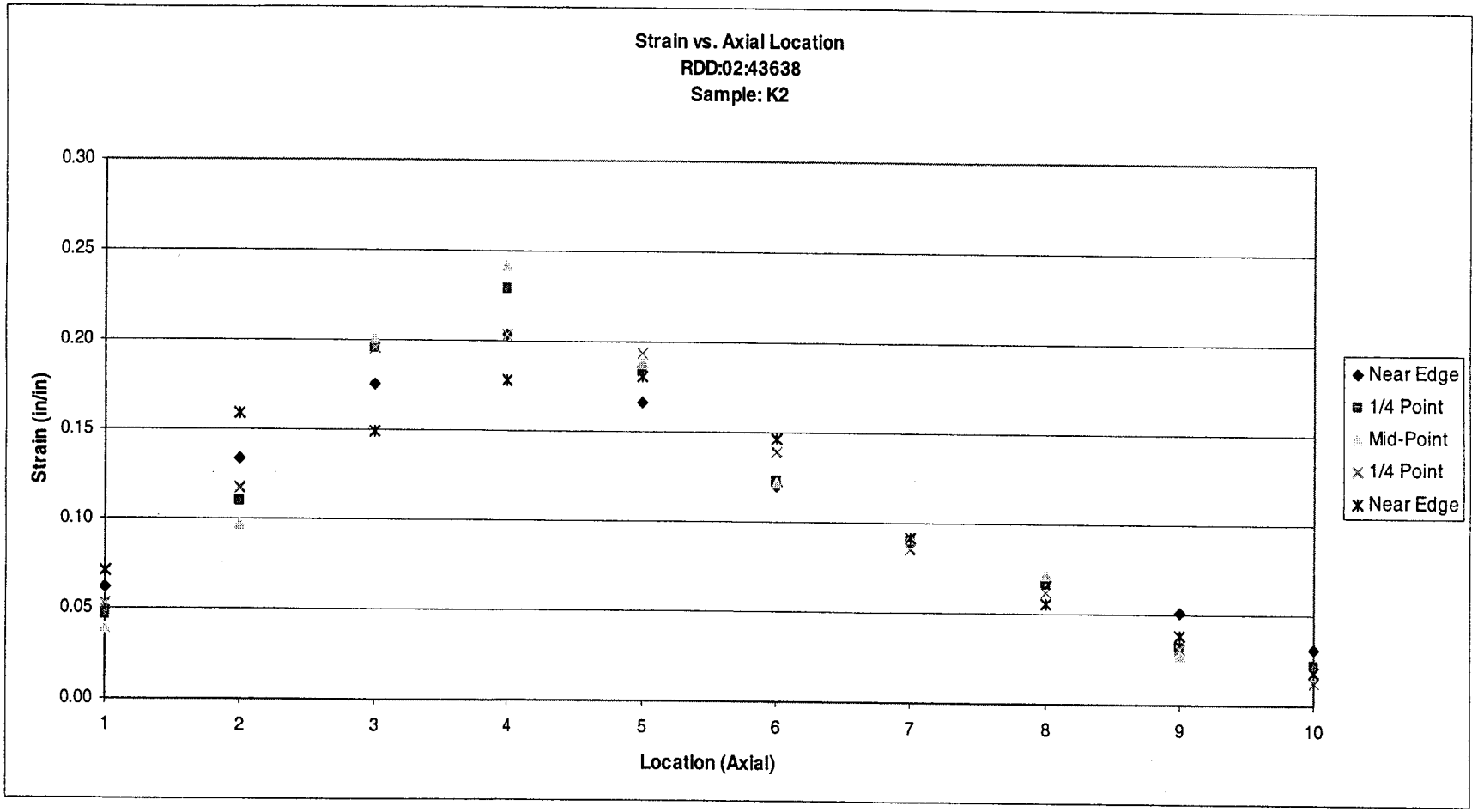
Strain vs. Axial Location
RDD:02:43638
Sample: K2
Strain (in/in)
0.30
0.25
0.20
0.15
0.10
0.05
0.00
1
2
3
4
5
6
7
8
9
10
Location (Axial)
Near Edge
1/4 Point
Mid-Point
1/4 Point
Near Edge

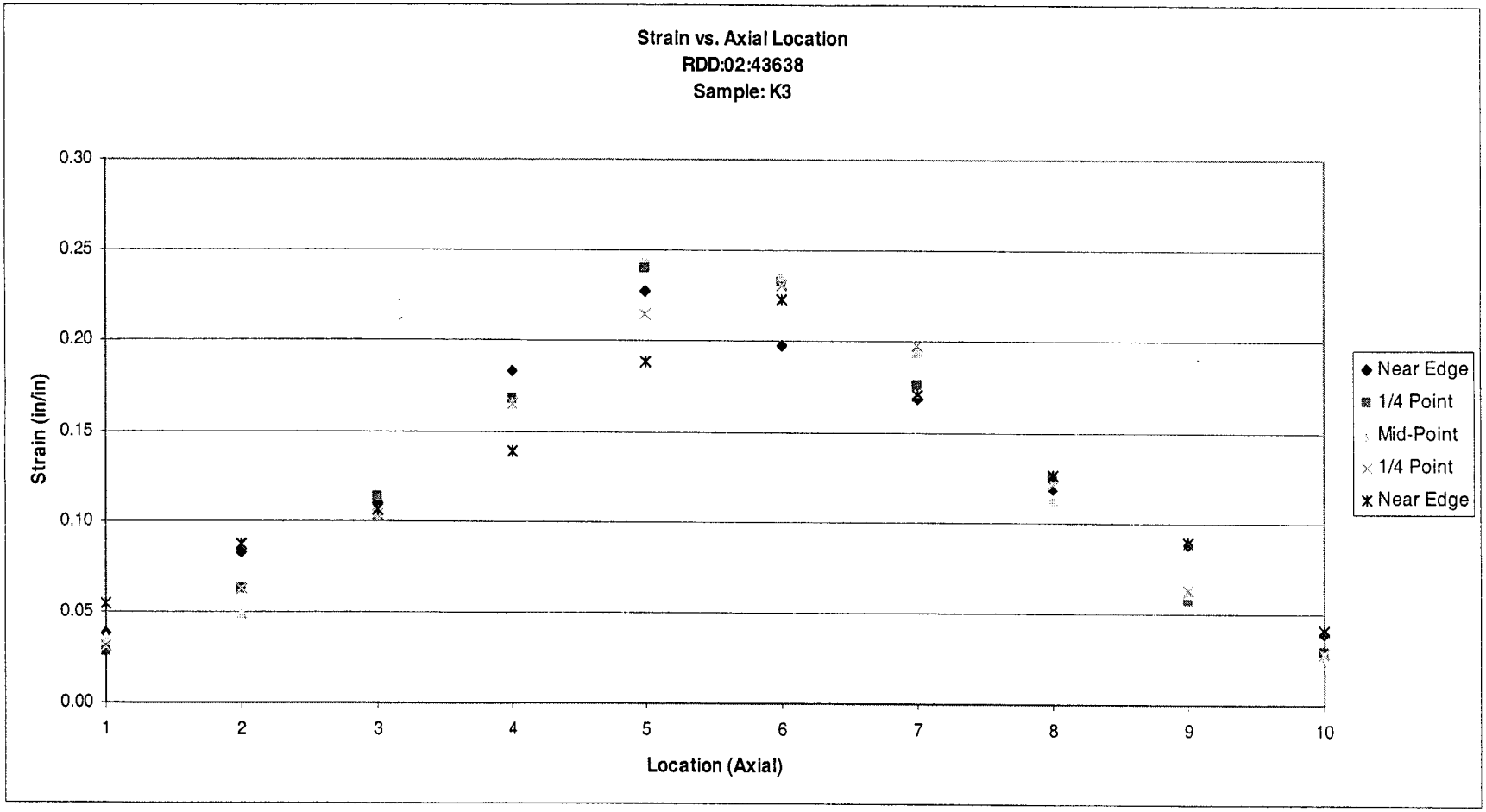
Strain vs. Axial Location
RDD:02:43638
Sample: K3
Strain (in/in)
0.30
0.25
0.20
0.15
0.10
0.05
0.00
1
2
3
4
5
6
7
8
9
10
Location (Axial)
Near Edge
1/4 Point
Mid-Point
1/4 Point
Near Edge

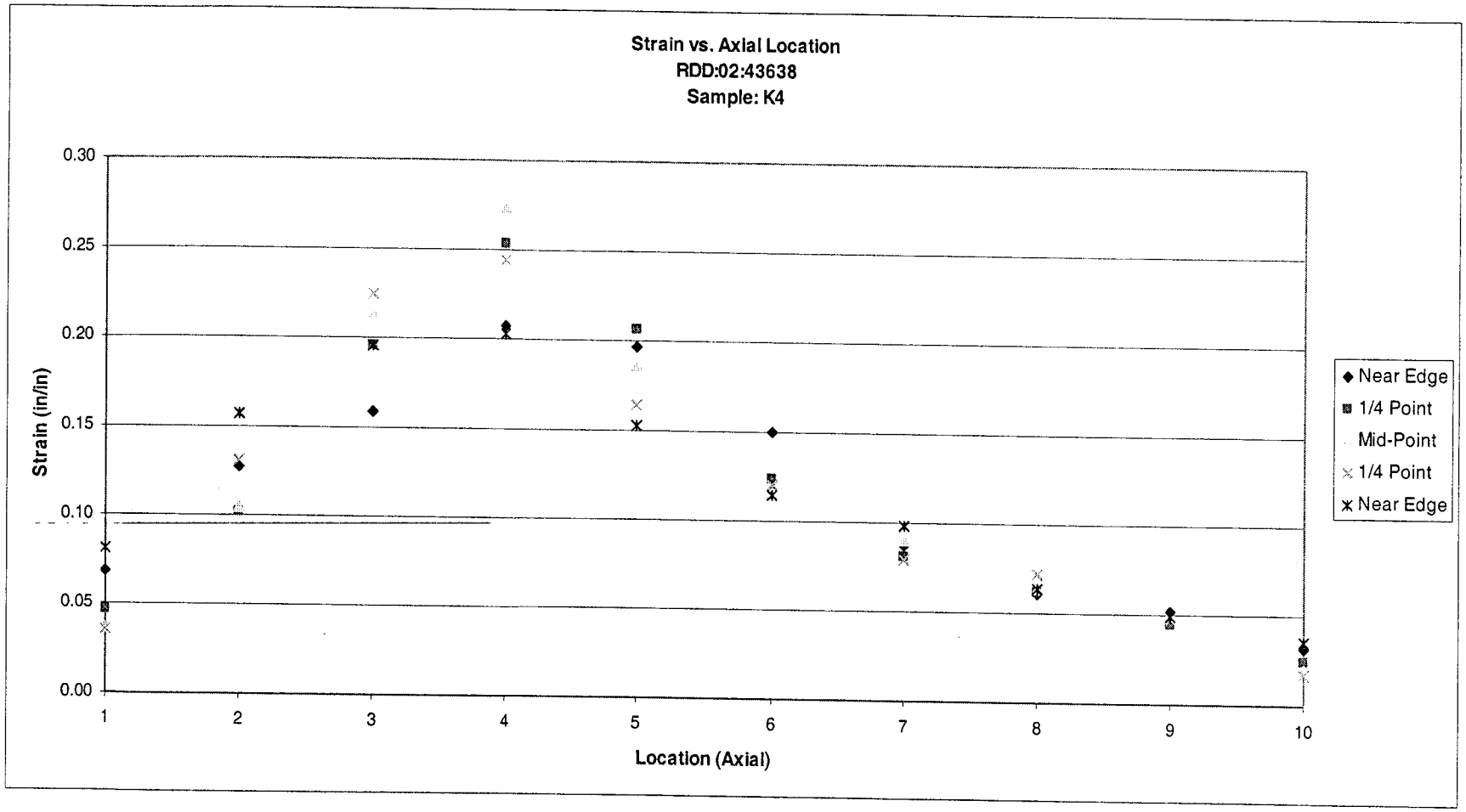
Strain vs. Axial Location
RDD:02:43638
Sample: K4
Strain (in/in)
0.30
0.25
0.20
0.15
0.10
0.05
0.00
1
2
3
4
5
6
7
8
9
10
Location (Axial)
Near Edge
1/4 Point
Mid-Point
1/4 Point
Near Edge

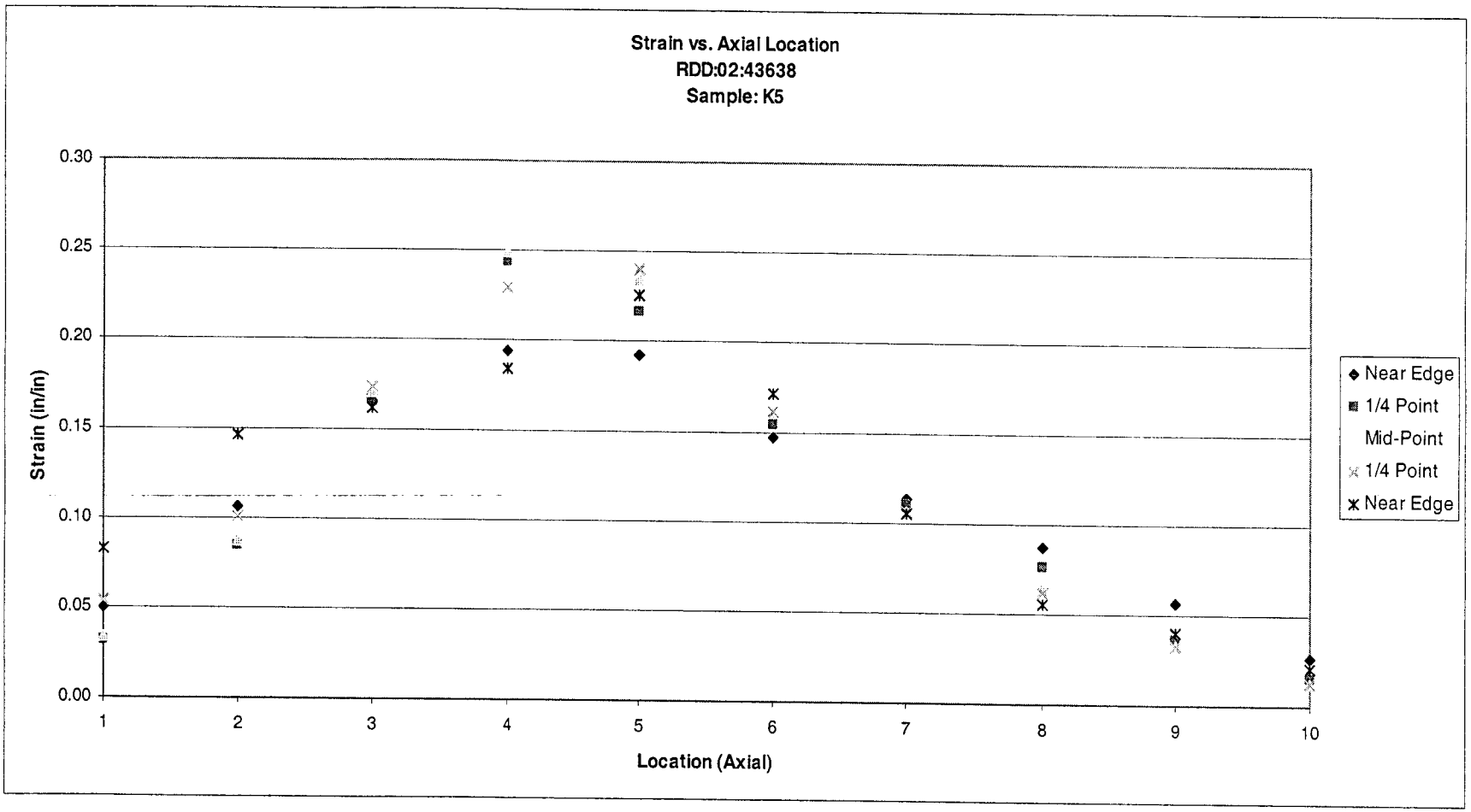
Strain vs. Axial Location
RDD:02:43638
Sample: K5
Strain (in/in)
0.30
0.25
0.20
0.15
0.10
0.05
0.00
1
2
3
4
5
6
7
8
9
10
Location (Axial)
Near Edge
1/4 Point
Mid-Point
1/4 Point
Near Edge

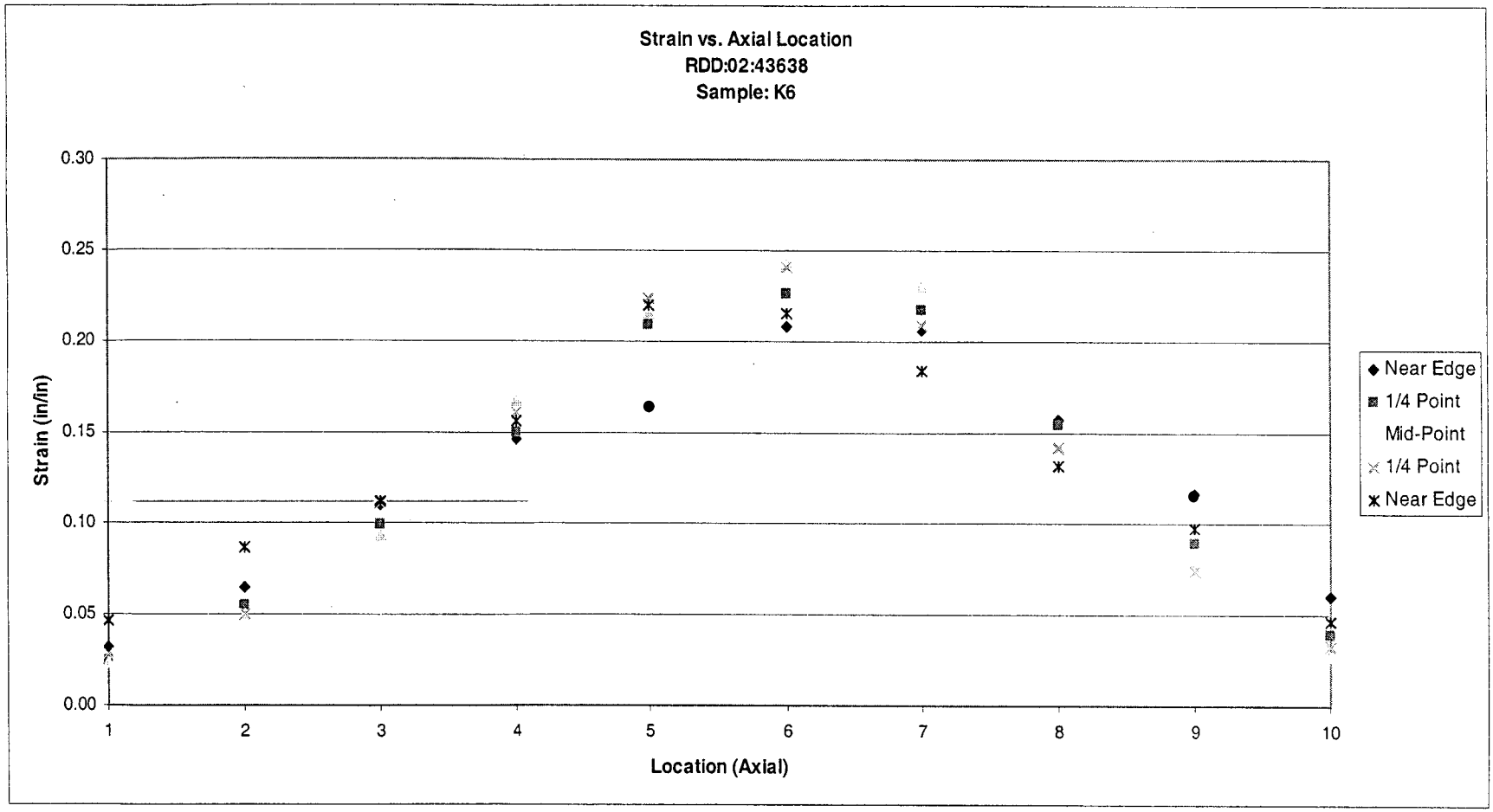
Strain vs. Axial Location
RDD:02:43638
Sample: K6
Strain (in/in)
0.30
0.25
0.20
0.15
0.10
0.05
0.00
1
2
3
4
5
6
7
8
9
10
Location (Axial)
Near Edge
1/4 Point
Mid-Point
1/4 Point
Near Edge

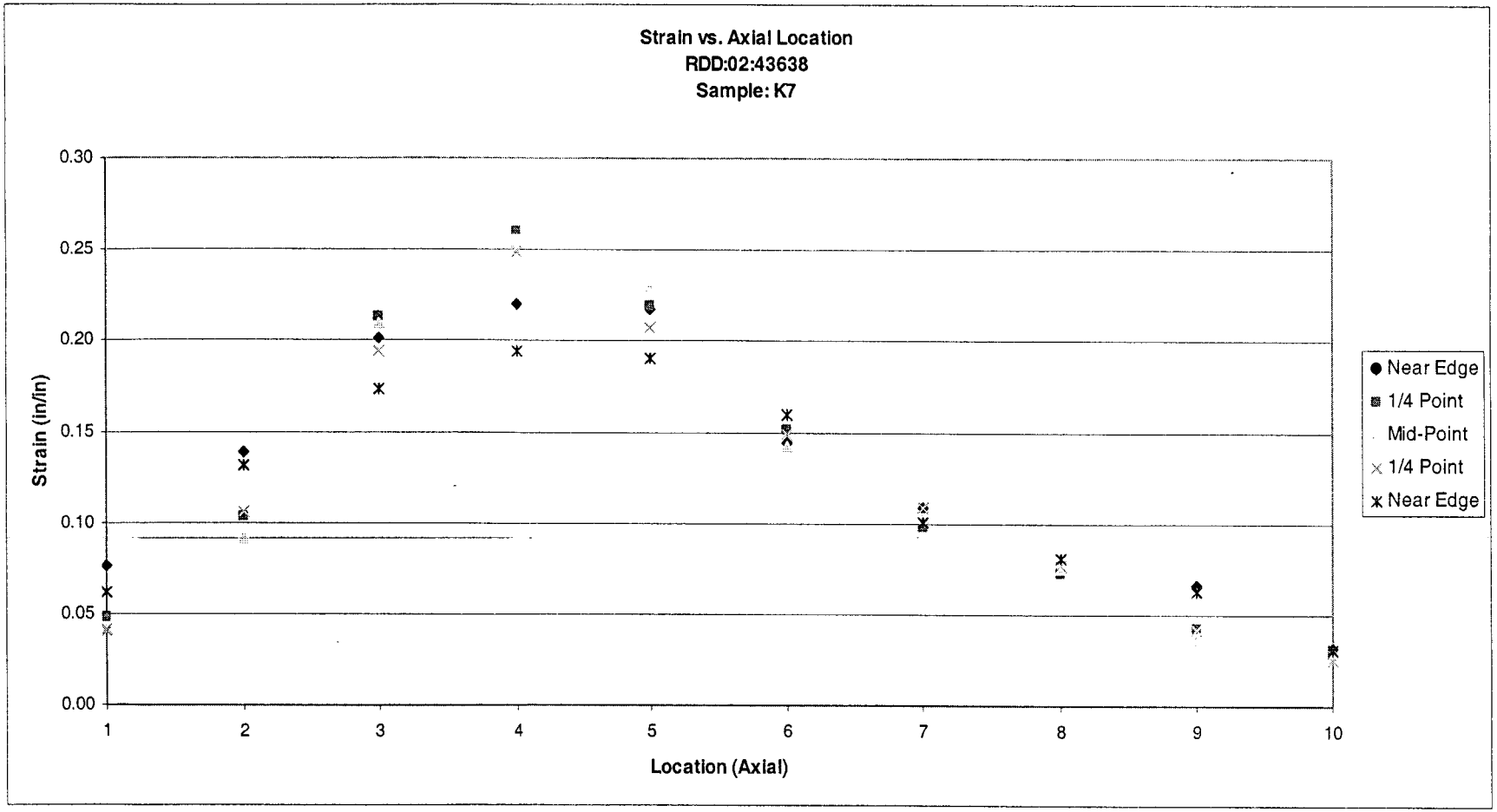
Strain vs. Axial Location
RDD:02:43638
Sample: K7
Strain (in/in)
0.30
0.25
0.20
0.15
0.10
0.05
0.00
1
2
3
4
5
6
7
8
9
10
Location (Axial)
Near Edge
1/4 Point
Mid-Point
1/4 Point
Near Edge

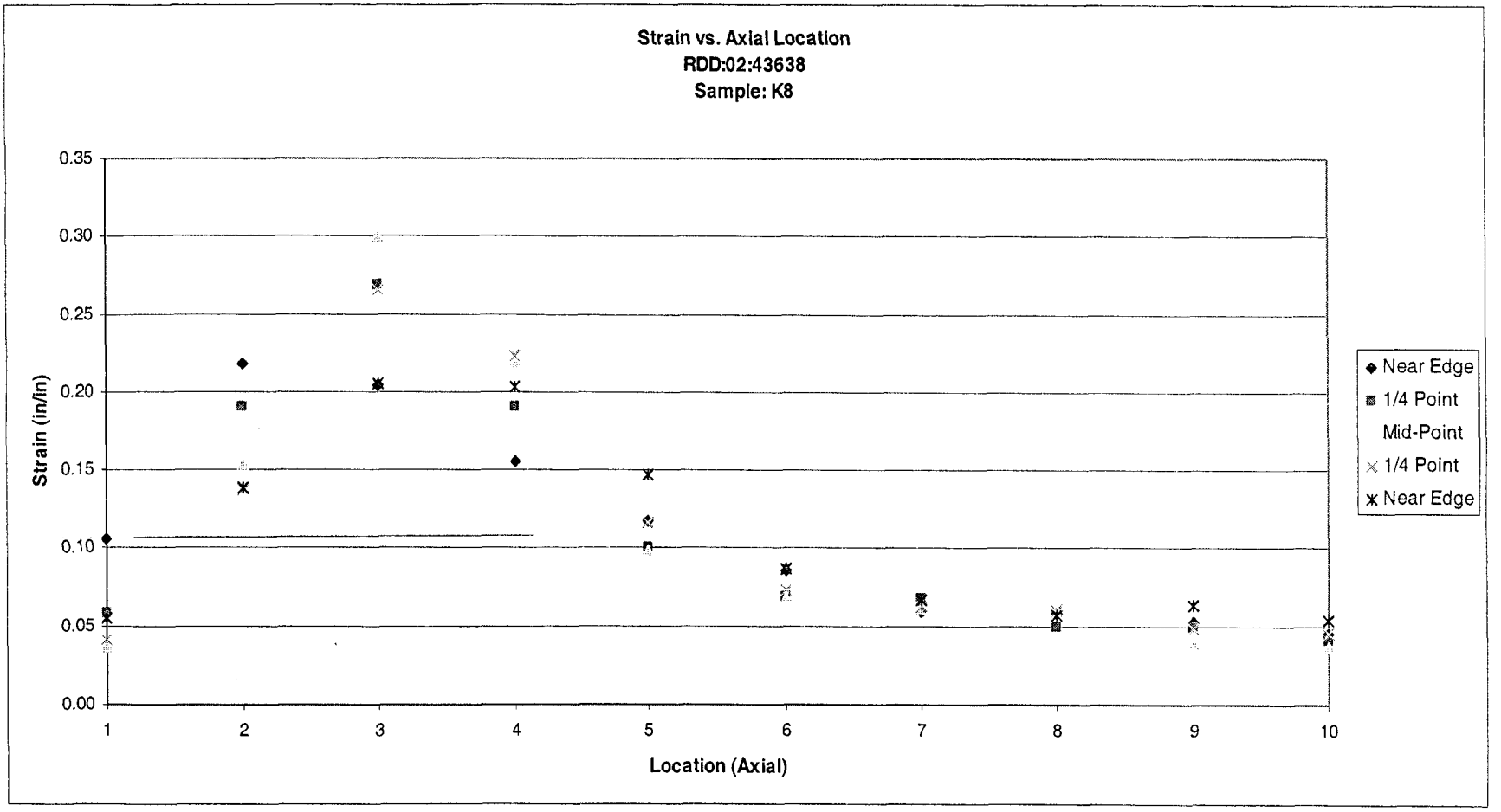
Strain vs. Axial Location
RDD:02:43638
Sample: K8
Strain (in/in)
0.35
0.30
0.25
0.20
0.15
0.10
0.05
0.00
1
2
3
4
5
6
7
8
9
10
Location (Axial)
Near Edge
1/4 Point
Mid-Point
1/4 Point
Near Edge

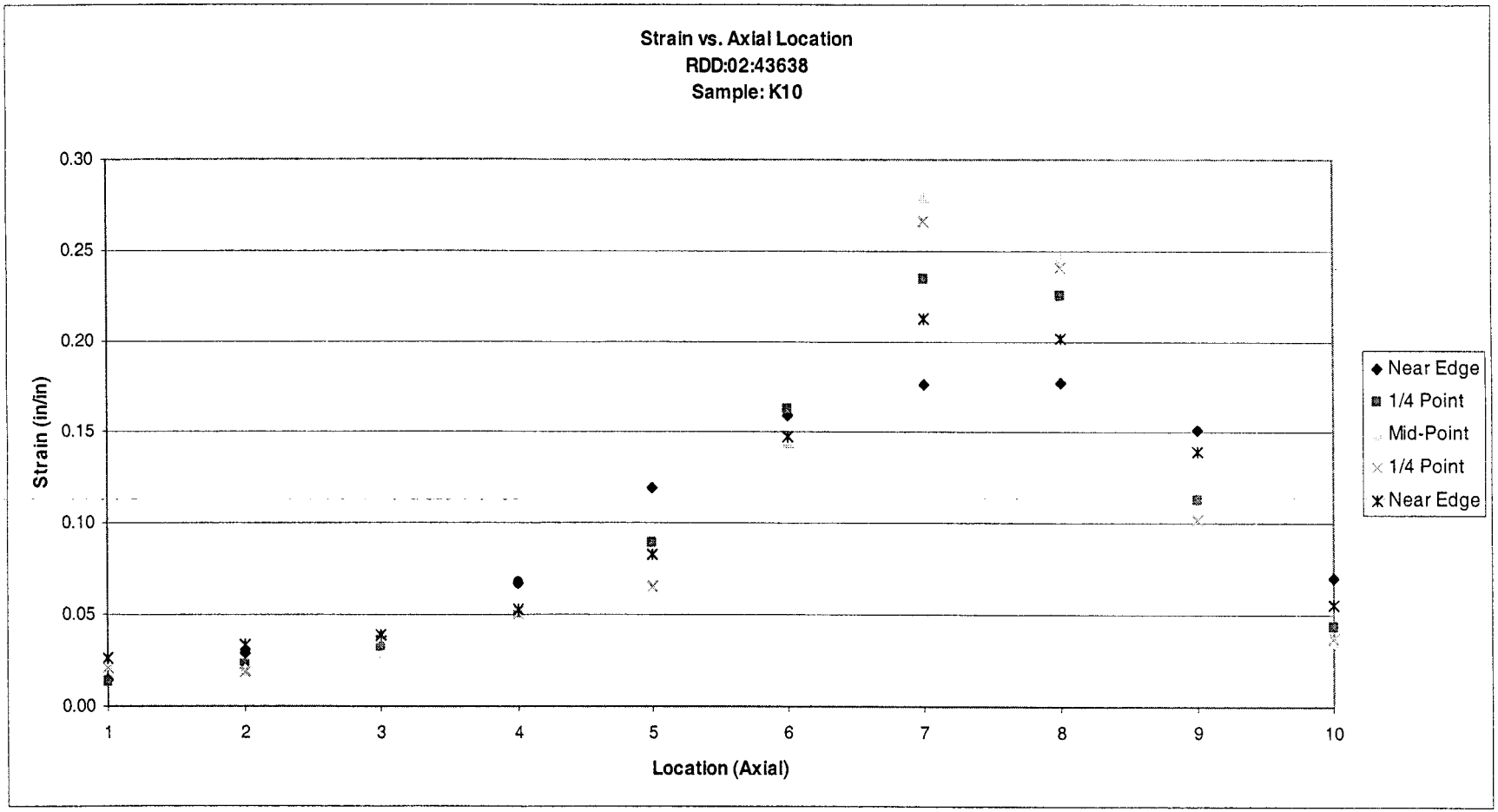
Strain vs. Axial Location
RDD:02:43638
Sample: K10
Strain (in/in)
0.30
0.25
0.20
0.15
0.10
0.05
0.00
1
2
3
4
5
6
7
8
9
10
Location (Axial)
Near Edge
1/4 Point
Mid-Point
1/4 Point
Near Edge

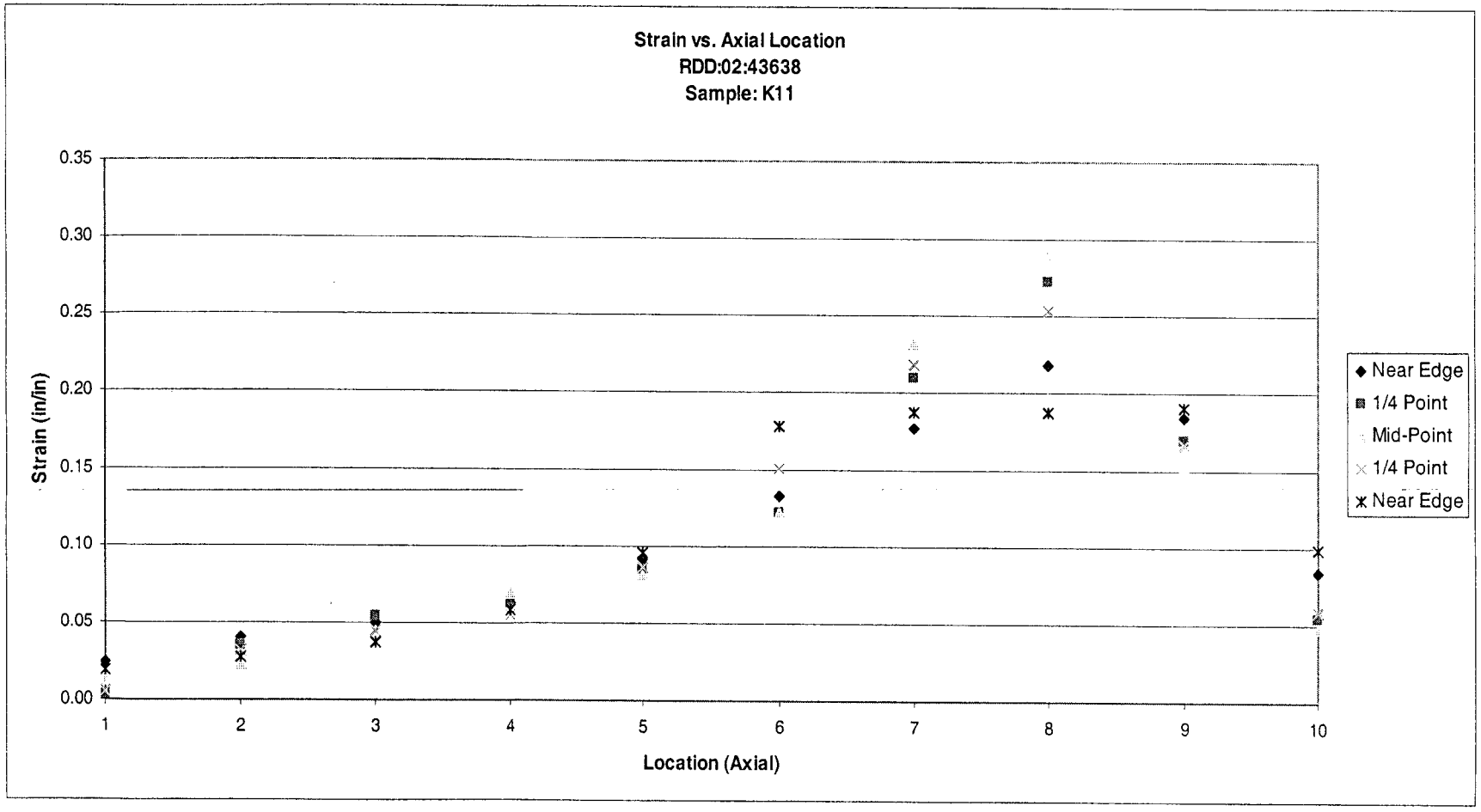
Strain vs. Axial Location
RDD:02:43638
Sample: K11
Strain (in/in)
0.35
0.30
0.25
0.20
0.15
0.10
0.05
0.00
1
2
3
4
5
6
7
8
9
10
Location (Axial)
Near Edge
1/4 Point
Mid-Point
1/4 Point
Near Edge

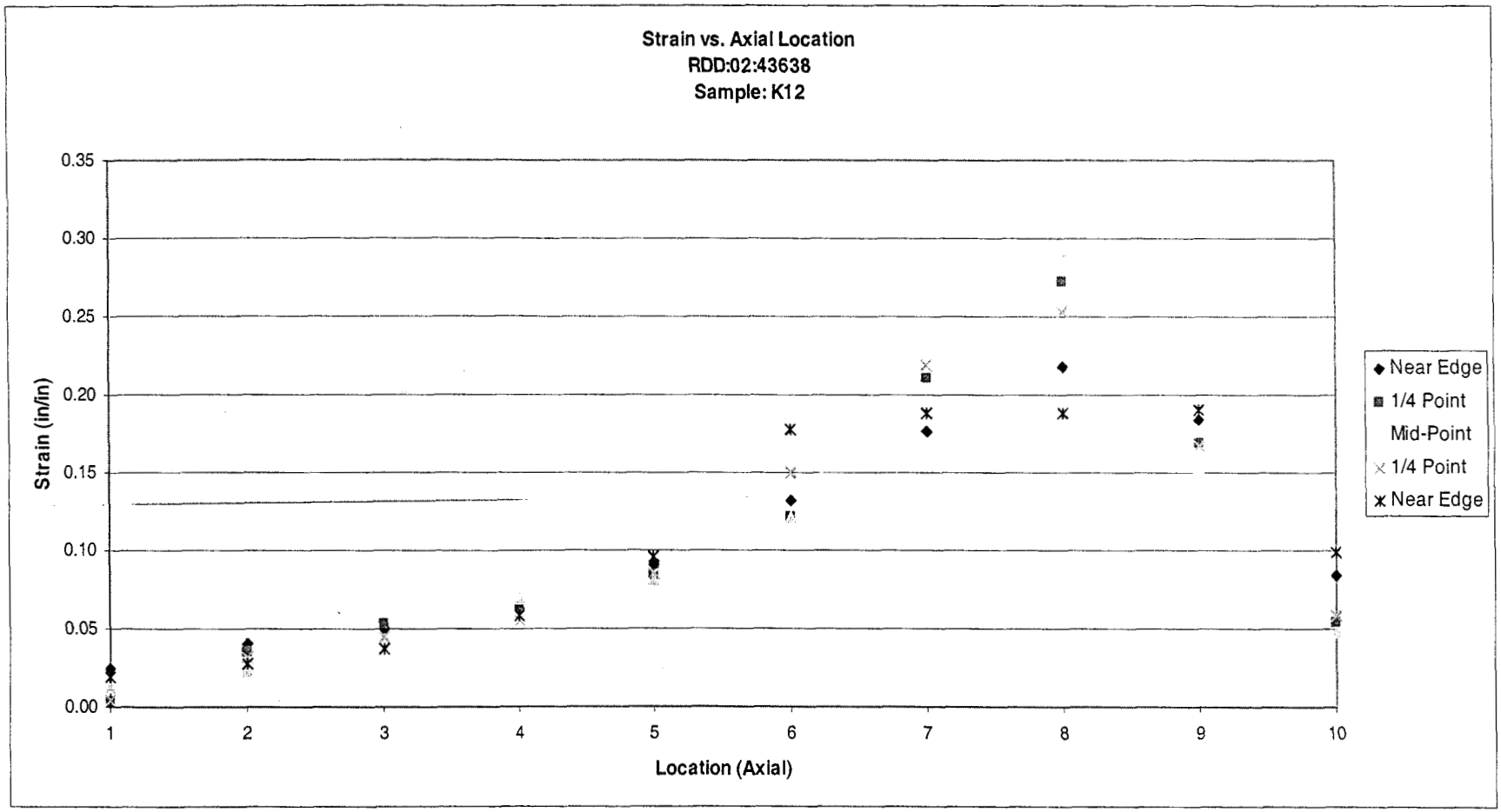
Strain vs. Axial Location
RDD:02:43638
Sample: K12
Strain (in/in)
0.35
0.30
0.25
0.20
0.15
0.10
0.05
0.00
1
2
3
4
5
6
7
8
9
10
Location (Axial)
Near Edge
1/4 Point
Mid-Point
1/4 Point
Near Edge

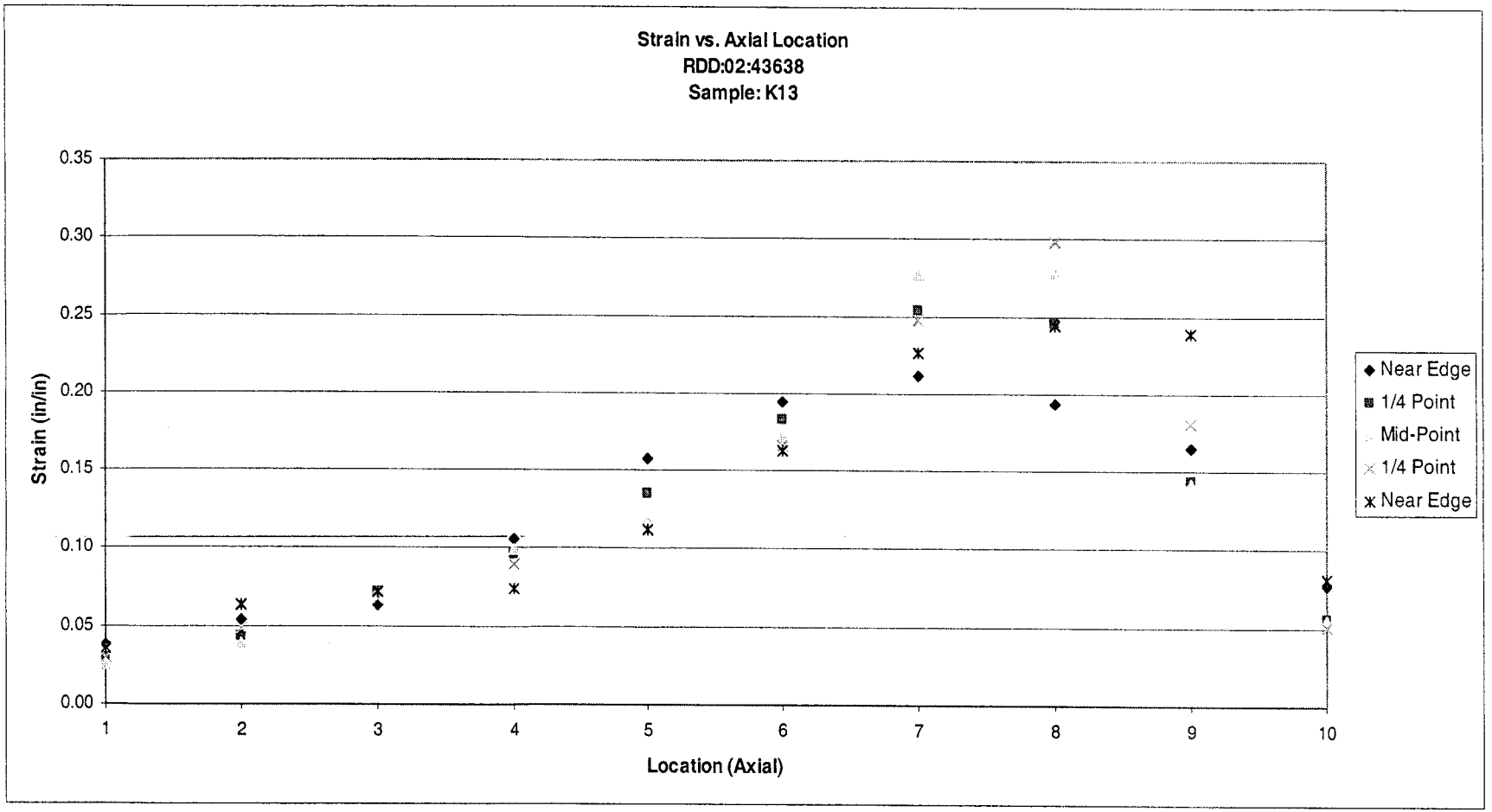
Strain vs. Axial Location
RDD:02:43638
Sample: K13
Strain (in/in)
0.35
0.30
0.25
0.20
0.15
0.10
0.05
0.00
1
2
3
4
5
6
7
8
9
10
Location (Axial)
Near Edge
1/4 Point
Mid-Point
1/4 Point
Near Edge

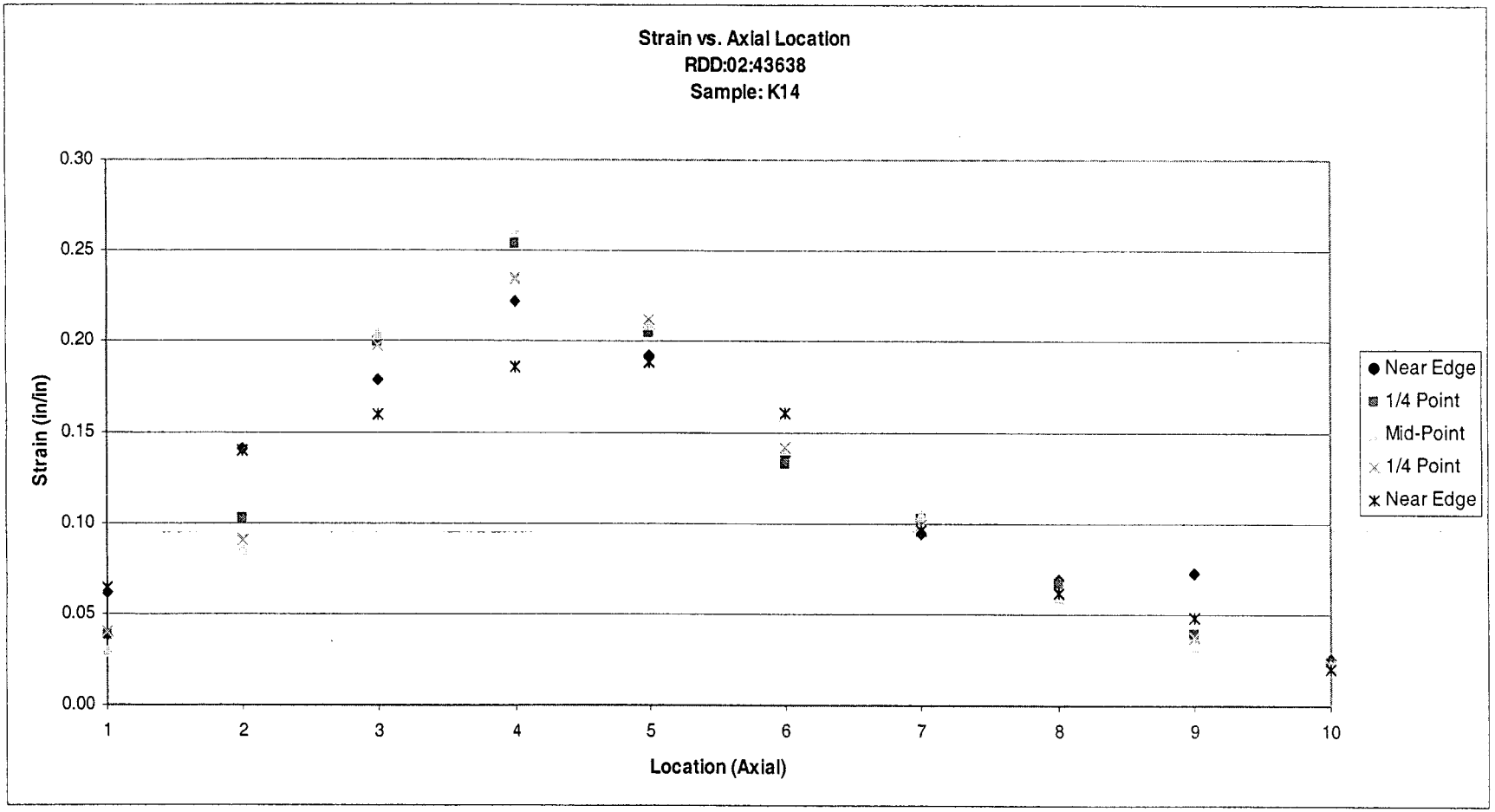
Strain vs. Axial Location
RDD:02:43638
Sample: K14
Strain (in/in)
0.30
0.25
0.20
0.15
0.10
0.05
0.00
1
2
3
4
5
6
7
8
9
10
Location (Axial)
Near Edge
1/4 Point
Mid-Point
1/4 Point
Near Edge

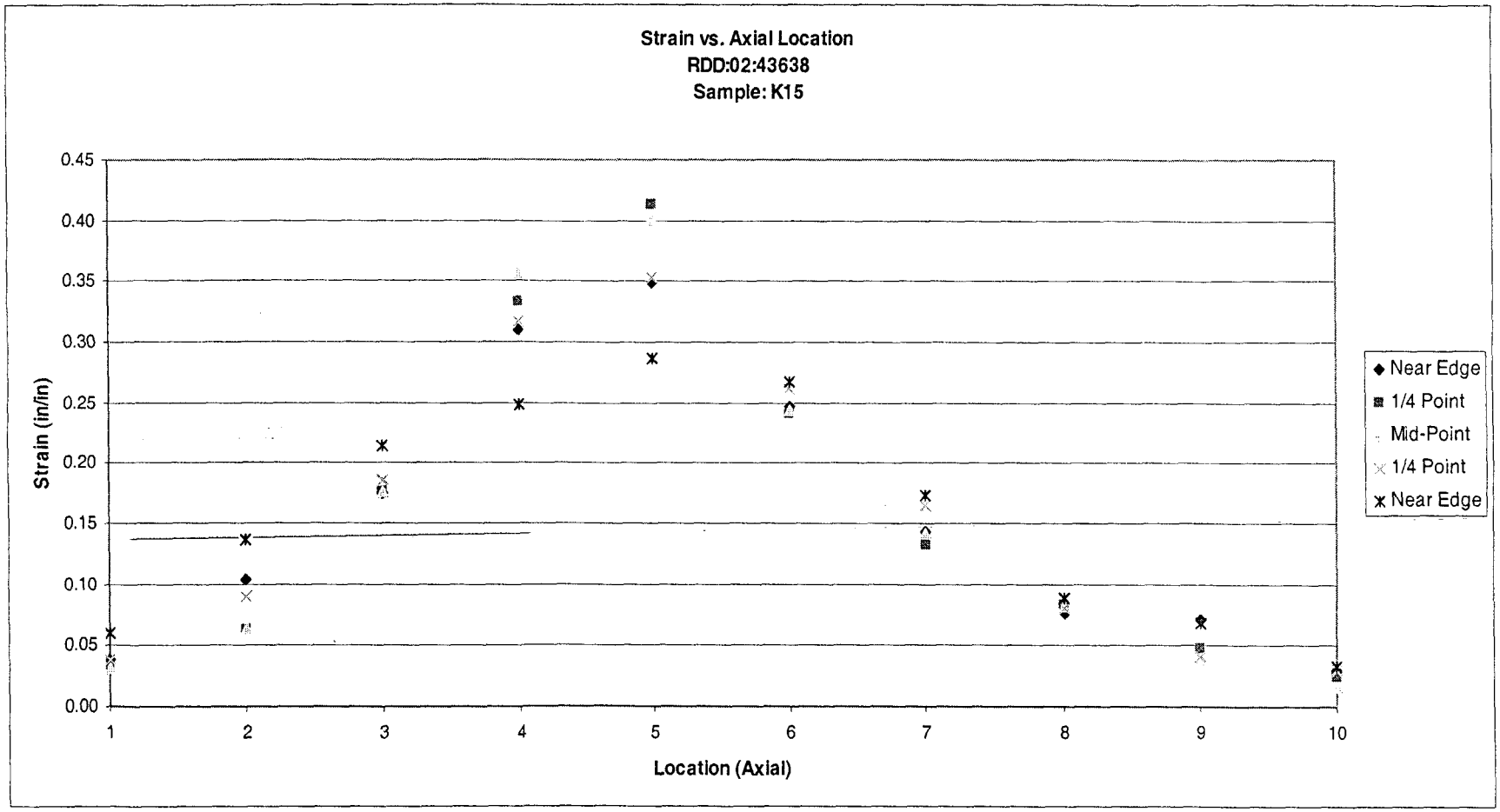
Strain vs. Axial Location
RDD:02:43638
Sample: K15
Strain (in/in)
0.45
0.40
0.35
0.30
0.25
0.20
0.15
0.10
0.05
0.00
1
2
3
4
5
6
7
8
9
10
Location (Axial)
Near Edge
1/4 Point
Mid-Point
1/4 Point
Near Edge

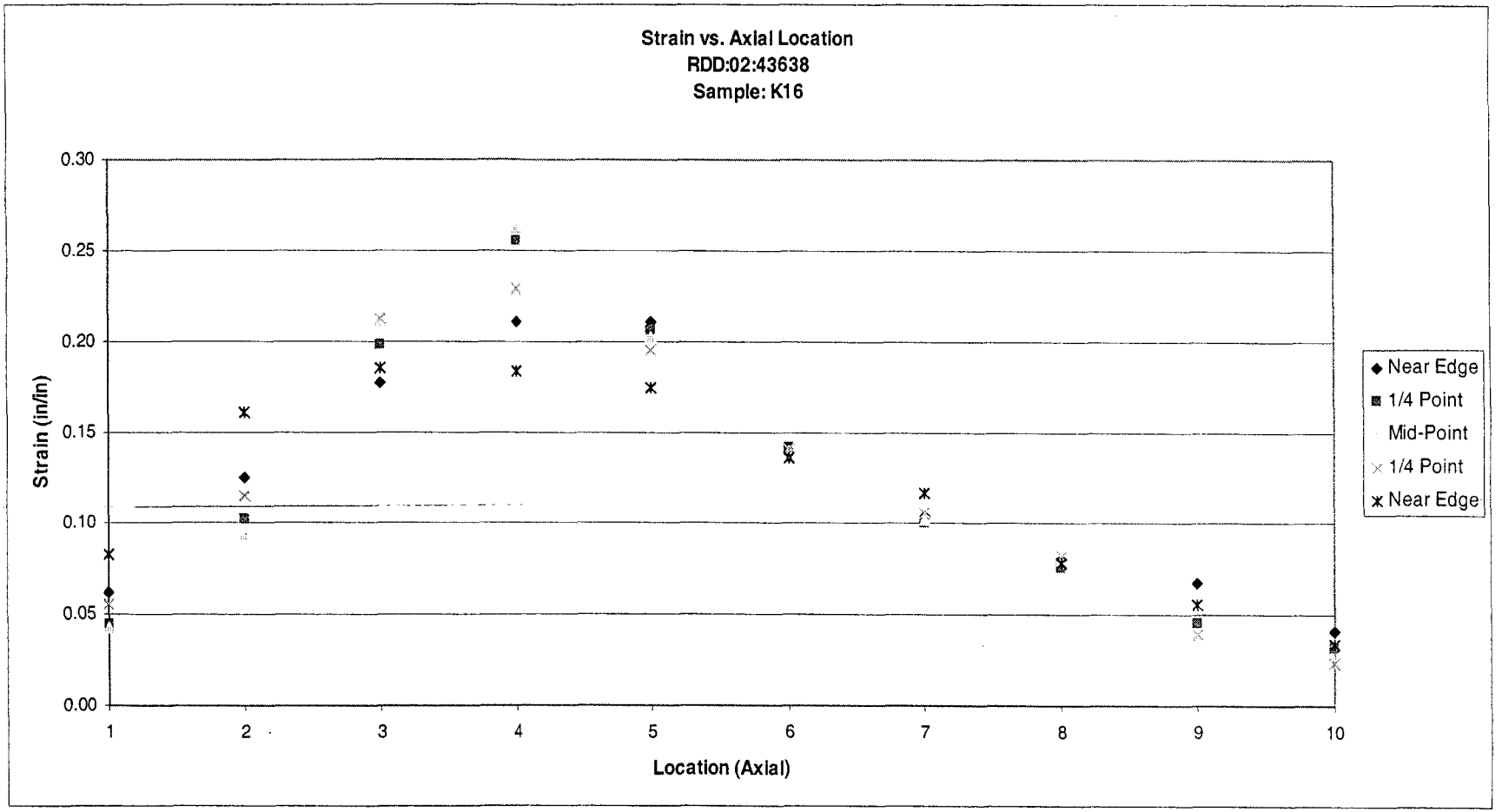
Strain vs. Axial Location
RDD:02:43638
Sample: K16
Strain (in/in)
0.30
0.25
0.20
0.15
0.10
0.05
0.00
1
2
3
4
5
6
7
8
9
10
Location (Axial)
Near Edge
1/4 Point
Mid-Point
1/4 Point
Near Edge

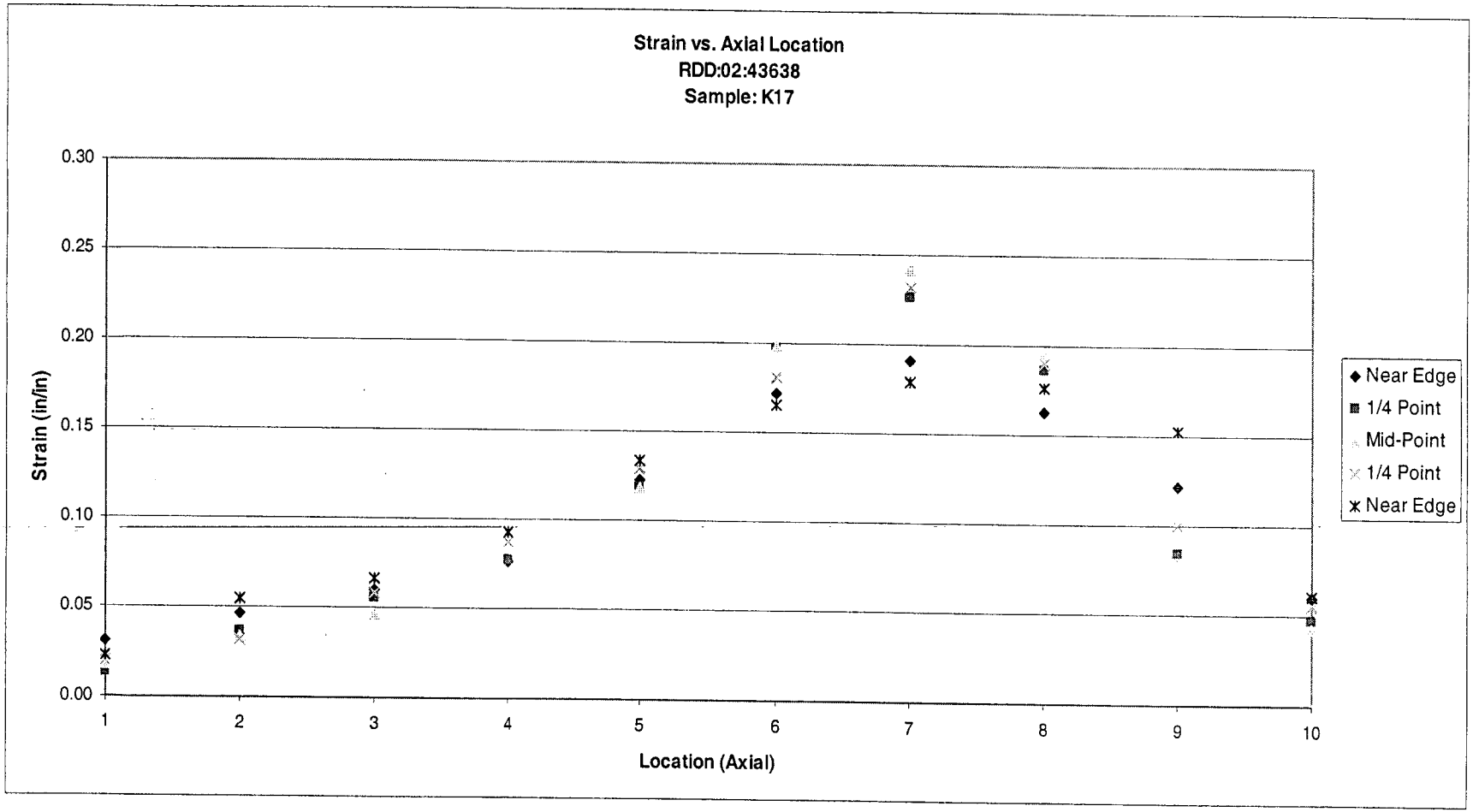
Strain vs. Axial Location
RDD:02:43638
Sample: K17
Strain (in/in)
0.30
0.25
0.20
0.15
0.10
0.05
0.00
1
2
3
4
5
6
7
8
9
10
Location (Axial)
Near Edge
1/4 Point
Mid-Point
1/4 Point
Near Edge

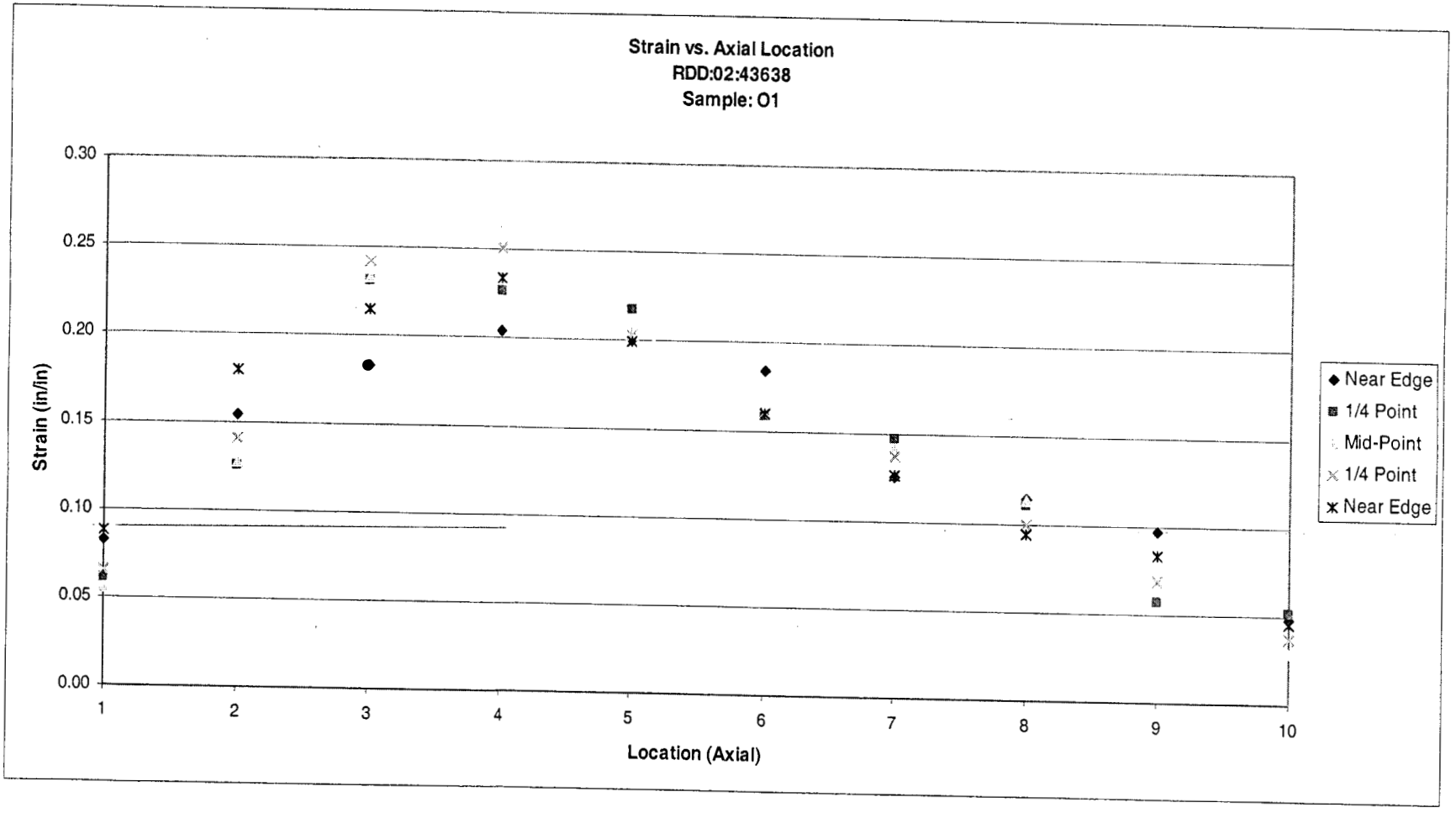
Strain vs. Axial Location
RDD:02:43638
Sample: O1
Strain (in/in)
0.30
0.25
0.20
0.15
0.10
0.05
0.00
1
2
3
4
5
6
7
8
9
10
Location (Axial)
Near Edge
1/4 Point
Mid-Point
1/4 Point
Near Edge

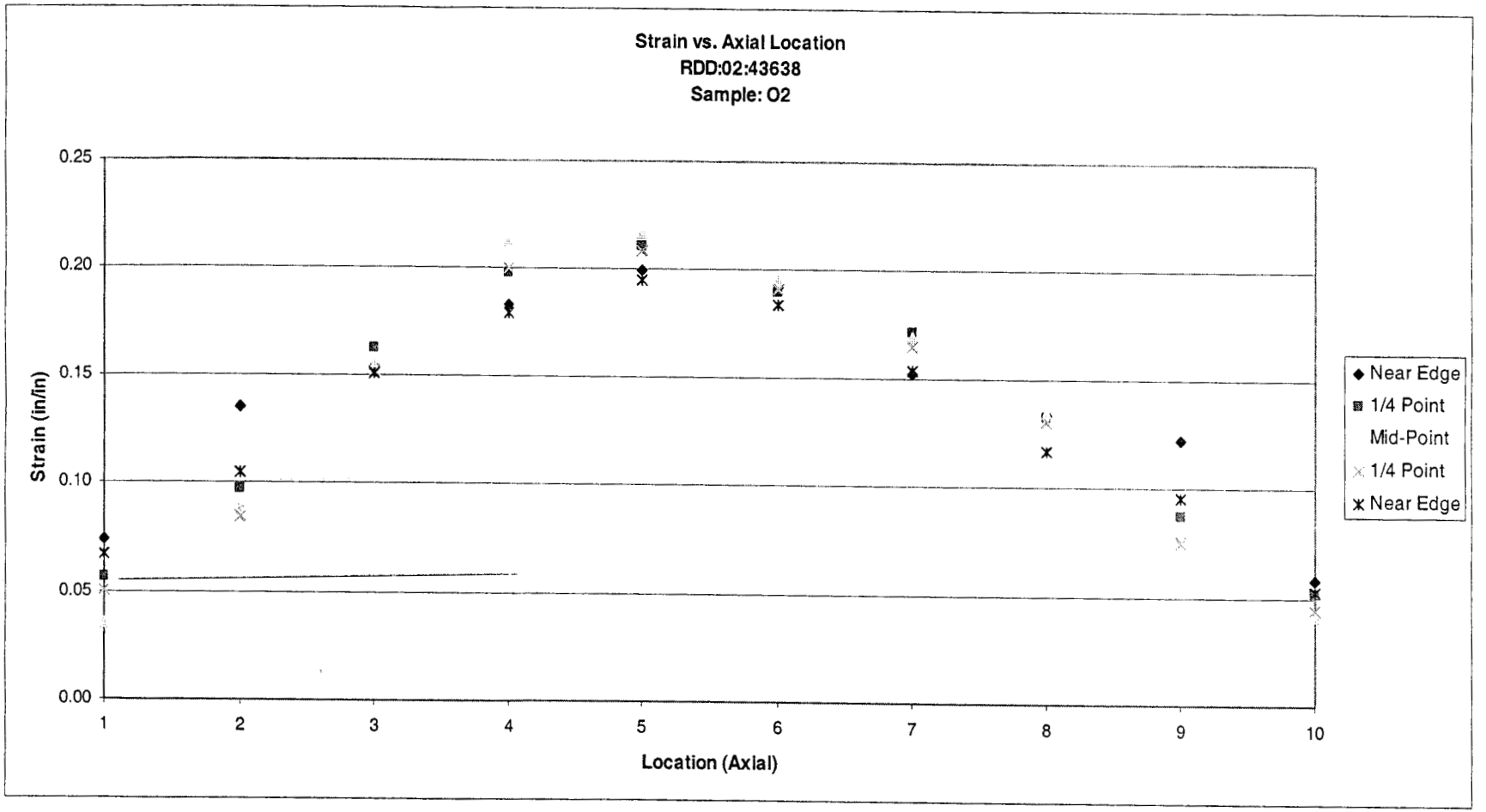
Strain vs. Axial Location
RDD:02:43638
Sample: O2
Strain (in/in)
0.25
0.20
0.15
0.10
0.05
0.00
1
2
3
4
5
6
7
8
9
10
Location (Axial)
Near Edge
1/4 Point
Mid-Point
1/4 Point
Near Edge

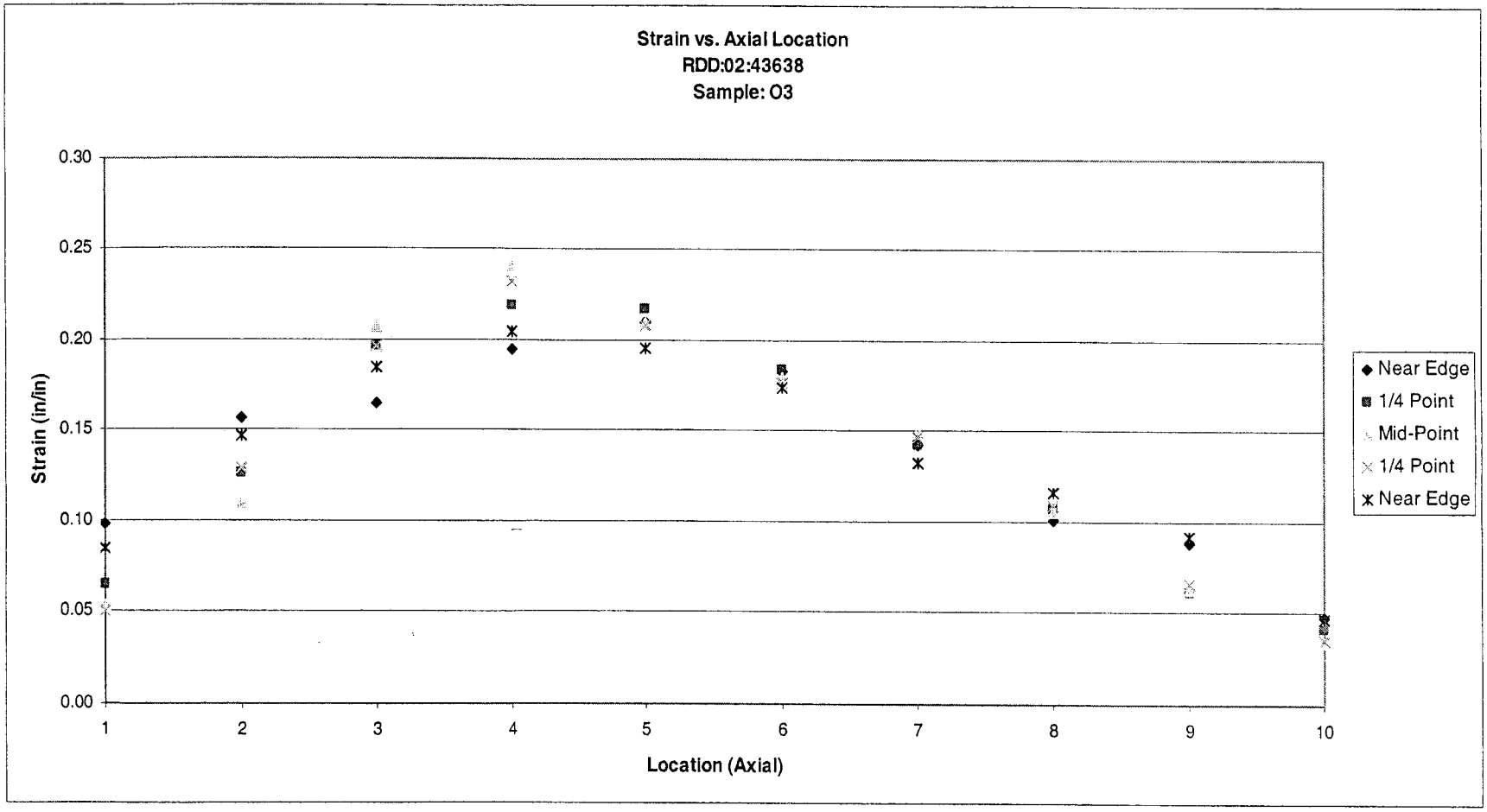
Strain vs. Axial Location
RDD:02:43638
Sample: O3
Strain (in/in)
0.30
0.25
0.20
0.15
0.10
0.05
0.00
1
2
3
4
5
6
7
8
9
10
Location (Axial)
Near Edge
1/4 Point
Mid-Point
1/4 Point
Near Edge

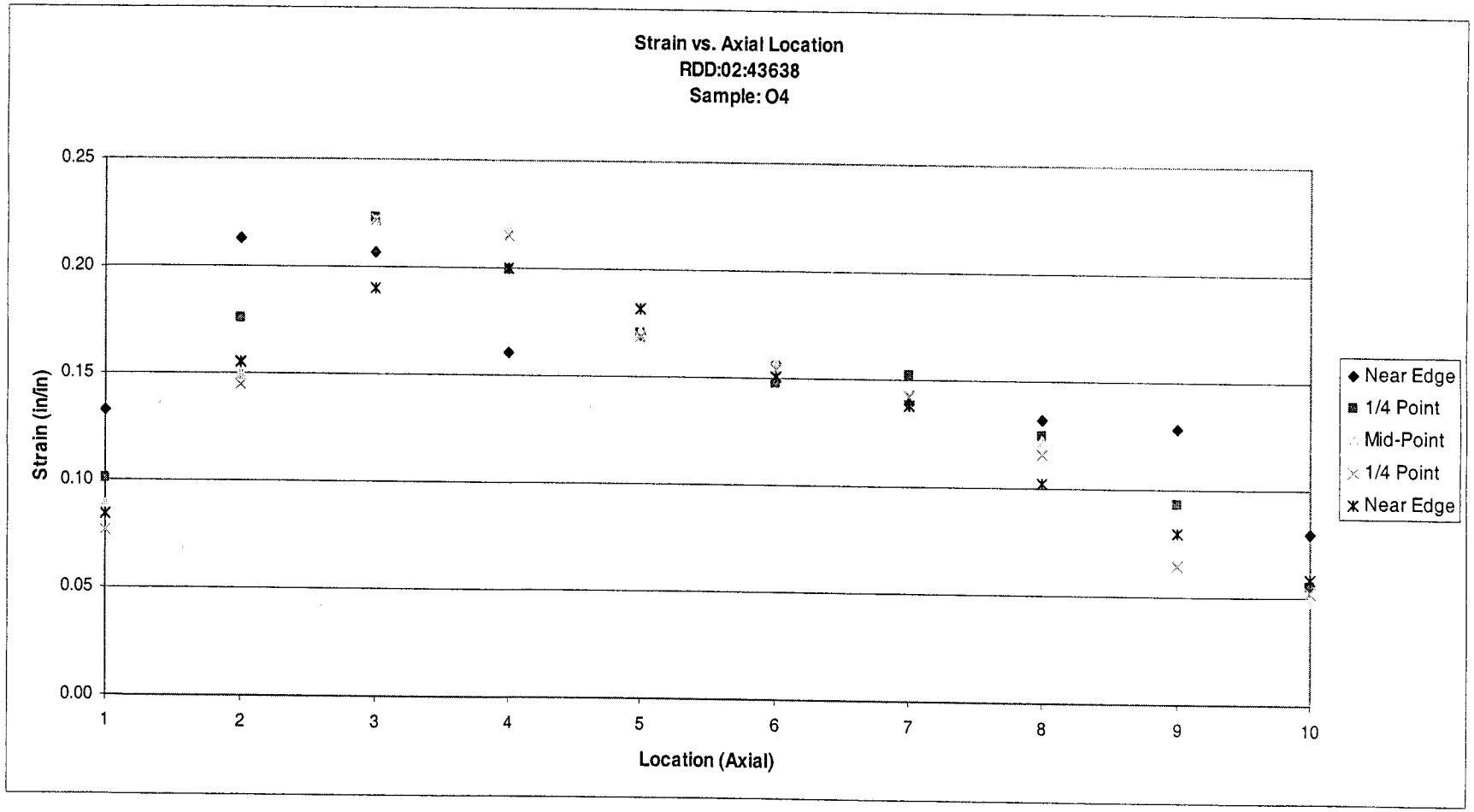
Strain vs. Axial Location
RDD:02:43638
Sample: O4
Strain (in/in)
0.25
0.20
0.15
0.10
0.05
0.00
1
2
3
4
5
6
7
8
9
10
Location (Axial)
Near Edge
1/4 Point
Mid-Point
1/4 Point
Near Edge

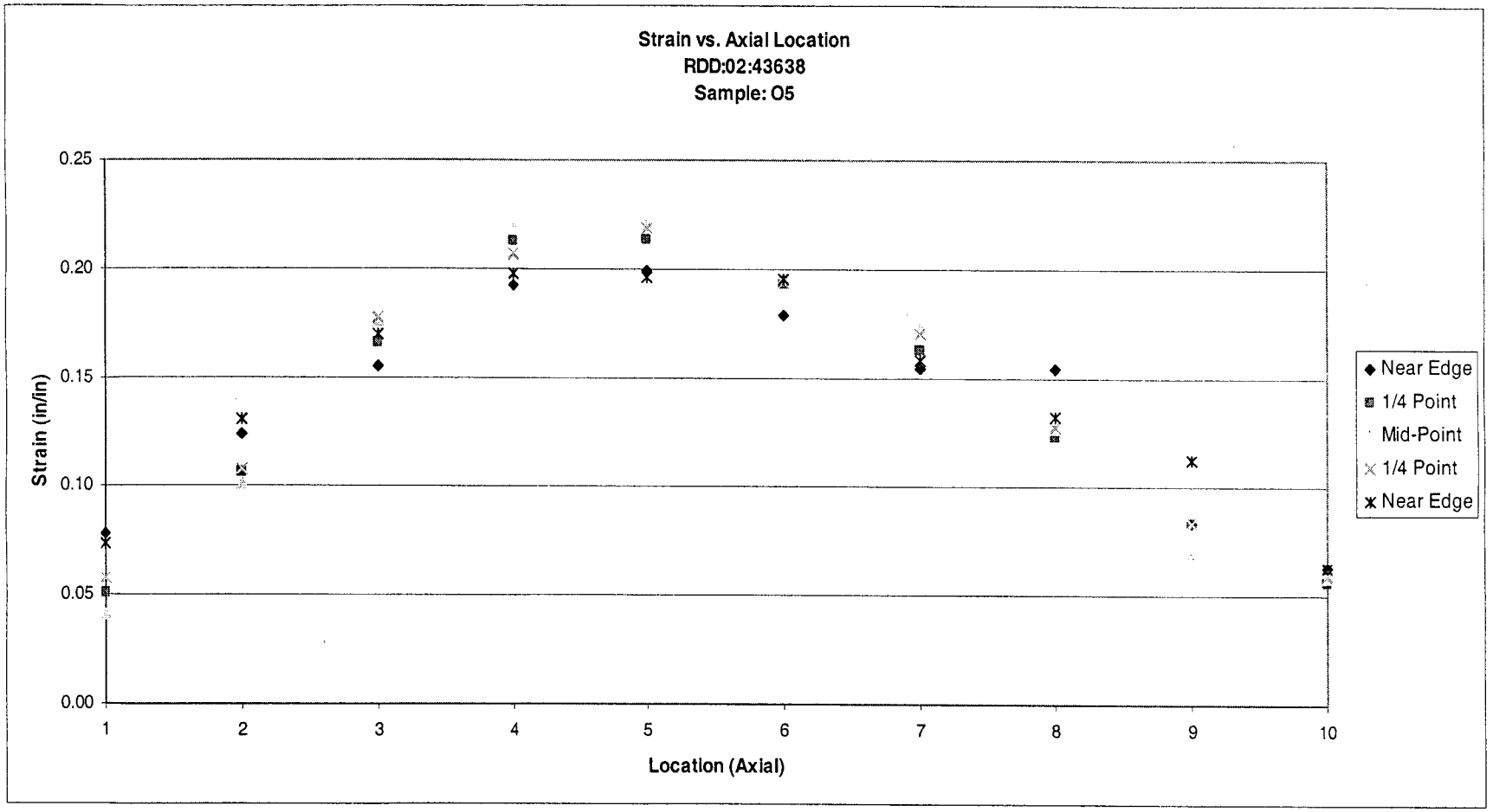
Strain vs. Axial Location
RDD:02:43638
Sample: O5
Strain (in/in)
0.25
0.20
0.15
0.10
0.05
0.00
1
2
3
4
5
6
7
8
9
10
Location (Axial)
Near Edge
1/4 Point
Mid-Point
1/4 Point
Near Edge

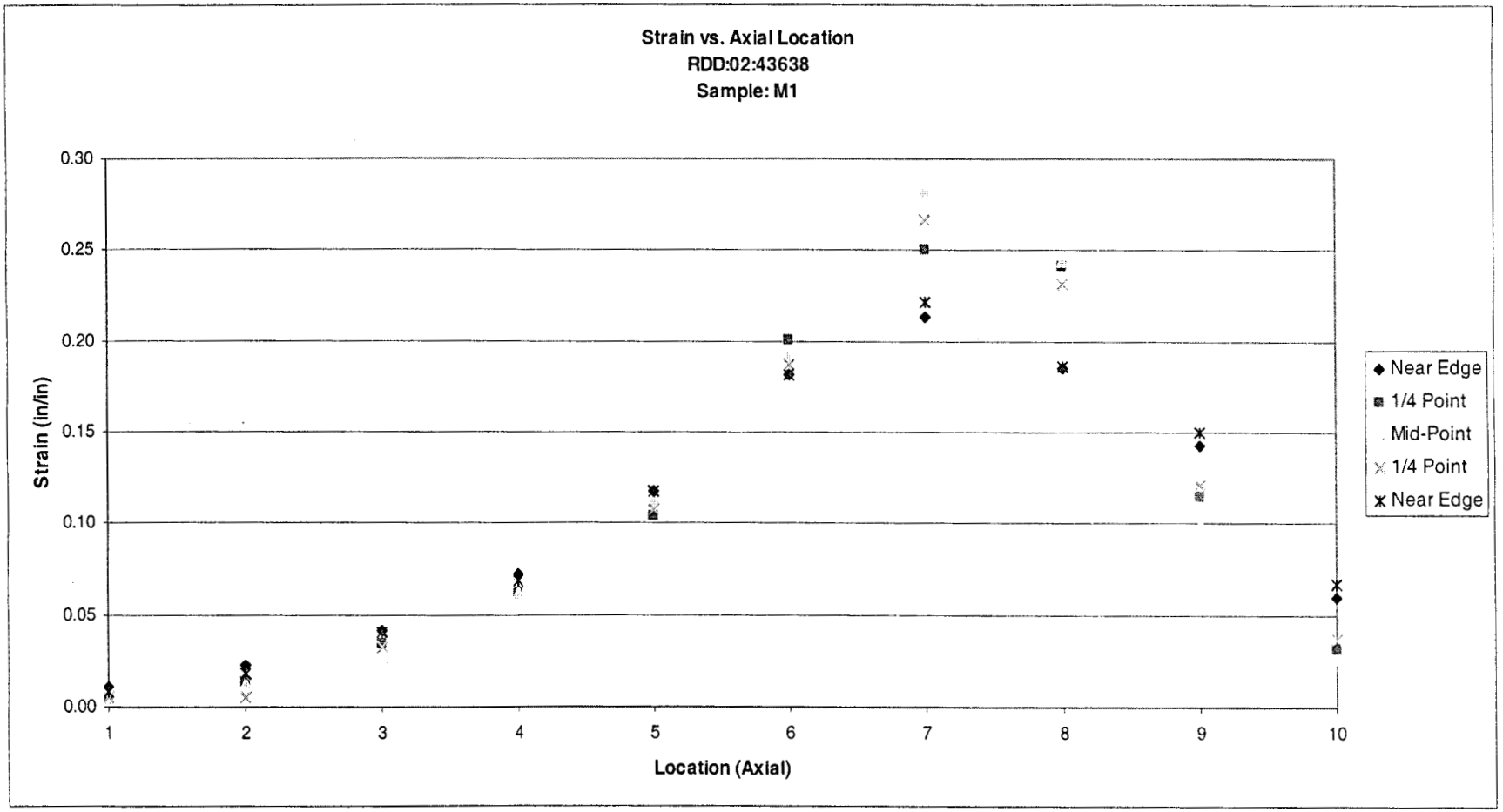
Strain vs. Axial Location
RDD:02:43638
Sample: M1
Strain (in/in)
0.30
0.25
0.20
0.15
0.10
0.05
0.00
1
2
3
4
5
6
7
8
9
10
Location (Axial)
Near Edge
1/4 Point
Mid-Point
1/4 Point
Near Edge

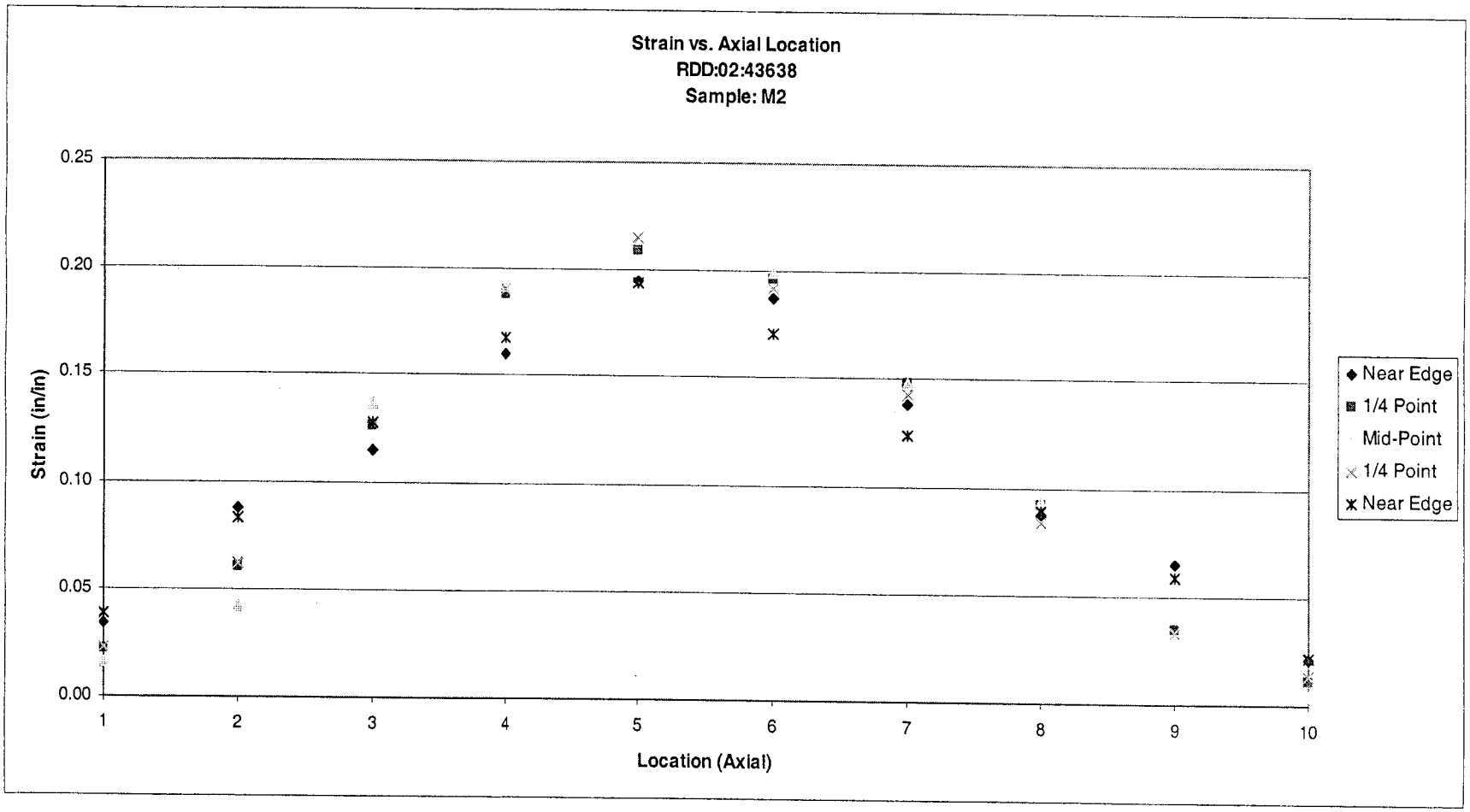
Strain vs. Axial Location
RDD:02:43638
Sample: M2
Strain (in/in)
0.25
0.20
0.15
0.10
0.05
0.00
1
2
3
4
5
6
7
8
9
10
Location (Axial)
Near Edge
1/4 Point
Mid-Point
1/4 Point
Near Edge

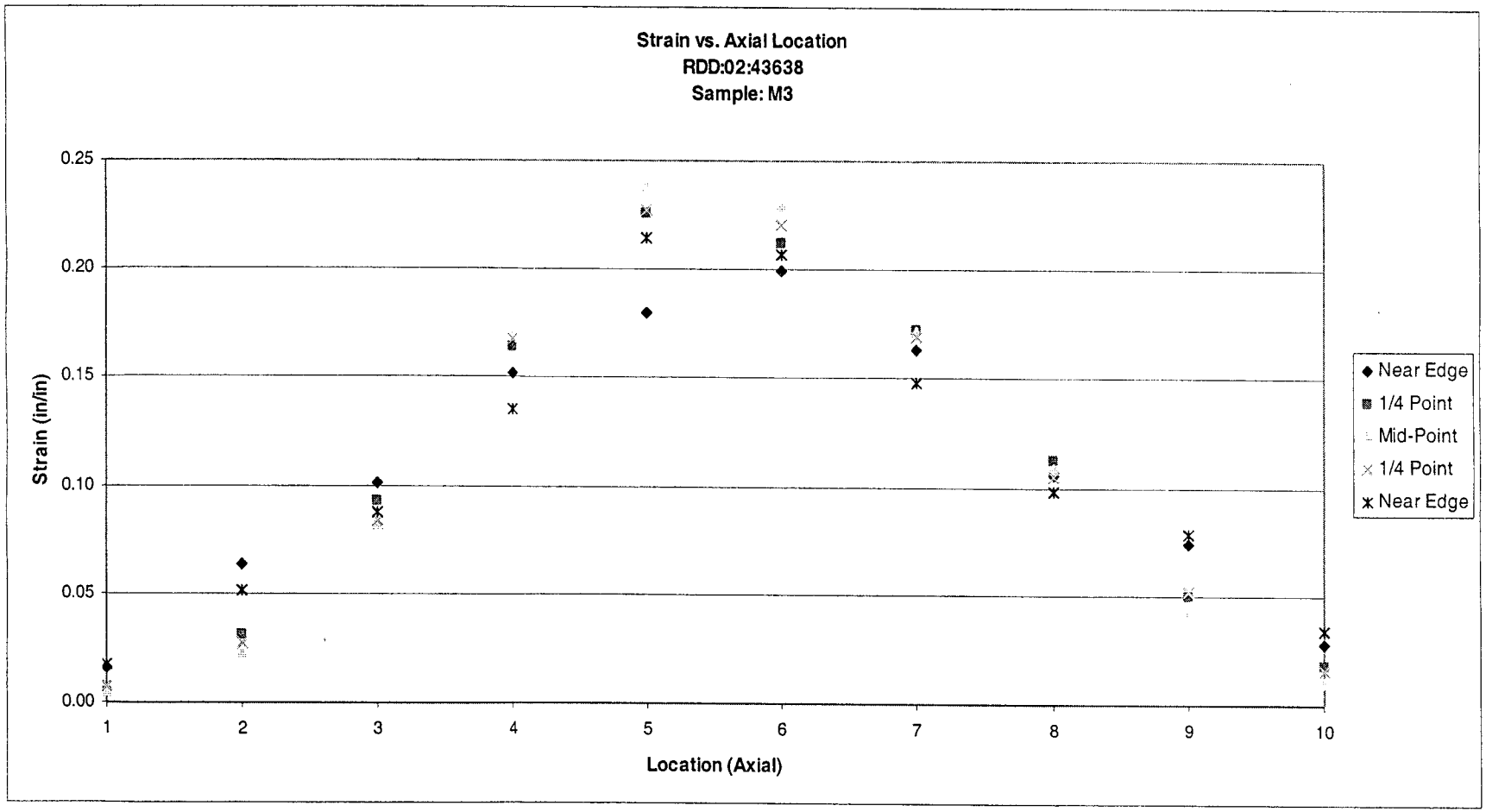
Strain vs. Axial Location
RDD:02:43638
Sample: M3
Strain (in/in)
0.25
0.20
0.15
0.10
0.05
0.00
1
2
3
4
5
6
7
8
9
10
Location (Axial)
Near Edge
1/4 Point
Mid-Point
1/4 Point
Near Edge

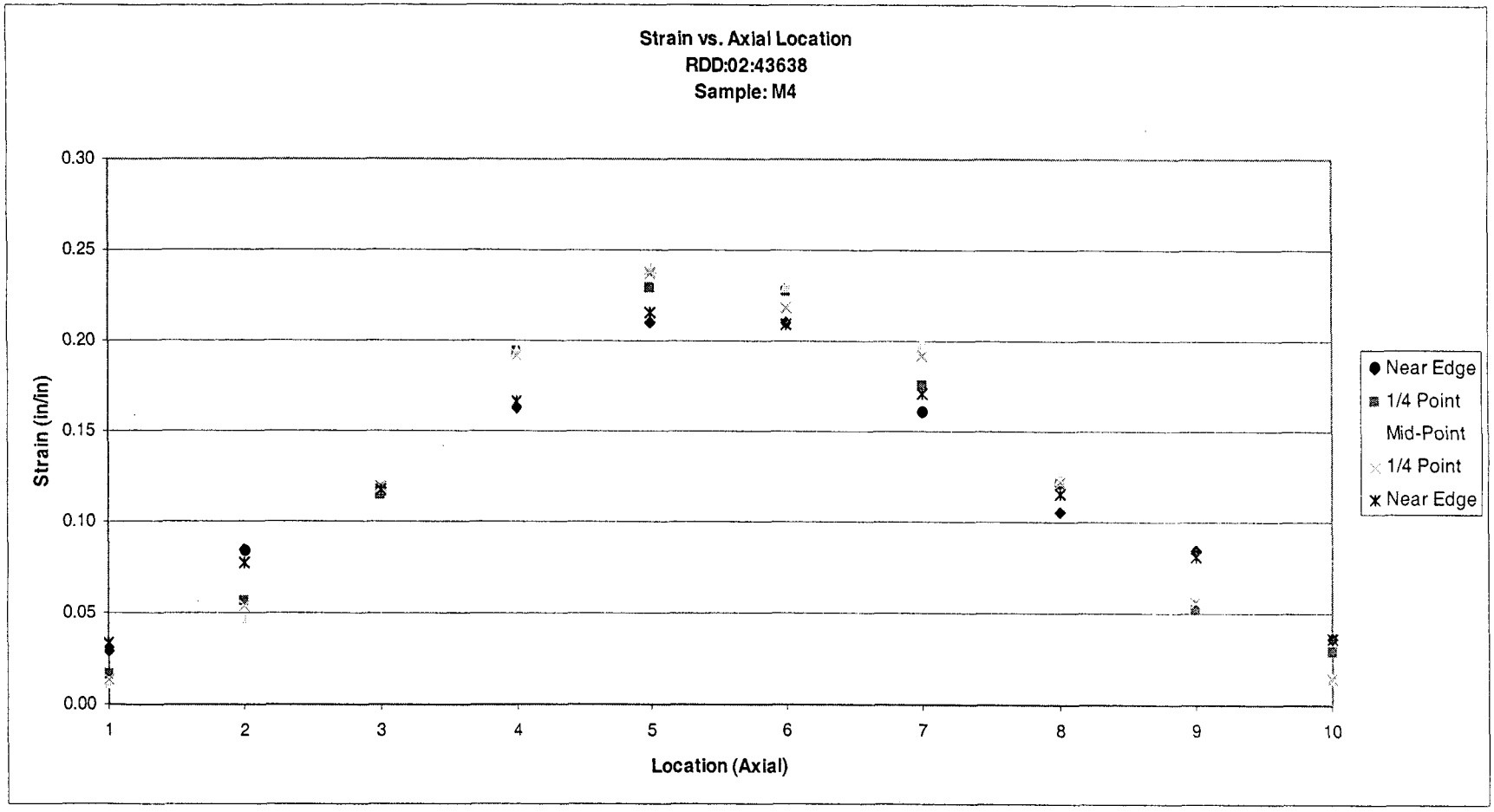
Strain vs. Axial Location
RDD:02:43638
Sample: M4
Strain (in/in)
0.30
0.25
0.20
0.15
0.10
0.05
0.00
1
2
3
4
5
6
7
8
9
10
Location (Axial)
Near Edge
1/4 Point
Mid-Point
1/4 Point
Near Edge

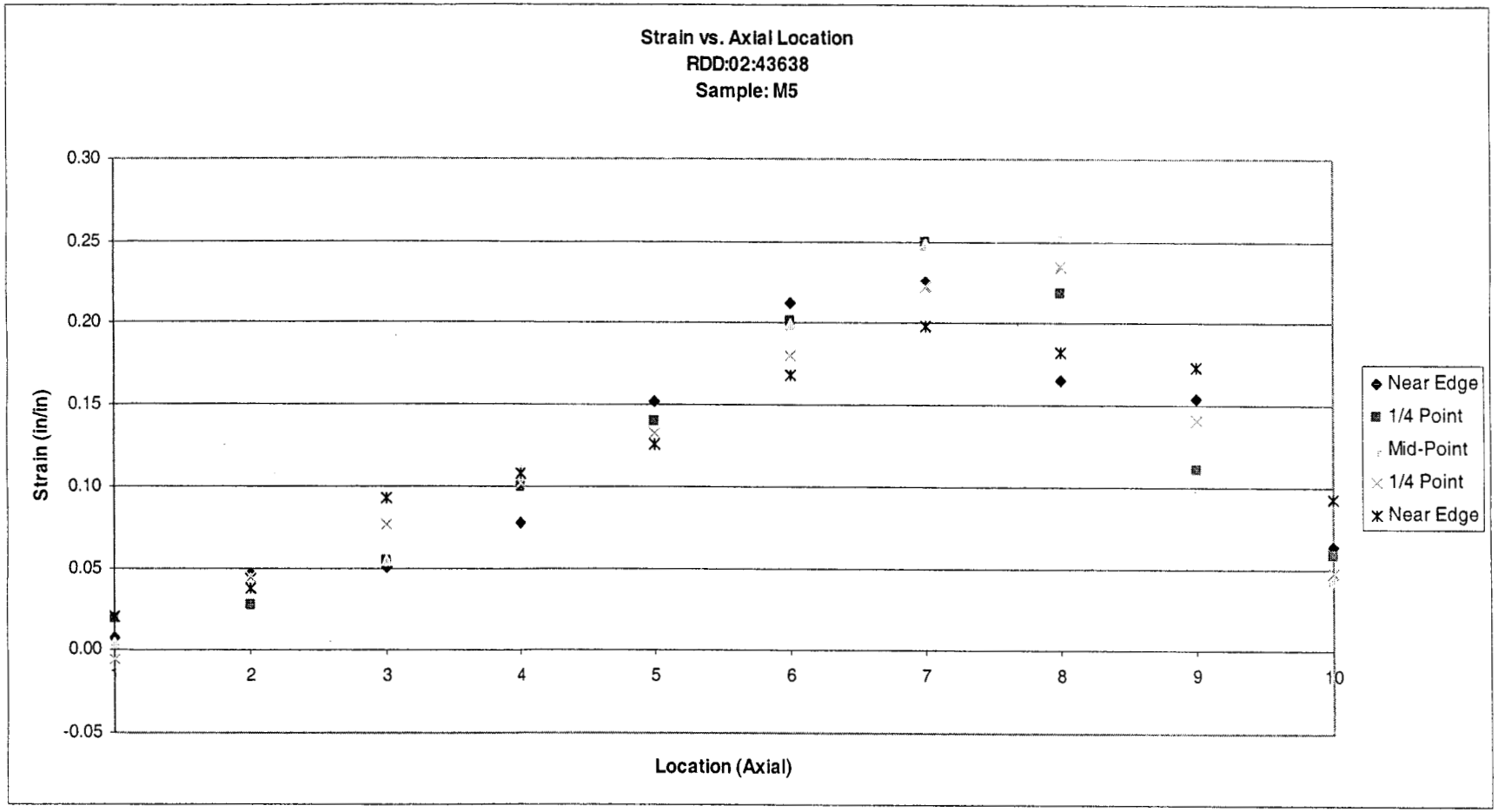
Strain vs. Axial Location
RDD:02:43638
Sample: M5
Strain (in/in)
0.30
0.25
0.20
0.15
0.10
0.05
0.00
-0.05
2
3
4
5
6
7
8
9
10
Location (Axial)
Near Edge
1/4 Point
Mid-Point
1/4 Point
Near Edge

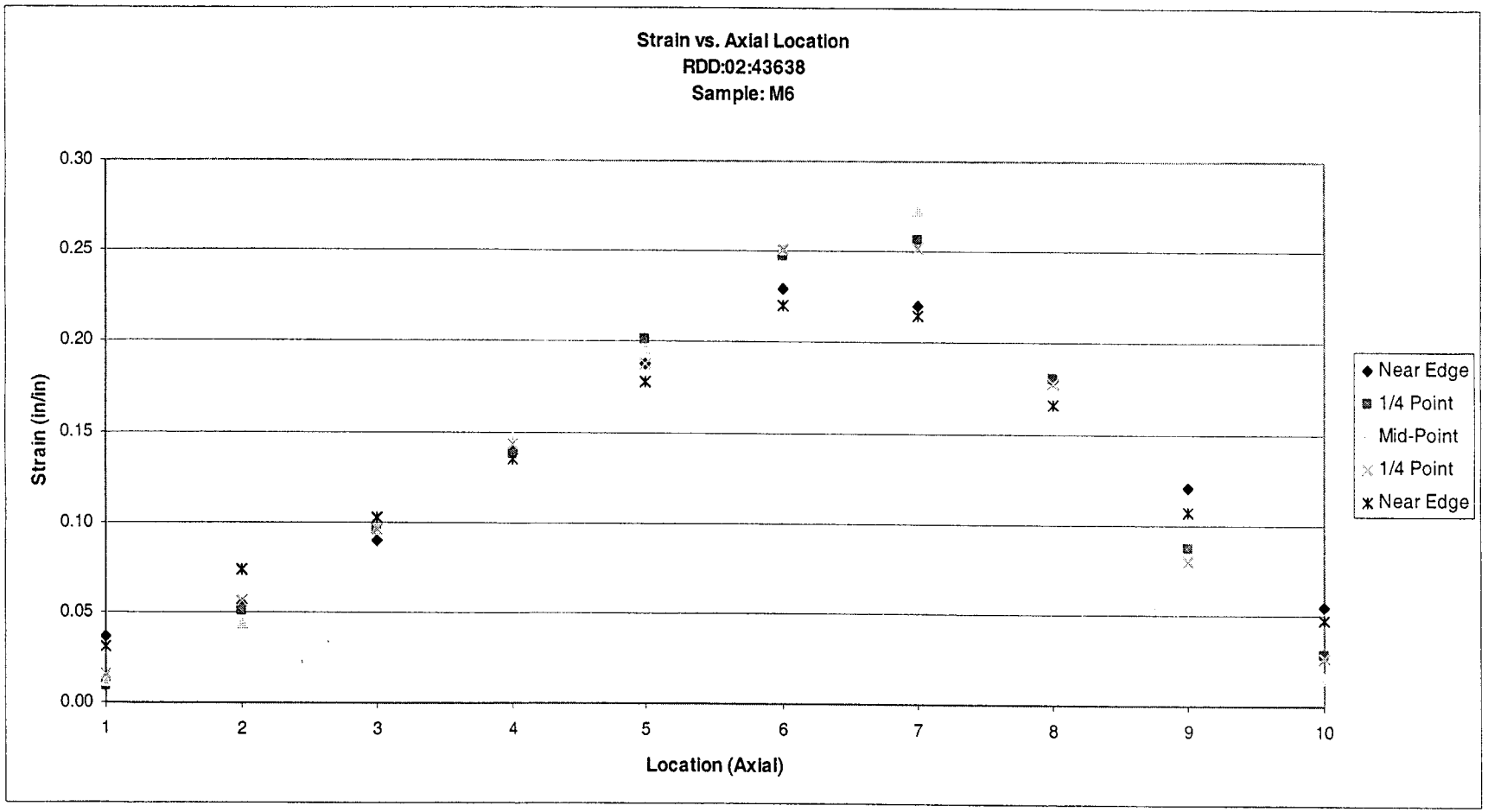
Strain vs. Axial Location
RDD:02:43638
Sample: M6
Strain (in/in)
0.30
0.25
0.20
0.15
0.10
0.05
0.00
1
2
3
4
5
6
7
8
9
10
Location (Axial)
Near Edge
1/4 Point
Mid-Point
1/4 Point
Near Edge

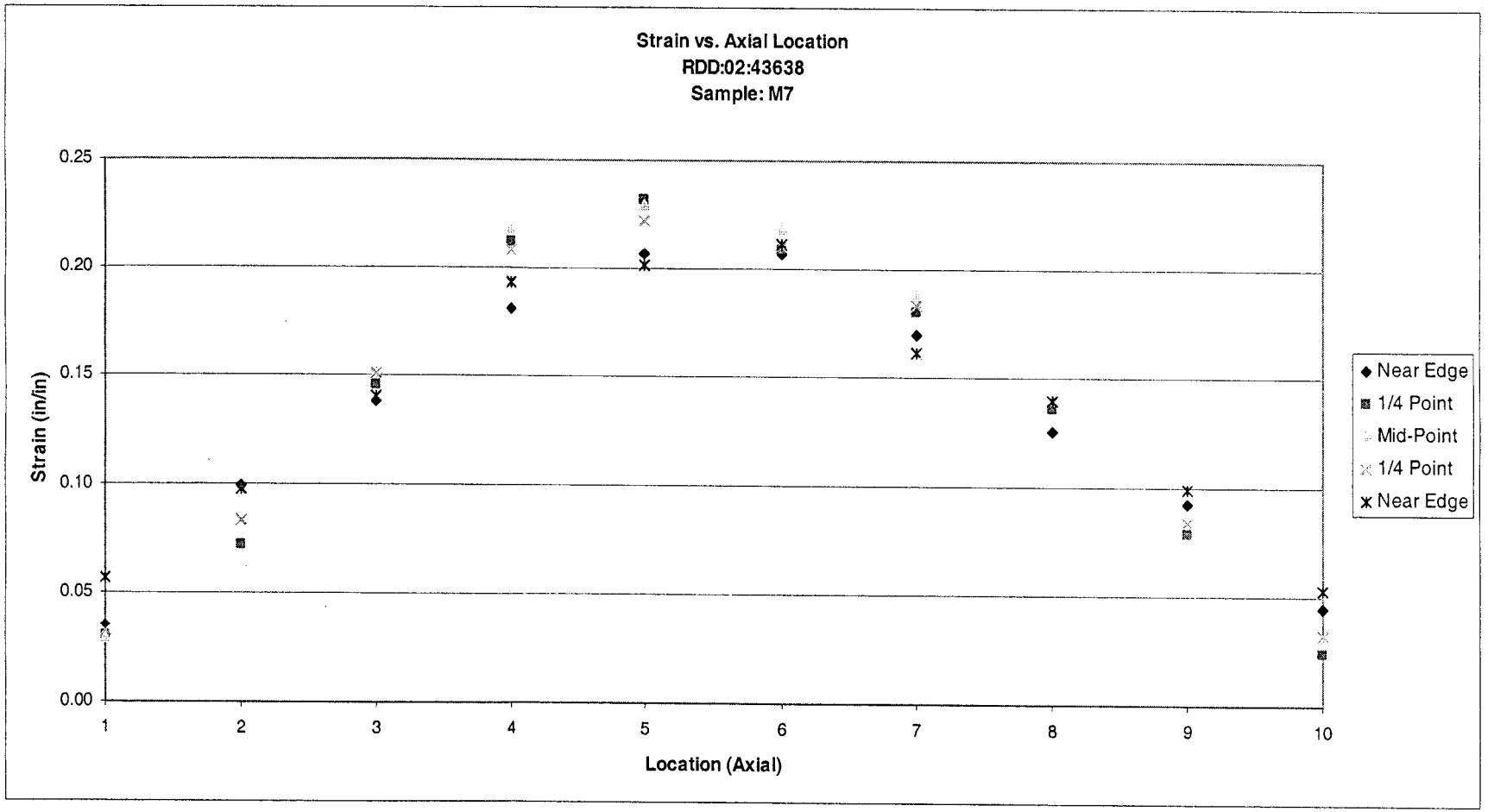
Strain vs. Axial Location
RDD:02:43638
Sample: M7
Strain (in/in)
0.25
0.20
0.15
0.10
0.05
0.00
1
2
3
4
5
6
7
8
9
10
Location (Axial)
Near Edge
1/4 Point
Mid-Point
1/4 Point
Near Edge

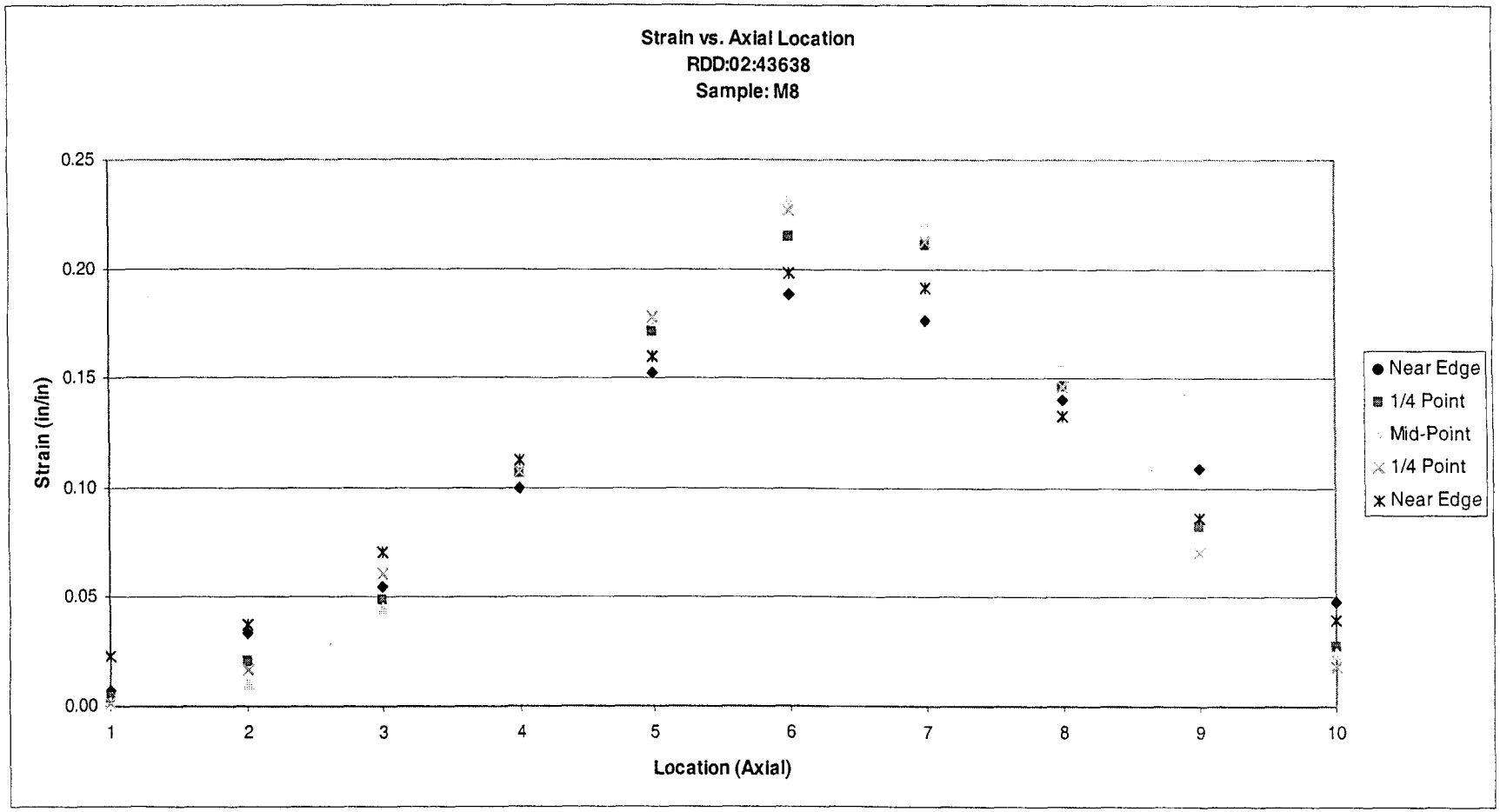
Strain vs. Axial Location
RDD:02:43638
Sample: M8
Strain (in/in)
0.25
0.20
0.15
0.10
0.05
0.00
1
2
3
4
5
6
7
8
9
10
Location (Axial)
Near Edge
1/4 Point
Mid-Point
1/4 Point
Near Edge

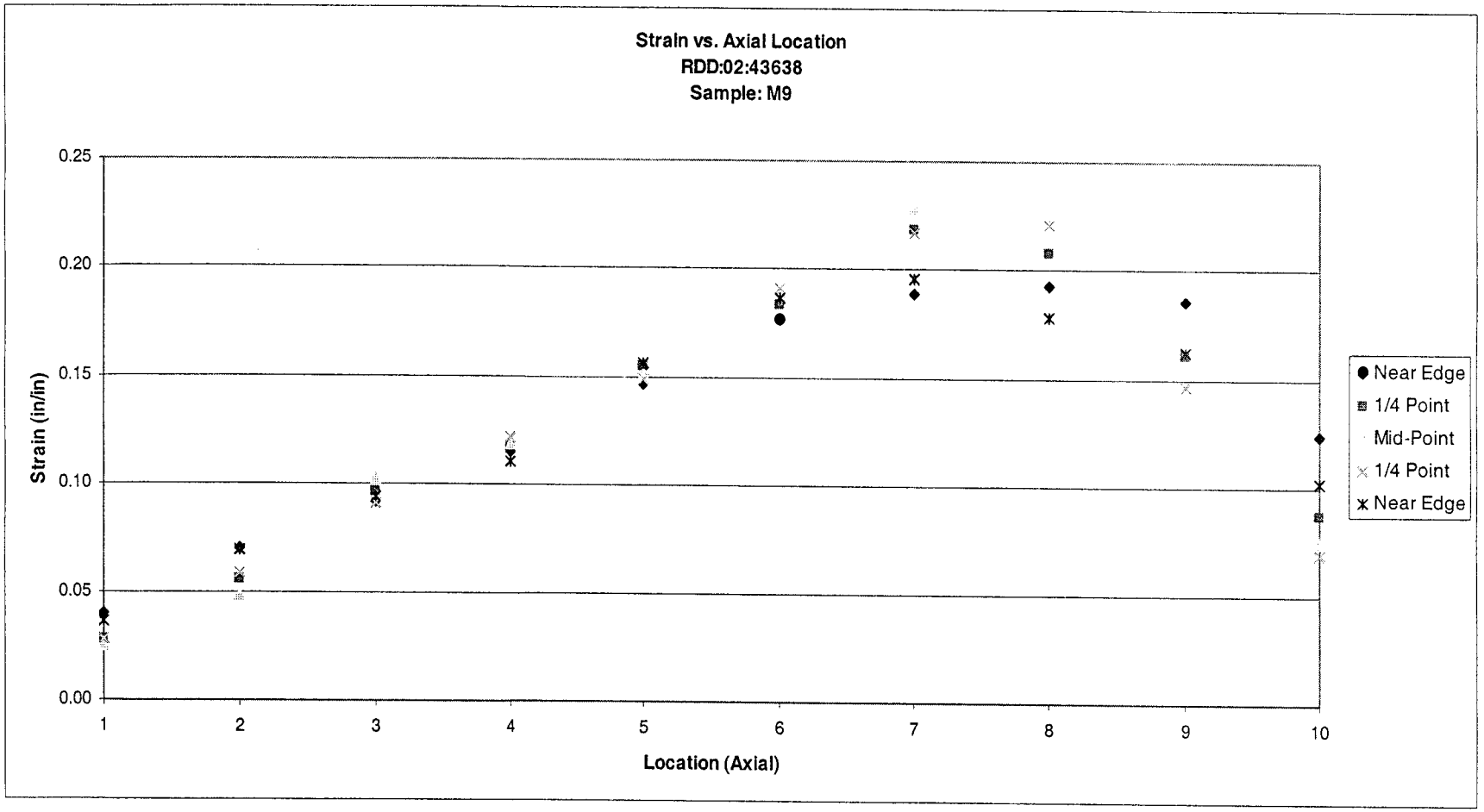
Strain vs. Axial Location
RDD:02:43638
Sample: M9
Strain (in/in)
0.25
0.20
0.15
0.10
0.05
0.00
1
2
3
4
5
6
7
8
9
10
Location (Axial)
Near Edge
1/4 Point
Mid-Point
1/4 Point
Near Edge

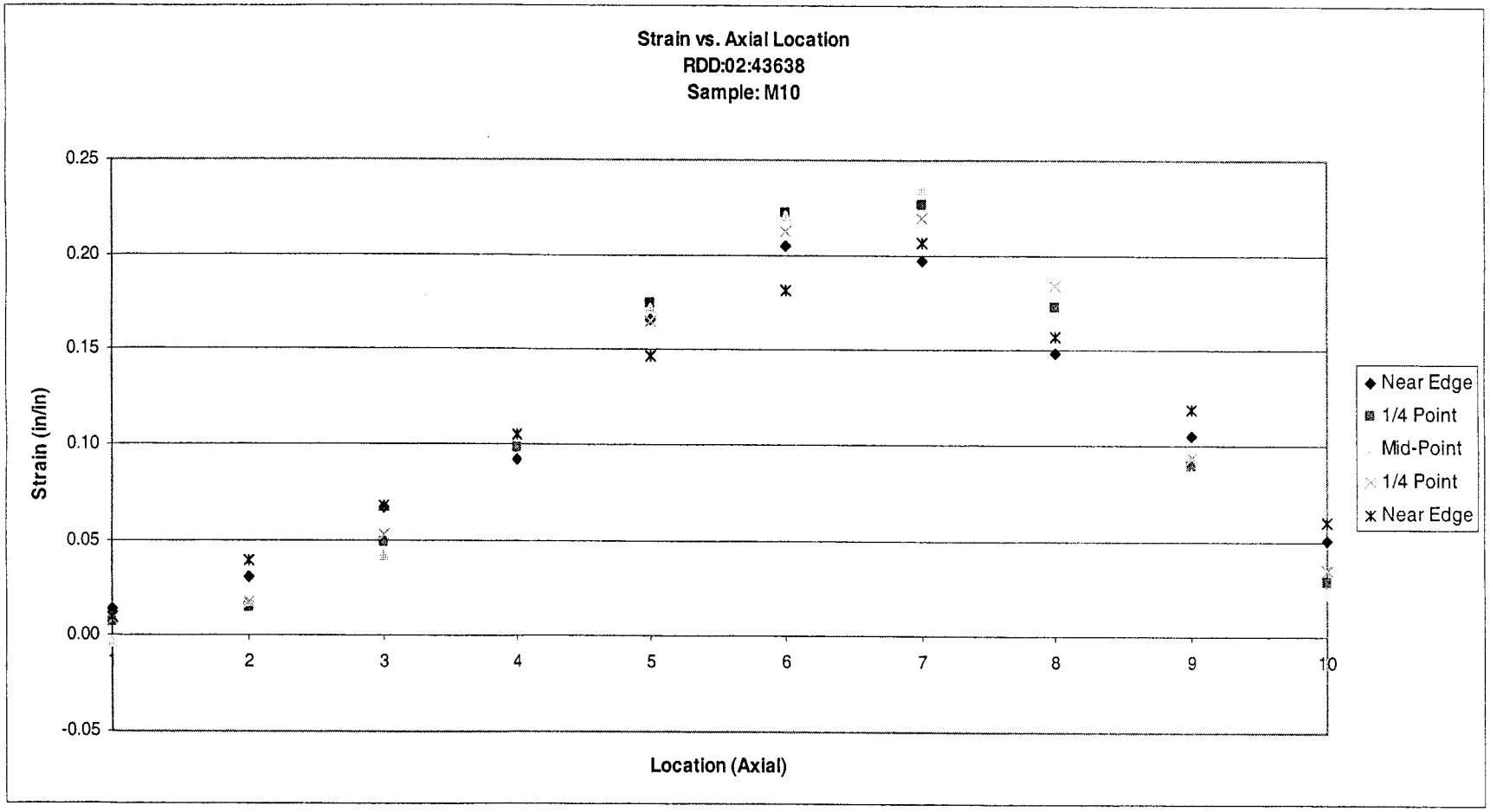
Strain vs. Axial Location
RDD:02:43638
Sample: M10
Strain (in/in)
0.25
0.20
0.15
0.10
0.05
0.00
-0.05
1
2
3
4
5
6
7
8
9
10
Location (Axial)
Near Edge
1/4 Point
Mid-Point
1/4 Point
Near Edge

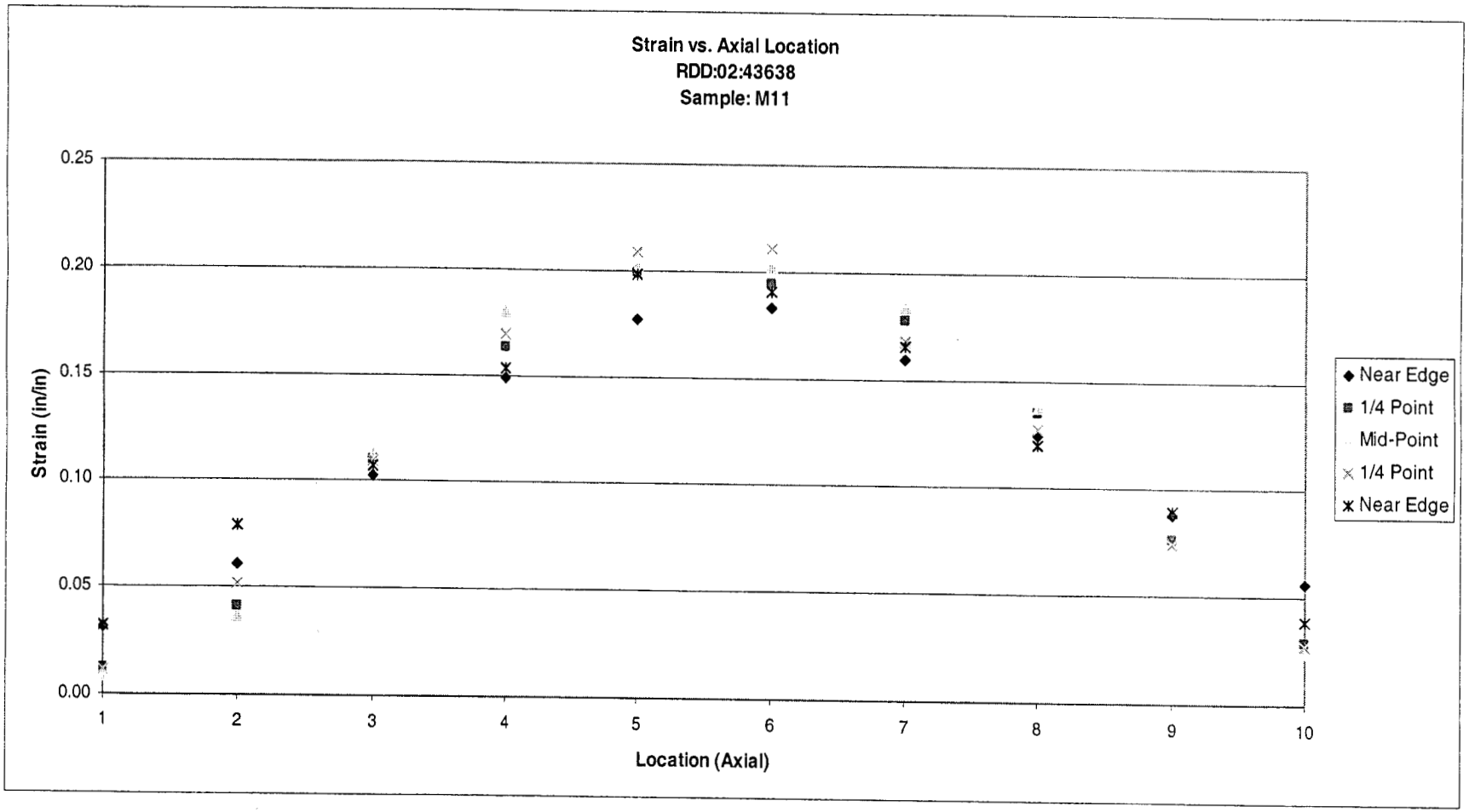
Strain vs. Axial Location
RDD:02:43638
Sample: M11
Strain (in/in)
0.25
0.20
0.15
0.10
0.05
0.00
1
2
3
4
5
6
7
8
9
10
Location (Axial)
Near Edge
1/4 Point
Mid-Point
1/4 Point
Near Edge

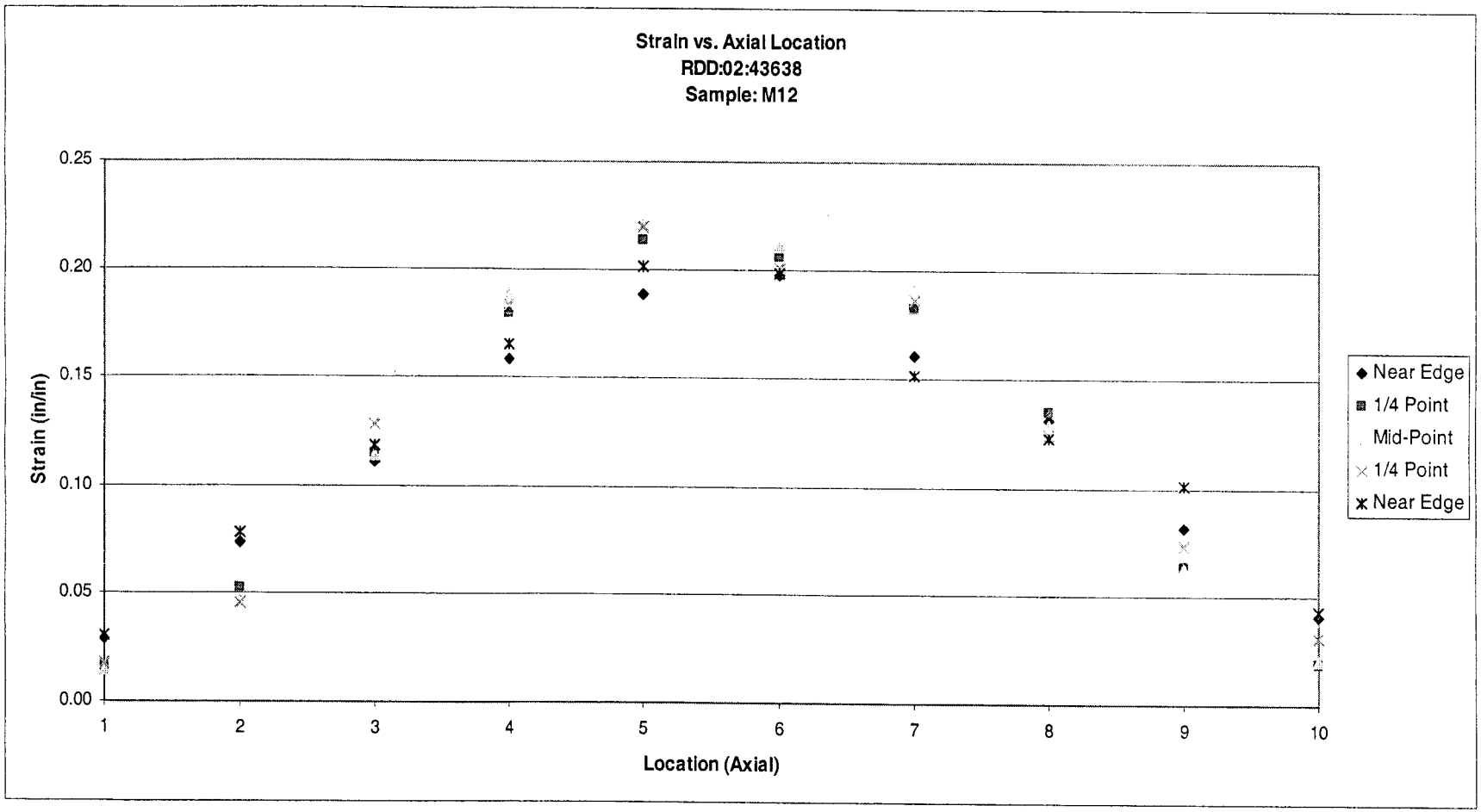
Strain vs. Axial Location
RDD:02:43638
Sample: M12
Strain (in/in)
0.25
0.20
0.15
0.10
0.05
0.00
1
2
3
4
5
6
7
8
9
10
Location (Axial)
Near Edge
1/4 Point
Mid-Point
1/4 Point
Near Edge

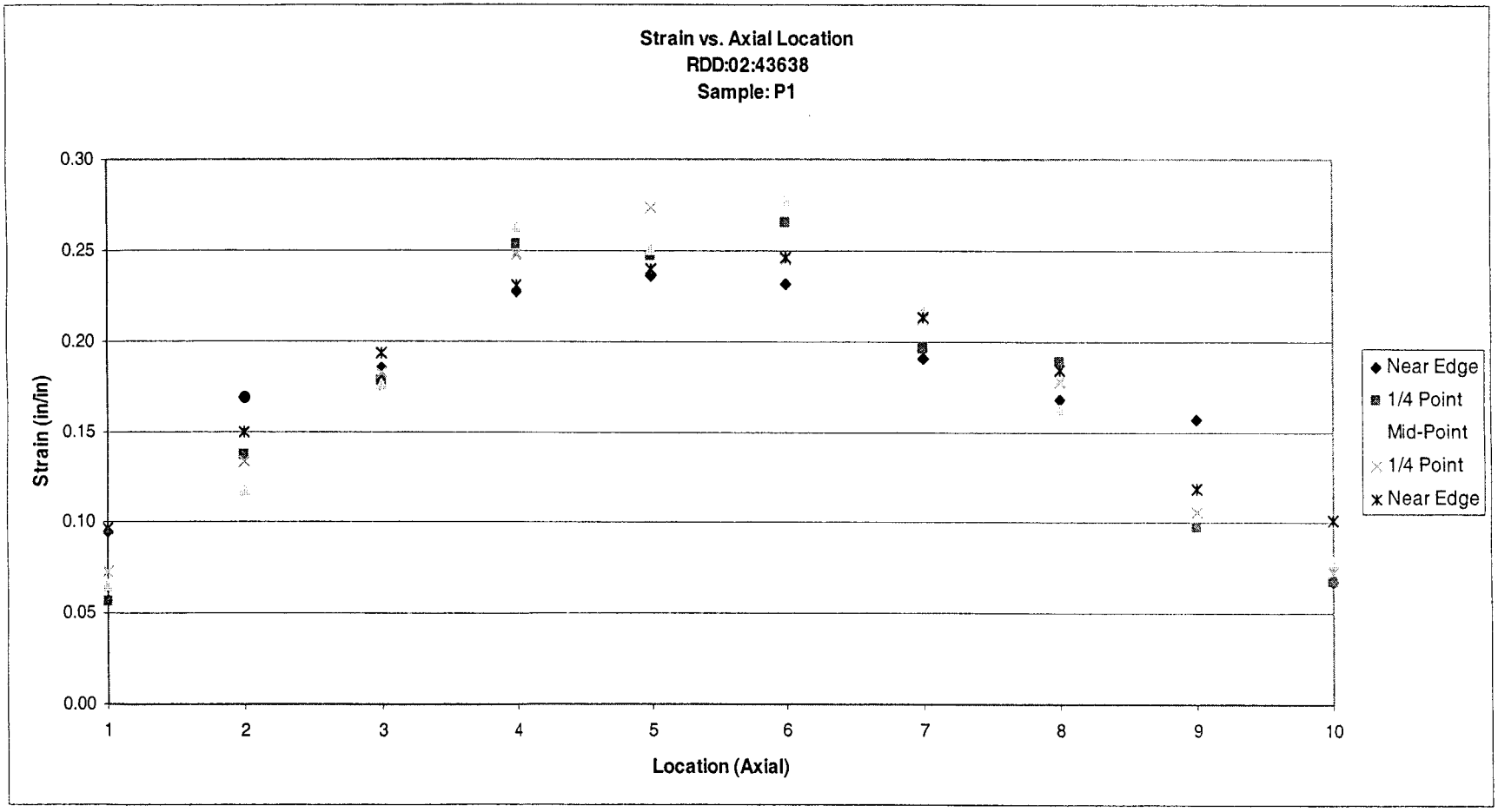
Strain vs. Axial Location
RDD:02:43638
Sample: P1
Strain (in/in)
0.30
0.25
0.20
0.15
0.10
0.05
0.00
1
2
3
4
5
6
7
8
9
10
Location (Axial)
Near Edge
1/4 Point
Mid-Point
1/4 Point
Near Edge

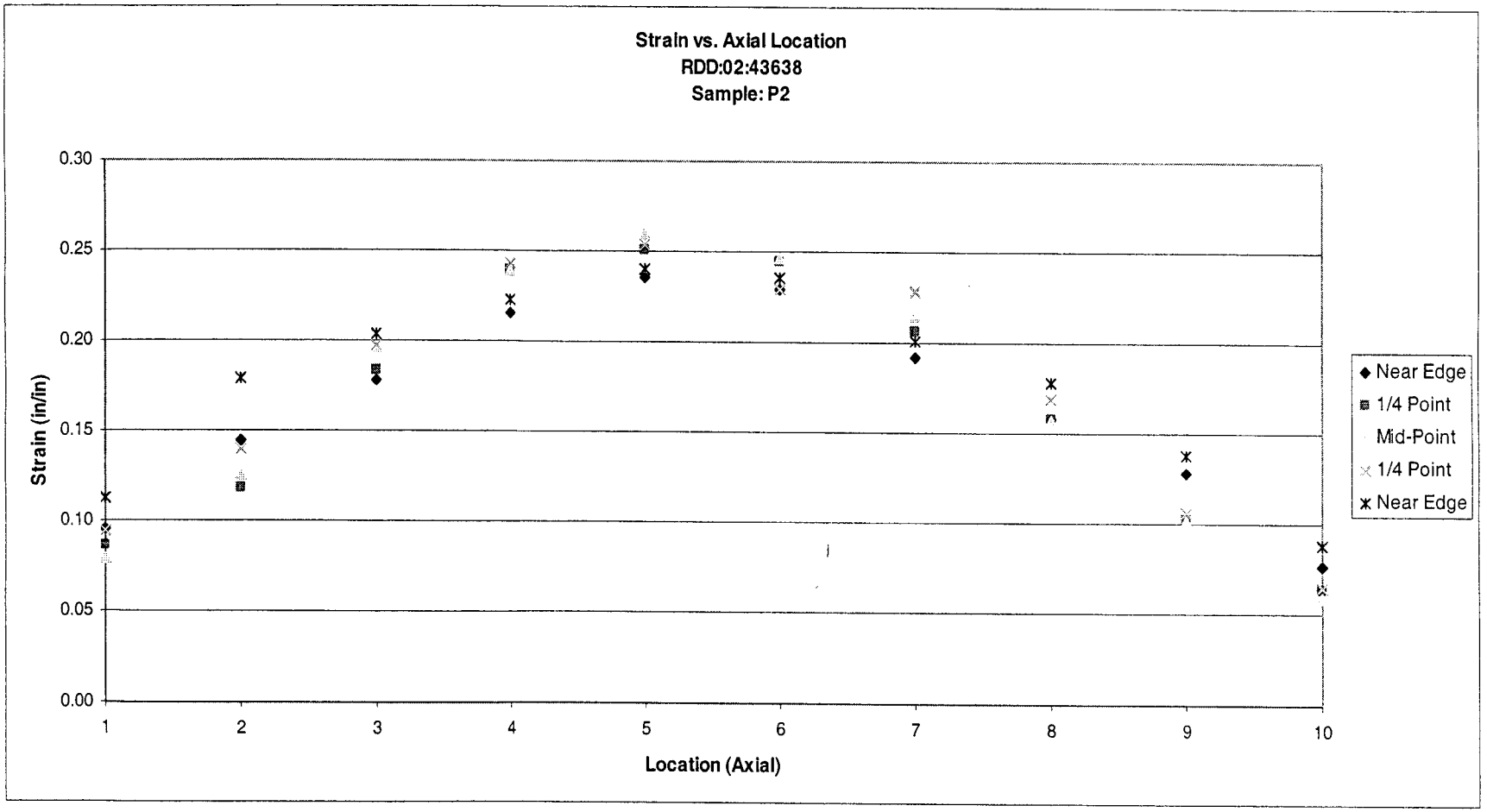
Strain vs. Axial Location
RDD:02:43638
Sample: P2
Strain (in/in)
0.30
0.25
0.20
0.15
0.10
0.05
0.00
1
2
3
4
5
6
7
8
9
10
Location (Axial)
Near Edge
1/4 Point
Mid-Point
1/4 Point
Near Edge

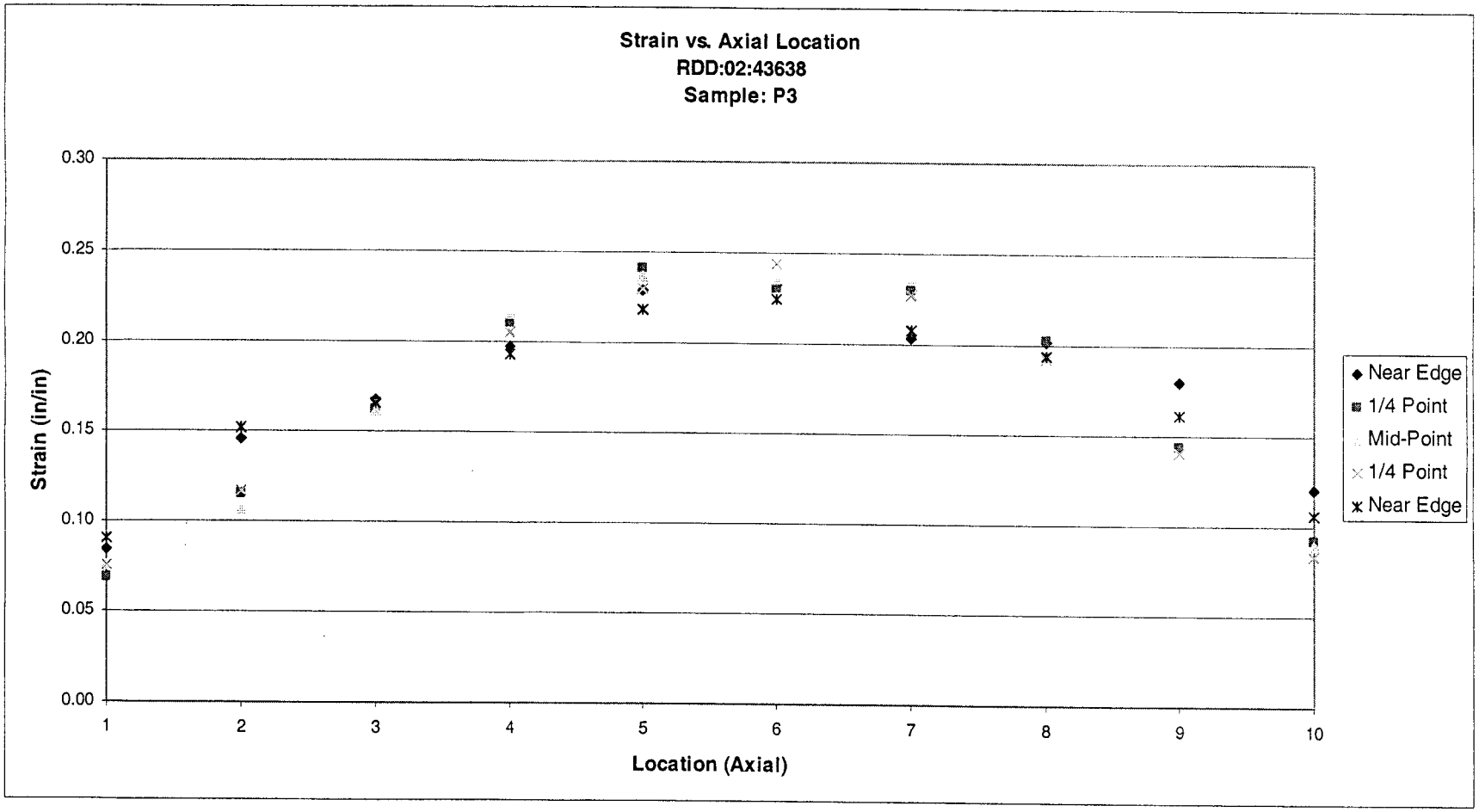
Strain vs. Axial Location
RDD:02:43638
Sample: P3
Strain (in/in)
0.30
0.25
0.20
0.15
0.10
0.05
0.00
1
2
3
4
5
6
7
8
9
10
Location (Axial)
Near Edge
1/4 Point
Mid-Point
1/4 Point
Near Edge

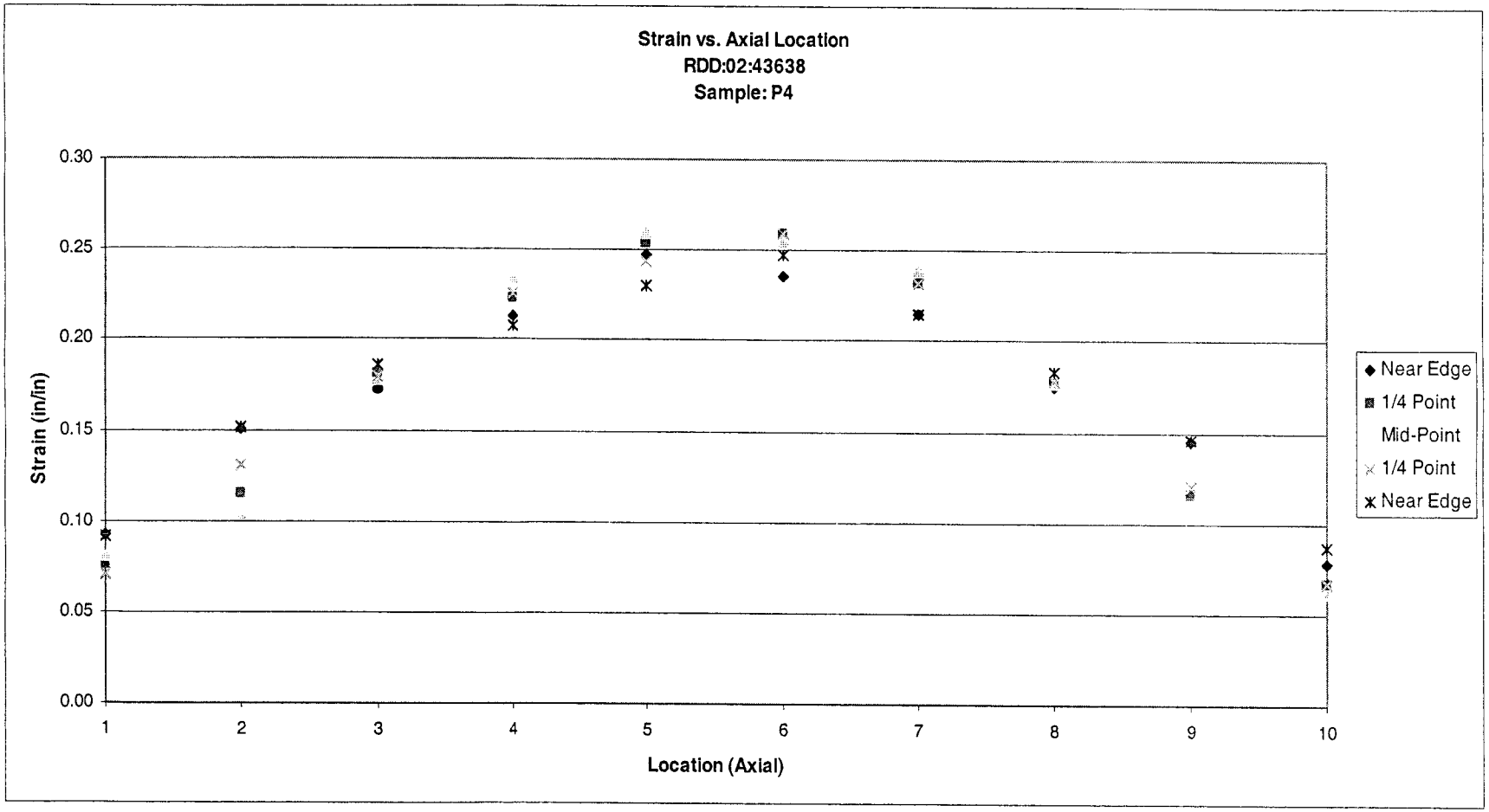
Strain vs. Axial Location
RDD:02:43638
Sample: P4
Strain (in/in)
0.30
0.25
0.20
0.15
0.10
0.05
0.00
1
2
3
4
5
6
7
8
9
10
Location (Axial)
Near Edge
1/4 Point
Mid-Point
1/4 Point
Near Edge

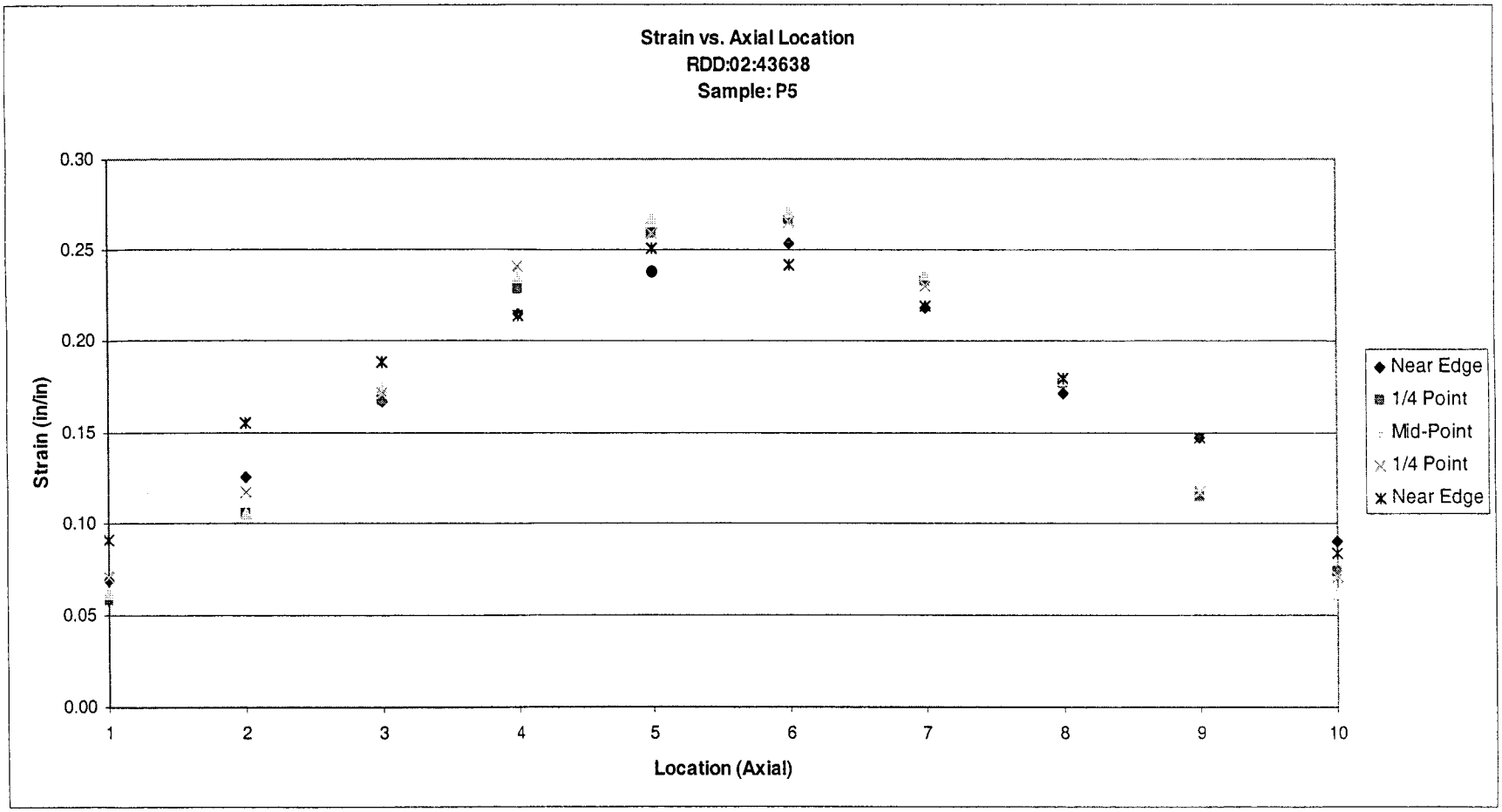
Strain vs. Axial Location
RDD:02:43638
Sample: P5
Strain (in/in)
0.30
0.25
0.20
0.15
0.10
0.05
0.00
1
2
3
4
5
6
7
8
9
10
Location (Axial)
Near Edge
1/4 Point
Mid-Point
1/4 Point
Near Edge

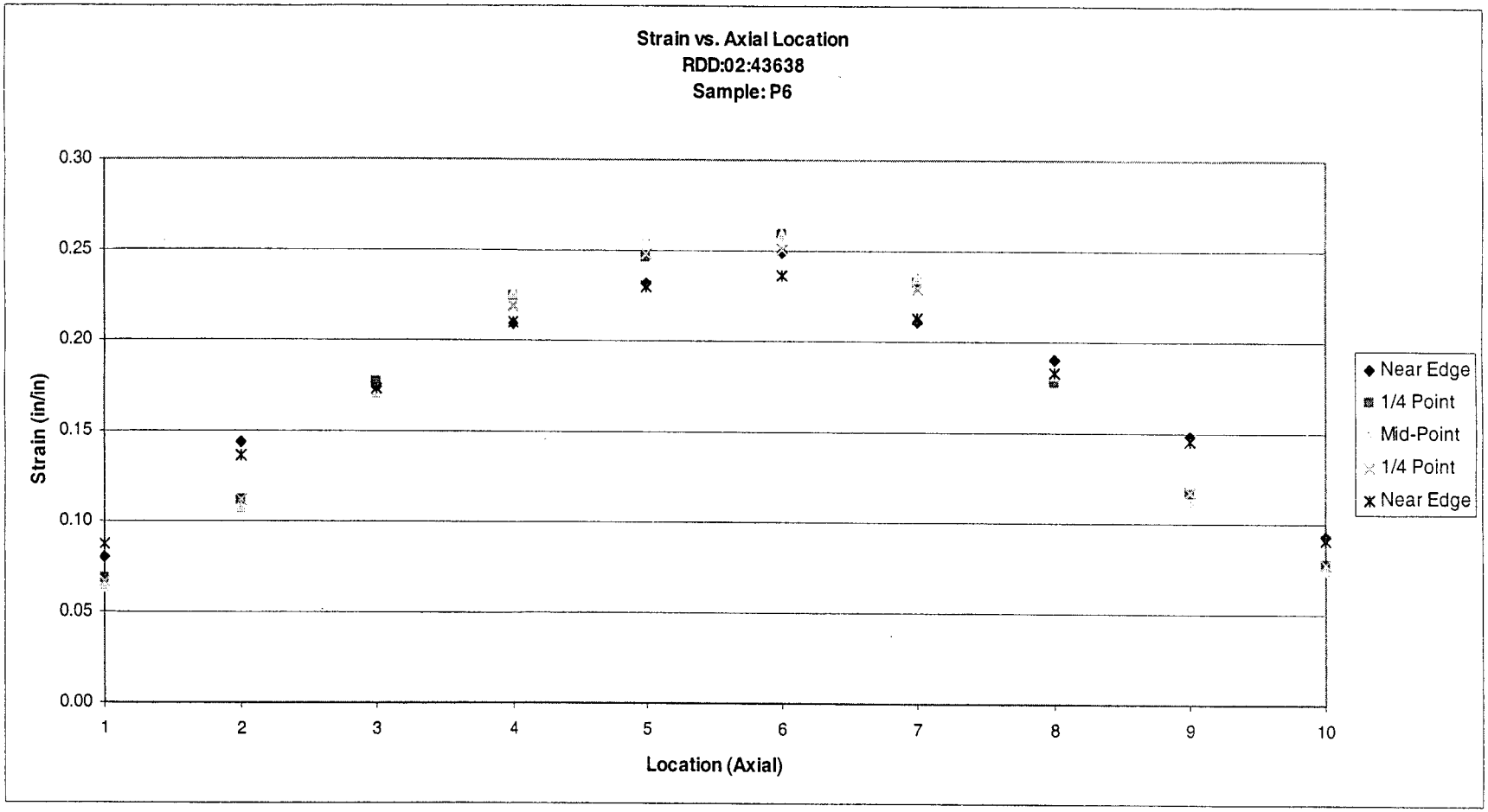
Strain vs. Axial Location
RDD:02:43638
Sample: P6
Strain (in/in)
0.30
0.25
0.20
0.15
0.10
0.05
0.00
1
2
3
4
5
6
7
8
9
10
Location (Axial)
Near Edge
1/4 Point
Mid-Point
1/4 Point
Near Edge

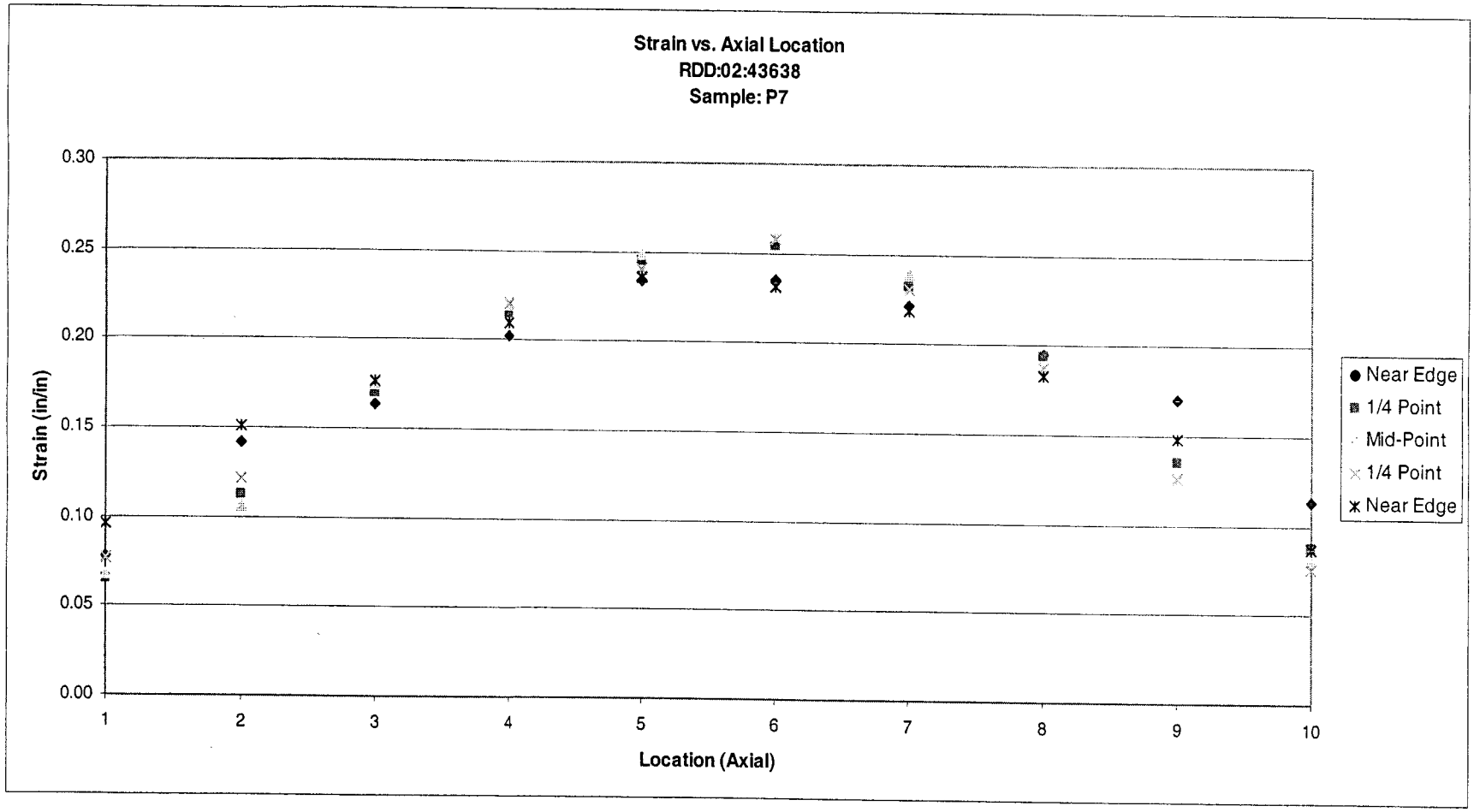
Strain vs. Axial Location
RDD:02:43638
Sample: P7
Strain (in/in)
0.30
0.25
0.20
0.15
0.10
0.05
0.00
1
2
3
4
5
6
7
8
9
10
Location (Axial)
Near Edge
1/4 Point
Mid-Point
1/4 Point
Near Edge

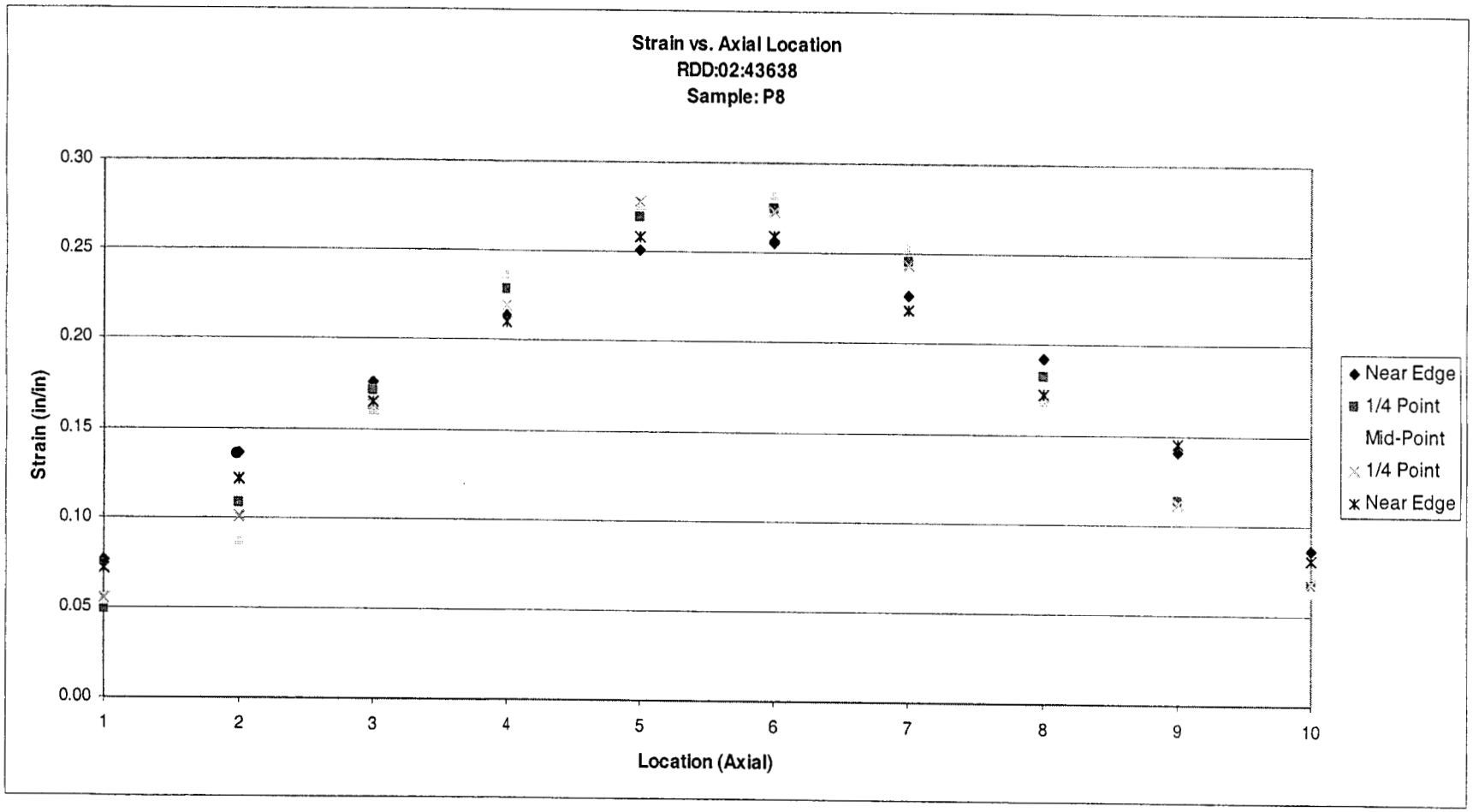
Strain vs. Axial Location
RDD:02:43638
Sample: P8
Strain (in/in)
0.30
0.25
0.20
0.15
0.10
0.05
0.00
1
2
3
4
5
6
7
8
9
10
Location (Axial)
Near Edge
1/4 Point
Mid-Point
1/4 Point
Near Edge

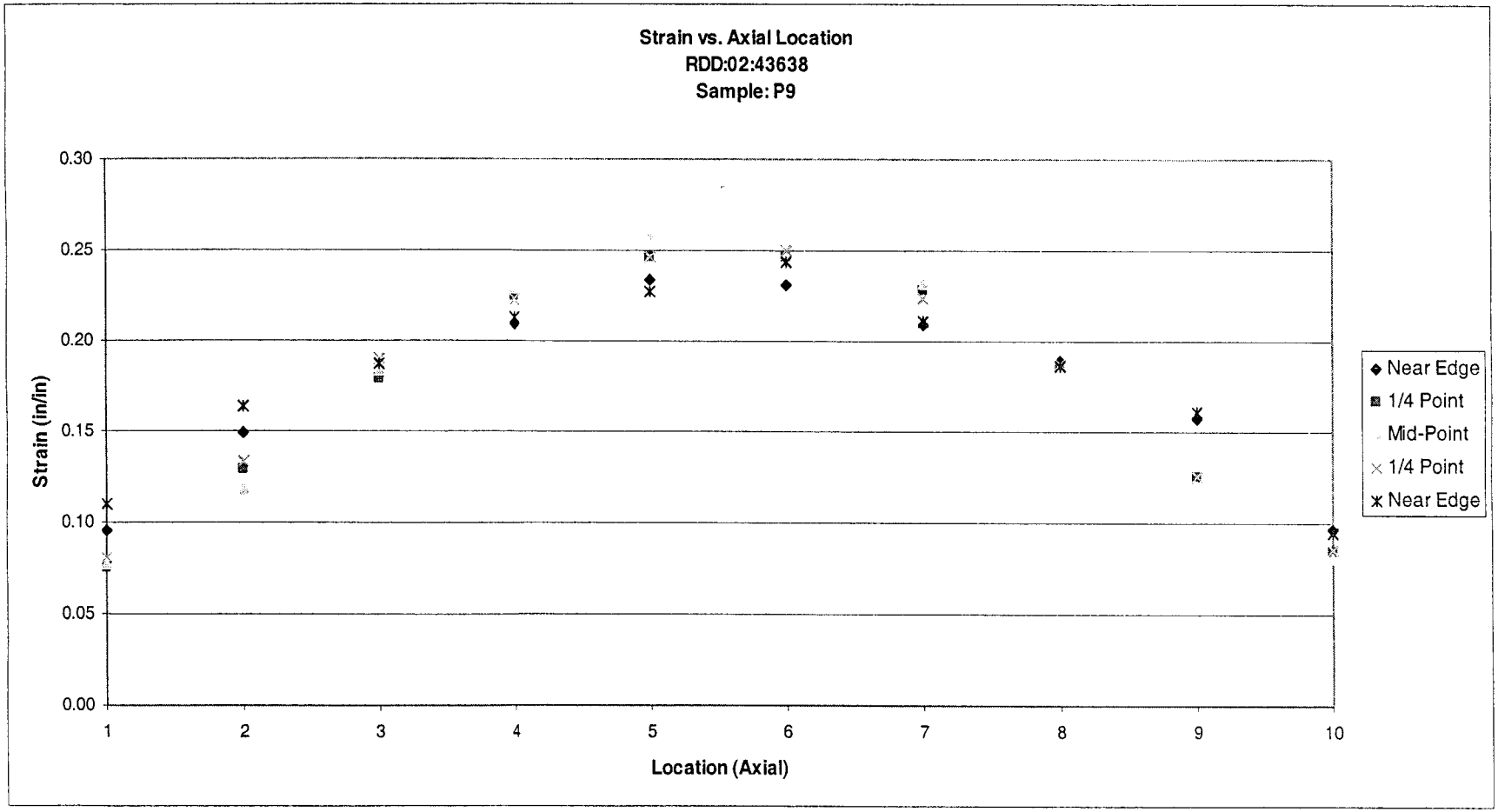
Strain vs. Axial Location
RDD:02:43638
Sample: P9
Strain (in/in)
0.30
0.25
0.20
0.15
0.10
0.05
0.00
1
2
3
4
5
6
7
8
9
10
Location (Axial)
Near Edge
1/4 Point
Mid-Point
1/4 Point
Near Edge

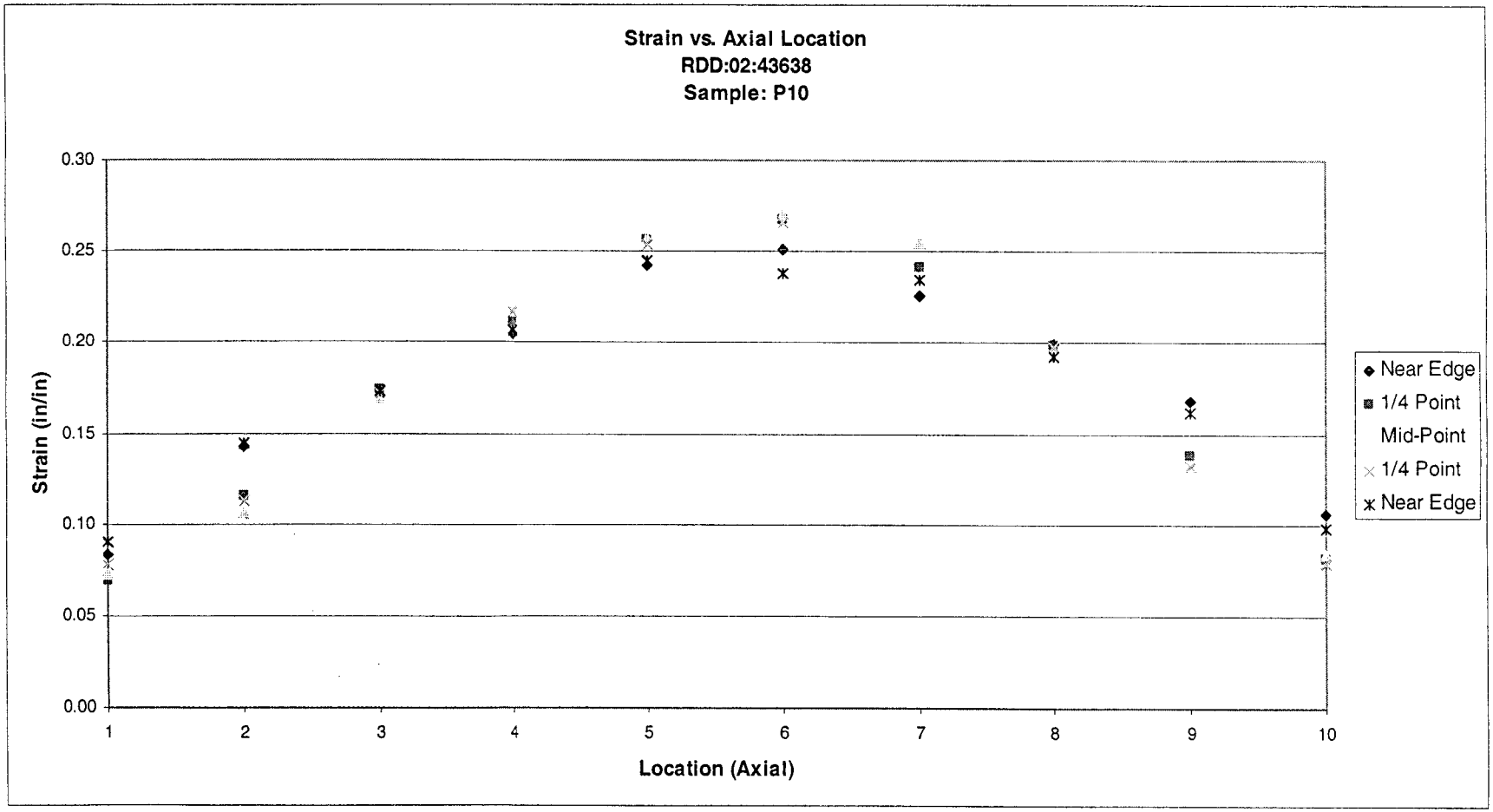
Strain vs. Axial Location
RDD:02:43638
Sample: P10
Strain (in/in)
0.30
0.25
0.20
0.15
0.10
0.05
0.00
1
2
3
4
5
6
7
8
9
10
Location (Axial)
Near Edge
1/4 Point
Mid-Point
1/4 Point
Near Edge

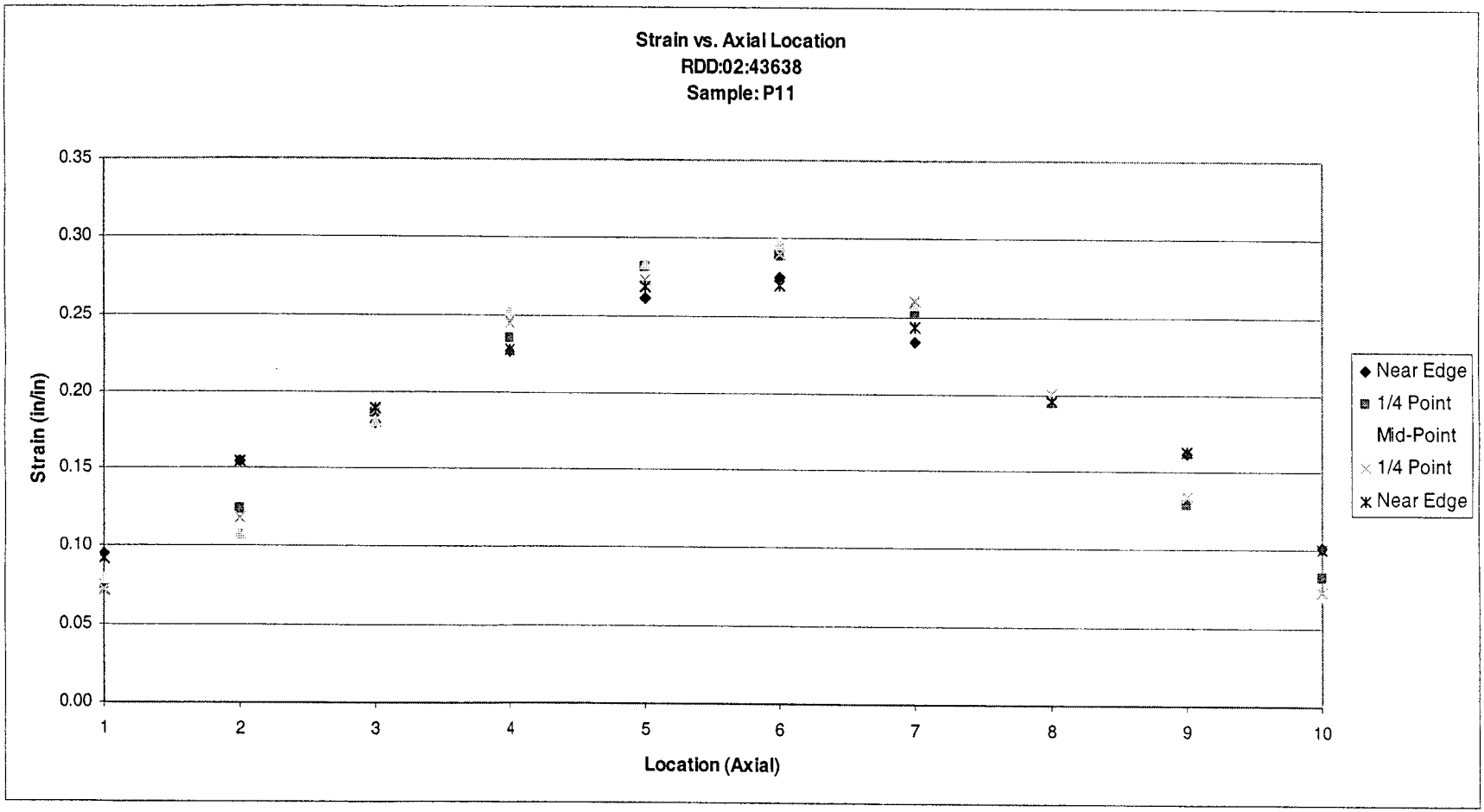
Strain vs. Axial Location
RDD:02:43638
Sample: P11
Strain (in/in)
0.35
0.30
0.25
0.20
0.15
0.10
0.05
0.00
1
2
3
4
5
6
7
8
9
10
Location (Axial)
Near Edge
1/4 Point
Mid-Point
1/4 Point
Near Edge

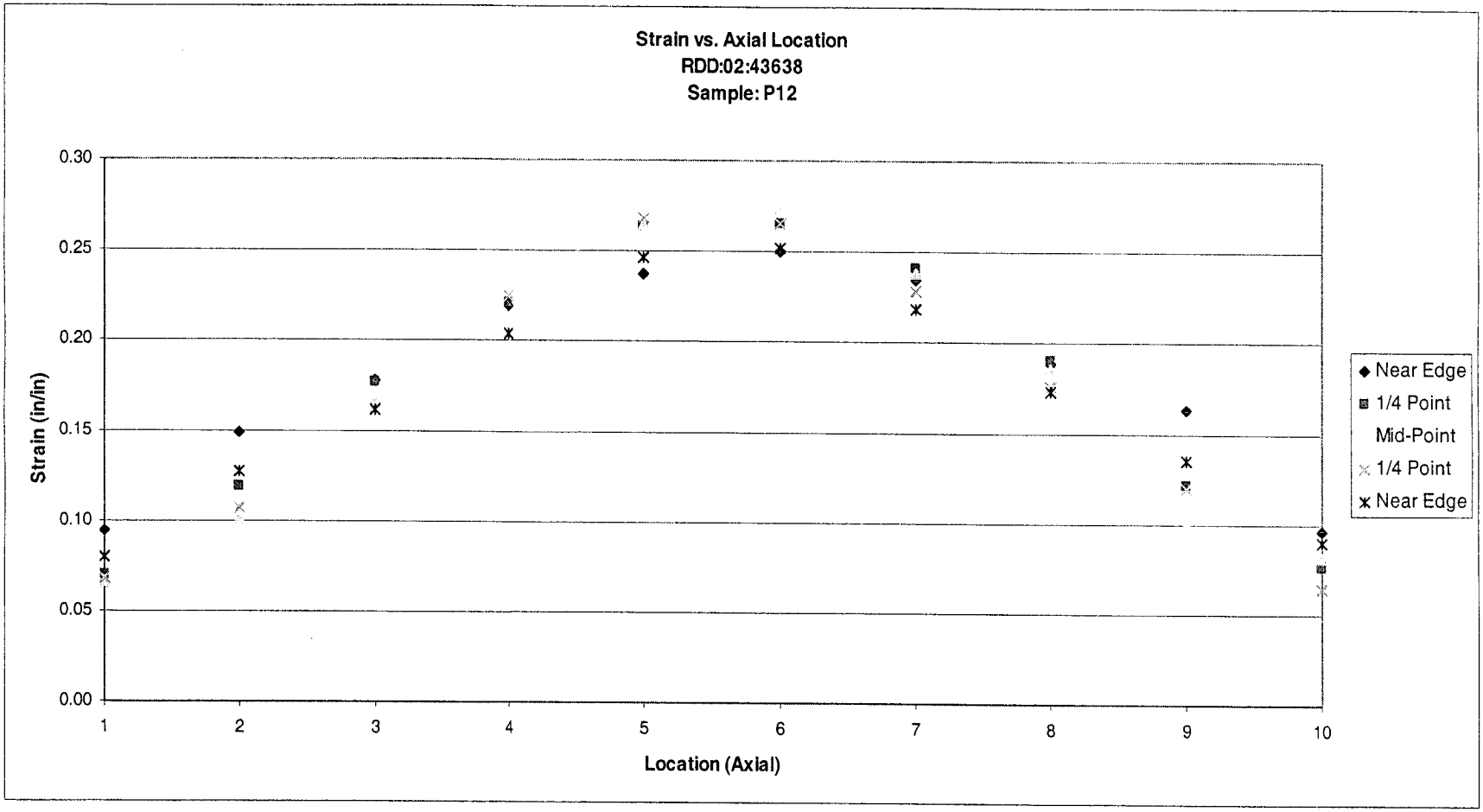
Strain vs. Axial Location
RDD:02:43638
Sample: P12
Strain (in/in)
0.30
0.25
0.20
0.15
0.10
0.05
0.00
1
2
3
4
5
6
7
8
9
10
Location (Axial)
Near Edge
1/4 Point
Mid-Point
1/4 Point
Near Edge

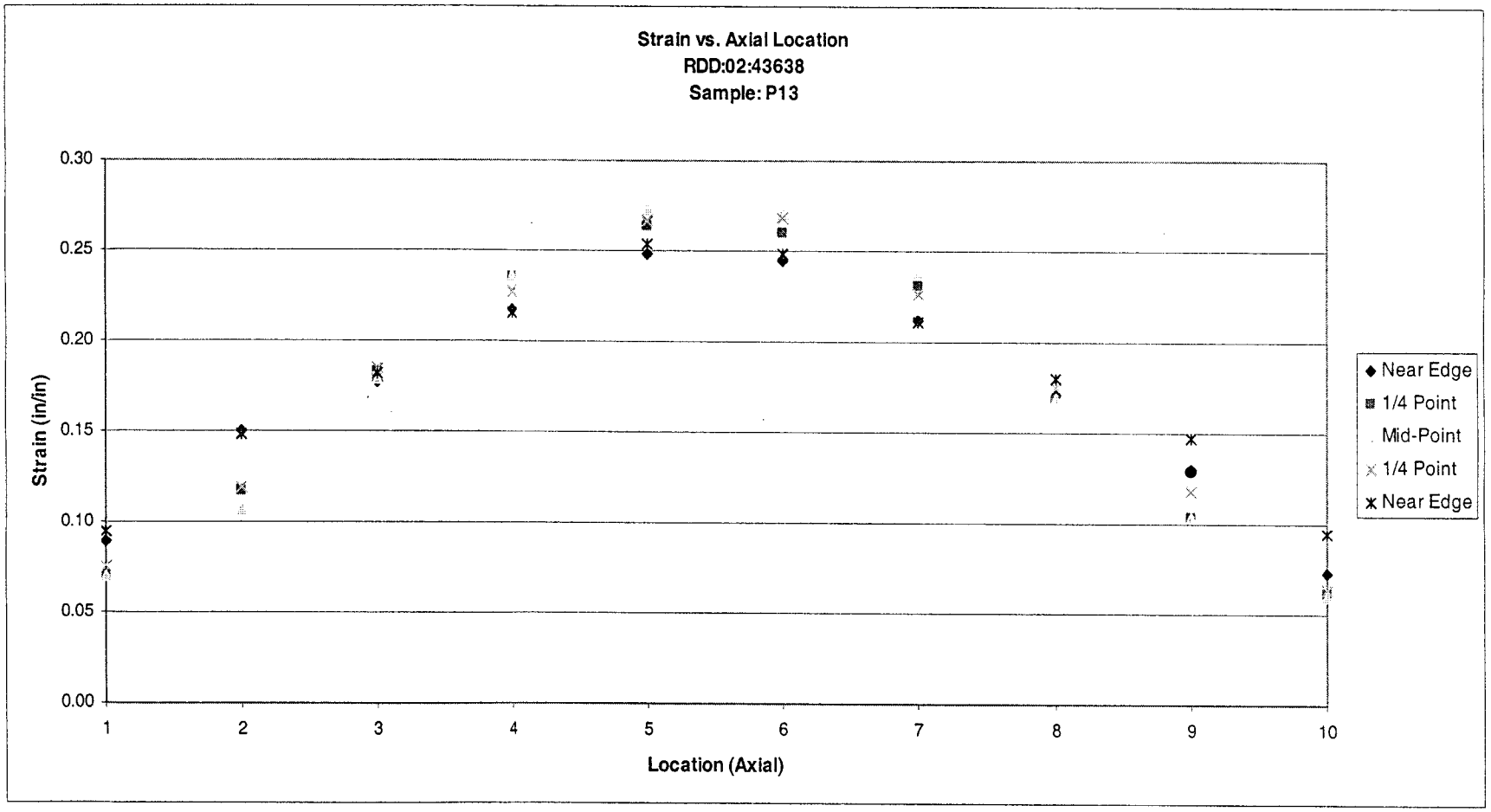
Strain vs. Axial Location
RDD:02:43638
Sample: P13
Strain (in/in)
0.30
0.25
0.20
0.15
0.10
0.05
0.00
1
2
3
4
5
6
7
8
9
10
Location (Axial)
Near Edge
1/4 Point
Mid-Point
1/4 Point
Near Edge

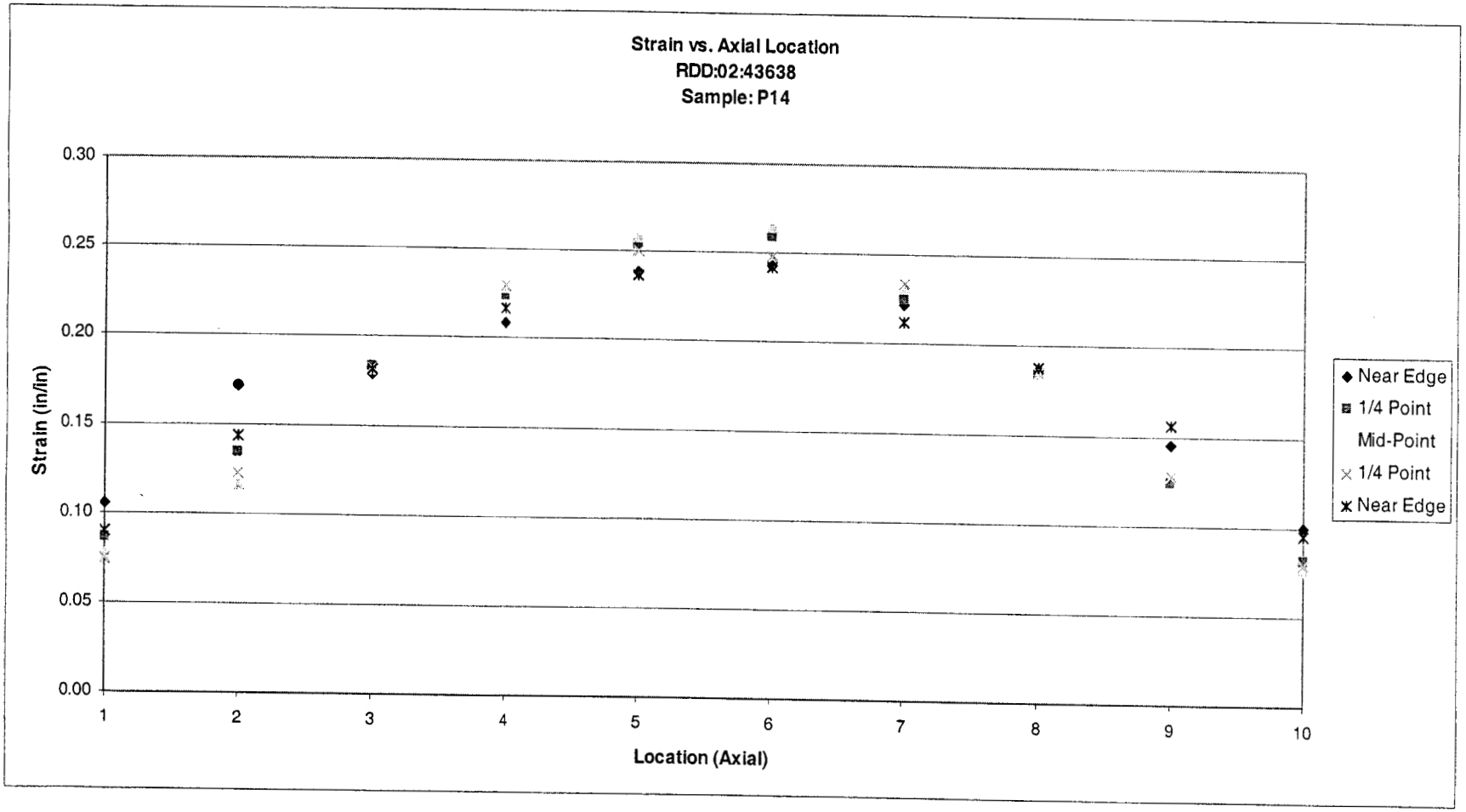
Strain vs. Axial Location
RDD:02:43638
Sample: P14
Strain (in/in)
0.30
0.25
0.20
0.15
0.10
0.05
0.00
1
2
3
4
5
6
7
8
9
10
Location (Axial)
Near Edge
1/4 Point
Mid-Point
1/4 Point
Near Edge

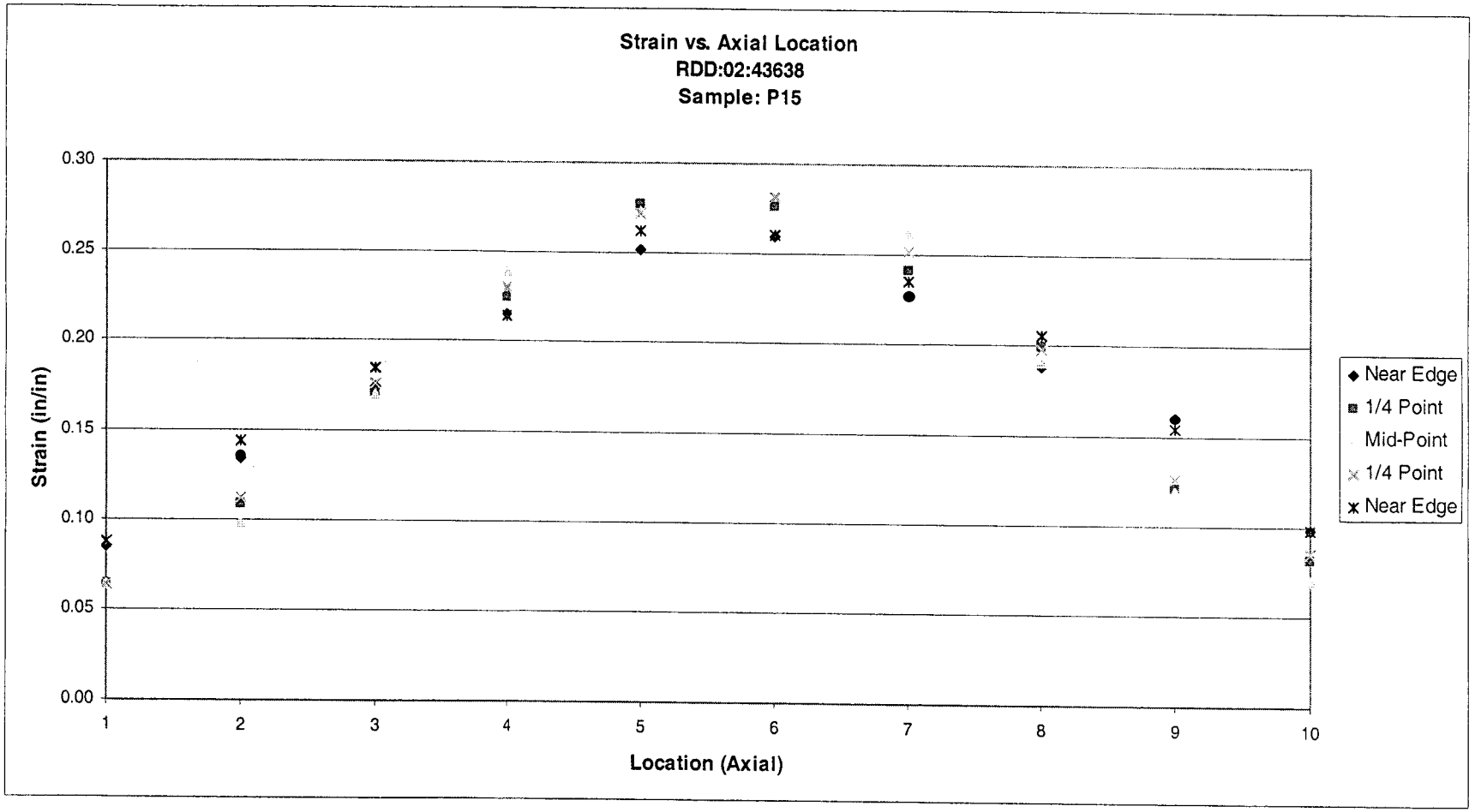
Strain vs. Axial Location
RDD:02:43638
Sample: P15
Strain (in/in)
0.30
0.25
0.20
0.15
0.10
0.05
0.00
1
2
3
4
5
6
7
8
9
10
Location (Axial)
Near Edge
1/4 Point
Mid-Point
1/4 Point
Near Edge

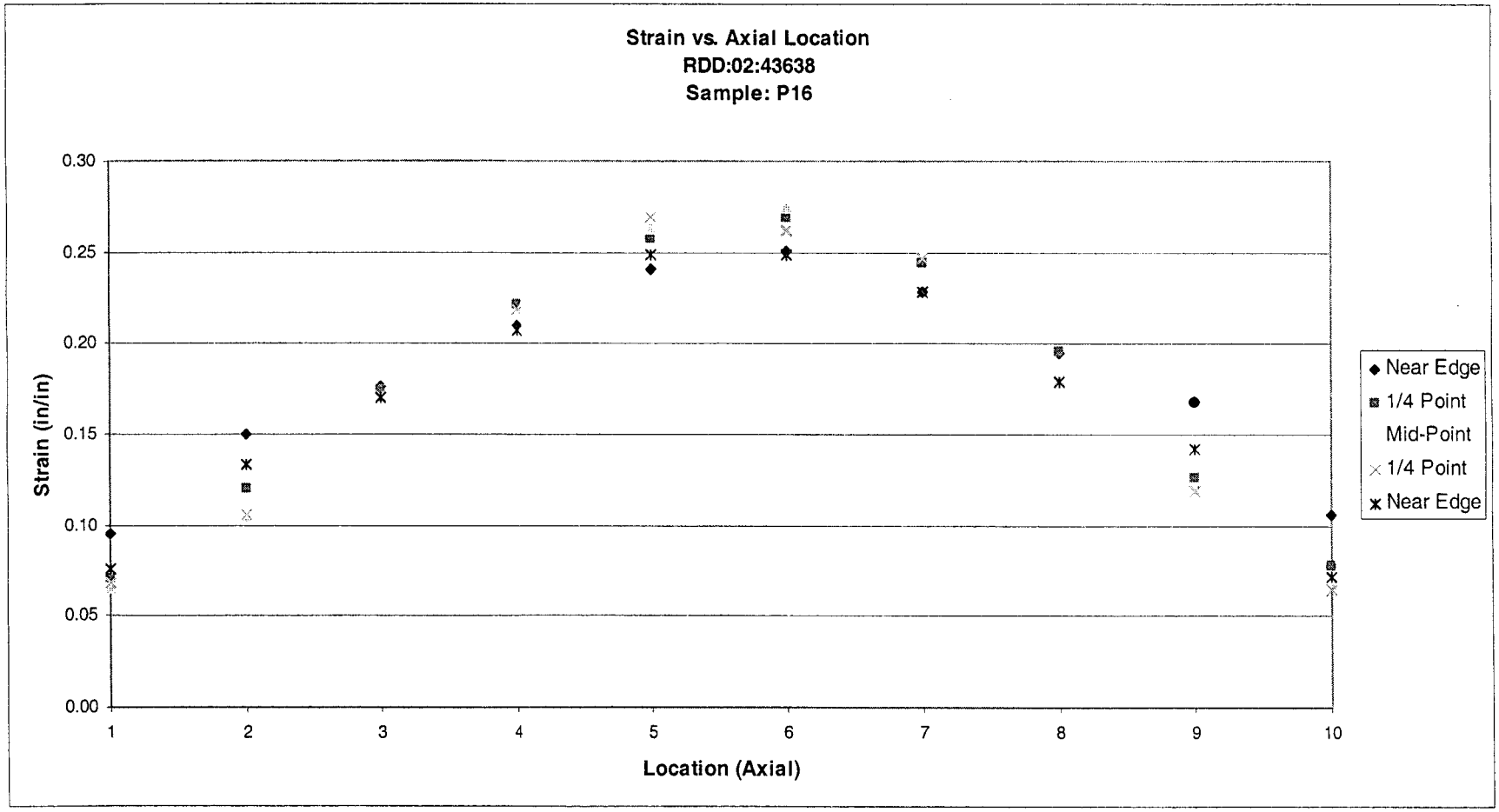
Strain vs. Axial Location
RDD:02:43638
Sample: P16
Strain (in/in)
0.30
0.25
0.20
0.15
0.10
0.05
0.00
1
2
3
4
5
6
7
8
9
10
Location (Axial)
Near Edge
1/4 Point
Mid-Point
1/4 Point
Near Edge

Appendix B-2 – Detailed Tables for Tensile Tests

SPECIMEN ID	TEST TEMP (F)	DIAM (in.)	G.L.orig (in.)	G.L.final (in.)	DIAM f-ave (in.)	AREAorig (sq in.)	AREAfinal (sq in.)	R.O.A. (%)	ELONG (%)	.2% Y.S. (KSI)	ULT. TS (KSI)	(m)	alpha
M-1-1-T1	71	0.160	0.640	0.72	0.110	0.02011	0.00942	53.2	12.5	87.1	88.5	n/a	n/a
M-1-1-T2	75	0.161	0.640	0.72	0.125	0.02036	0.01217	40.2	12.5	86.8	88.2	n/a	n/a
M-1-1-T3	652	0.158	0.640	0.75	0.108	0.01961	0.00908	53.7	17.2	75.9	86.2	23.74	0.066
M-1-1-T4	653	0.159	0.640	0.78	0.106	0.01986	0.00874	56.0	21.9	75.9	84.9	34.2	0.013
M-5-2-T1	71	0.160	0.640	0.79	0.104	0.02011	0.00849	57.8	23.4	65.4	83.0	8.49	4.733
M-5-2-T2	75	0.160	0.640	0.78	0.106	0.02011	0.00874	56.5	21.9	66.5	83.9	7.52	5.464
M-5-2-T3	650	0.161	0.640	0.79	0.104	0.02036	0.00849	58.3	23.4	55.8	77.0	10.27	5.769
M-5-2-T4	651	0.158	0.640	0.82	0.101	0.01961	0.00793	59.5	28.1	56.3	78.6	7.74	2.426
M-9-3-T1	72	0.158	0.640	0.84	0.092	0.01961	0.00665	66.1	31.3	47.5	72.3	4.64	2.035
M-9-3-T2	75	0.159	0.640	0.87	0.092	0.01986	0.00665	66.5	35.9	46.4	72.0	4.59	2.172
M-9-3-T3	652	0.159	0.640	0.84	0.090	0.01986	0.00629	68.3	31.3	27.5	73.4	3.79	3.079
M-9-3-T4	651	0.160	0.640	0.89	0.087	0.02011	0.00594	70.4	39.1	27.1	73.1	3.74	3.301
K-1-1-T1	72	0.159	0.640	0.68	0.125	0.01986	0.01217	38.7	6.3	101.4	101.9	n/a	n/a
K-1-1-T2	75	0.159	0.640	0.680	0.125	0.01986	0.01217	38.7	6.3	104.8	105.3	n/a	n/a
K-1-1-T3	649	0.160	0.640	0.720	0.131	0.02011	0.01338	33.5	12.5	89.9	102.2	14.61	1.916
K-1-1-T4	649	0.158	0.640	0.720	0.131	0.01961	0.01338	31.8	12.5	90.3	101.5	15.74	1.337
K-5-2-T1	72	0.155	0.640	0.740	0.117	0.01887	0.01075	43.0	15.6	82.3	100.8	n/a	n/a
K-5-2-T2	76	0.159	0.640	0.750	0.120	0.01986	0.01122	43.5	17.2	80.1	99.5	n/a	n/a
K-5-2-T3	649	0.160	0.640	0.760	0.128	0.02011	0.01277	36.5	18.8	70.5	92.5	9.89	1.697
K-5-2-T4	651	0.157	0.640	0.750	0.128	0.01936	0.01277	34.0	17.2	72.1	93.6	n/a	n/a
K-10-3-T1	71	0.160	0.640	0.820	0.097	0.02011	0.00739	63.2	28.1	53.1	87.3	4.67	3.987
K-10-3-T2	76	0.159	0.640	0.830	0.097	0.01986	0.00731	63.2	29.7	52.8	86.7	5.83	1.962
K-10-3-T3	649	0.158	0.640	0.830	0.105	0.01961	0.00858	56.3	29.7	39.5	95.5	3.76	2.597
K-10-3-T4	649	0.159	0.640	0.840	0.103	0.01986	0.00825	58.4	31.3	37.2	94.6	3.73	2.965

SPECIMEN ID	TEST TEMP (F)	DIAM (in.)	G.L.orig (in.)	G.L.final (in.)	DIAM f-ave (in.)	AREAorig (sq in.)	AREAfinal (sq in.)	R.O.A. (%)	ELONG (%)	.2% Y.S. (KSI)	ULT. TS (KSI)	(m)	alpha
K-18-5-T1	71	0.160	0.640	0.730	0.112	0.02011	0.00985	51.0	14.1	106.5	106.5	n/a	n/a
K-18-5-T2	75	0.160	0.640	0.730	0.110	0.02011	0.00950	52.7	14.1	102.8	104.5	n/a	n/a
K-18-5-T3	650	0.156	0.640	0.760	0.115	0.01911	0.01039	45.7	18.8	85.9	101.2	12.95	1.494
K-18-5-T4	652	0.157	0.640	0.770	0.114	0.01936	0.01021	47.3	20.3	86.9	101.7	11.49	1.897
O-1-1-T1	71	0.161	0.640	0.740	0.098	0.02036	0.00754	62.9	15.6	96.8	97.0	n/a	n/a
O-1-1-T2	75	0.159	0.640	0.740	0.098	0.01986	0.00754	62.0	15.6	98.6	99.3	n/a	n/a
O-1-1-T3	649	0.159	0.640	0.780	0.102	0.01986	0.00809	59.2	21.9	83.9	95.8	14.7	2.149
O-1-1-T4	650	0.160	0.640	0.780	0.103	0.02011	0.00833	58.6	21.9	82.8	95.3	15.21	1.185
P-1-1-T1	71	0.159	0.640	0.730	0.104	0.01986	0.00849	57.2	14.1	94.0	94.5	n/a	n/a
P-1-1-T2	75	0.158	0.640	0.740	0.102	0.01961	0.00817	58.3	15.6	93.1	94.1	n/a	n/a
P-1-1-T3	650	0.160	0.640	0.760	0.129	0.02011	0.01297	35.5	18.8	79.9	91.9	11.83	1.453
P-1-1-T4	651	0.159	0.640	0.760	0.111	0.01986	0.00959	51.7	18.8	81.1	91.2	15.81	0.037
P-5-2-T1	71	0.160	0.640	0.780	0.101	0.02011	0.00801	60.2	21.9	68.3	85.5	10.91	0.847
P-5-2-T2	74	0.157	0.640	0.770	0.100	0.01936	0.00785	59.4	20.3	69.3	86.1	10.59	0.875
P-5-2-T3	651	0.160	0.640	0.780	0.103	0.02011	0.00825	59.0	21.9	60.1	76.6	10.61	2.261
P-5-2-T4	649	0.157	0.640	0.780	0.102	0.01936	0.00817	57.8	21.9	60.8	77.3	9.34	2.181
P-9-3-T1	71	0.157	0.640	0.870	0.081	0.01936	0.00515	73.4	35.9	49.1	72.3	4.13	7.801
P-9-3-T2	71	0.160	0.640	0.880	0.085	0.02011	0.00561	72.1	37.5	48.3	71.7	4.47	6.896
P-9-3-T3	651	0.157	0.640	0.860	0.082	0.01936	0.00528	72.7	34.4	27.6	69.2	4.24	7.745
P-9-3-T4	650	0.159	0.640	0.860	0.086	0.01986	0.00581	70.7	34.4	27.9	68.9	4.24	7.899

Annex C – Creep Crack Growth Test Results

Annex B describes how formulae were obtained for analysis of the raw test data. The Reduction of these data yielded the CCG test results that are outlined in the following tables and figure.

The crack lengths as indicated per the test procedure were confirmed for each specimen in the metallographic examinations described in Annex E. The metallographic specimens were used to determine the physical crack length at the center-line of each specimen. In some cases, no cracks were found. Only those having actual physical cracks were completely analyzed for C*. The crack lengths were adjusted in accordance with the equations in Annex B.

Data for Analysis:

The following data was used in the analysis of the CCG tests. The stress exponent, m, was obtained from the average tensile results discussed in Annex B. The creep exponent, n, was obtained from literature.[1] The creep exponent is a function of the material condition. The step change in the value is based a yield strength difference discussed in the reference. If the material is above a certain yield strength one value is used, otherwise the second value is used. The normalization and stress relief heat treatments are detailed in Annex B.

Table C-1 – m & n Values and 650°F Used in Analysis

Material	Condition	n	m
Heat M	ACW20	11.8	29.0
Heat D	ACW20	11.8	15.2
Heat D	ACW20 + SR	11.8	9.9
Heat D	ACW20 + N	2.4	3.8
Heat D	ACW10	11.8	15.0
Heat P	ACW20	11.8	13.8
Heat P	ACW20 + SR	11.8	10.0

Note: ACW20 = As-cold worked to a 20% pre-strain.
ACW10 = As-cold worked to a 10% pre-strain.
ACW20 + SR = As-cold worked (20%) followed by stress relief.
ACW20 + N = As-cold worked (20%) followed by normalization.

Results:

The CCG specimens were tested at 650°F using the specimen configuration described in Annex B. Using the equations in Annex B and the above material properties, the following results were obtained.

Table C-2 – Creep Crack Growth Rate Results

Material	ID	Condition	da/dt (in/hr)	C* (in * kip)/(in^2 * hr)	dv_c/dt / dv/dt
Heat M	M-3-1	ACW20	4.00×10^{-5}	8.40×10^{-4}	0.487
Heat D	K-2-1	ACW20	3.22×10^{-5}	8.40×10^{-4}	0.931
	K-3-1	ACW20	4.54×10^{-5}	8.40×10^{-4}	0.982
Heat D	K-6-2	ACW20 + SR	9.53×10^{-6}	9.60×10^{-5}	0.986
	K-7-6	ACW20 + SR	1.49×10^{-4}	7.80×10^{-4}	0.945
		ACW20 + SR	1.97×10^{-4}	9.10×10^{-4}	0.910
Heat D	K-11-3	ACW20 + N	1.02×10^{-5}	1.90×10^{-4}	0.982
	K-12-3	ACW20 + N	1.42×10^{-4}	2.19×10^{-3}	0.967
Heat D	K-19-5	ACW10	2.28×10^{-5}	1.30×10^{-4}	0.982
	K-21-5	ACW10	1.36×10^{-4}	3.77×10^{-3}	0.870
Heat P	P-2-1	ACW20	1.61×10^{-5}	1.48×10^{-4}	0.929
	P-3-1	ACW20	6.67×10^{-5}	1.38×10^{-3}	0.886
Heat P	P-6-2	ACW20 + SR	1.35×10^{-5}	3.10×10^{-4}	0.962

Discussion:

ASTM[2] defines a ratio between the displacement due to creep crack growth rate and the total displacement.

$$C = \frac{\dot{v}_c}{\dot{v}}$$

$\dot{v}_c$ - displacement due to creep crack growth rate defined in Annex B

$\dot{v}$ - total displacement rate

If C is larger than 0.8 then the cracking occurs uniquely with respect to C*, and time dependent crack growth is occurring. If C is between 0.5 and 0.8 the relationship between C* and the cracking is less unique and must be plotted with data that has C greater than 0.8 to determine if C* is the correct correlation parameter.

As the results in Table C-1 show, most of the data has a C value greater than 0.8. As seen in the Annex E, M-3-1 has a mixed fracture mode consisting of both tearing and creep. This

mixed mode manifests itself in the C ratio as a value of 0.487. Although the C parameter is not strictly within range, the data for M-3-1 was plotted with the data from then specimens with C greater than 0.8. This data shows that the crack tip parameter C* can be used for the correlation parameter.

Another interesting observation can be made with respect to the results. As observed on Figure C-1, if cracking occurs in a specimen, the rate of cracking is dependent solely on the crack tip parameter C*. The ramification of this phenomenon is interesting because a test could be devised to rank materials by a crack / no-crack method.

References

1. Gill, Y, "Creep Crack Growth Characterization of SA-106C Carbon Steel," Georgia Institute of Technology, Ph.D. Thesis, March 1994.

2. ASTM E1457-92, "Standard Test Method for Measurement of Creep Crack Growth Rates in Metals", American Society for Testing and Materials, West Conshohocken, PA, April 1992.

Figure C-1 – Compilation of Test Results

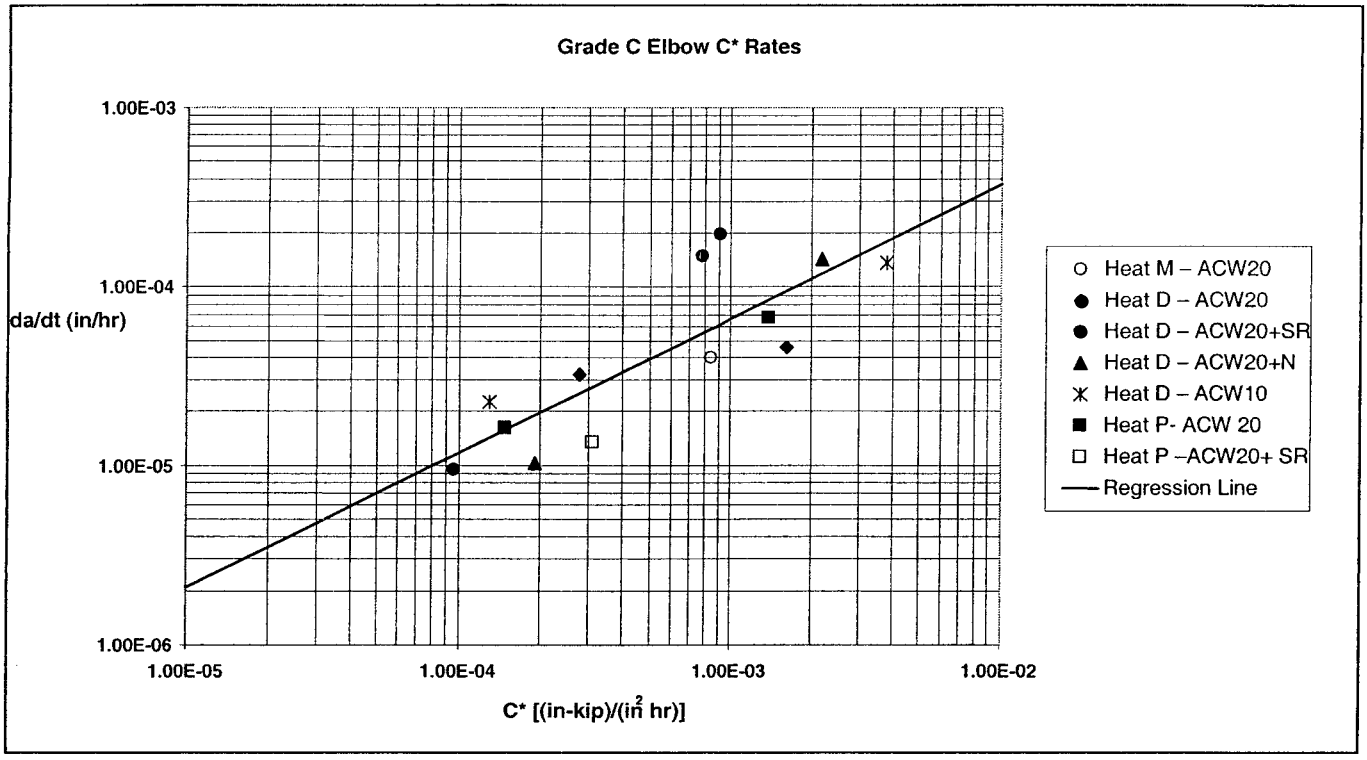

Annex D – C* Analysis

This annex summarizes work done to develop the C*(t)-Integral parameter for use in creep crack growth testing of a pin-loaded single edge notched tension (SENT) specimen. This type specimen was chosen in order to obtain creep crack growth data for this project for the reasons described in Annex B. The development of the C*(t) expression follows the approach given in the current ASTM Standard Test Method for Measurement of Creep Crack Growth Rates in Metals, E1457-98 Draft dated January 2000. While this draft standard recommends the compact tension, C(T), specimen, use of other geometries such as the single edge notched tension (SENT) specimen are permitted. This project used SENT specimen types to provide test data which will simulate constraint effects seen in the cracking that was experienced in service. For service-exposed cold bent elbows, creep crack growth was observed in the longitudinal direction on the extrados of elbows. The constraint of the cracked C(T) specimen of E1457-98 will not accurately model the constraint of the cracked cold bent elbow.

According to E1457-98, once a specimen type is selected, a creep fracture parameter denoted by C*(t) is needed to correlate the measured creep crack growth rate from the selected specimen for creep-ductile materials. This correlation, in turn, can be used to establish the remaining life of the cracked elbows in service provided the specimen is a close simulation of the cracked elbow's constraint. The C*(t) expression in this annex is expressed in terms of an η- factor which is a function of the crack length (a) to specimen width (w), and the Norton's power law creep exponent, n. The η-factor provides a relationship between the measured displacement rate at the pin to the applied load at the pin. Plots and tables are provided in this report for the η-factor for "a/w" versus "n" as well as recommendations for the selection of the ranges of test variables and possible corrections required to the measured displacement rates.

Background:

As has been mentioned elsewhere in this report, failure of cold bent elbows made of carbon-manganese (C-Mn) steel containing steam-water mixtures and operating at 300-420°C have been observed over the last 30 years both in the U.S. and in Europe. The Europeans have recently completed a four-year program that has addressed these failures. This program has been summarized by the writer.[1] In their program, the Europeans performed numerous creep crack growth tests using pressurized tubes, pipes, compact tension, and three-point bend test specimens. They concluded that there is a significant effect of geometry constraint on the results of their creep crack growth measurements.[2]

Almost all of the creep crack growth testing work in this country has been limited to the compact C(T) specimen, which provides a conservative estimate of creep crack growth rates in creep-ductile materials. However, a few years ago, MTI proposed to DOE that a different type specimen might be more appropriate for simulating the creep crack growth observed in the cold bent elbow failures in the USA. Observations of the actual failed elbows indicated that the cracking initiated on the extrados of the elbow in the longitudinal direction propagating through the elbow wall thickness. The primary driving force is the hoop stress (due to

pressurization of the piping) perpendicular to the cracking direction. The use of the compact specimen while producing some tensile loading perpendicular to the crack direction also produces a bending stress which causes a different constraint at the crack tip than would be caused by pressurization of the cracked elbow. In the proposal to DOE, MTI suggested that a more realistic specimen type to measure and better understand the cracked elbow problem is that of a shallow cracked pin-loaded single edge notched tension (SENT) specimen as shown in Figure D-1. In order to perform the testing and the analyses required to reduce the data from these proposed tests, an expression for a creep fracture mechanics correlation parameter is required. This annex discusses the development of such a parameter for the SENT test specimen.

Introduction:

The accepted ASTM standard test method E1457-98 for determining creep crack growth rates in metals at elevated temperatures recommends the compact tension C(T) as shown in Figure D-2. The creep crack growth rate, $\dot{a}(t)$, is to be expressed in terms of the magnitude of various crack growth rate parameters such as C*(t), C_t, or K as defined and discussed in ASTM E1457-98. The choice of the crack growth rate parameter depends on the material behavior and how well this parameter correlates with $\dot{a}(t)$. Two types of material behavior at high temperature during crack growth tests are possible; creep-ductile or creep-brittle. For creep-ductile materials, the growth rates involve time-dependent creep strains at the crack tip and the crack growth rate, $\dot{a}(t)$, can usually be correlated with C*(t). For creep-brittle materials, the growth occurs at low creep ductilities (high creep exponent, n). The time dependent creep strains are usually dominated by elastic strains and the correlating parameter is the linear elastic fracture mechanics (LEFM) parameter K, well-known for planar cracked specimen types from Tada's handbook.[3]

Since only steady-state creep crack growth rate behavior is addressed in ASTM E1457-98, a unique correlation exists between $\dot{a}(t)$ and the appropriate crack growth correlation parameter. European studies[4] have determined that this unique parameter is C* or C*(t) for C-Mn steels at 360°C. Test results on C-Mn steels at 360°C in Figure D-3 (taken from Reference 4) demonstrate the correlations found using the C* parameter.

MTI's testing will determine whether C*(t) or K for MTI's samples of C-Mn gives the best correlation with the measured $\dot{a}(t)$ rates. According to ASTM E1457-98, the C*(t)-integral parameter for the compact tension specimen can be determined by using

$$C^*(t) = \frac{P\dot{v}_c}{B_N(w-a)} \frac{n}{n+1} \left(2+0.522 \frac{w-a}{w}\right) \qquad (1)$$

where P is the applied constant load at the pins, $\dot{v}_c$ is the additional displacement rate at the loading pins due to the crack that is directly associated with the accumulation of creep strains. This displacement rate, $\dot{v}_c$, can be determined from the total measured displacement rate, $\dot{v}$,

caused by the crack using the expression given in ASTM E1457-98, paragraph 10.4.2 knowing the stress intensity factor K for the SENT the specimen. $P/B_n(w\text{-}a)$ is the net section tensile stress on the compact specimen. "n" is the creep exponent given in the relationship between minimum the creep rate and applied stress. The value of "n" may be obtained from creep test data in accordance with ASTM E139, or if creep tests are not performed, an accepted value of "n" from the literature can be used. Note that in the above equation, the term "$2 + 0.522 \bullet (w\text{-}a)/w$" is sometimes referred to as the "η-factor". For the compact tension specimen, the η-factor given in ASTM E1457-98 was determined by a semi-empirical method from

$$C^*(t) = -\frac{1}{B}\int_0^{\dot{v}_c}\left(\frac{\partial P}{\partial a}\right)_{\dot{v}_c} d\dot{v}_c \qquad (2)$$

per Reference 5. Note the resultant expression for C*(t) given by Eq. (1) is valid for a/w Δ 0.40.

An alternate numerical approach for determining C*(t) is based on estimating C*(t) for a power-law creeping material using Norton's law

$$\dot{\varepsilon}_c / \dot{\varepsilon}_o = \alpha(\sigma/\sigma_o)^n \qquad (3)$$

where $\dot{\varepsilon}_c$ is the strain rate due to creep and σ is the applied stress. C*(t) is obtained from the fully-plastic J-estimation expression for power-law hardening materials[6] by simply replacing plastic strains and plastic displacements by their respective rates. The most accurate published SENT specimen fully-plastic expressions for $J_{plastic}$ (or C*(t)) and the load point displacement (rate) due to the crack, v_c or $\dot{v}_c$, under uniform tensile loading (see Figure D-4) are given by

$$C^*(t) = \alpha\sigma_o\,\dot{\varepsilon}_o(w-a)\frac{a}{w}h_1(a/w,n)(P'/P'_o)^{n+1} \qquad (4)$$

and

$$\dot{v}_c = \alpha\dot{\varepsilon}_o\,a h_3(a/w,n)(P'/P'_o)^n \qquad (5)$$

where w is the SENT specimen width (see Figures D-1 and D-4), P' is the load per unit thickness (or $P = P'B_N$) where B_N is the effective thickness, and P'_o is the reference load per unit thickness = $\frac{2}{\sqrt{3}}(1.26)\,\gamma\,(w\text{-}a)\,\sigma_o$ with γ given by

$$\gamma = \sqrt{1+\left(\frac{1}{w/a-1}\right)^2} - \frac{1}{(w/a-1)} \qquad (6)$$

For a rigid-perfectly plastic SENT panel ($n \rightarrow \infty$), P'_o is the plane strain limit load per unit thickness (or $P_o = P'_o B_N$) provided 1.26 γ is the correct plastic crack constraint factor.

The selection of plane strain values of 1.26γ and the respective h_1 and h_3 functions is consistent with the plane strain C*(t) expression given for the CT specimen in E1457-98.

Numerical Results for SENT Specimen:

The η-factor as discussed above can be easily obtained for the SENT specimen by dividing Eq. (4) by Eq. (5) which results in

$$\frac{C^*(t)}{\dot{\Delta}_c} = \frac{\sigma(w-a)a}{wa}\frac{h_1}{h_3}\frac{P'}{P_o'} \tag{7}$$

or

$$C^*(t) = \frac{1.455 P \dot{v}_c}{B_N w \gamma}\frac{h_1}{h_3} \tag{8}$$

where P is the total load and B_N is the net thickness of the SENT specimen. To be consistent with the compact specimen plane strain C*(t) expression in Eq. (1), Eq. (8) is recast as

$$C^*(t) = \frac{P \dot{v}_c}{B_N (w-a)}\frac{n}{n+1}\eta_P \tag{9}$$

where

$$\eta_P = \frac{n+1}{n}\frac{(1-a/w)}{\gamma'}\frac{h_1}{h_3} \tag{10}$$

and $\gamma' = \gamma/1.455$ where γ is given by Eq. (6). Note that η_P for the SENT specimen is a function of both the crack depth to specimen width ratio, a/w, and the creep exponent, n, while the η_P expression for the compact specimen is a function of only "a/w".
Table I presents η_P values for the SENT specimen versus "a/w" and "n" for n = 5, 7, 10, 13, and 16.

Table I: ETA Plastic (η_P) For SENT versus a/w

a/w	n					Average η_P
	5	7	10	13	16	
0.03125	12.80	9.15	6.40	4.92	4.00	7.45
0.0625	6.84	4.89	3.42	2.63	2.14	3.98
0.125	3.57	2.70	2.03	1.66	1.45	2.28
0.250	2.01	1.68	1.49	1.43	1.42	1.61
0.375	1.98	1.93	1.95	1.97	1.96	1.96
0.500	2.43	2.45	2.47	2.47	2.47	2.46
0.625	2.60	2.60	2.59	2.60	2.58	2.59
0.750	2.44	2.43	2.41	2.41	2.40	2.42
0.875	2.22	2.20	2.20	2.20	2.17	2.20
1.000	2.00	2.00	2.00	2.00	2.00	2.00

Also presented in the last column of Table I is the average η_P factor per each value of "a/w". Note that for cracks, a/w Δ 0.375, the values of η_P are independent of the creep exponent, n. A plot of $(\eta_P)_{average}$ versus a/w is shown in Figure D-5. To illustrate the effect of n on η_P, Figure D-6 presents all the values of η_P versus n. The values of h_1 and h_3 used in the determination of η_P (Eq. (10)) are based on the fully plastic plane strain solutions found in Reference 6. In Reference 6, finite element analysis results were presented for a SENT specimen loaded under uniform traction σ_{yy} imposed on the ends of the specimen as shown in Figure D-4, so that the load per unit thickness was set to

$$P' = w\,\sigma_{yy}\,(x, \pm L) \tag{11}$$

The total length of the finite element model was 2L with L/w = 3. According to discussions presented in Reference 6, previous numerical calculations have shown that this length to width ratio is sufficient to eliminate any dependence of C*(t) and $\dot{v}_c$ on specimen length.

Furthermore, Reference 6 concluded that the numerical results presented in their paper for both h_1 and h_3 would pertain to an infinite panel length. Discussion of this assumption on the accuracy of Eq. (8) will be addressed later in the report for shorter test specimen lengths (L/w < 3). Note that values of h_1 and h_3 given in Reference 6 were limited to a/w Δ 0.125 and a/w Ω 0.875. In Reference 7, expressions were provided to obtain the ratio of h_3/h_1 in Eq. (10) in the limit for both a/w $\rightarrow$ 0 and a/w $\rightarrow$ 1.0. The equation used to obtain the ratio h_3/h_1, and in turn, η_P for a/w = 0.03125 and 0.0625 was

$$2.91\left(\frac{1}{n+1}\right)\left(\frac{b}{a}\right)\frac{h_3}{h_1} = 1, \tag{12}$$

and, for a/w = 0.875 and 1.000, was

$$1.455\left(\frac{n}{n+1}\right)\left(\frac{b}{a}\right)\frac{h_3}{h_1}=1 \tag{13}$$

The discussion of the derivation of these equations is given in Reference 7.

Comparison with C(T) and SENT Length Effects:

In comparing the η_P-factors for the compact C(T) specimen with the SENT specimen, it must be noted that the ASTM E1457-98 standard limits the starter crack to $a_o/w \Delta 0.45$ so that for the range of validity of η_P for the C(T) specimen, the maximum difference in the η_P value occurs at $a/w = 0.625$ with the C(T), η_P factor approximately 15% lower. At $a/w = 0.45$, the C(T), η_P factor is within 1.6%.

The length to width effect on the expression of the SENT specimen can be assessed using the following arguments. In actual tests, the total load-point displacement value due to creep, $\dot{v}$, is measured. However, the expression given by Eq. (5) is for the load-point displacement rate due to the crack, $\dot{v}_c$. The total displacement rate is given by

$$\dot{v} = \dot{v}_c + v_{nc} \tag{14}$$

where $\dot{v}_{nc}$ is the displacement rate of the specimen without a crack. If it can be demonstrated that $\dot{v}_{nc}$ is small relative to $\dot{v}_c$ for the SENT specimen, then $\dot{v}$ can be substituted for $\dot{v}_c$ in Eq. (9). Note for the C(T) specimen, no such correction is required.[8] The displacement rate in the absence of the crack (no crack) for the SENT specimen is,

$$\dot{v}_{nc} = \sqrt{3}\,L\,\alpha\,\dot{\varepsilon}_o\left(\sqrt{3}\,P'/2w\sigma_o\right)^n \tag{15}$$

for plane strain conditions, and if Eq. (5) is divided by Eq. (15), then

$$\frac{\dot{v}_c}{\dot{v}_{nc}} = \frac{ah_3}{\sqrt{3}\,L}\left(\frac{2w\sigma_o}{\sqrt{3}\,P_o'}\right)^n \tag{16}$$

or substituting for P_o' given in the line above Eq. (6), the result is

$$\frac{\dot{v}_c}{\dot{v}_{nc}} = \frac{w}{L}\left\{\frac{1}{\sqrt{3}}\frac{a}{w}h_3\left(\frac{0.794}{(1-a/w)\gamma}\right)^n\right\} \tag{17}$$

where γ is given by Eq. (6).
If F(a/w,n) is defined by,

$$F(a/w,n) = \frac{1}{\sqrt{3}}\frac{a}{w} h_3 \left(\frac{0.794}{(1-a/w)\gamma}\right)^n , \qquad (18)$$

then

$$\frac{\dot{v}_c}{\dot{v}_{nc}} = F(a/w,n)\frac{w}{L} \qquad (19)$$

Note now that $\dot{v}_c / \dot{v}_{nc}$ is directly proportional to the ratio of SENT specimen width over half specimen length. Table II presents calculated values of F(a/w,n) for plane strain conditions using values of h_3 from Reference 6. Only values of n = 5, 7, and 10 are shown.

Table II
Variation of F(a/w,n)

a/w	n	F(a/w,n)
		Plane Strain
0.125	5	0.27
	7	0.47
	10	0.91
0.25	5	1.90
	7	3.97
	10	10.66
0.375	5	10.94
	7	35.40
	10	208.19
0.5	5	118.57
	7	1017.25
	10	26990.00
0.625	5	4474.50
	7	1.66×10^5
	10	4.03×10^7

Note that the cracked-body displacement rate, $\dot{v}_c$ in Eq. (19), dominates when n is large for any SENT geometry ratio, w/L. For very long specimens (w/L small), Eq. (19) predicts that the uncracked-body displacement rate, $\dot{v}_{nc}$, dominate the total displacement rate, $\dot{v}$, for any given n and a/w value.

To develop a relationship for C*(t) in terms of the measured displacement rate, $\dot{v}$, independent of the specimen length, 2L, for a given a/w and n, the component of the displacement rate due to the crack, $\dot{v}_c$, must dominate (see Eq. (14)). For a 10% error in the C* expression, $\dot{v}_c / \dot{v}_{nc} \Delta 10$ and for a w/L of 0.59 (MTI's current SENT specimen size),

$$10 \; \Omega \; 0.59 \; F(a/w,n) \tag{20}$$

or

$$F(a/w,n) \; \Delta \; 16.95 \tag{21}$$

or, from Table II, a/w Δ 0.375, and n Δ 6. MTI's current planned initial crack length is approximately $a_o/w = 0.296$. If this initial size is used, then a 20% error in C*(t), equivalent to $\dot{v}_c / \dot{v}_{nc} \; \Delta \; 5$, would result in

$$F(a/w,n) \; \Delta \; 8.47 \tag{22}$$

or

a/w Δ 0.25, and n Δ 10 from Table II,

or

a/w Δ 0.375, and n Δ 5 from Table II.

Note that reported values of the creep exponent have ranged from n=11 to n=18 for C-Mn steels at 360°C.[4,9,10] Therefore, the total load-displacement rate, $\dot{v}$, can be used in place of $\dot{v}_c$ in Eq. (9) for determining the C*(t) parameter. From Table II using Eq. (17), the error in C*(t) would be between 10% and 20% depending on the value of the creep exponent, n.

Conclusions:

Based on the study presented in this annex, the expressions developed for C*(t) as given by Equations (9) and (10) can be used in the testing of SENT specimens. It is recommended that η_p be determined from Figure D-5 (or be taken from Table I) provided nΔ10 and a/w Δ 0.250. If the initial crack length to specimen width, a_o/w, is greater than 0.30, and nΔ10, the proposed specimen size of w/L = 0.59 will give calculated C*(t) within 15% if the measured load-point displacement rates, $\dot{v}$, are used from the tests.

Recommendations:

In the future, to better quantify the error in calculated C*(t), it is recommended that the creep exponent be determined experimentally for the materials tested. Once n is known, the error in C*(t) using the measured total load-point displacement rate can be determined accurately from the equations and tables given in this annex.

References

1. J. M. Bloom, "European Program BE 7463 - Creep Crack Growth in Carbon-Manganese Steels at 300°C - 420°C", MTI Letter Report RDD:00:43638-001-000:00R, September 20, 2000.

2. Synthesis Report BE7463, "Creep Crack Growth in Carbon-Manganese Steels at 300°-420°C", 1/5/94 to 30/4/98.

3. H. Tada, P.C. Paris, and G.R. Irwin, "The Stress Analysis of Cracks Handbook," Del Research Corporation, Hellertown, PA, 1973.

4. O. Kwon, K.M. Nikbin, G.A. Welstan, and K.V. Jata, "Crack Growth in the Presence of Limited Creep Deformation," Engineering Fracture Mechanics, Vol. 62, January 1999.

5. A. Saxena, "Evaluation of C* for the Characterization of Creep Crack Growth Behavior in 304 Stainless Steel," Fracture Mechanics, Twelfth Conference, 1980, ASTM STP 700, ASTM, pp 131-151.

6. C.F. Shih and A. Needleman, "Fully Plastic Crack Problems; Part 1: Solutions by a Penalty Method, J. Applied Mechanics, Vol. 106, March 1984.

7. C.F. Shih and A. Needleman, "Fully Plastic Crack Problems: Part 2: Application of Consistency Checks," J. Applied Mechanics, Vol. 106, March 1984.

8. A. Saxena, Private Communication, October 2000.

9. G. Yancy, "Creep Crack Growth Characterization of SA-106C Carbon Steel," Ph.D. Thesis, Materials Department of Georgia Institute of Technology, March 1994.

10. G.T. Neate, "Creep Crack Growth in Cold Formed C-Mn Steels at 360°C," Materials Science and Engineering, Vol. 3, 1987.

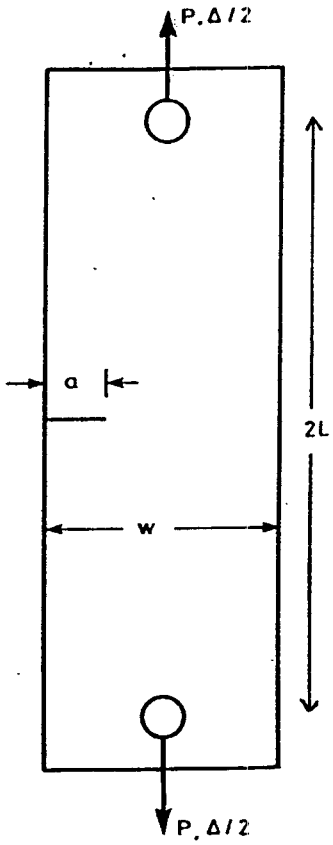

Figure D-1: The pin-loaded single edge notched tension (SENT) specimen

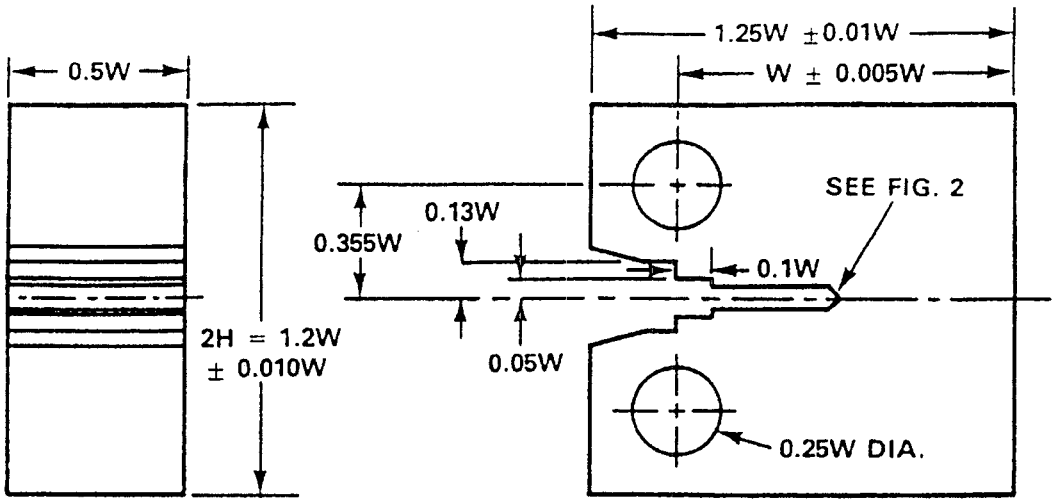

Figure D-2: Drawing of standard C(T) specimen

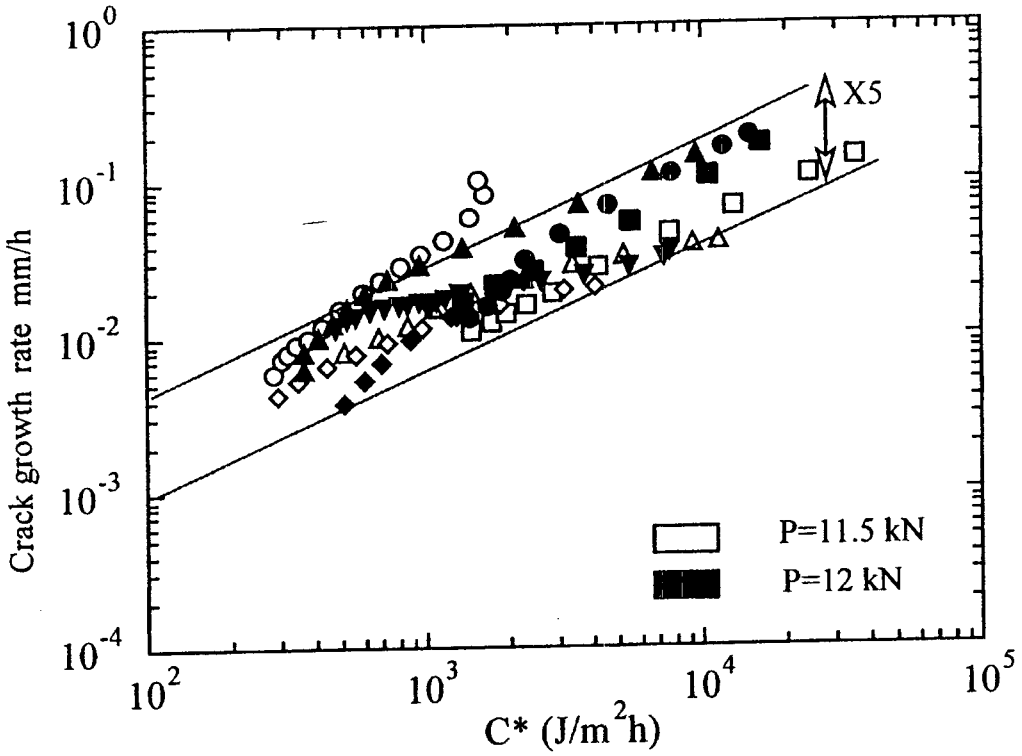

Figure D-3: Creep crack growth rate versus C* for C-Mn steel at 360°C

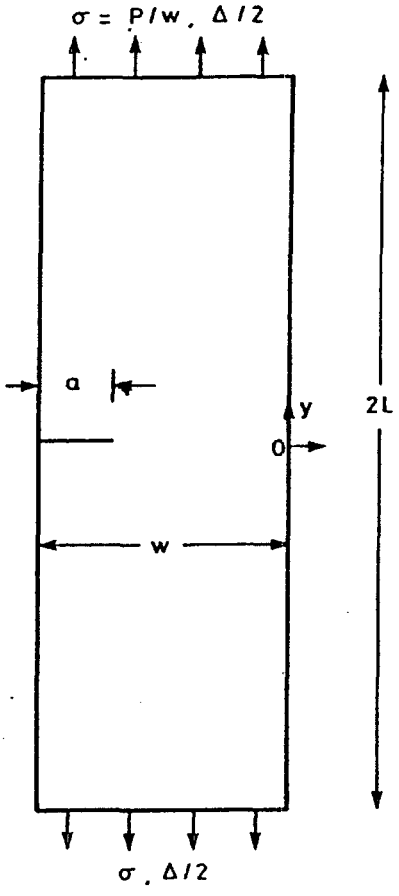

Figure D-4: **The finite-element geometry used in Reference 5. Unit thickness is assumed. The end stress σ is uniformly distributed over the ends y = ± L. Similarly, the displacement Δ (or v) is the averaged value across the width w of the specimen.**

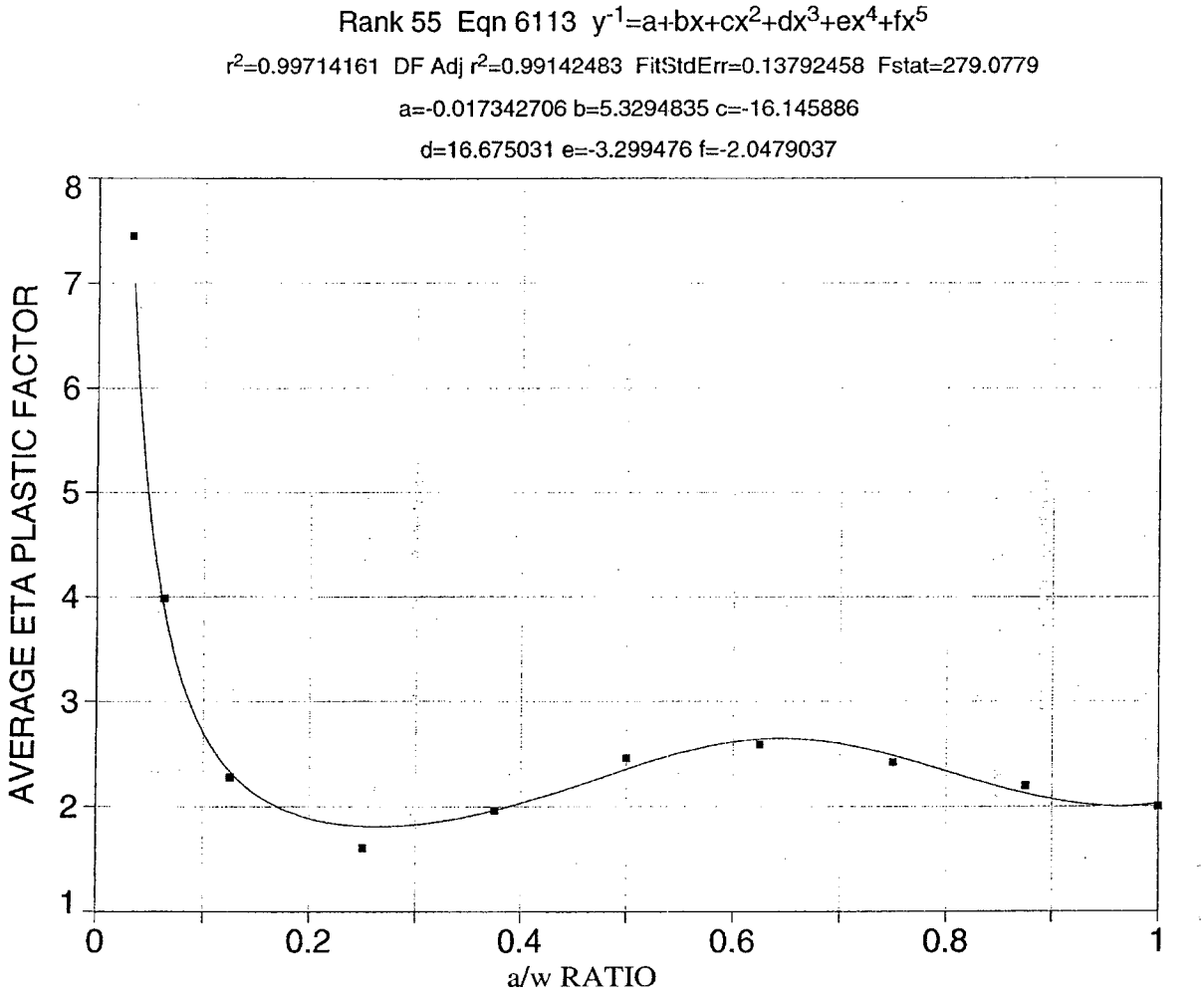

Figure 5: Average ETA Plastic versus a/w

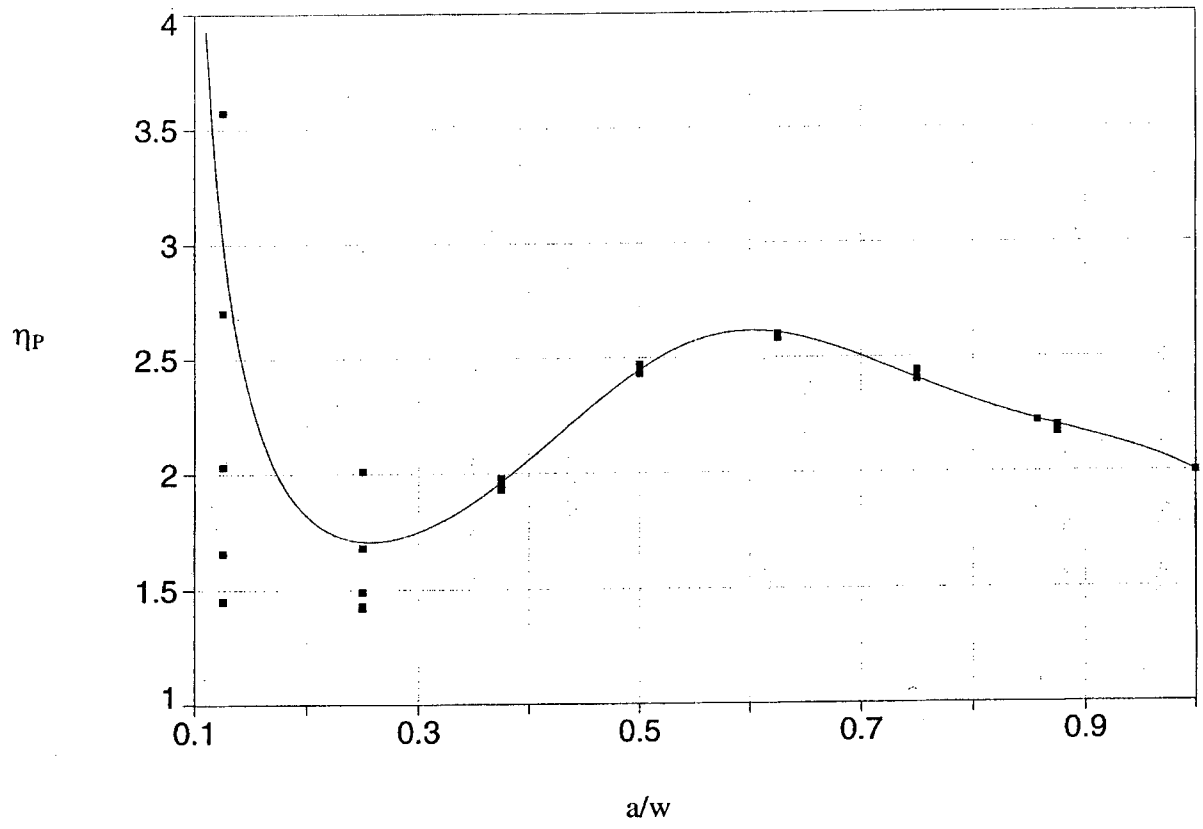

Figure D-6: η_P versus a/w for n = 5, 7, 10, 13, 16

Annex E: Examination of Test Specimens

This annex describes examinations of the CCG test specimens after testing had been completed. The examinations served several purposes.

First, metallographic examinations were used to verify the validity of the fracture mechanics approach. The fracture mechanics testing procedure determined the presence, or lack of, CCG based on the sensed position of the crack front as a function of time. During testing, the crack front position could not be measured directly. Instead, it was inferred by the electric potential drop (EDP) technique. In this technique, the position of the crack front is calculated based on measurements of the remaining cross sectional area as the crack advances. While this technique is well-established and accepted, it was felt that actual physical measurements of the crack front position were needed to confirm the accuracy of the EDP measurement.

Second, metallographic examinations were performed to document the microstructure of each specimen. It is understood that, depending on composition and processing route, the carbon-manganese steels that comply with the SA106 or SA210, Grade C specifications can evidence a range of microstructures all of which are acceptable per the standard. This examination documented the microstructure of each specimen, and compared it with that of the other specimens. The microstructure in the vicinity of the notch was of particular concern, since typically the creep crack front moved only a short distance (tens of mils) during testing. After that, and with continued loading, the crack advanced more rapidly, ultimately by a tearing mechanism. The crack path was examined to determine if the crack followed preferred microstructural features.

The scanning electron microscope (SEM) was used to further characterize the crack path. The SEM also was used to characterize the fracture surfaces, and to correlate them with the underlying microstructure. These examinations were final confirmation of the CCG mechanism which yields distinctive features both within the microstructure and on the fracture surface itself. The energy dispersive analysis by x-ray, (EDAX), capabilities of the SEM were used in an attempt to determine whether the grain boundaries were enriched in tramp elements, or otherwise.

Previous investigators had indicated that sensitivity to CCG could be related to the hardness of the material, with harder materials being more sensitive. The hardness of each of each test specimen was determined and recorded.

Previous investigators also suggested that sensitivity to CCG could be related to the size of the plastic zone in advance of the notch, with materials having a small plastic zone being more sensitive than others.

The following provides a description of the procedures and results of the aforementioned examinations.

Confirmation of Crack Length:

Each of the (22) test specimens listed in the Results Matrix (Table 1) was examined in the following manner.

First, the outer surfaces of these specimens were visually inspected using low power light optics. It was anticipated that the crack might not advance at an equal rate across its' entire front. Recall that the specimen was side-grooved to help focus strain into the desired test plane. The visual examination looked for evidence of cracking along the notch, and in the plane of the side-grooves. Of particular interest was the location where the notch and the side-grooves intersect.

Examination revealed that, for the cases where the fracture mechanics procedure clearly indicated that the specimen was either cracked or torn, there was evidence of cracking along the entire length of the notch. However, in one case it was difficult for the CCG test technique to distinguish between cracking and blunting (test specimen P-6). In this case, small cracks were noted at corners of the specimen (at the point where the notch intersects the side-grooves). These corner cracks did not extend along the length of the notch. Nor did they extend far into the specimens. Thus, only a small change in signal would be anticipated. These corner cracks may have been anomalies related to machining difficulties in aligning the notch with the side grooves for this particular specimen. In any case, the corners clearly are areas of high stress relative to other locations within the test specimen.

After the visual examination, all (22) test specimens were cut into two pieces along the centerline of the specimen on a plane perpendicular to crack propagation. One of these two halves was mounted, polished and etched to allow for physical measurement of the crack length at that point. Physical measurements of crack length were taken using an optical microscope having a calibrated stage micrometer. The other half the test specimen was chilled in liquid nitrogen then broken open to reveal the shape of the crack front. This was intended to ensure that crack advancement was essentially parallel to the notch, thus ensuring that a measurement taken along the centerline would provide a reasonably good approximation of the crack length.

Table E-1 shows the results of the investigations of both halves of the test specimen. This table also shows the predicted results as per the fracture mechanics technique. A relatively good correlation is indicated between the fracture mechanics prediction and the results of the physical examination. However, sample P-6, which exhibited corner-cracking was selected for further evaluation to further clarify the mode of cracking in this region. It also should be noted that sample K-3 exhibited a "stepped" crack front that resulted from uneven crack advancement along planes in front of the notch. This sample was analyzed further to gain an understanding of the cause for this peculiar fracture surface appearance.

Microstructure:

The (22) polished and etched specimens described above were used to characterize the microstructure of each specimen in terms of constituents present, grain size, and other characteristics. Figures E-1 through E-22 provide optical micrographs showing the microstructural characteristics of each sample. If the test specimen cracked, then the figures also show the crack path through each sample. Tables E-2 through E-5 provide a record of the results of these examinations in terms of grain size and any other pertinent features. These tables also record crack characteristics and the crack path followed through the microstructure. Lastly, they record the results of bulk hardness tests taken for each sample. The recorded hardness result represents an average of three measurements on an individual specimen.

The results of this examination are summarized below:

- The microstructure was consistently ferrite-pearlite as would be expected for these hot-finished, seamless, carbon-manganese steel pipes. The grain sizes varied from 5.5 to 8; however, no correlations could be made between grain size and susceptibility to CCG.
- The hardness tests show, as would be expected, that the as-cold-worked hardness had the highest values, (92.2 to 99.2 HRB).These then dropped off due to stress relief at 1250 F, (85.1 to 93.9 HRB). They further dropped off due to the normalization heat treatment. (74.9 to 84.9 HRB). While it is recognized that the most sensitive heat of material (Heat D) had the highest initial hardness, review of the data in Tables E-2 through E-5 show no clear correlation between hardness and sensitivity to CCG.
- Banding was noted in some specimens (particularly for Heats D and P. It is interesting to note that Heat D was termed "dirty" and Heat P was "intermediate" in terms of cleanliness. Lastly, as will be described in detail later, one of Heat D specimens showed cracking out of plane. This is suggestive of a particularly susceptible material, and thus this specimen is worthy of the more detailed investigation that later will be described.
- The metallographic examination revealed the crack path to be primarily along ferrite-ferrite and ferrite-pearlite boundaries. However, it also was found to cut across pearlite colonies.
- Grain boundary separations were noted in advance of the crack, and adjacent to the notch in some cases. It is almost certain that these and the crack itself connect to the surface of the sample. This is deduced from the fact that all of the cracks were oxide-lined.
- There is little or no evidence of local plastic deformation associated with the creep cracks.
- There is extensive local deformation associated with the tearing that occurred toward the end of testing. Local deformation is also suggested to link the creep-related grain boundary separations that formed in advance of the crack as it grew.
- In one case (for sample M-3), tearing is indicated close to the notch while creep is indicated deeper into the sample. However, in most cases, creep cracking extends from the notch. This then transitions to tearing as the crack grows. The cause the performance of sample M-3 is not clear.

Scanning Electron Microscopic (SEM) Examination:

Microstructure – The SEM also was used to characterize the microstructure. Figure E-23 provides a low magnification view of the CCG extending from the tip of the notch in specimen K-7. Recall, that this particular specimen was from Heat D having both poor cleanliness and high free nitrogen. This sample was in the stress relieved condition. Noted in this figure is the fact that, in this plane, the crack does not extend back to the tip of the notch. This raises the question as to the location of the most severe stresses in the test specimen design. However, closer examination revealed that all of the cracking in this plane was oxide-filled. This is taken as a strong indication that this crack links to the surface at some point. The fact that the crack wanders so extensively suggests that its' path is more affected by the presence of locally weaken regions, and less affected by the stress distribution at the tip of the notch or the growing crack.

Figure E-24 shows higher magnification views of oxide filled grain boundary separations in advance of the crack tip, see the "boxed" area in Figure E-23 as a reference. EDAX analysis of these showed no evidence of enrichment in tramp elements or otherwise. Oxygen was the only foreign element indicated. It should be noted, however, that the volume of material sampled during EDAX is relatively large, and a more detailed surface analysis, perhaps using Auger electron spectrometry (AES), may be required to definitively characterize the composition in the vicinity of grain boundaries.

Figure E-25 provides a low magnification view of a similar creep crack that extended from the notch in specimen P-2. This sample was from Heat P which was intermediate in terms of steel cleanliness and free nitrogen content. The P-2 sample was in the as-cold worked condition. The cracking in evidence is very similar to that shown for the K-2 sample from Heat D; however, in this case, the cracking extends to the surface at the tip of the notch in the plane examined.

Figure E-26 provides higher magnification views of the cracking in advance of the crack tip. Again, it is oxide-filled and along grain boundaries within the microstructure.

General Fractography - The SEM was used to characterize the fracture surface of specimens that experienced CCG. The intent was to draw correlations between the appearance of the fracture and the underlying microstructure, and hopefully to gain a better understanding of the cracking mechanism.

Figure E-27 shows the appearance of the fracture surface on sample K-2. This sample is different than those discussed above in that, during testing, the crack was allowed to grow beyond the CCG cracking zone. This zone, indicated as Area 1, in Figure E-27, extended typically less than 60 mils into the specimen (see Table E-1). For this sample, cracking in the CCG region took approximately 377 hours to initiate and propagate to the extent shown (about 30 mils). In contrast, crack growth beyond the CCG region happened rapidly. This is known because, in the testing procedure, measurements to determine the position of the crack front are taken at 15 minute intervals, and testing was discontinued when excessive displacement was

indicated. The crack in sample K-2 extended from Area 1 through Areas 2 and 3 in a total of 17 minutes, at which point testing was discontinued. Only the ligament in Area 4 remained at the end of testing. This "forced fracture" was induced by chilling in nitrogen and striking the sample so as to open the crack and preserve the fracture surface.

As might be expected, the fracture surface in Area 1 was primarily intergranular and thus correlated well with the crack path as indicated by the metallographic cross sections discussed above. The appearance for the fracture surface is shown at progressively higher magnifications in Figures E-28a, b, c, and d. These show grain boundary facets having significant surface relief. The side cracking in evidence is suggestive of the weakness along these boundaries, particularly considering that this cracking is in a plane that at times is parallel to the loading direction. Ductility is indicated in some locations that appear to link separated boundaries. This also is consistent with the metallographic evidence of the condition in advance of the crack tip, as shown in Figures E-23 through E-26.

The characteristics of the fracture surface in Area 2 are particularly significant. This fracture surface is shown at progressively higher magnifications in Figures E-29a, b, and c. As can be seen, the fracture is again predominantly intergranular with some local regions of ductility. Again side cracking is in evidence. The grain boundary facets in this case are flat, without significant surface relief. This likely is due to the fact that in the crack in CCG zone was oxidized as it grew over a long period of time. The evidence of surface relief is taken to be indicative of the oxidation that occurred during testing over a 30 day period.

The fact that Area 2 cracked via an intergranular mode in a relatively short period of time suggests that the properties of the material at the time of crack extension were such as to favor low ductility and an intergranular crack path. This area may well have been accumulating fatigue damage as testing progressed; however, by whatever means it certainly appears to have suffered embrittlement.

As the crack grew beyond Area 2 and into Area 3 it transitioned to a ductile-tearing mode. This is evidenced in the dimpled-rupture fracture appearance shown in the fractographs in Figure E-30. Some preference for local grain boundary separations are suggested in this region also (compare the scale of the features in Figure E-30 with the grain boundary separations shown in Figure E-29). However, cracking in this region is almost entirely ductile. This fact lends support the hypothesis that the intergranular features of Area 2 were due to the combined effects of accumulated creep damage and weakened grain boundaries.

Figure E-31 was taken for completeness to demonstrate the appearance of the final low temperature fracture for this specimen. As can be seen, it is entirely by cleavage as would be expected.

Examination of Corner-Cracked Test Specimen (P-6):

Of particular interest are the results for Sample P-6. In this case, fracture mechanics was unclear regarding whether the specimen test results were indicative of either blunting or creep. Visual examination showed cracking at the corners of the specimen where the notch

intersected the side groove. When this sample was broken open, it was apparent, due to oxidation of the fracture surface, that only corner cracking had occurred.

SEM examination of the fracture surface at the corner revealed it to be primarily intergranular which is characteristic of creep crack extension. Figure E-32a shows a low magnification SEM image of the fracture that indicates the location of the corner crack. Figure E-32b shows the fracture surface appearance which confirms that this cracking was due to a creep mechanism. This is deduced from comparing the fracture appearance for the corner-cracked region with that in the CCG region of the K-2 sample, (compare Figure E-32b with E-28b). Figure E-32b also shows three areas investigated at higher magnification. Figures E-33a, b, and c provide these images. The image in Figure E-33b shows that the corner crack was primarily intergranular, and thus creep-related. The images in Figures E-33a and E-33b show the transition between this region and the cleavage fracture that was generated when this crack was broken open.

Based on the above, it seems apparent that this sample was suffering from incipient creep damage. This suggests that the material condition being evaluated (i.e. Heat P after stress relief) was on the borderline between good and bad performance. This is deduced from the fact that only one of the two Heat P stress relieved test sample (P-6 and P-7) exhibited signs of creep damage. Furthermore, the creep damage on sample P-6 was in evidence only at the highly stressed corners of the specimen.

Examination of Test Specimen with "Stepped" Crack Advancement (K-3):

Recall that sample K-3 evidence a peculiar stepped crack front that was worthy of further investigation. In this case, creep cracking advanced from the notch to a different extent on multiple planes. Figure E-34 shows the appearance of this fracture surface at low magnification. The most prominent features are that there several significant cracks extending perpendicular to the fracture surface and into the body of the specimen. Consideration of the fact that these cracks are parallel to the loading axis during test suggests that this orientation is stress to only a fraction of the stress needed to drive the crack in its' intended crack plane. Cracking under this lower stress suggests that this out-of-plane cracking is follows planes of significant weakness in the material.

At this point, it is appropriate to offer a comment about the test specimen orientation relative to the cracking experienced in service. It should be recalled that cracking in service initiated at the external surface and ran toward the internal surface on a radial plane that was parallel to the long axis of the pipe. This is a potential plane of material weakness in that, stringers and other inclusions typically align themselves with the axis of the pipe. Ideally, the creep test specimen would be designed to sample this plane with the test crack running in the same direction and in the same plane as the failure. However, due to geometric considerations, the test specimen geometry caused the test cracks to run in what would have been the circumferential direction on a plane perpendicular to the pipe long axis (see Figure E-36). Thus, the test crack was running across the potential planes of weakness and not with them. Test results in this orientation may well predict more resistance to CCG in service. This possibility is explored in the work that is described below.

In the light of the above, the out-of-plane cracking experience in sample K-3 would be in a plane roughly parallel to the internal and external surfaces of the pipe. Since this plane it is aligned with the pipe axis, it is possible that this reasonably could be a plane of weakness within the pipe; however, it is not on the plane that would actually have failed in service.

Metallographic cross sections were prepared to show orthogonal views of the underlying microstructure (on the planes indicated in Figure E-36). These are shown in Figures E-37 through E-40. Significant banding was noted for the samples selected from Heats M, K, and P. The observed banding is consistent with the potential for planes of weakness concentric with the tube cross section. These would be in line with the out-of-plane cracks present in sample K-3.

It seems likely that these planes of weakness were the cause of the "stepped" crack front exhibited on sample K-3. Figure E-35 roughly maps out areas of intergranular cracking and cleavage in the vicinity of the notch. Recall, that the areas of intergranular cracking were generated during CCG testing, and the cleavage fracture surfaces were generated after the testing was completed. It was noted that this cleavage appears to be associated with, and adjacent to out-of-plane cracks. From this, it is speculated that the out-of-plane cracking relieves stresses locally so that the creep process is slowed in these regions. Thus, at the end of testing uncracked ligaments remained adjacent to the out-of-plane cracks.

Figure E-41 shows the appearance of cleavage adjacent to an out-of-plane crack. While it is not easily depicted, it should be noted that the fracture surfaces within the out-of-plane crack have an intergranular appearance.

Figure E-42 shows the appearance in the CCG zone of sample K-3. The intergranular characteristic of this region is somewhat less apparent than for some of the other samples. However, it clearly is not ductile.

To further understand the out-of-plane cracking, a metallographic sample was sectioned along the X-X' line in Figure E-34. The plane that was revealed then was polished and etched, and is shown in Figure E-43, and at higher magnifications in Figures E-44 and E-45. These suggest that the out-of-plane cracking followed the same paths as were followed in the plane of the test crack. This is further taken as evidence of local weakness in these areas.

Table E-1 Comparison of Predicted Results Versus Actual

Heat	Sample	Fracture Mechanics Predicted Result	Actual Result	Measured Crack Length, (mils)	Comments
M	M-2	Blunting	Blunting	N/A	• Blunting is indicated by the lack of cracking anywhere along the notch.
	M-3	Creep plus tearing	Creep plus tearing	45	• Crack growth due to tearing near to notch and creep away from notch.
	M-6	Blunting	Blunting	N/A	
	M-7	Blunting	Blunting	N/A	
	M-10	Blunting	Blunting	N/A	
	M-11	Blunting	Blunting	N/A	
D	K-2	Creep plus tearing	Creep	Could not be determined	• Specimen separated into two pieces. • Creep is indicated by a tight crack with no evidence of local plastic deformation.
	K-3	Creep	Creep	111	• Stepped crack front.
	K-6	Creep plus tearing	Creep plus tearing	Could not be determined	• Specimen separated into two pieces. • Creep indicated near to notch with tearing as crack grew.
	K-7	Creep	Creep	37	• Straight crack front.
	K-11	Creep	Creep	17	• Generally straight crack front, however, increased crack extension at corners.
	K-12	Creep plus tearing	Creep	34	
	K-19	Creep plus tearing	Creep	23	
	K-21	Creep plus tearing.	Creep plus tearing	Could not be determined.	• Specimen separated into two pieces.
O	O-2	Blunting or Creep	Blunting	N/A	
	O-3	Blunting	Blunting	N/A	
P	P-2	Creep	Creep	59	• Straight crack front.
	P-3	Creep	Creep	57	• Straight crack front.
	P-6	Blunting	Incipient Creep	N/A	• Incipient creep cracking observed at intersection between notch and side grooves.
	P-7	Blunting	Blunting	N/A	
	P-10	Blunting	Blunting	N/A	
	P-11	Blunting	Blunting	N/A	

Table E-2 Metallographic Examination Results for Samples From Heat M

Sample	Condition	Hardness, (HRB)	Microstructure	Crack Characteristics	Comments:
M-2	As-cold worked, 20%	95.4	- Ferrite/pearlite. - Grain size = 6.5 - Banded structure.	- Not cracked.	• No deformation noted at tip of notch, Fig. E-1. • Significant banding noted, Fig. E-41.
M-3	As-cold worked, 20%	94.6	- Ferrite/pearlite. - Grain size = 7.5 - No banding	- Tearing noted close to notch tip. - Creep cracking noted with crack extension.	• Significant displacement noted along crack, Fig. E-2a. • Grain distortion noted near crack tip, Fig. E-2b. • Intergranular creep crack extension away from notch, Fig. E-2c.
M-6	Stress relieved	87.1	- Ferrite/pearlite. - Grain size = 6.5 - No banding	- Not cracked.	• No deformation noted at tip of notch, Fig. E-3.
M-7	Stress relieved	88.3	- Ferrite/pearlite. - Grain size = 7 - No banding	- Not cracked.	• Minor plasticity noted at tip of notch, Fig. E-4b.
M-10	Normalized	76.0	- Ferrite/pearlite. - Grain size = 8 - No banding	- Not cracked.	• No deformation noted at tip of notch, Fig. E-5.
M-11	Normalized	75.9	- Ferrite/pearlite. - Grain size = 7.5 - No banding	- Not cracked.	• Possible minor deformation at tip of notch, Fig. E-6.

Table E-3 Metallographic Examination Results for Samples From Heat O

Sample	Condition	Hardness, (HRB)	Microstructure	Crack Characteristics	Comments:
O-2	As-cold worked, 20%	92.2	- Ferrite/pearlite. - Grain size = 7 - No banding	- Not cracked.	• No deformation noted at crack tip, Fig. E-7. • The lack of banding in this sample is illustrated in Fig. E-43.
O-3	As-cold worked, 20%	94.8	- Ferrite/pearlite. - Grain size = 6.5 - Banding noted.	- Not cracked.	• No deformation noted at crack tip, Fig. E-8.

Table E-4 Metallographic Examination Results for Samples From Heat P

Sample	Condition	Hardness, (HRB)	Microstructure	Crack Characteristics	Comments:
P-2	As-cold worked, 20%	93.3	- Ferrite/pearlite. - Grain size = 6 - Banded structure.	- Creep cracking in evidence. - No evidence of plastic deformation along crack, Fig. E-9a	•Creep cracking through pealite colonies and along ferrite/ferrite and ferrite/pearlite boundaries, Fig. E-9c •Not all cracks connect to the surface in this plane. •All cracks appear to be oxide coated, Fig. E-9c. •Banding noted and documented, Figure E-44.
P-3	As-cold worked, 20%	93.6	- Ferrite/pearlite. - Grain size = 6 - Banded structure.	- See above.	•See above, however, Fig. E10c distinctly shows crack path and lack of local deformation.
P-6	Stress relieved	85.1	- Ferrite/pearlite. - Grain size = 6 - Banded structure.	- Incipient crack in plane examined, Fig. E-11c.	•Creep cracking of corners, Figs. E-32 and E-33.
P-7	Stress relieved	87.5	- Ferrite/pearlite. - Grain size = 5.5 - Banded structure.	- Not cracked.	•No deformation noted at crack tip, Fig. E-12.
P-10	Normalized	77.1	- Ferrite/pearlite. - Grain size = 8 - Slight banding noted.	- Not cracked.	•Normalization seems to reduce banding while stress relief does not, compare, Fig, E12a and Fig. E-13a.
P-11	Normalized	80.3	- Ferrite/pearlite. - Grain size = 8 - Slight banding noted.	- Not cracked.	•Potential deformation at notch tip, Fig. E-14.

Table E-5 Metallographic Examination Results for Samples From Heat D

Sample	Condition	Hardness, (HRB)	Microstructure	Crack Characteristics	Comments:
K-2	As-cold worked, 20%	99.2	- Ferrite/pearlite. - Grain size = 6 - Banded structure.	- Specimen split into two pieces during test, Fig. E-15a.	•No evidence of plastic deformation near notch. Cracks are oxide coated, Fig. E-15c. •Extensive banding noted, Fig. E-42.
K-3	As-cold worked, 20%	98.9	- Ferrite/pearlite. - Grain size = 6 - Banded structure.	- Creep cracking in evidence.	•No evidence of plastic deformation along crack, Fig. E-16a and E-16c.
K-6	Stress relieved	91.4	- Ferrite/pearlite. - Grain size = 5.5 - Banded structure.	- Specimen split into two pieces during test, Fig. E-17a..	•Secondary cracking creep voids near notch and along fracture surface, Fig. E-17c.
K-7	Stress relieved	93.9	- Ferrite/pearlite. - Grain size = 6 - Banded structure.	- Creep cracking in evidence.	• Creep cracking along ferrite-ferrite and ferrite-pearlite boundaries, and across pearlite colonies, Fig. E-18c.
K-11	Normalized	82.0	- Ferrite/pearlite. - Grain size = 8 - No banding	- Creep cracking in evidence.	•Normalization eliminated evidence of banding, compare Fig. E-18a with Fig. E-19a.
K-12	Normalized	84.9	- Ferrite/pearlite. - Grain size = 8 - No banding	- Creep cracking in evidence.	•Incipient cracking noted along notch in addition to the main creep crack, Fig. E-20d.
K-19	As-cold worked, 10%	96.3	- Ferrite/pearlite. - Grain size = 7.5 - Banded structure.	- Creep cracking in evidence.	•Hardness high but not quite as high as for 20% pre-strain.
K-21	As-cold worked, 10%	95.7	- Ferrite/pearlite. - Grain size = 7 - Banded structure.	- Specimen split into two pieces during test, Fig. E-22a.	•Secondary cracking creep voids near notch and along fracture surface, Fig. E-22c.

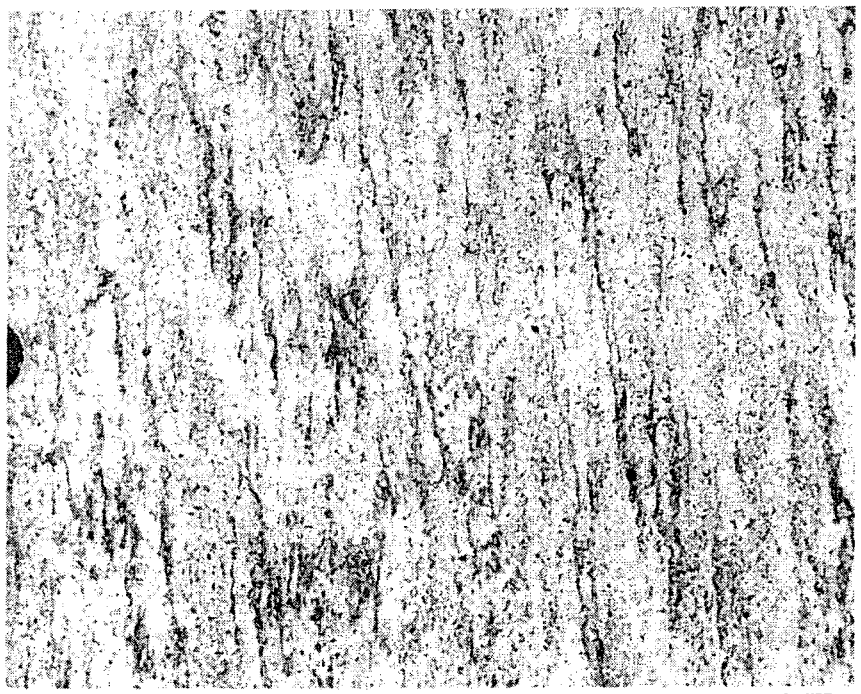

Figure E-1: Test Specimen M-2 – As-Cold Worked Microstructure

Note: No cracking or tearing was found in this specimen

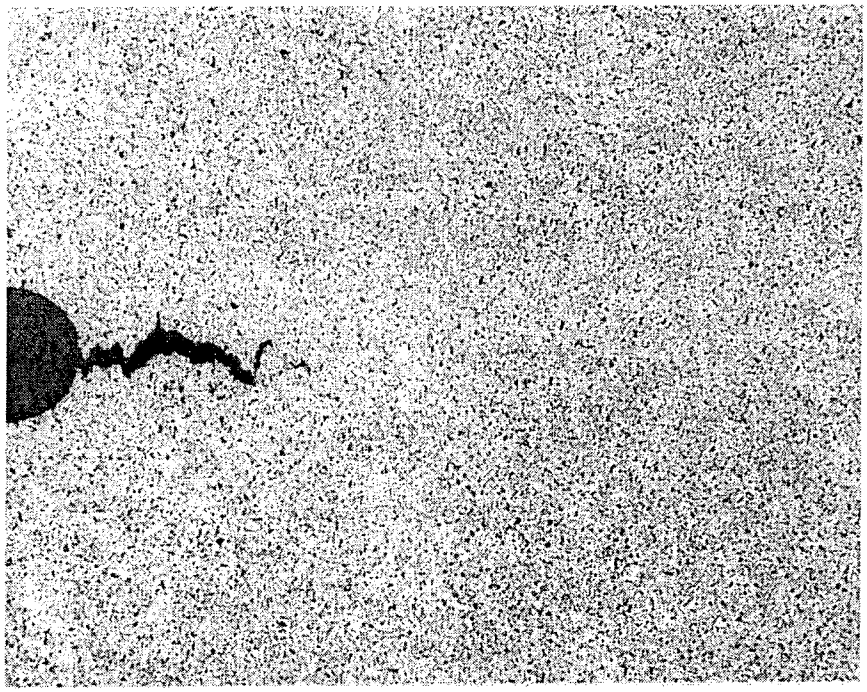

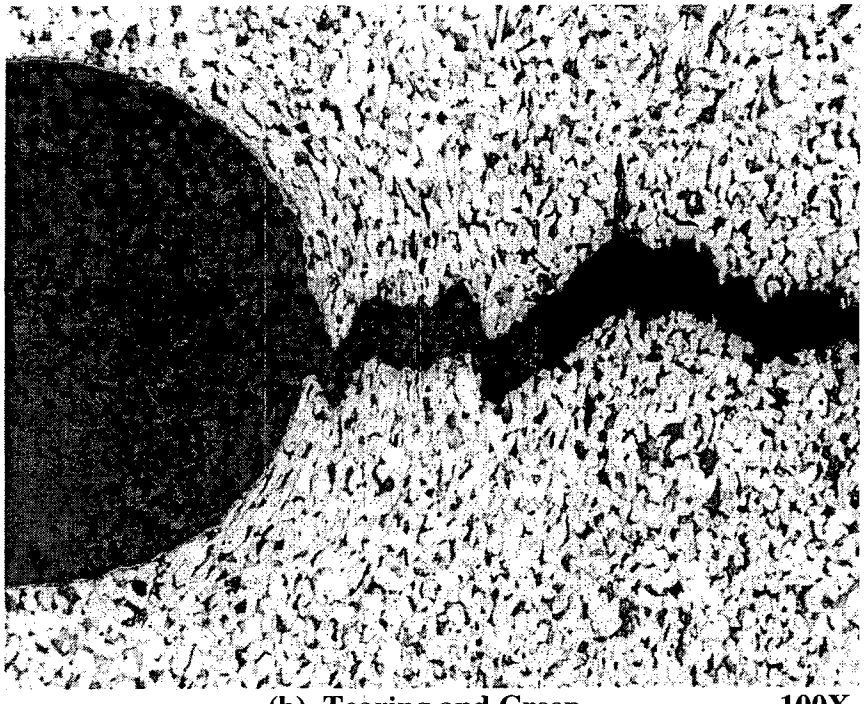

Figure E-2: Test Specimen M-3 – As-Cold Worked Microstructure

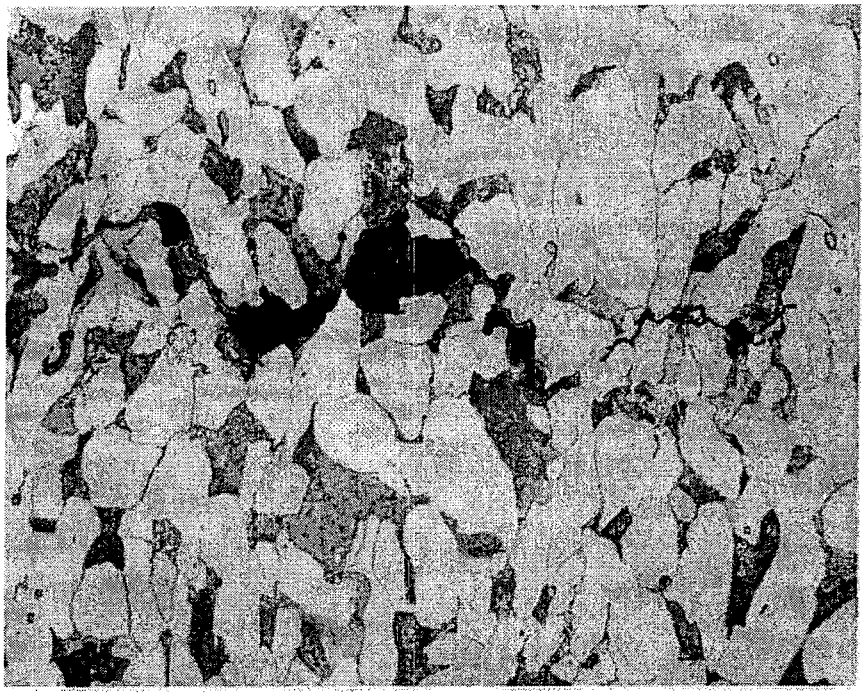

(c) Creep Cracking 500X

Figure E-2, Cont.: Test Specimen M-3 – As-Cold Worked Microstructure

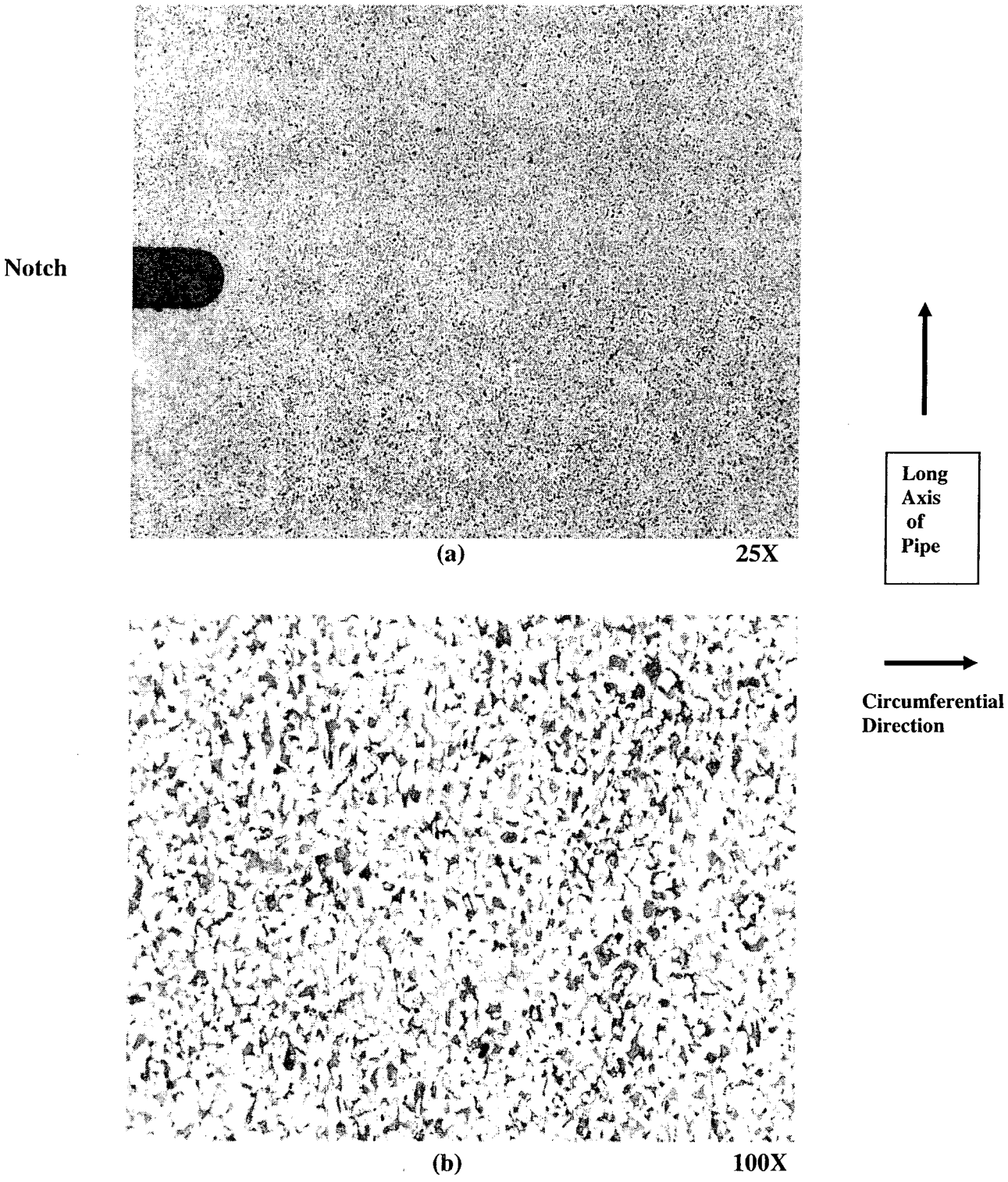

Figure E-3: Test Specimen M-6 – Stress Relieved Microstructure

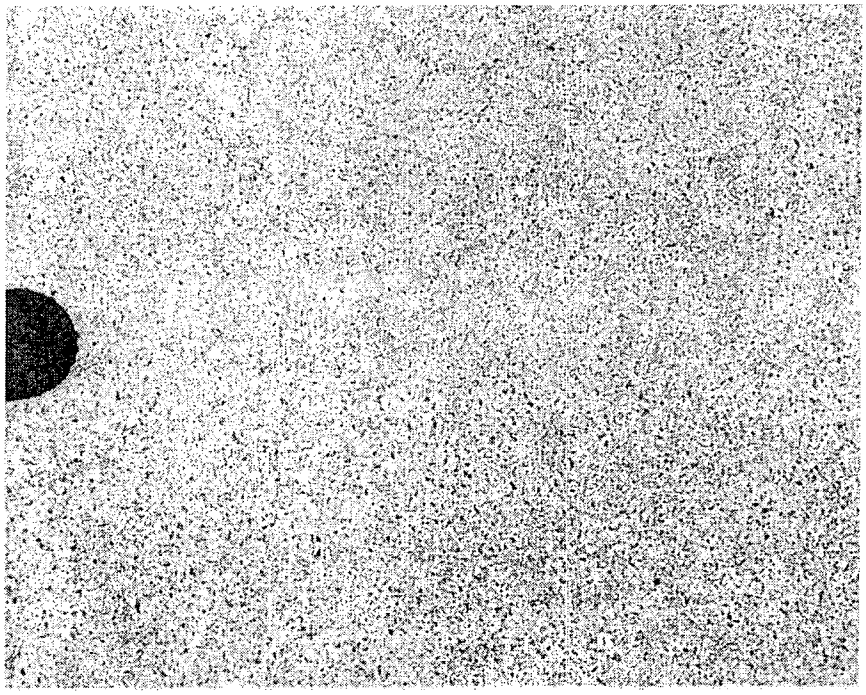

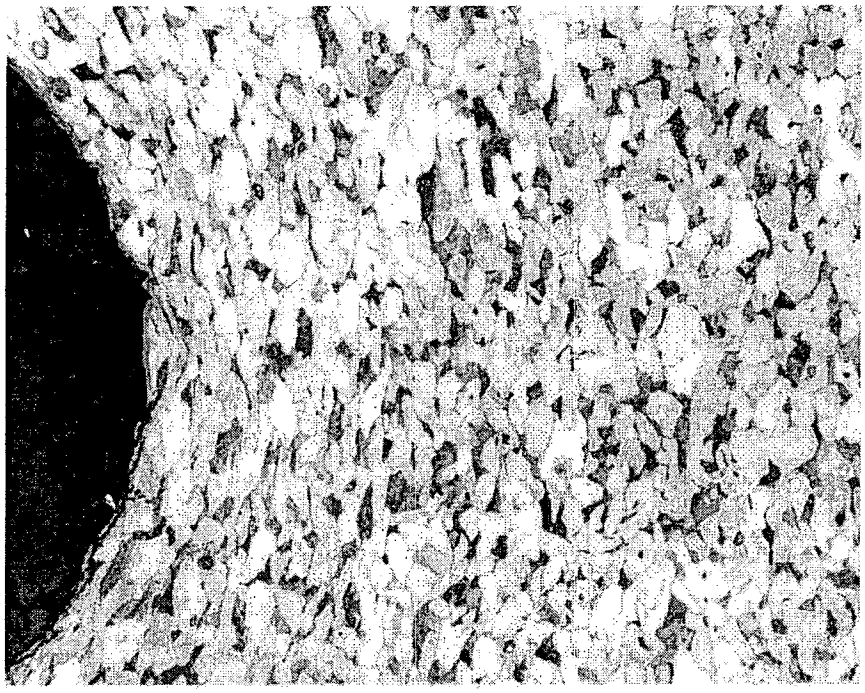

(b) Minor Plasticity at Tip of Notch 200X

Figure E-4: Test Specimen M-7 – Stress Relieved Microstructure

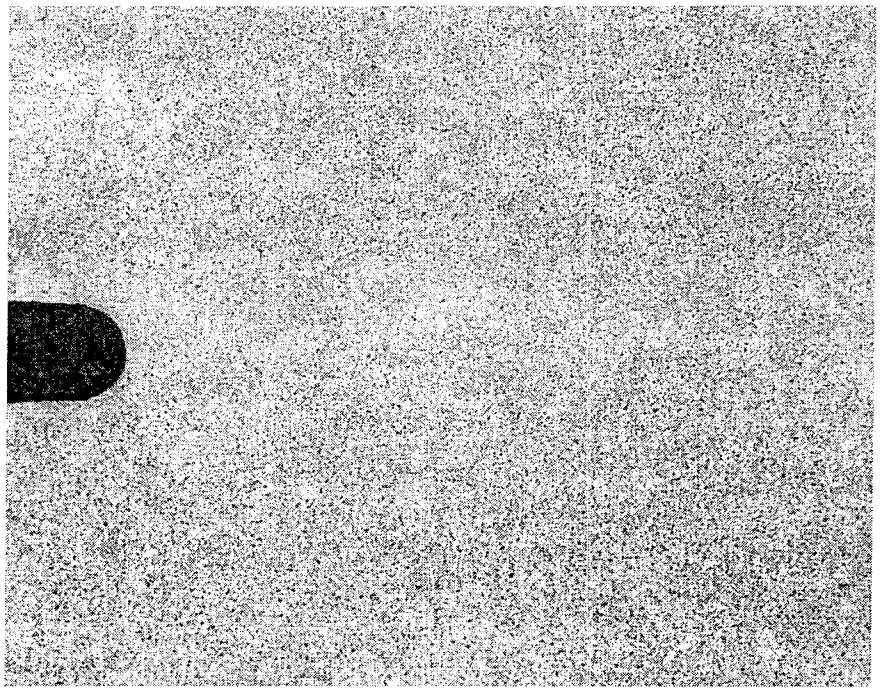

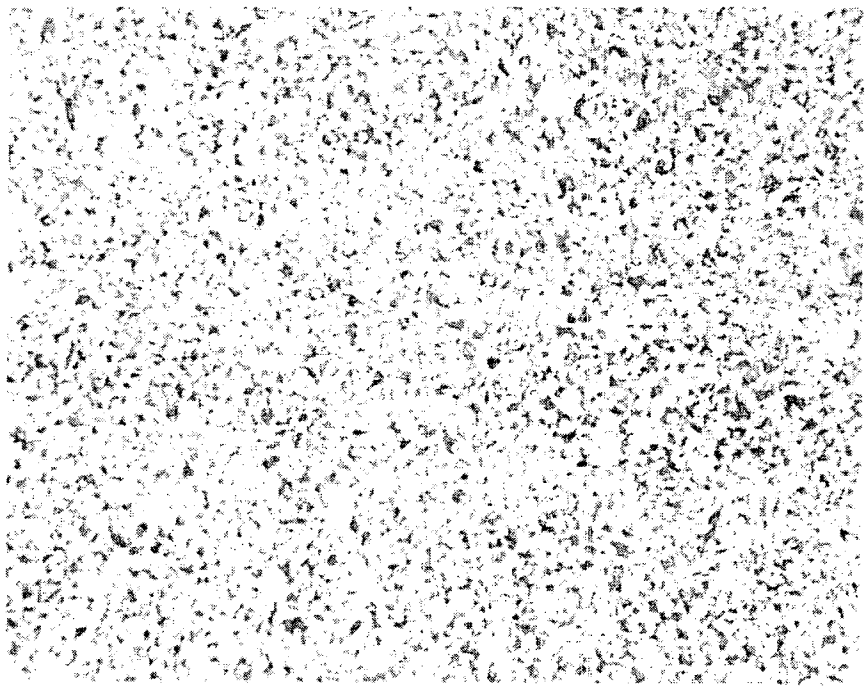

Figure E-5: Test Specimen M-10 – Normalized Microstructure

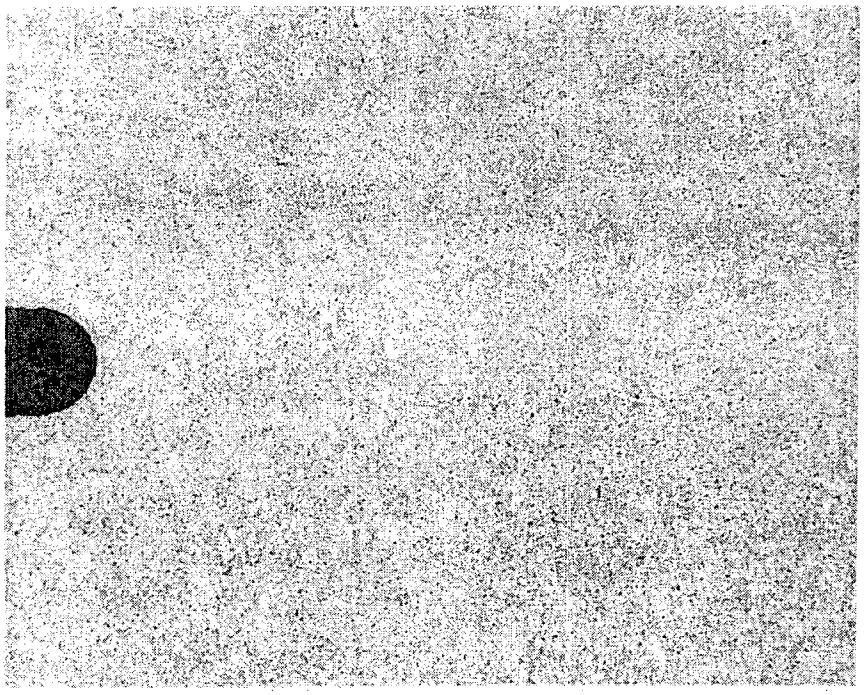

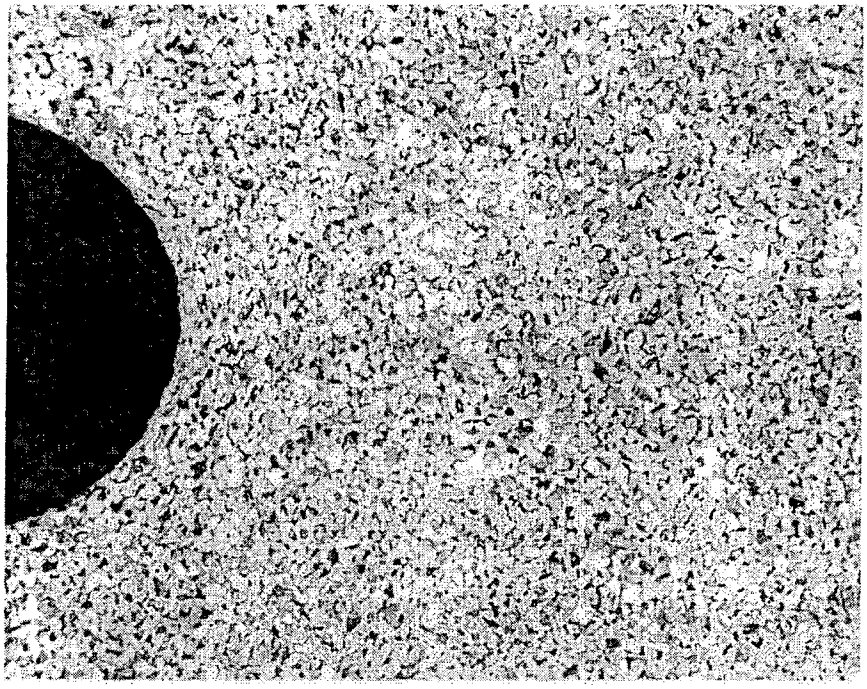

Figure E-6: Test Specimen M-11 – Normalized Microstructure

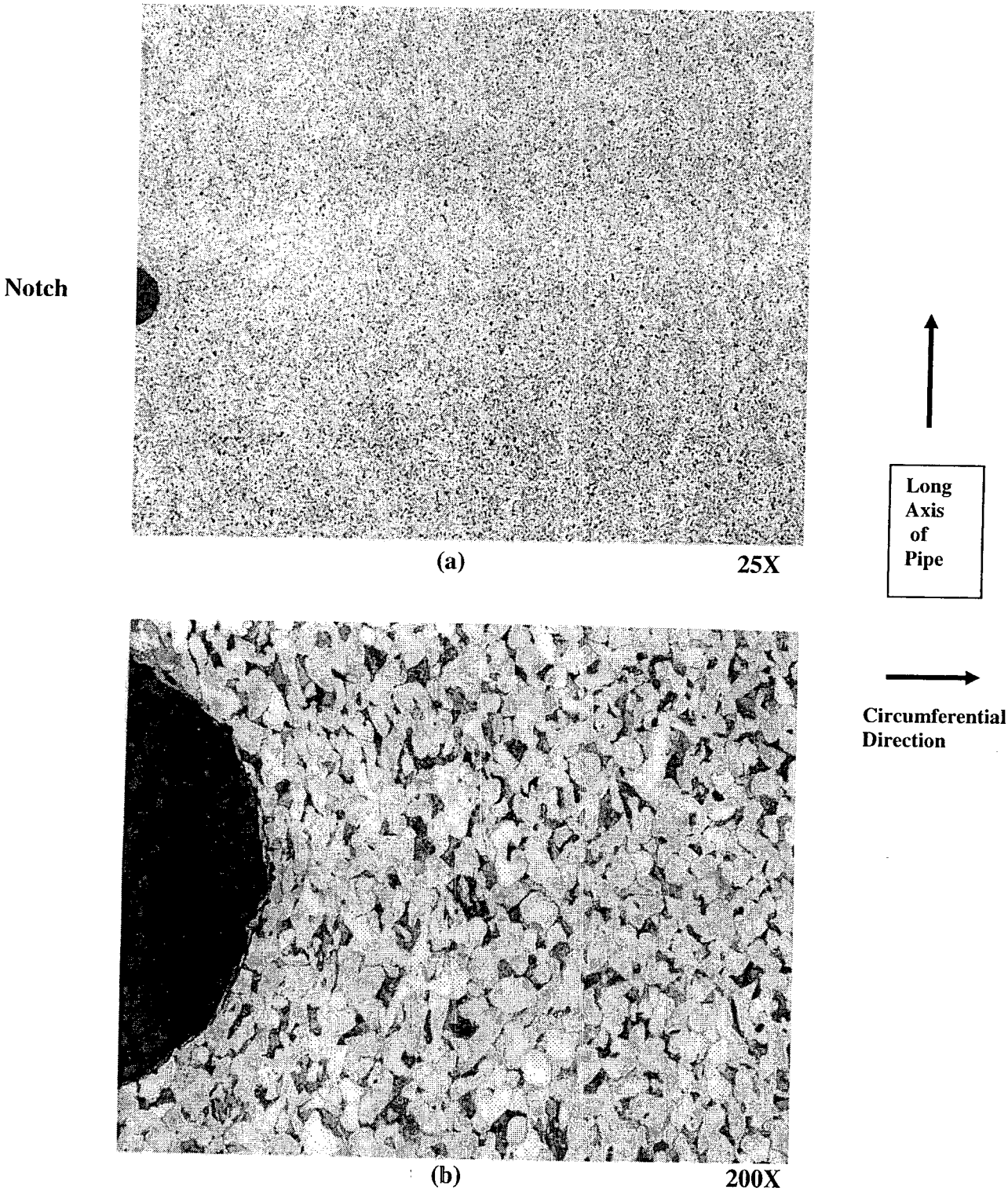

Figure E-7: Test Specimen O-2 – As-Cold Worked Microstructure

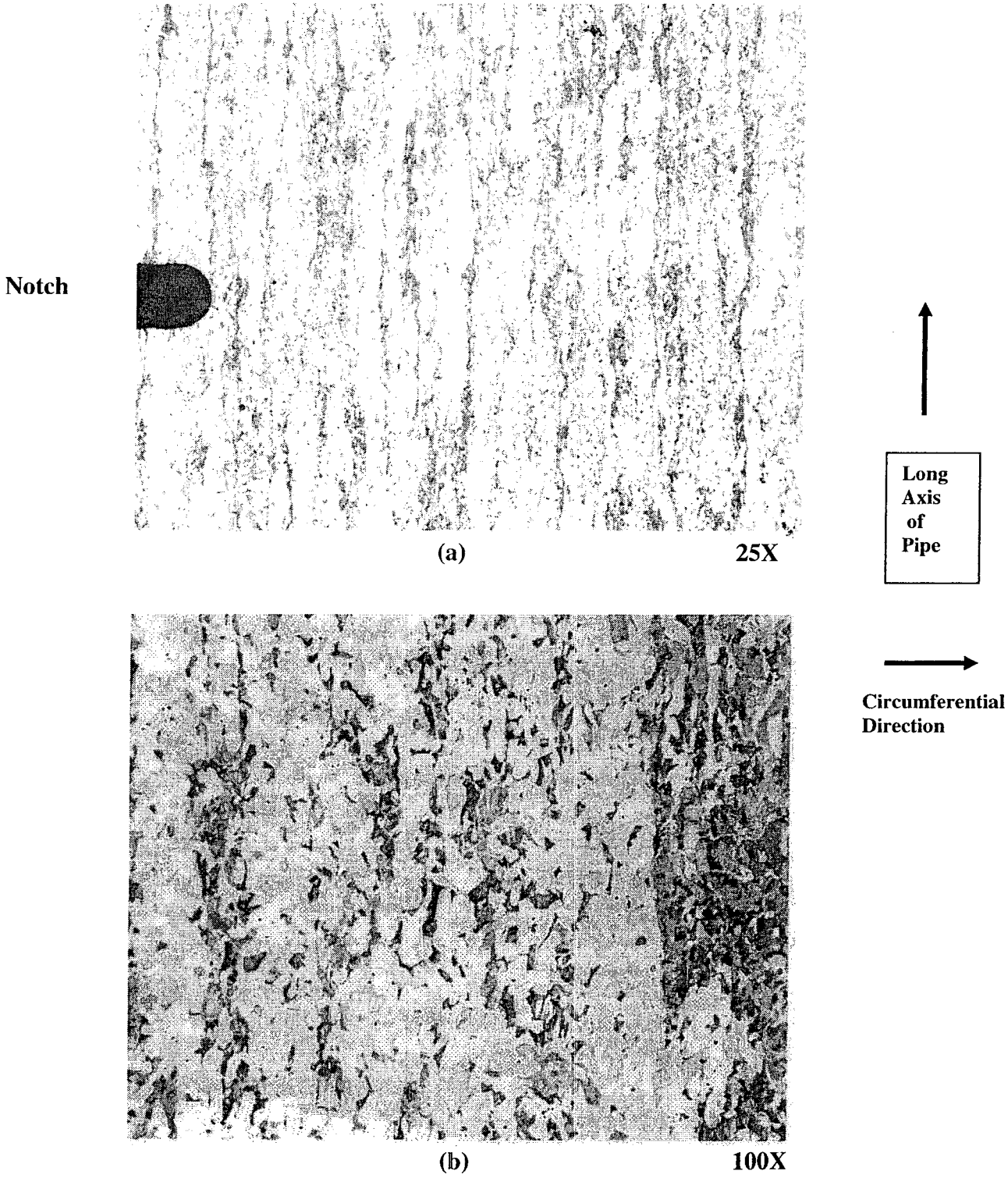

Figure E-8: Test Specimen O-3 – As-Cold Worked Microstructure

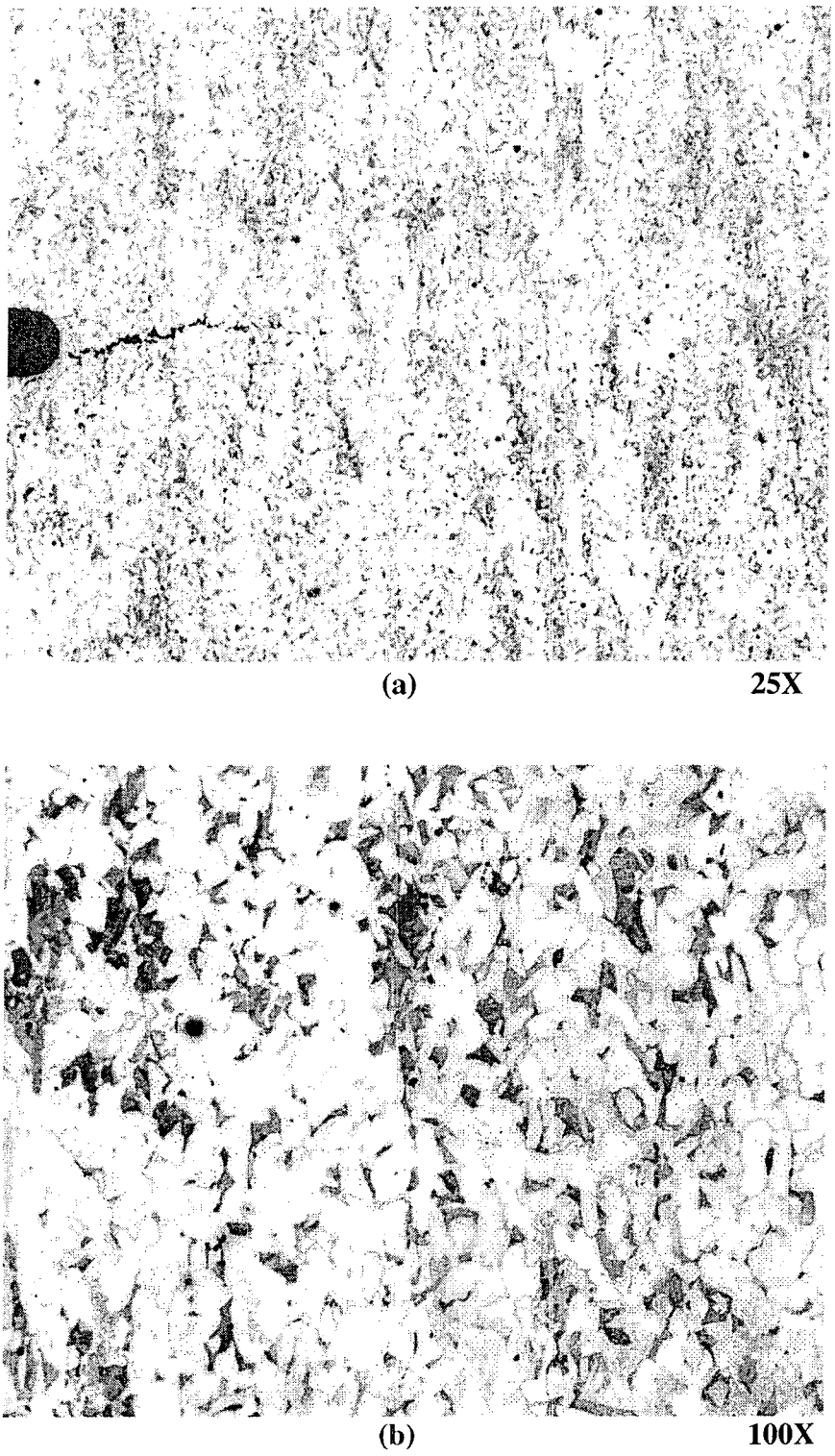

Figure E-9: Test Specimen P-2 – As-Cold Worked Microstructure

(c) Creep Cracking 500X

Figure E-9, Cont.: Test Specimen P-2 – As-Cold Worked Microstructure

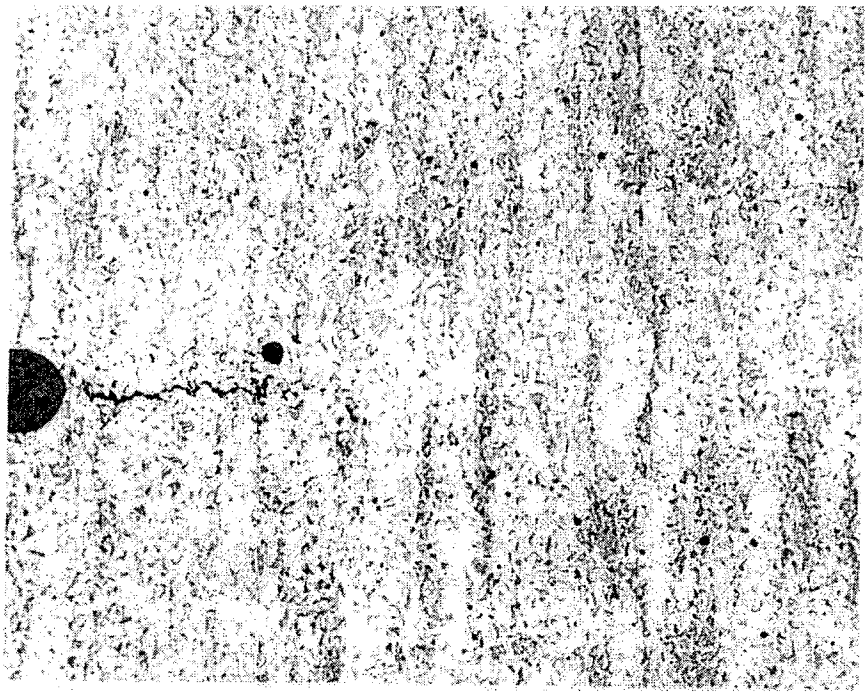

Figure E-10: Test Specimen P-3 – As-Cold Worked Microstructure

(c) Creep Cracking **500X**

Figure E-10, Cont.: Test Specimen P-3 – As-Cold Worked Microstructure

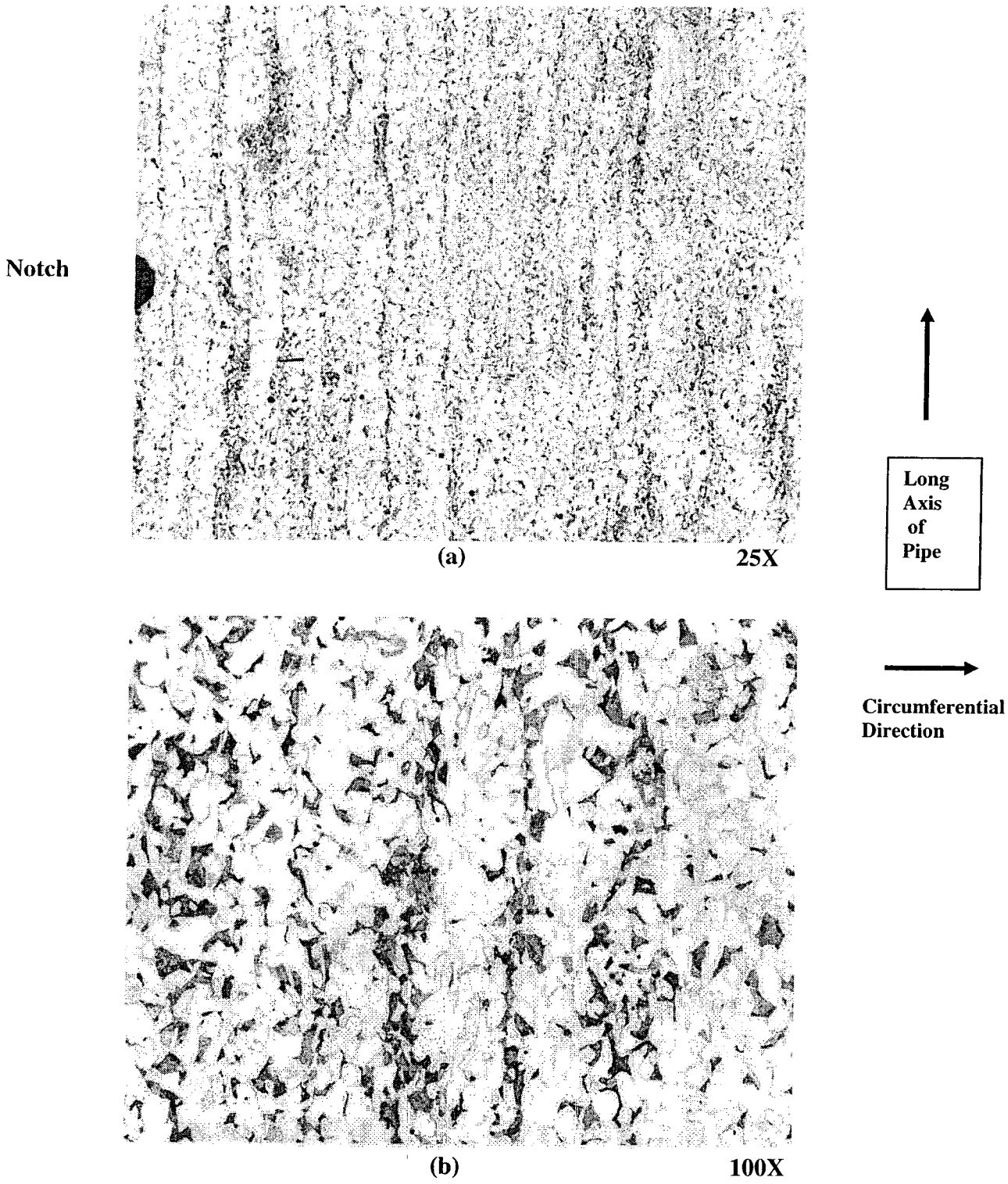

Figure E-11: Test Specimen P-6 – Stress Relieved Microstructure

(c) Incipient Creep 500X

Figure E-11, Cont.: Test Specimen P-6 – Stress Relieved Microstructure

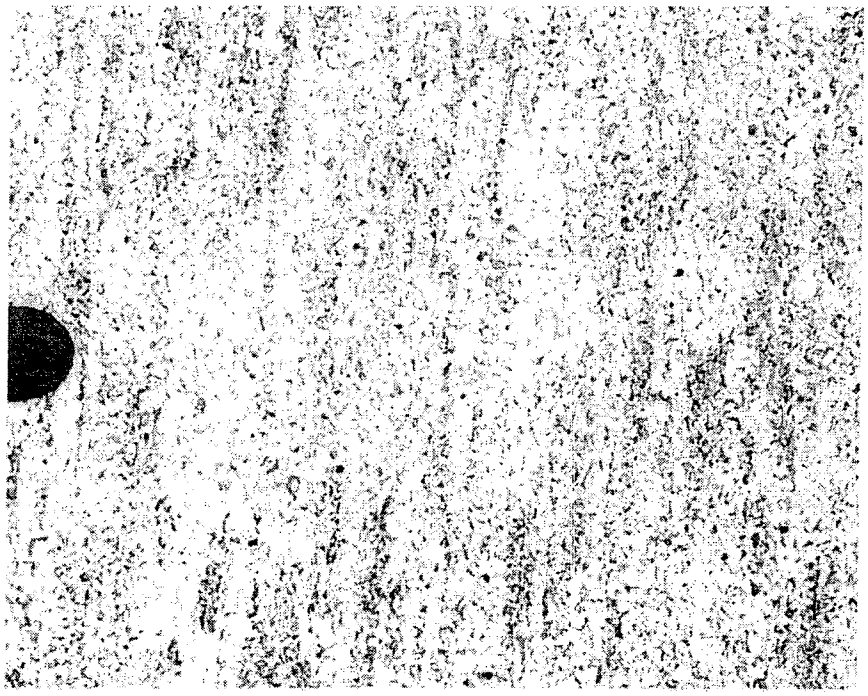

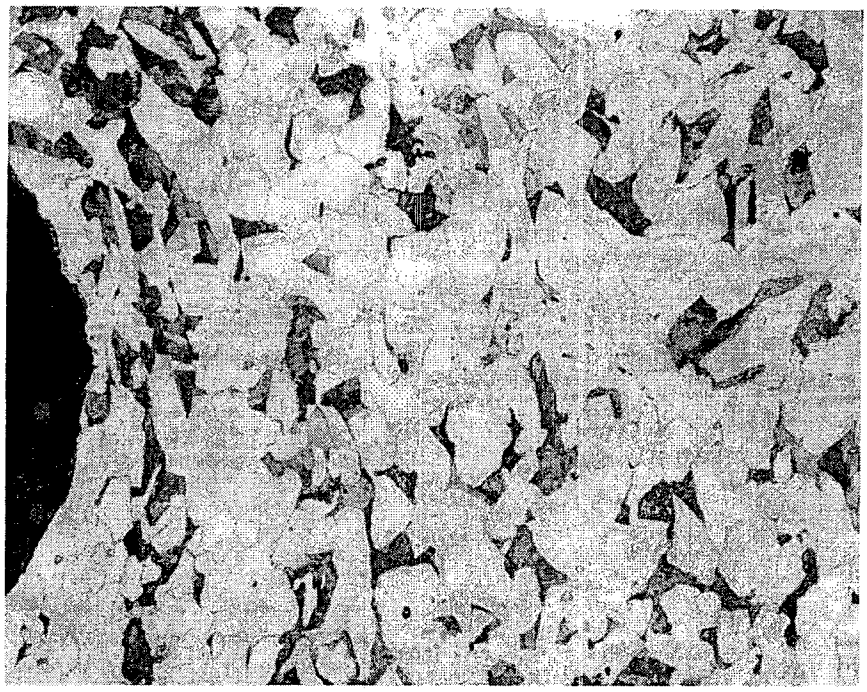

Figure E-12: Test Specimen P-7 – Stress Relieved Microstructure

Note: No cracking or tearing was found in this specimen

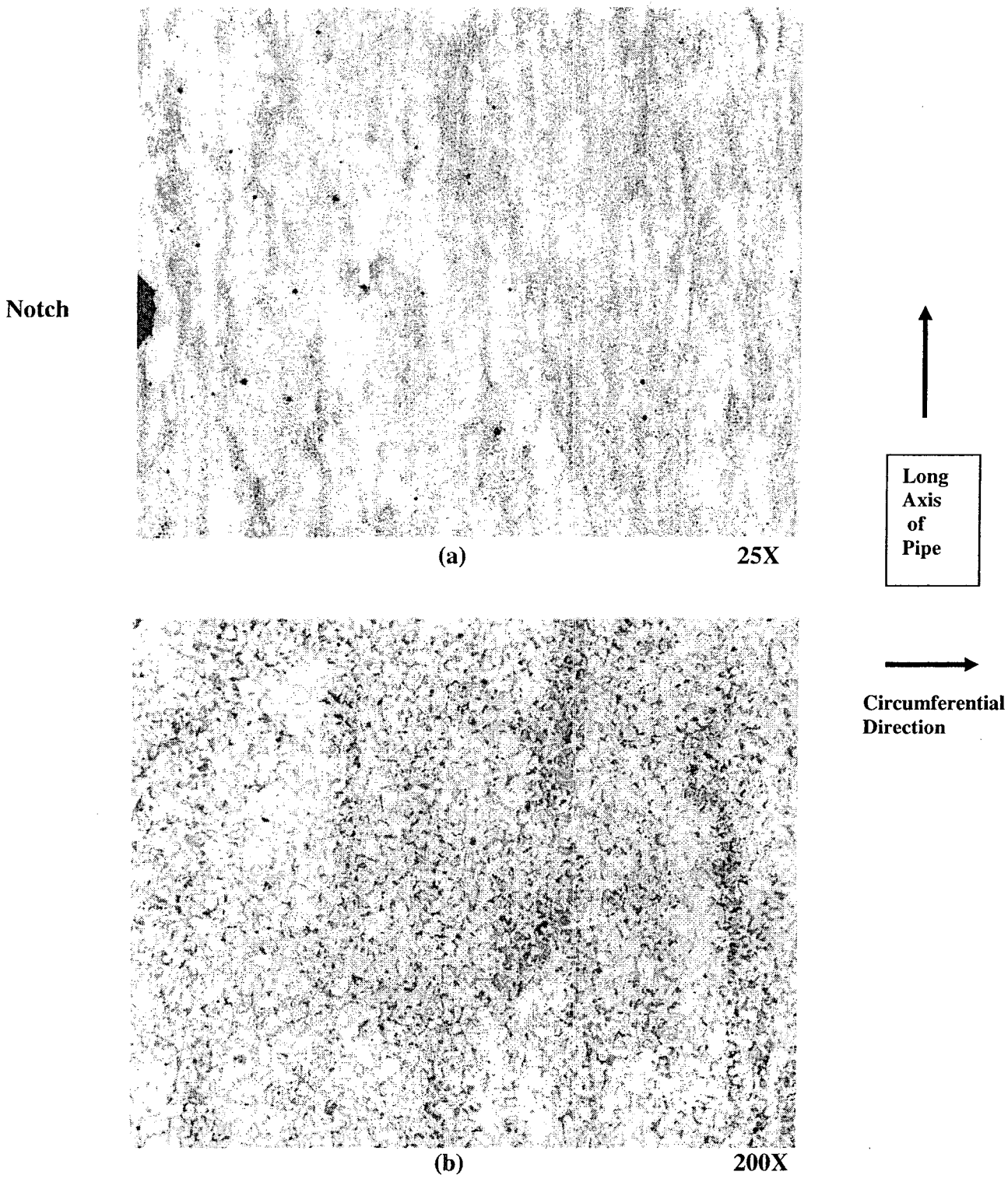

Figure E-13: Test Specimen P-10 – Normalized Microstructure

Note: No cracking or tearing was found in this specimen

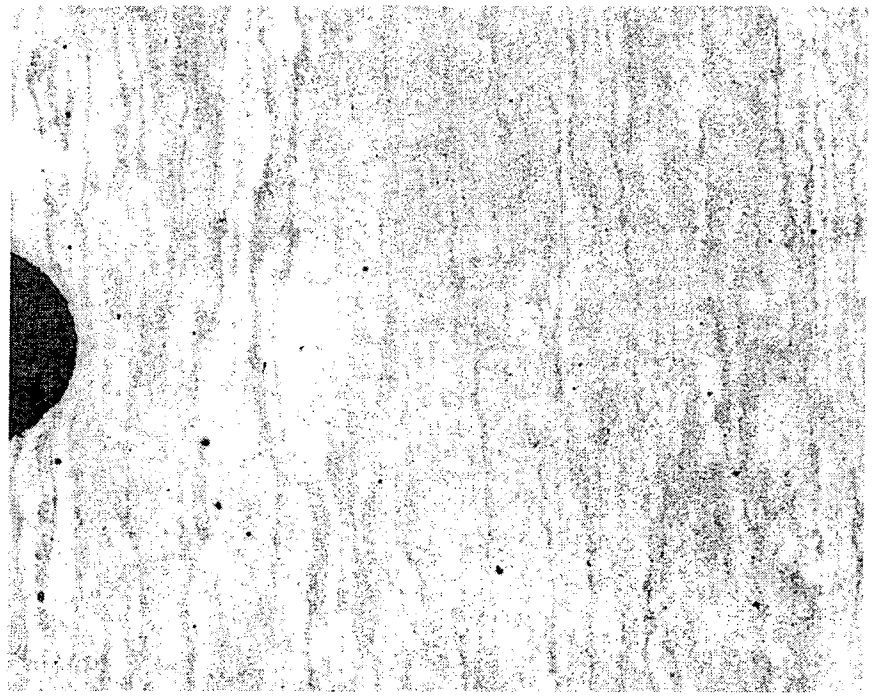

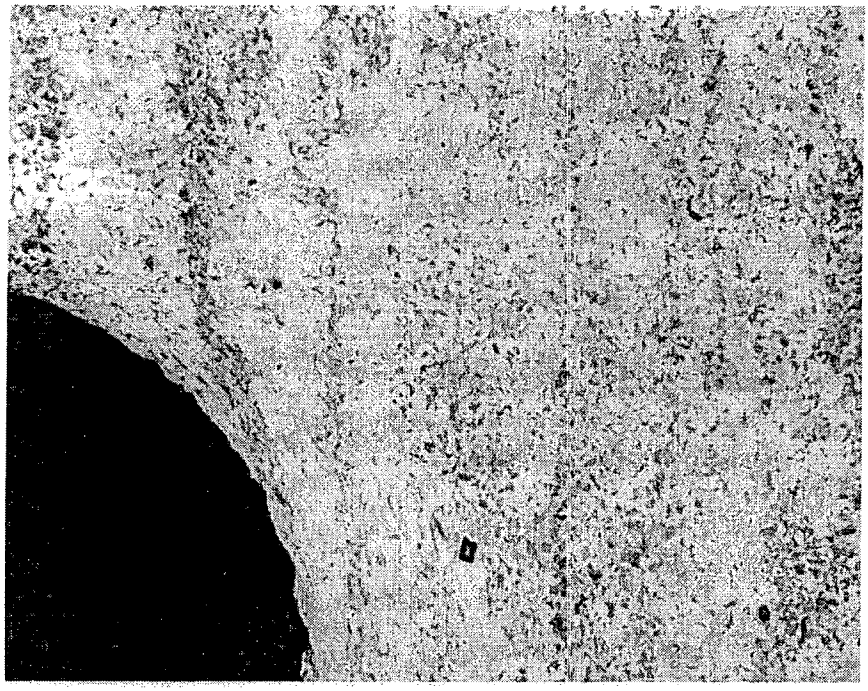

Figure E-14: Test Specimen P-11 – Normalized Microstructure

Note: No cracking or tearing was found in this specimen

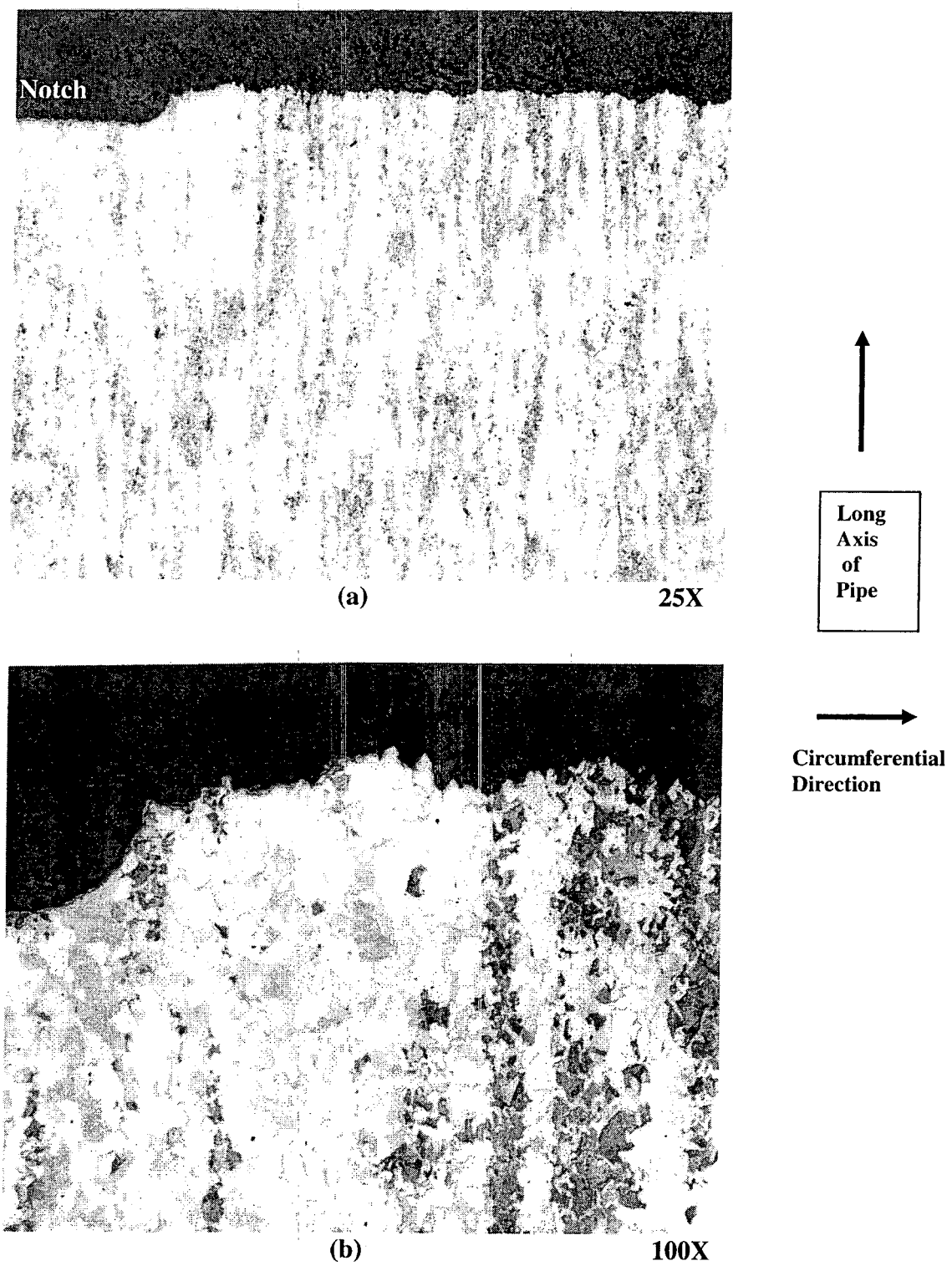

Figure E-15: Test Specimen K-2 – As-Cold Worked Microstructure

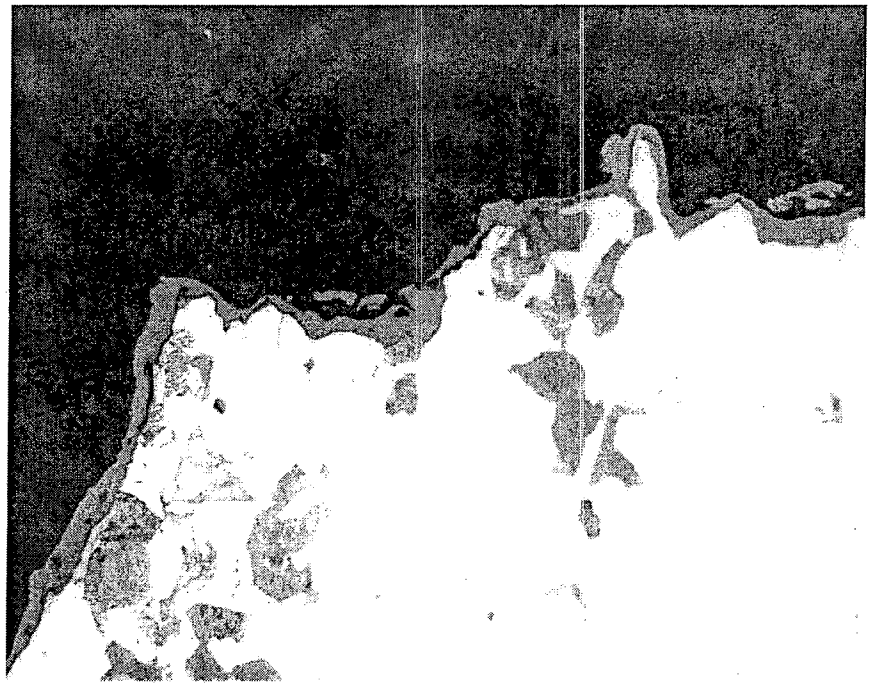

Figure E-15, Cont: Test Specimen K-2 – As-Cold Worked Microstructure

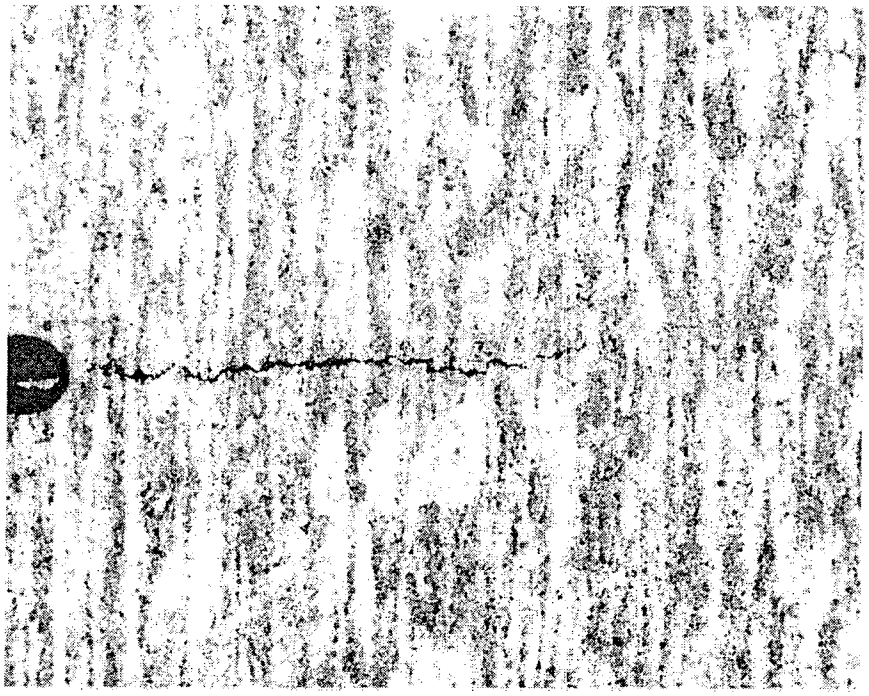

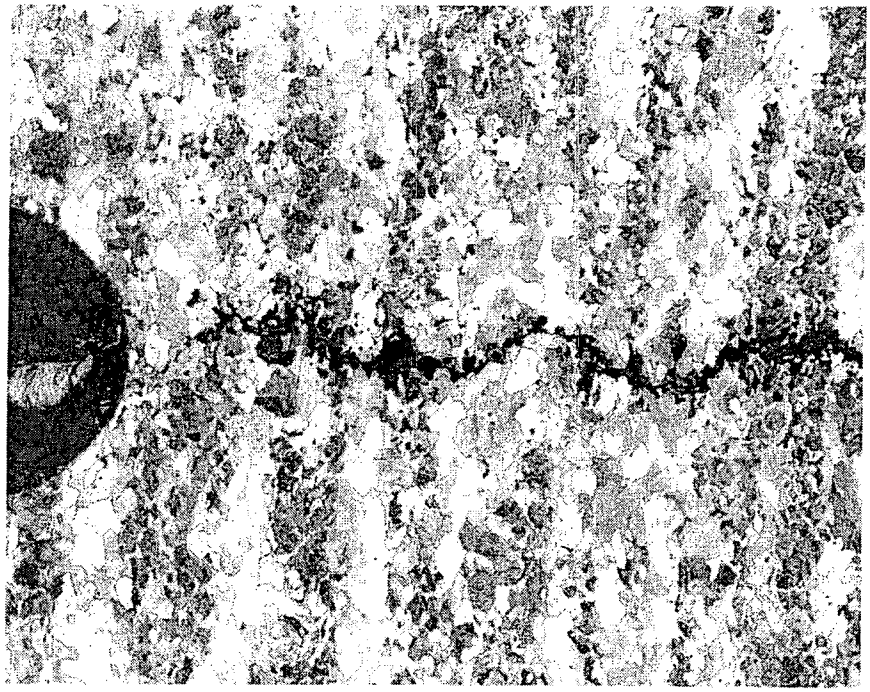

Figure E-16: Test Specimen K-3 – As-Cold Worked Microstructure

(c) Creep Cracking Near Notch 500X

Figure E-16, Cont.: Test Specimen K-3 – As-Cold Worked Microstructure

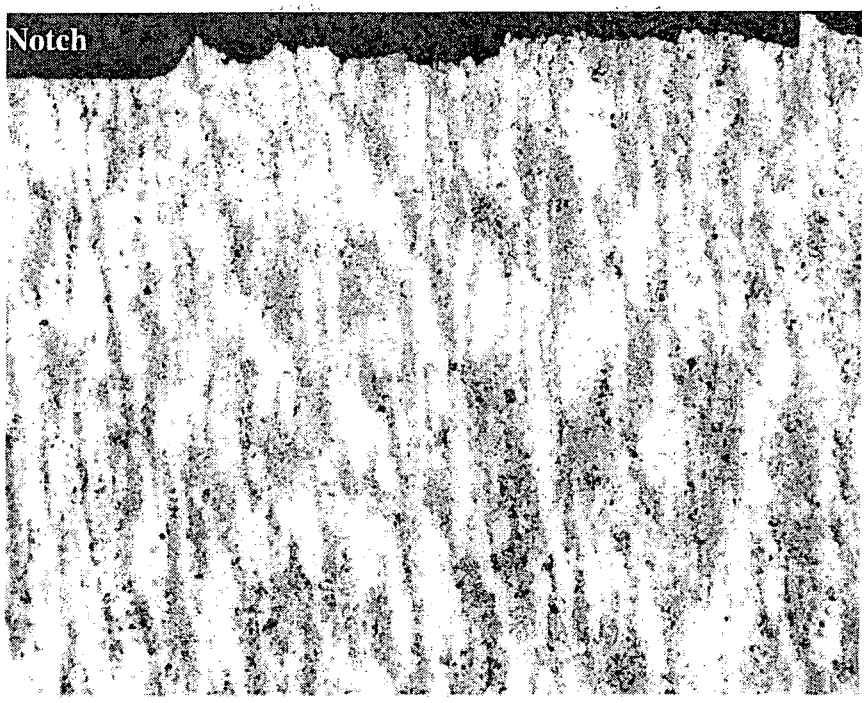

(a) 25X

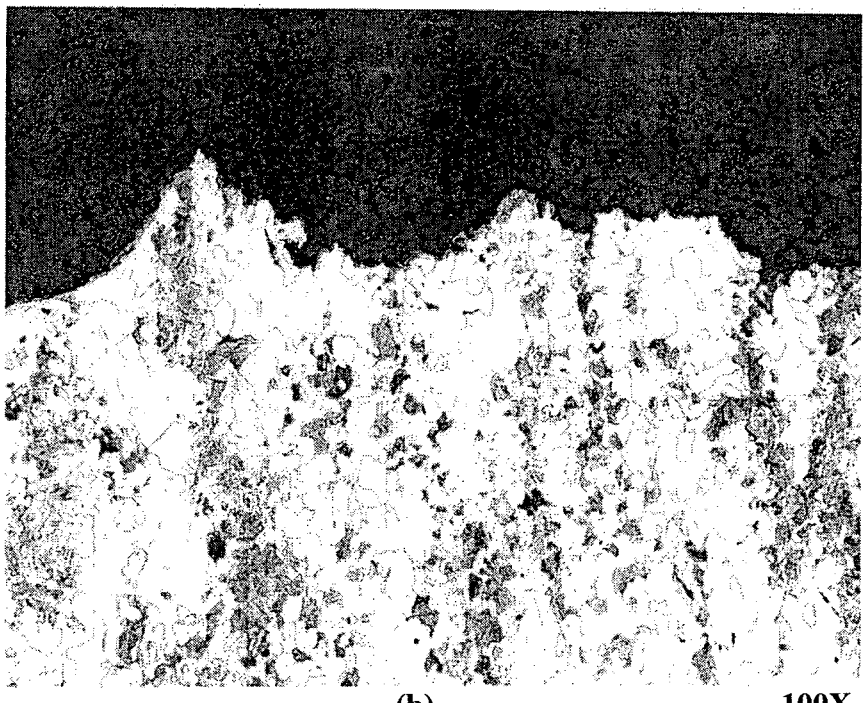

(b) 100X

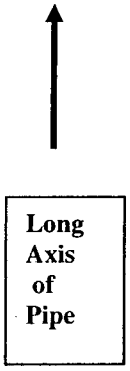

Circumferential Direction

Figure E-17: Test Specimen K-6 – Stress Relieved Microstructure

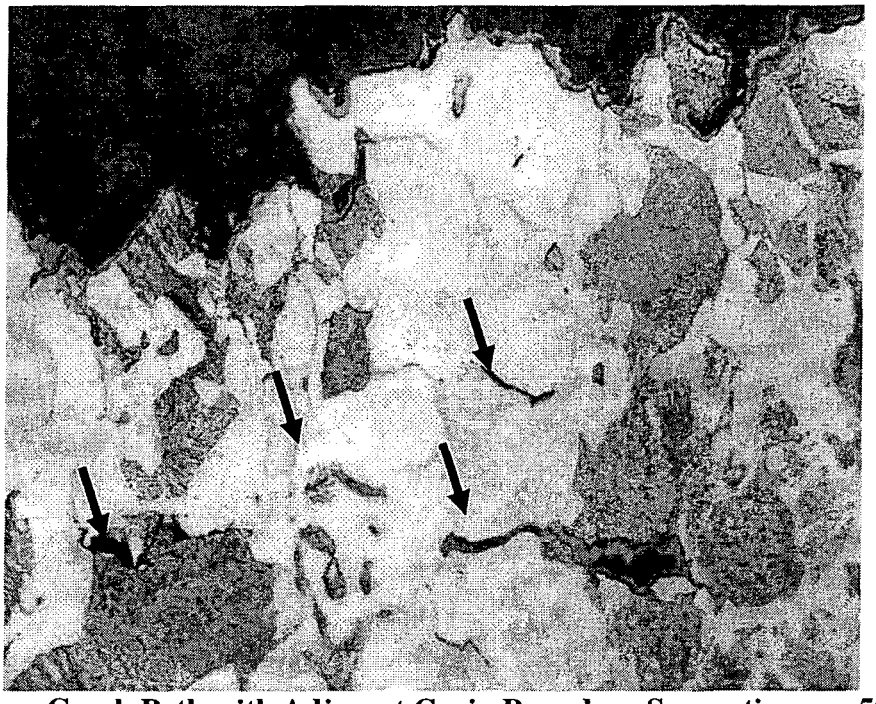

(c) Creep Crack Path with Adjacent Grain Boundary Separations 500X

Figure E-17, Cont: Test Specimen K-6 – Stress Relieved Microstructure

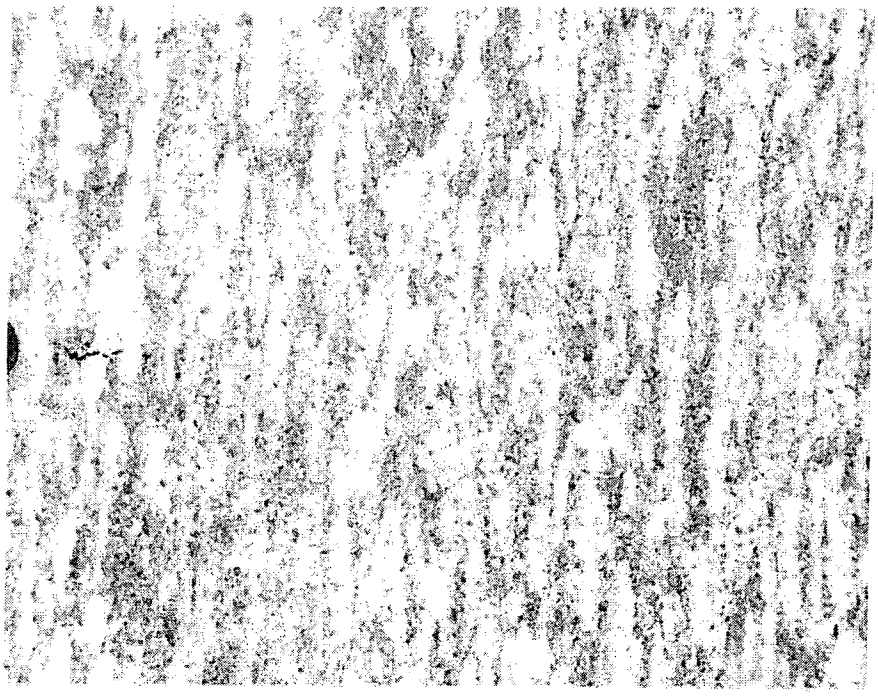

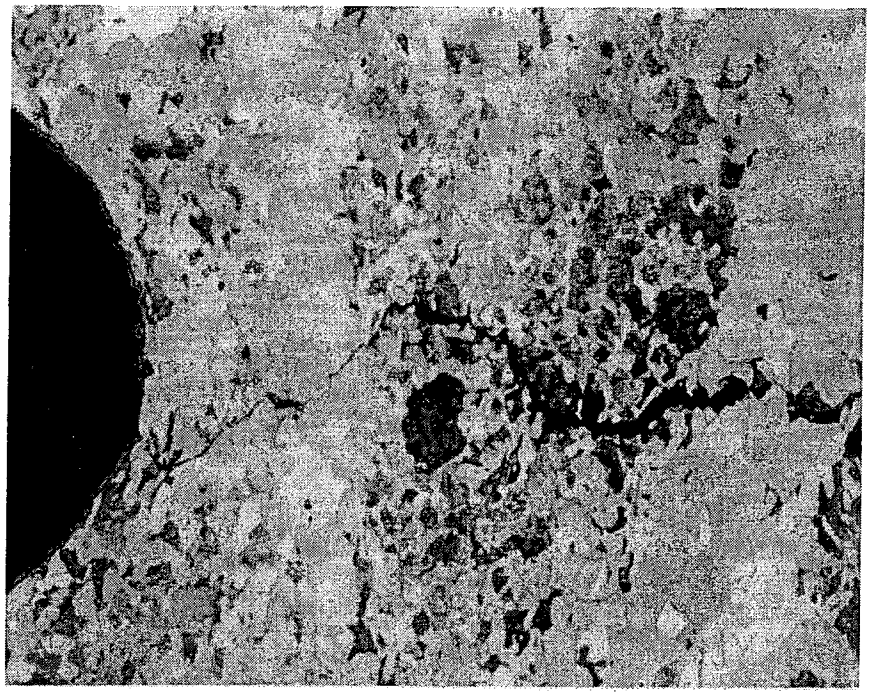

Figure E-18: Test Specimen K-7 – Stress Relieved Microstructure

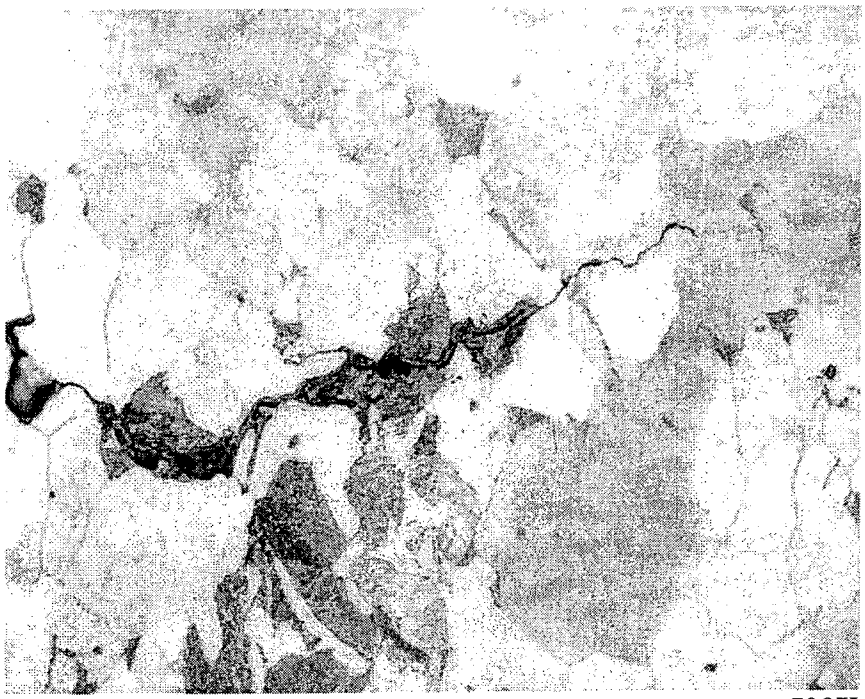

(c) Creep Crack Path **500X**

Figure E-18, Cont: Test Specimen K-7 – Stress Relieved Microstructure

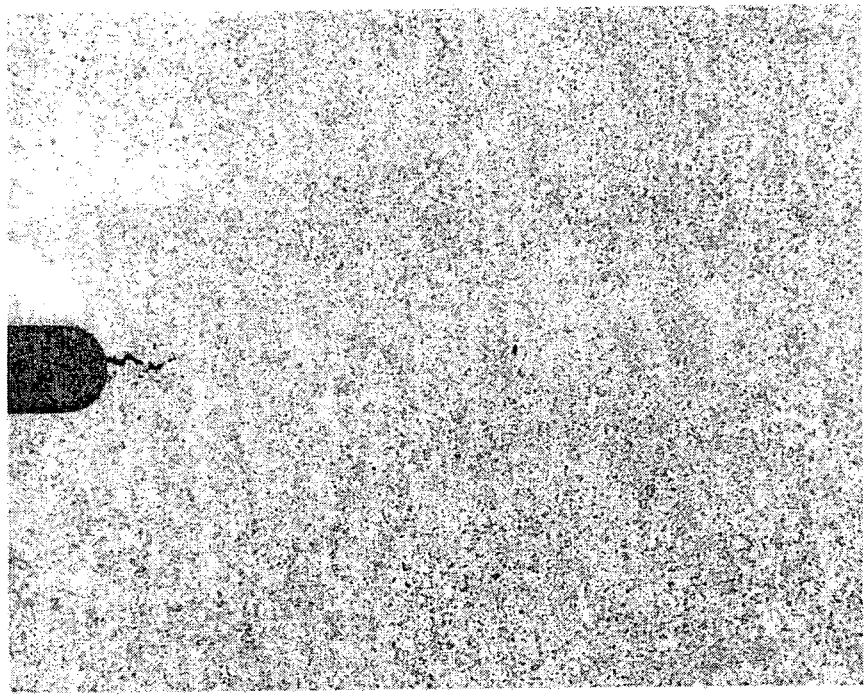

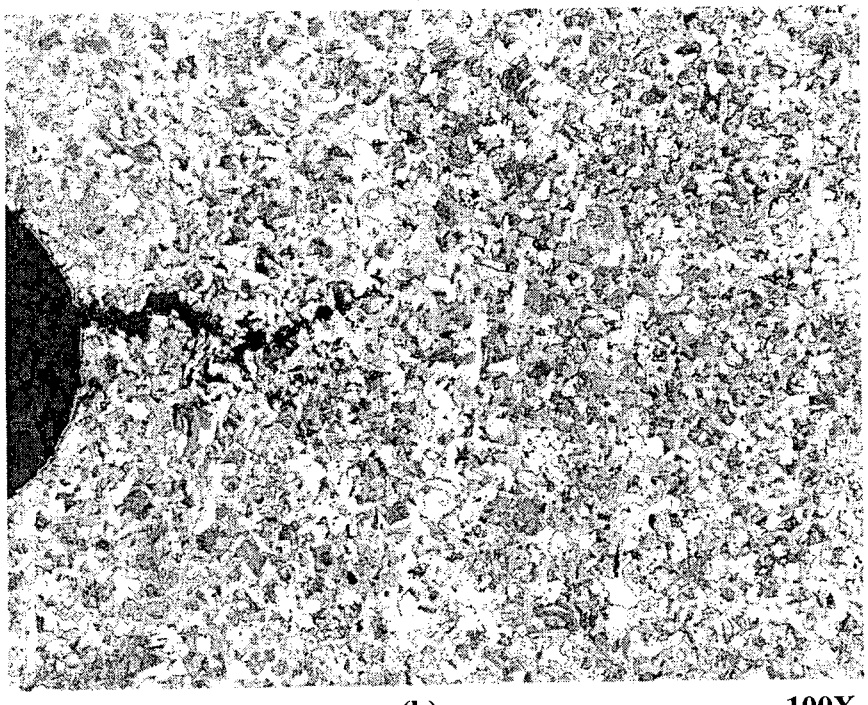

Figure E-19: Test Specimen K-11 – Normalized Microstructure

(c) Creep Crack Path 500X

Figure E-19, Cont: Test Specimen K-11 – Normalized Microstructure

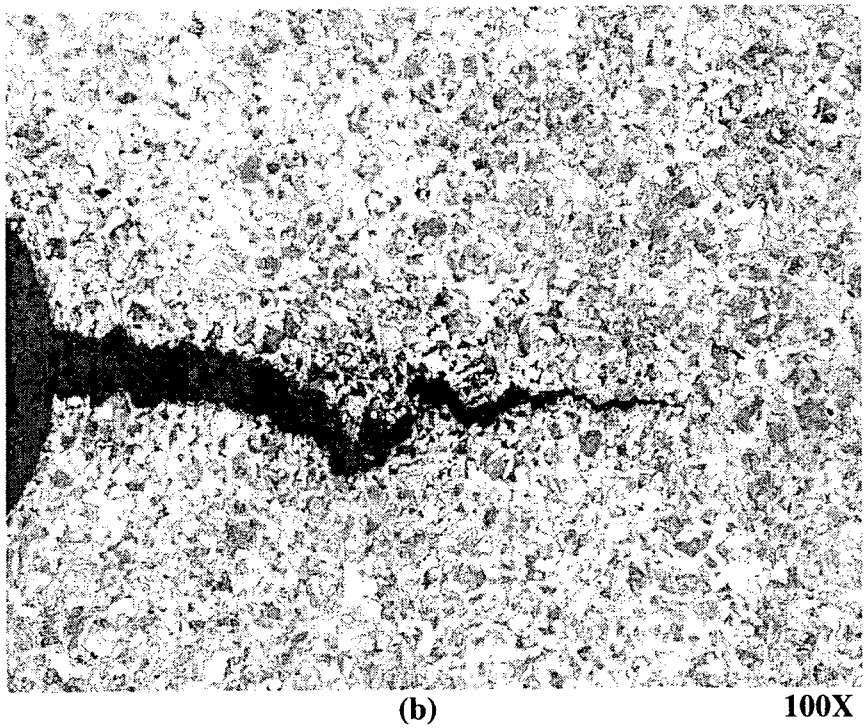

Figure E-20: Test Specimen K-12 – Normalized Microstructure

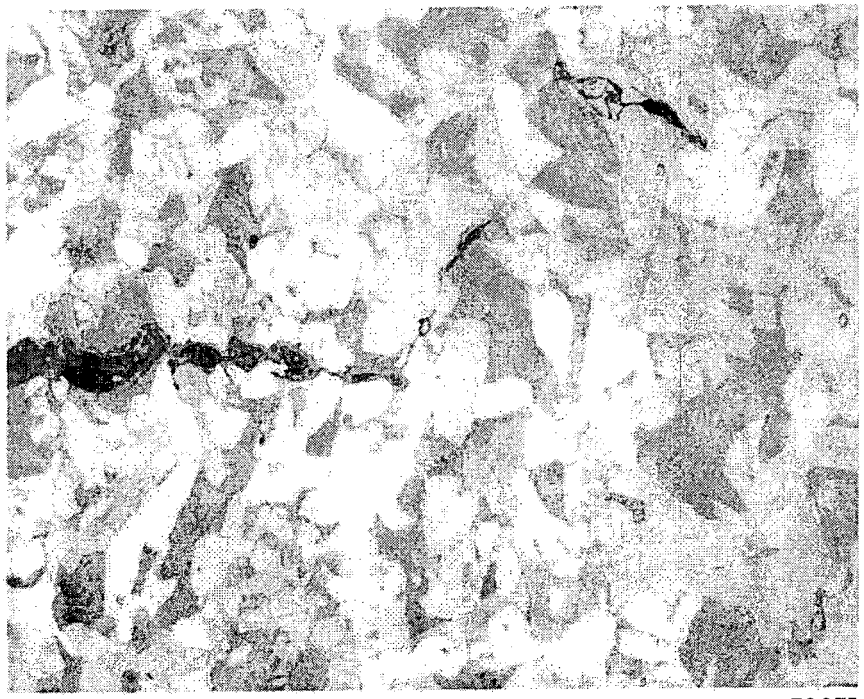

(c) Creep Crack Path **500X**

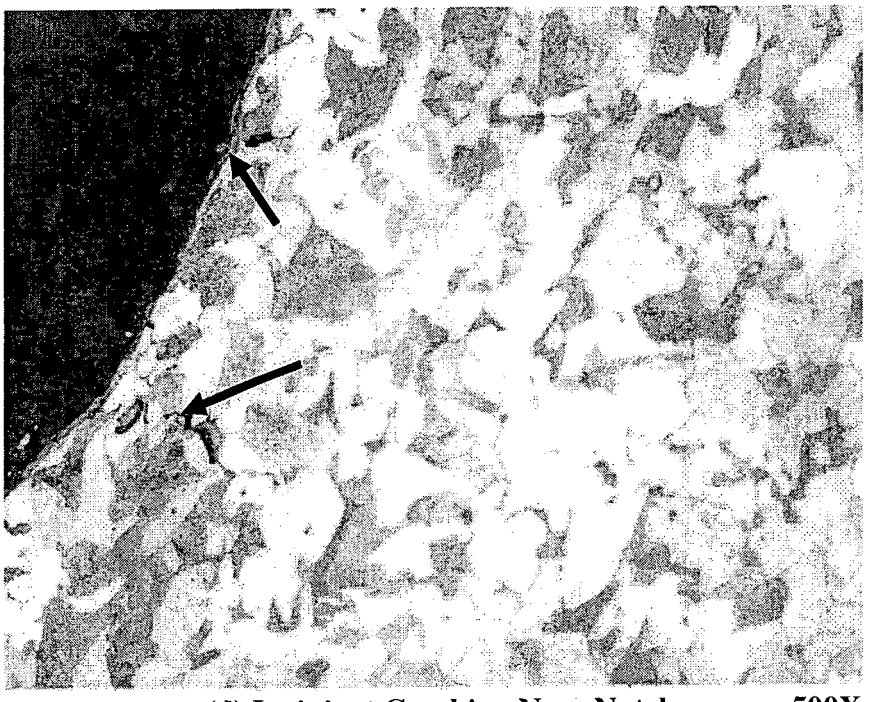

(d) Incipient Cracking Near Notch **500X**

Figure E-20, Cont: Test Specimen K-12 – Normalized Microstructure

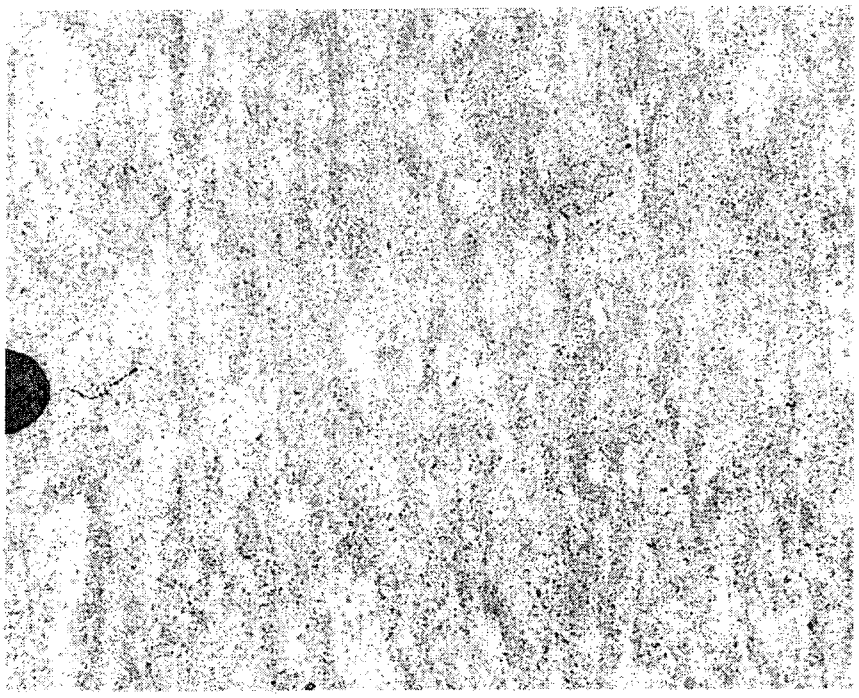

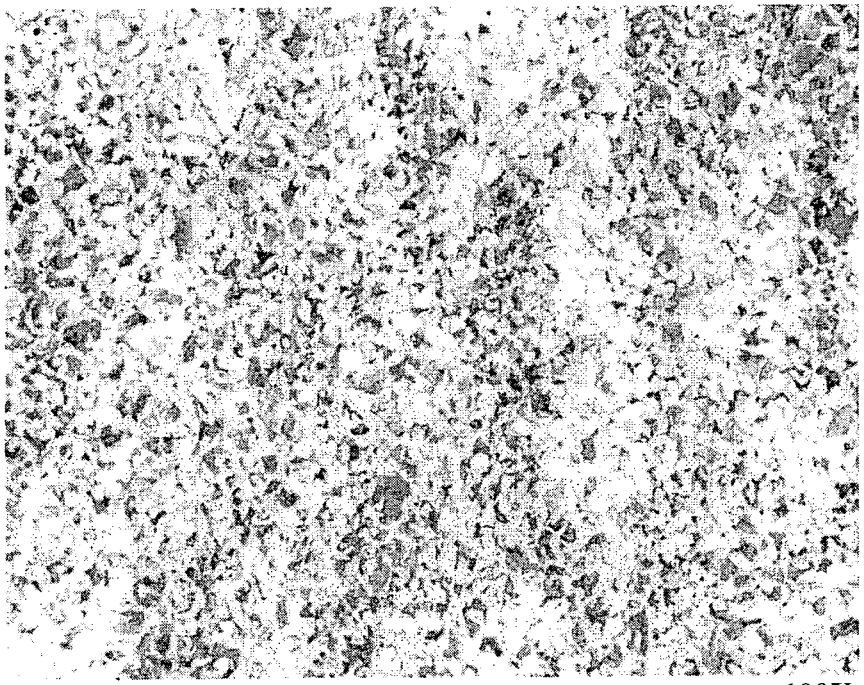

Figure E-21: Test Specimen K-19 – As-Cold Worked (10%)

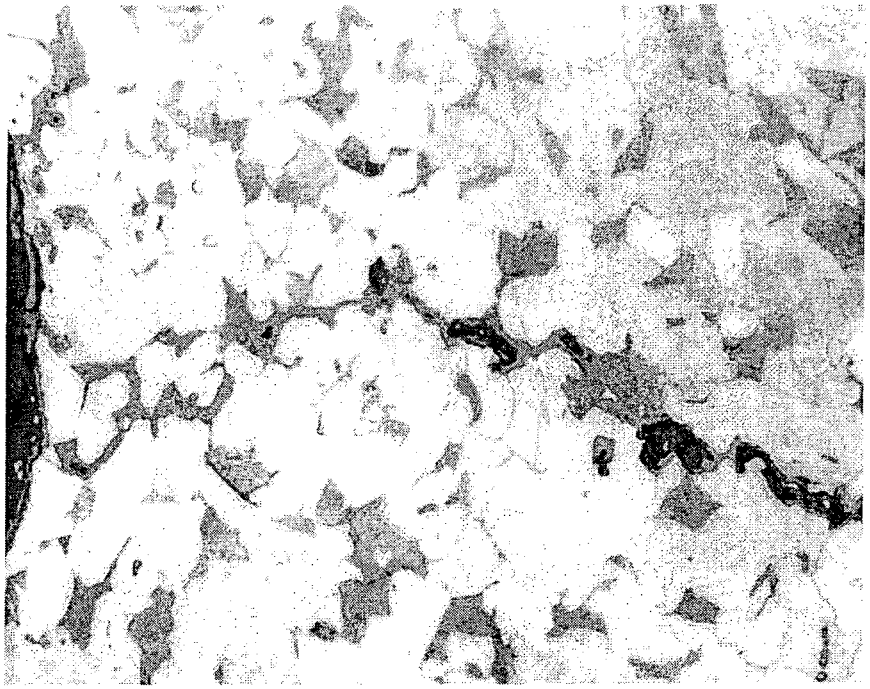

(c) Creep Crack Path 500X

Figure E-21, Cont: Test Specimen K-19 – As-Cold worked (10%)

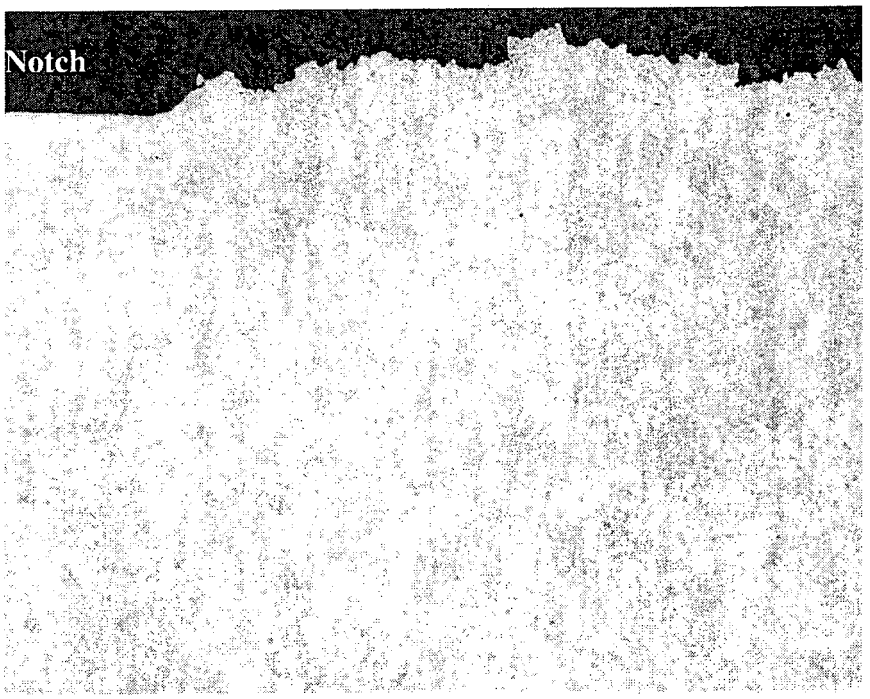

(a) 25X

(b) 100X

Long Axis of Pipe

Circumferential Direction

Figure E-22: Test Specimen K-21 – As-Cold Worked (10%)

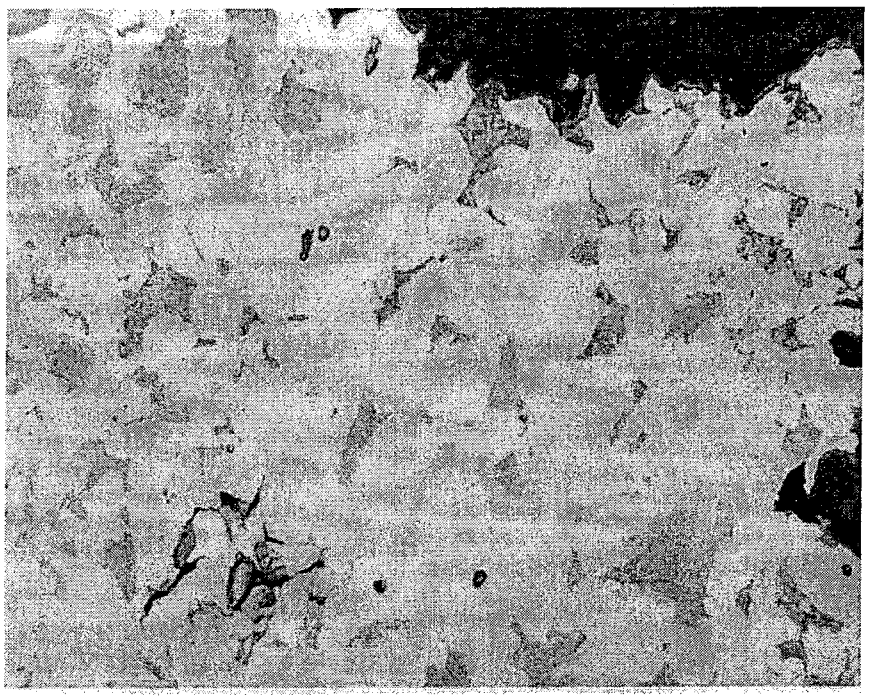

(c) Creep Crack Path with Adjacent Grain Boundary Separations 500X

Figure E-22, Cont.: Test Specimen K-21 – As-Cold worked (10%)

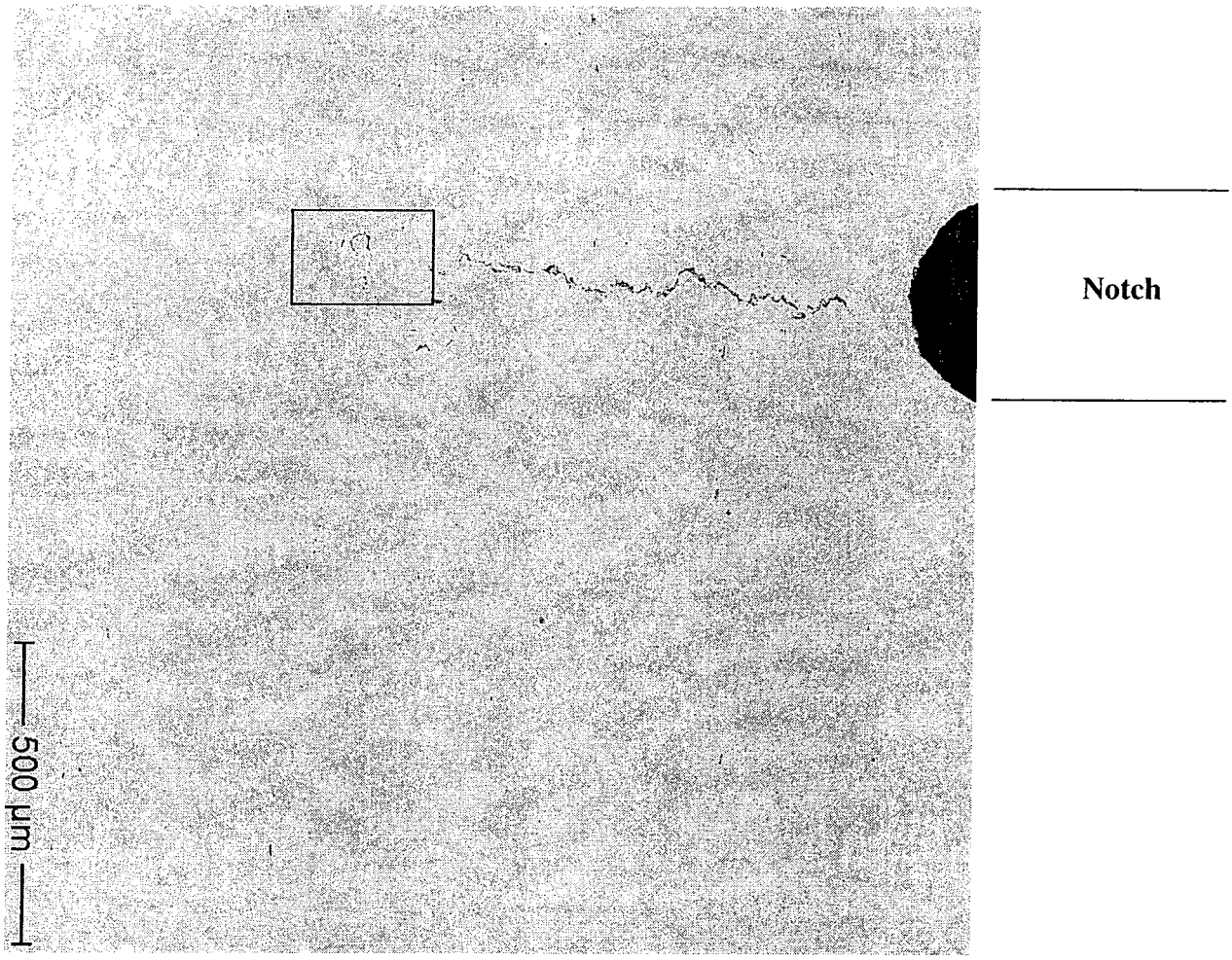

Figure E-23 Low Magnification View of Creep Crack Growth Extending From Notch for Test Specimen K-7

Note: Box indicates area shown at a higher magnification in Figure E-24

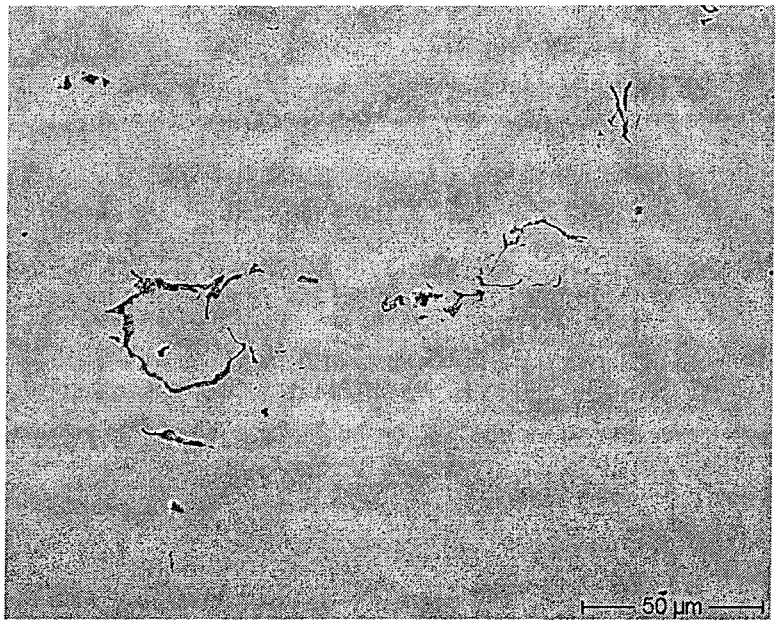

(a) 500x

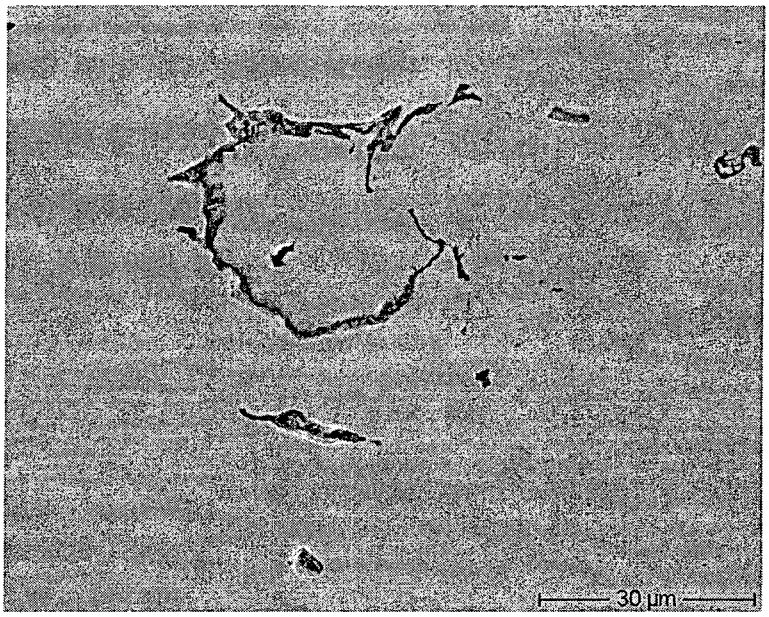

(b) 1000x

Figure E-24: Higher Magnification View of Oxide-Filled Grain Boundary Separations in Advance of the Crack Tip Shown in Figure E-23

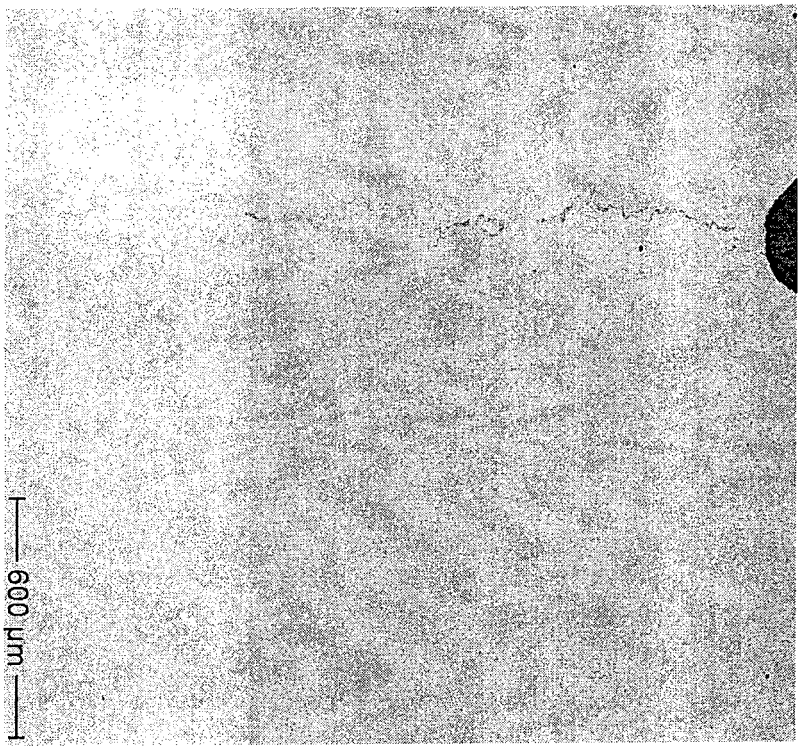

Figure E-25: Low Magnification View of Creep Crack Growth Extending from Notch for Test Specimen P-2.

(a)

(b)

Figure E-26: **Higher magnification View of Oxide-Filled Grain Boundary Separations in Advance of the Crack Tip Shown in Figure E-25**

Note: Box in Figure E-26a shows location of higher magnification view shown in Figure E-26b.

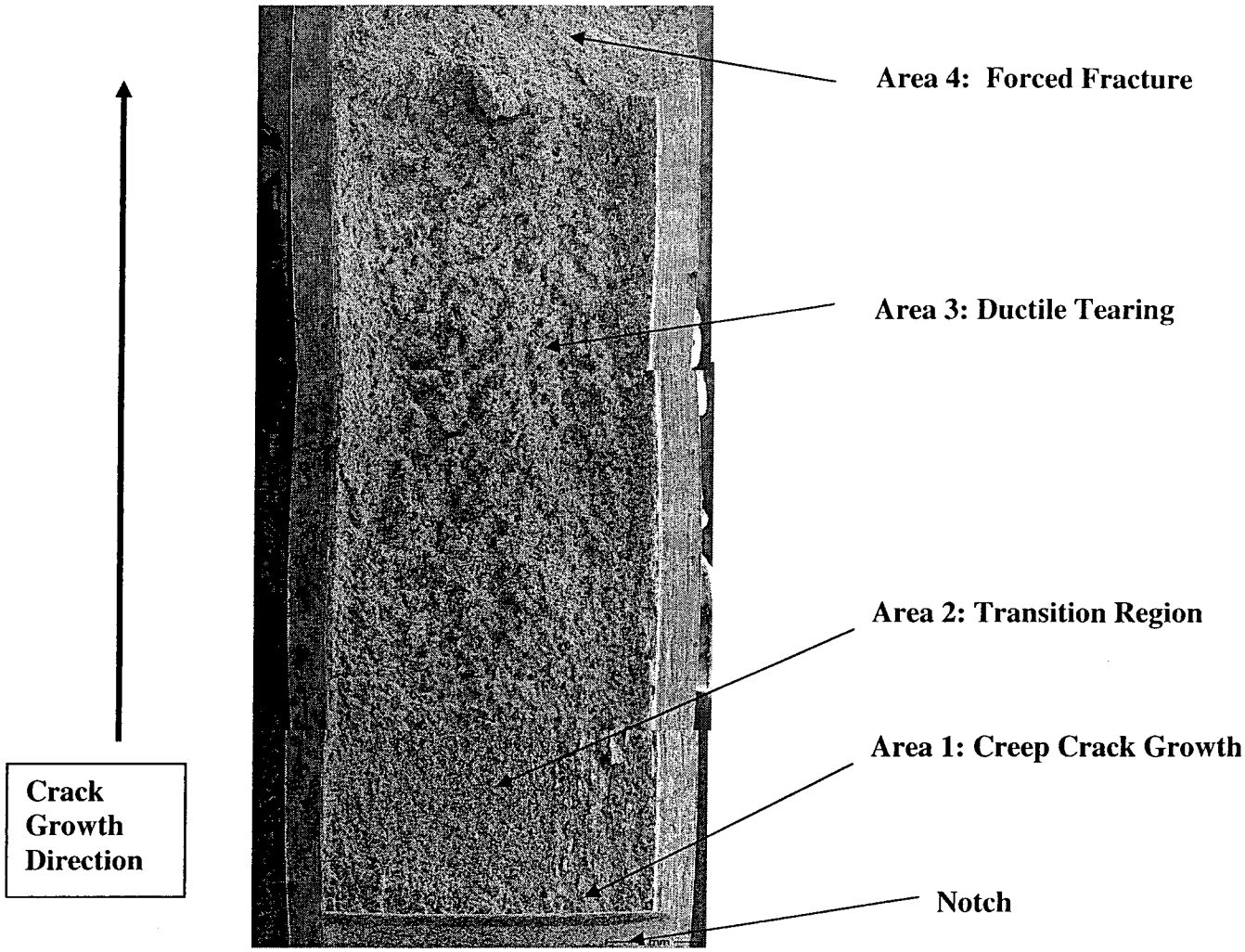

Figure E-27: Features of Fracture Surface That Exhibited CCG Then Tearing

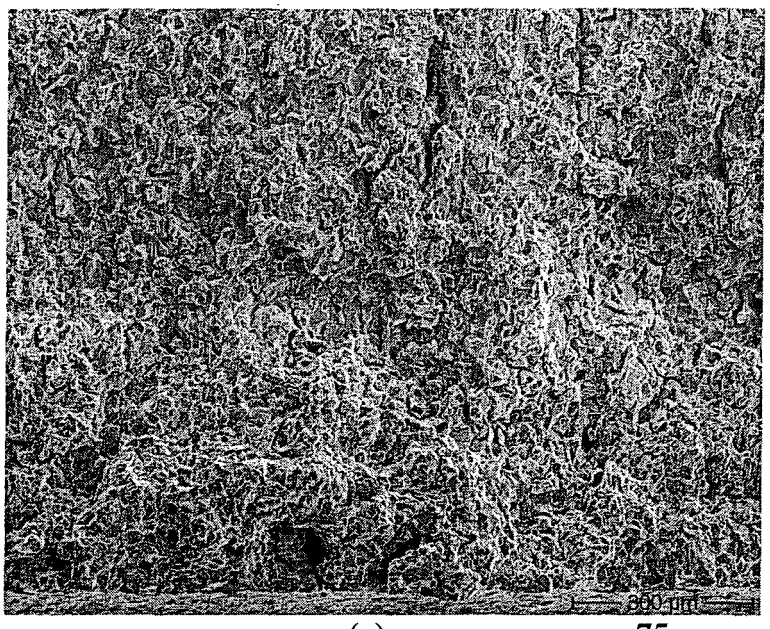

(a) 75x

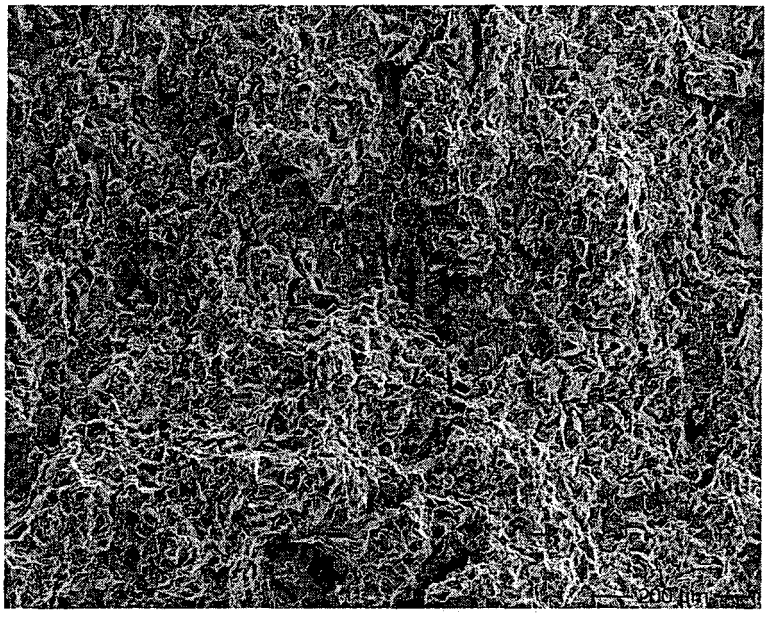

(b) 100x

Figure E-28:

Progressively Higher Magnification Views of Area 1 – Predominantly Intergranular With Only Limited Ductility.

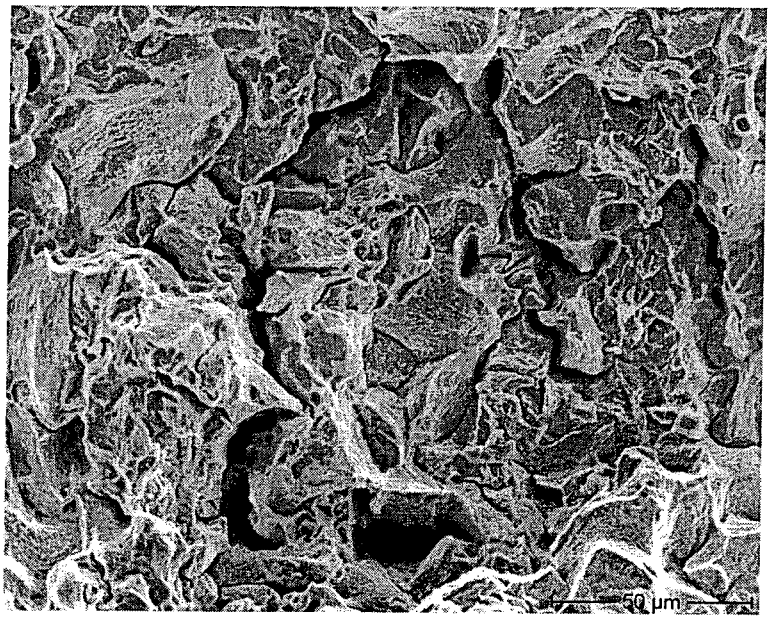

(c) 500x

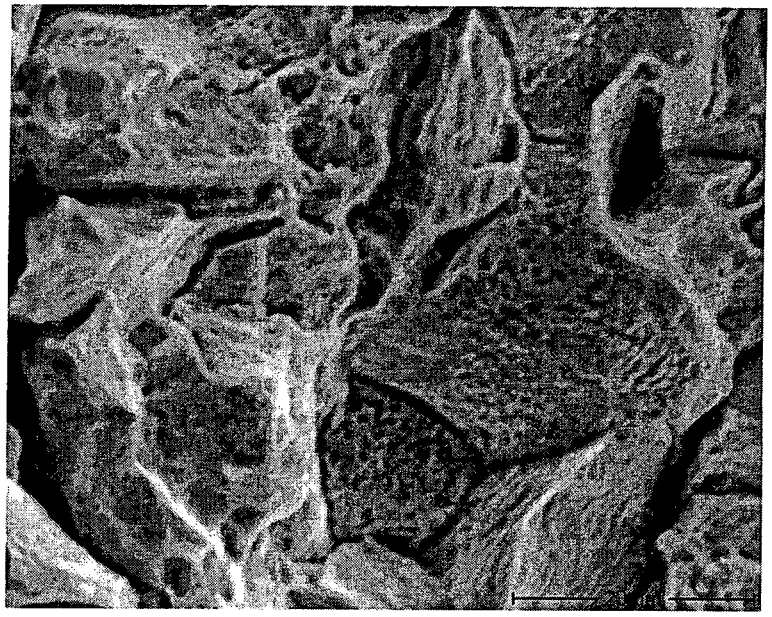

(d) 1500x

Figure E-28, Cont.:

Progressively Higher Magnification Views of Area 1 – Predominantly Intergranular With Only Limited Ductility.

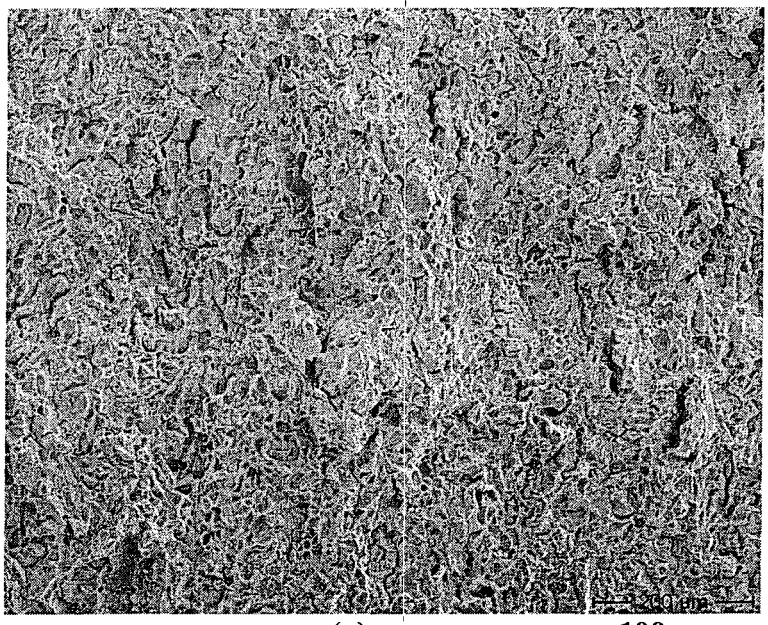

(a) 100x

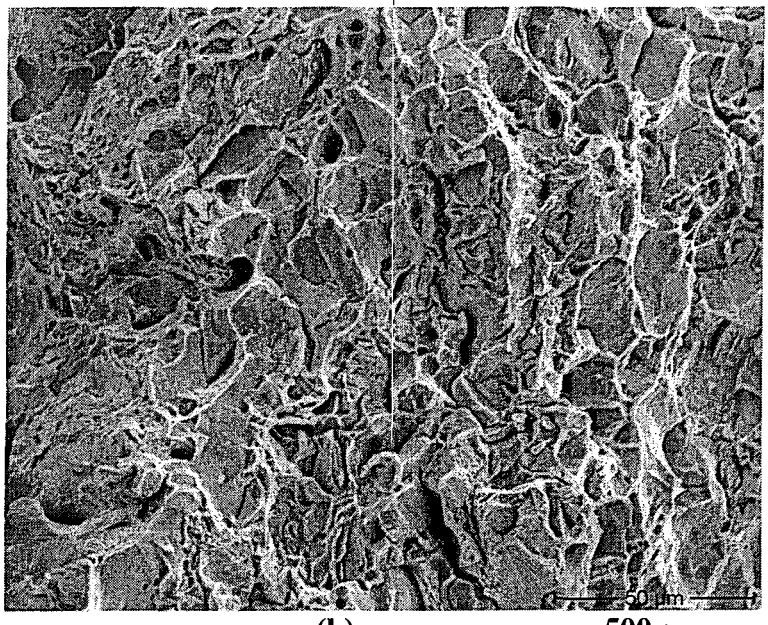

(b) 500x

Figure E-29:
Progressively Higher Magnification Views of Area 2 – Mostly Intergranular With Local Regions of Ductility.

Note: Local ductility is best seen at 500X,

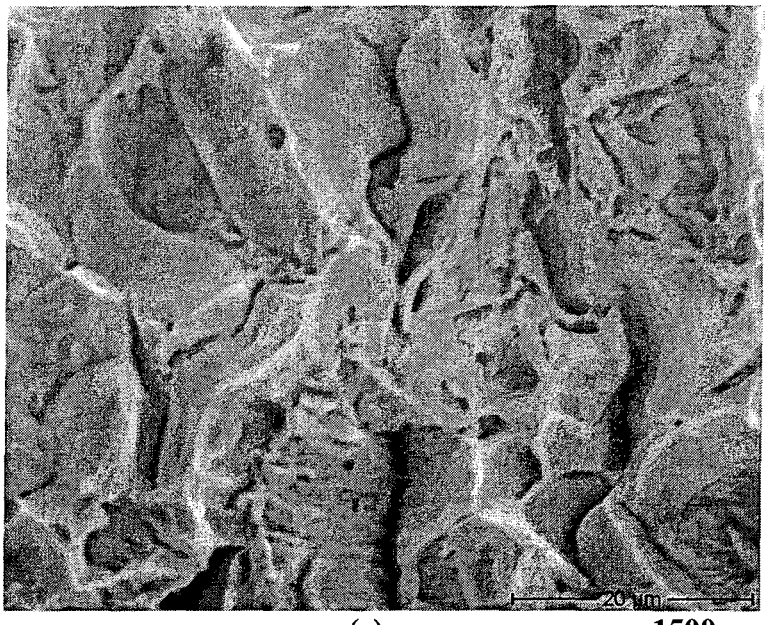

(c) 1500x

Figure E-29, Cont. :

Progressively Higher Magnification Views of Area 2 – Intergranular With Somewhat More Ductility.

Note: Local ductility is best seen at 500X,

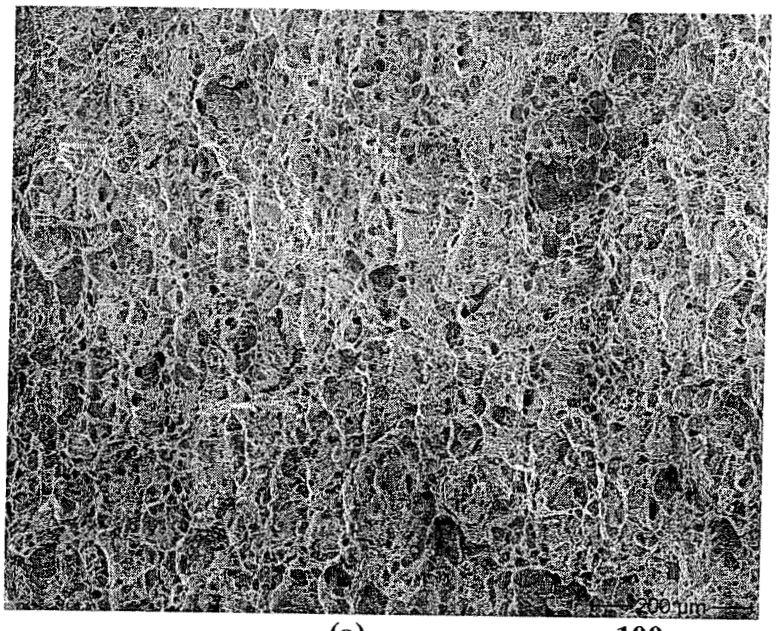

(a) 100x

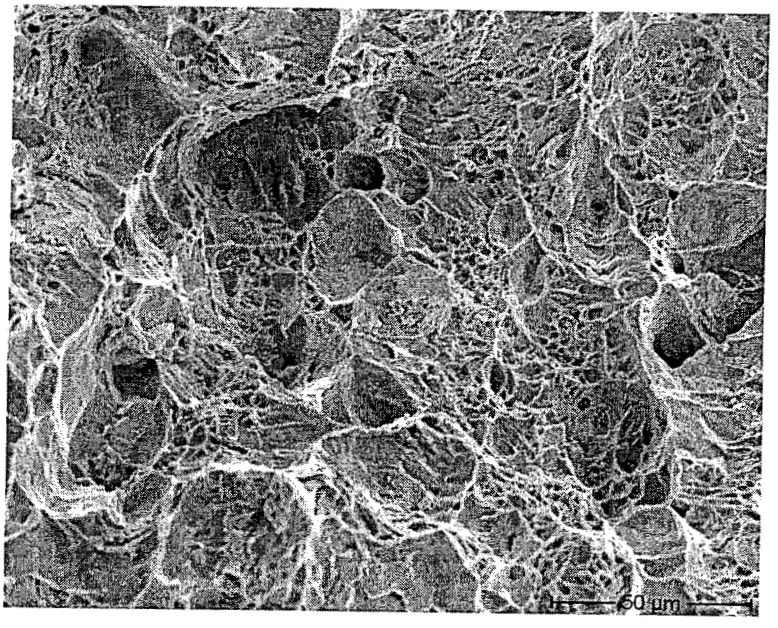

(b) 500x

Figure E-30:

Progressively Higher Magnification Views of Area 3 – Predominantly ductile

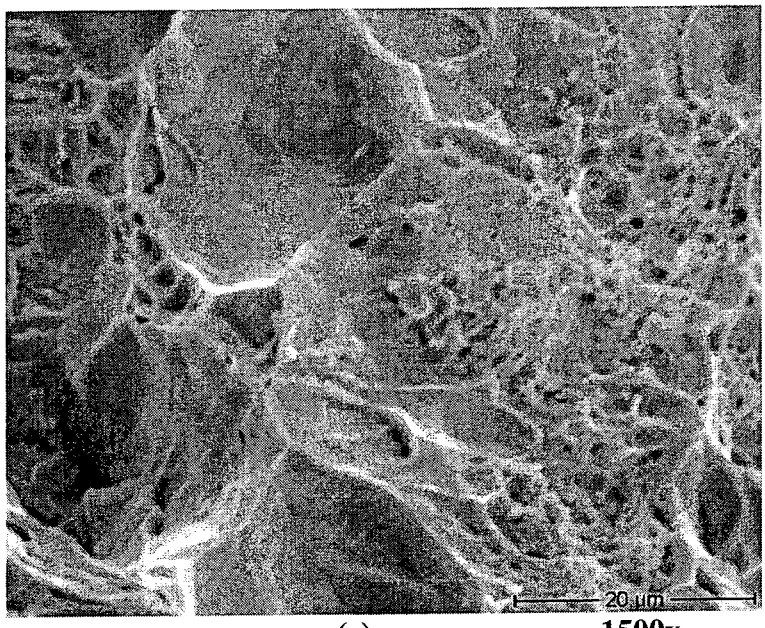

(c) 1500x

Figure E-30, Cont.

Progressively Higher Magnification Views of Area 3 – Predominantly ductile

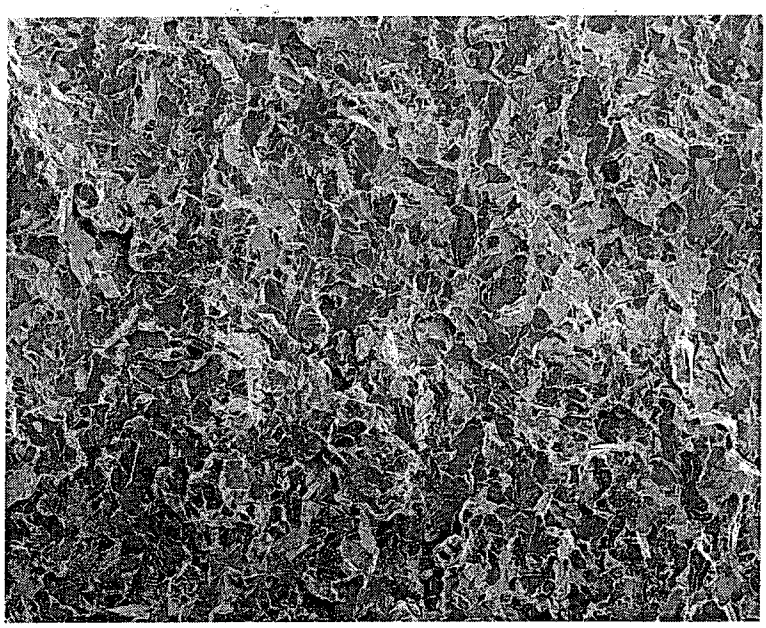

(a) 100x

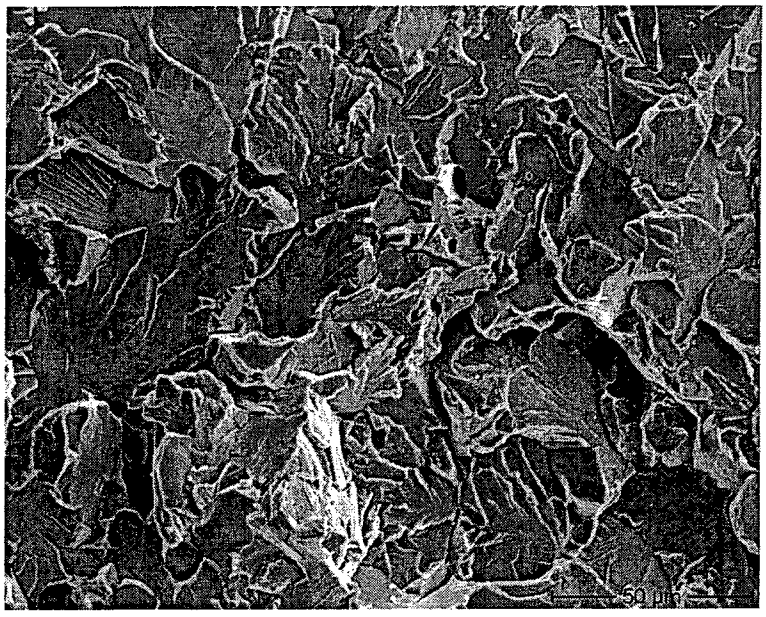

(b) 500x

Figure E-31:

Progressively Higher Magnification Views of Area 4 – Cleavage

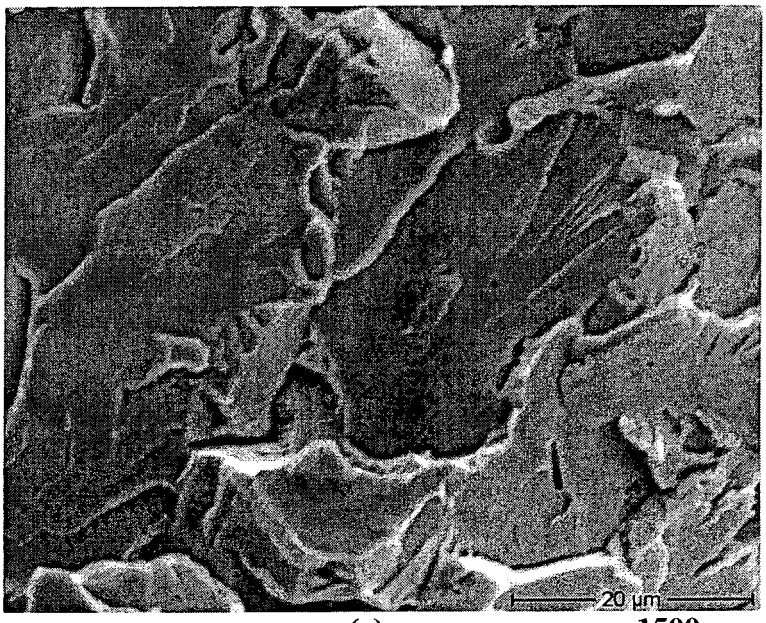

(c) 1500x

Figure E-31, Cont.:

Progressively Higher Magnification Views of Area 4 – Cleavage

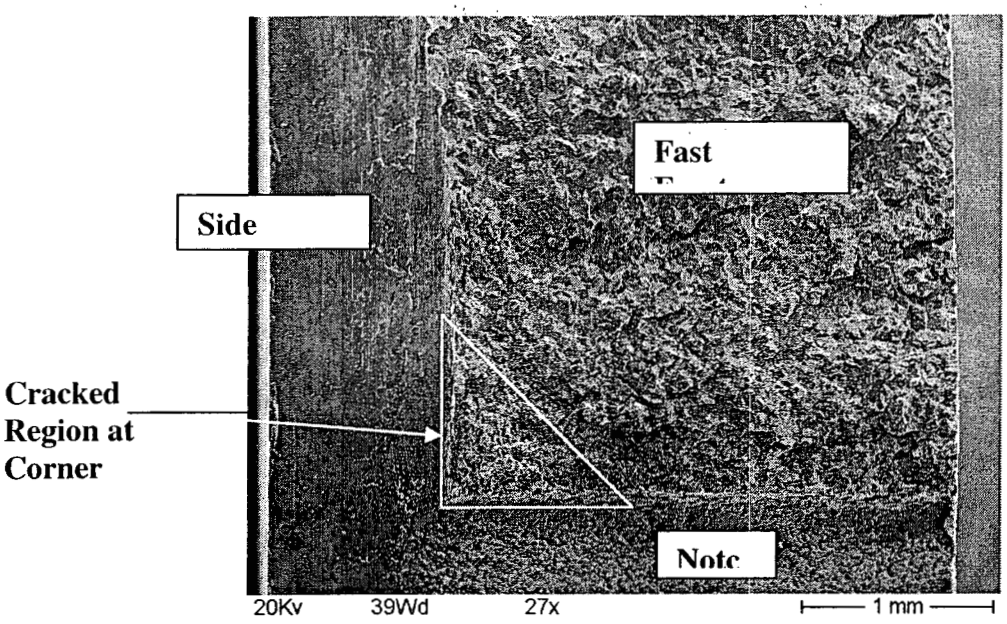

Figure E-32a: Corner Crack at Intersection of Side Groove and Notch

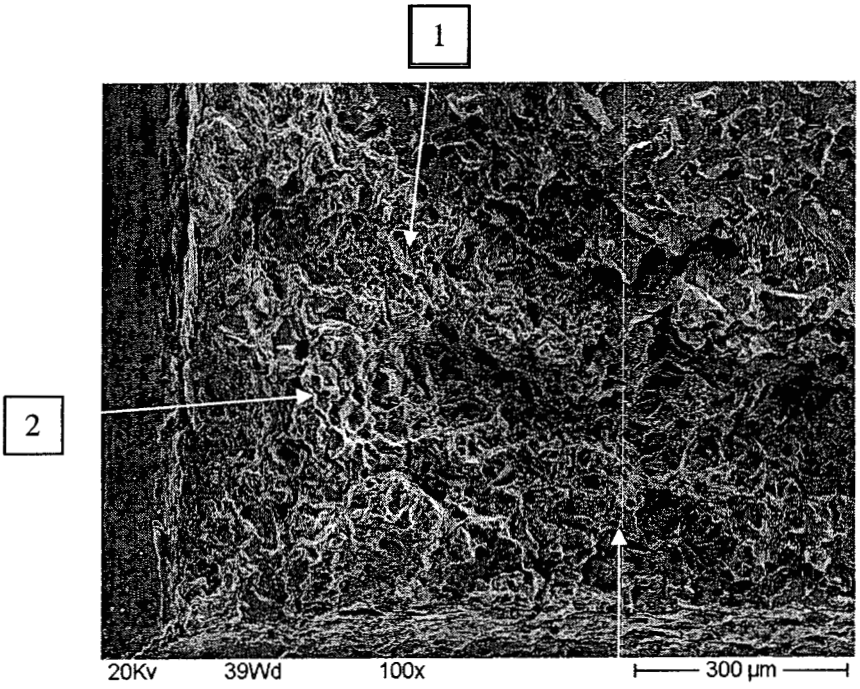

Figure E-32b: Higher Magnification View of Corner Highlighted Above

Note: Numbered areas are shown at higher magnification in Figure E-32.

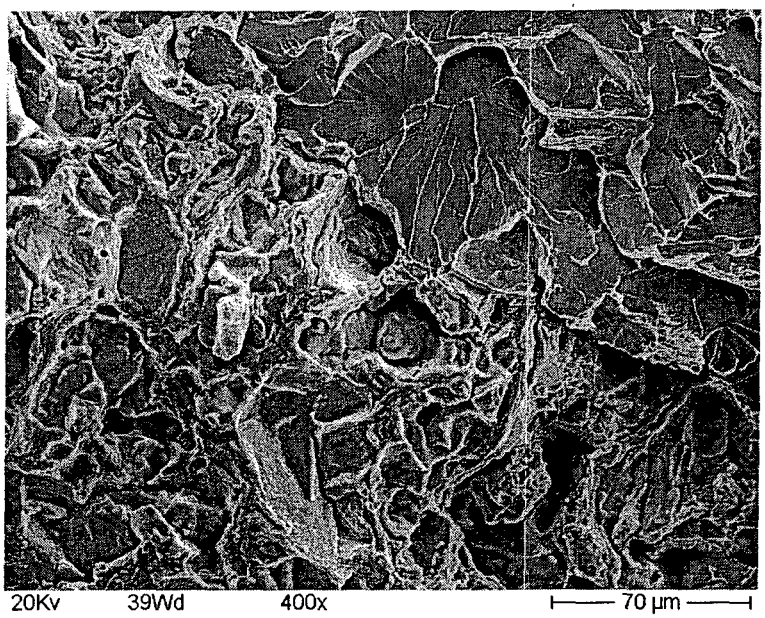

a) Area 1 – Transition to Cleavage

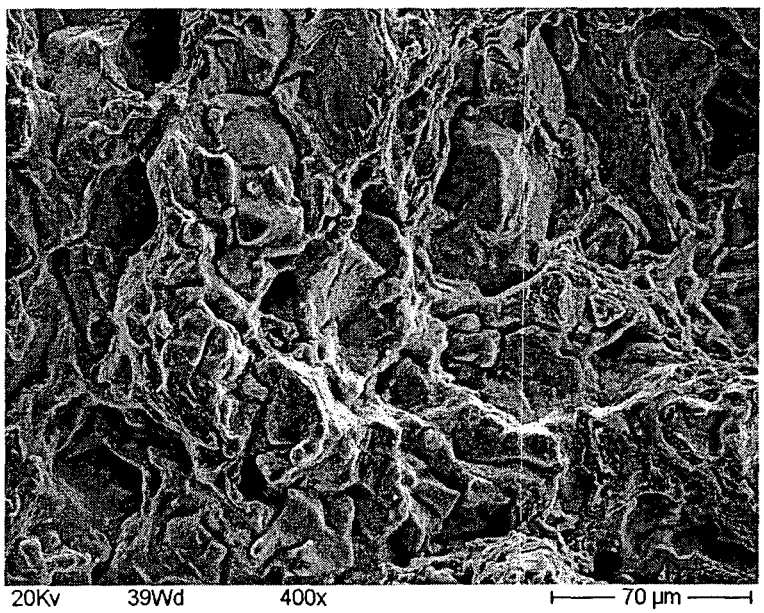

b) Area 2 – Intergranular Typical of Creep Crack Growth

Figure E-33: Appearance of Fracture Surface in Corner Crack

Note: Compare Area 2 fracture surface with that shown in Figure E-28c or with E-29c

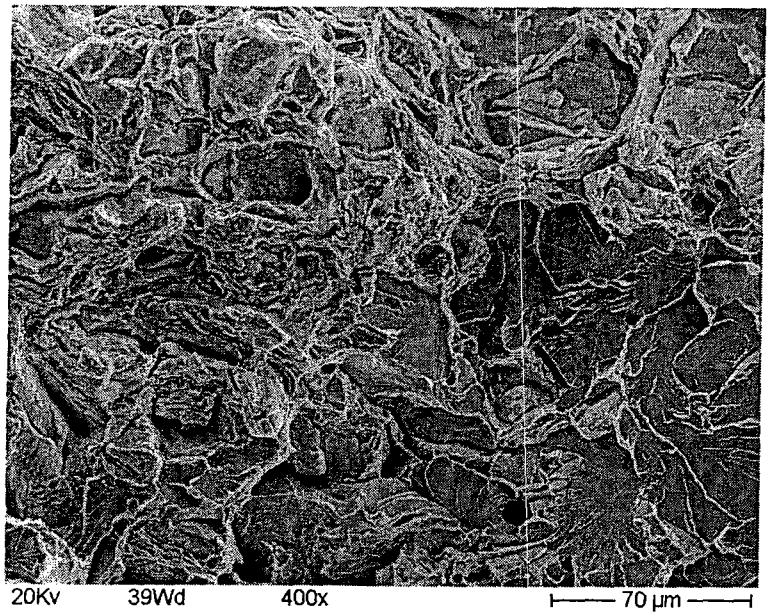

c) Area 3 – Transition to Cleavage

Figure E-33, Cont.: Appearance of Fracture Surface in Corner Crack

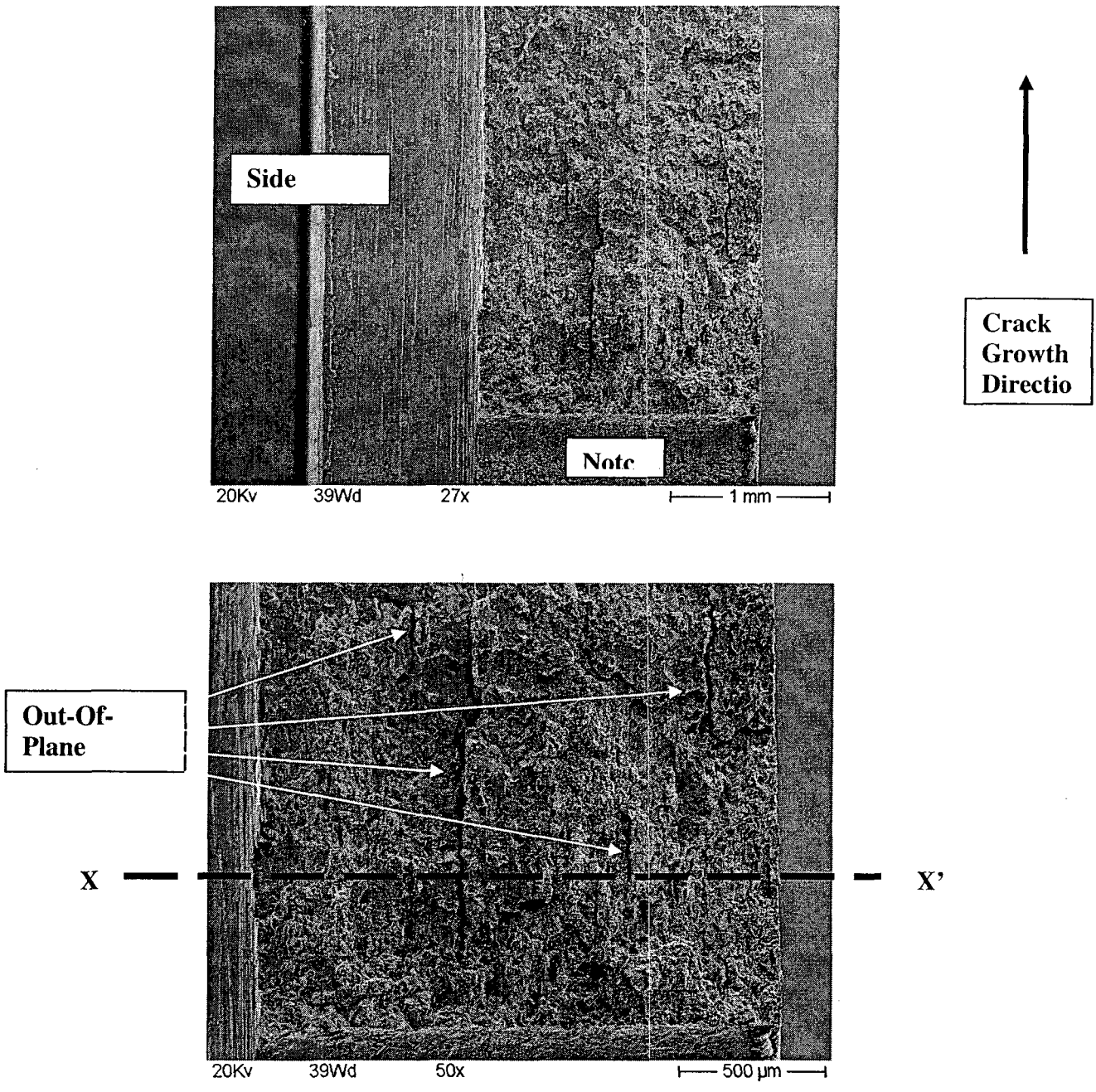

Figure E-34: Discontinuous Crack Front in Sample K-3 with Out-Of-Plane Cracking

Note: The X-X' line shows the plane sectioned and polished to examine the microstructure associated with the out-of-plane cracks.

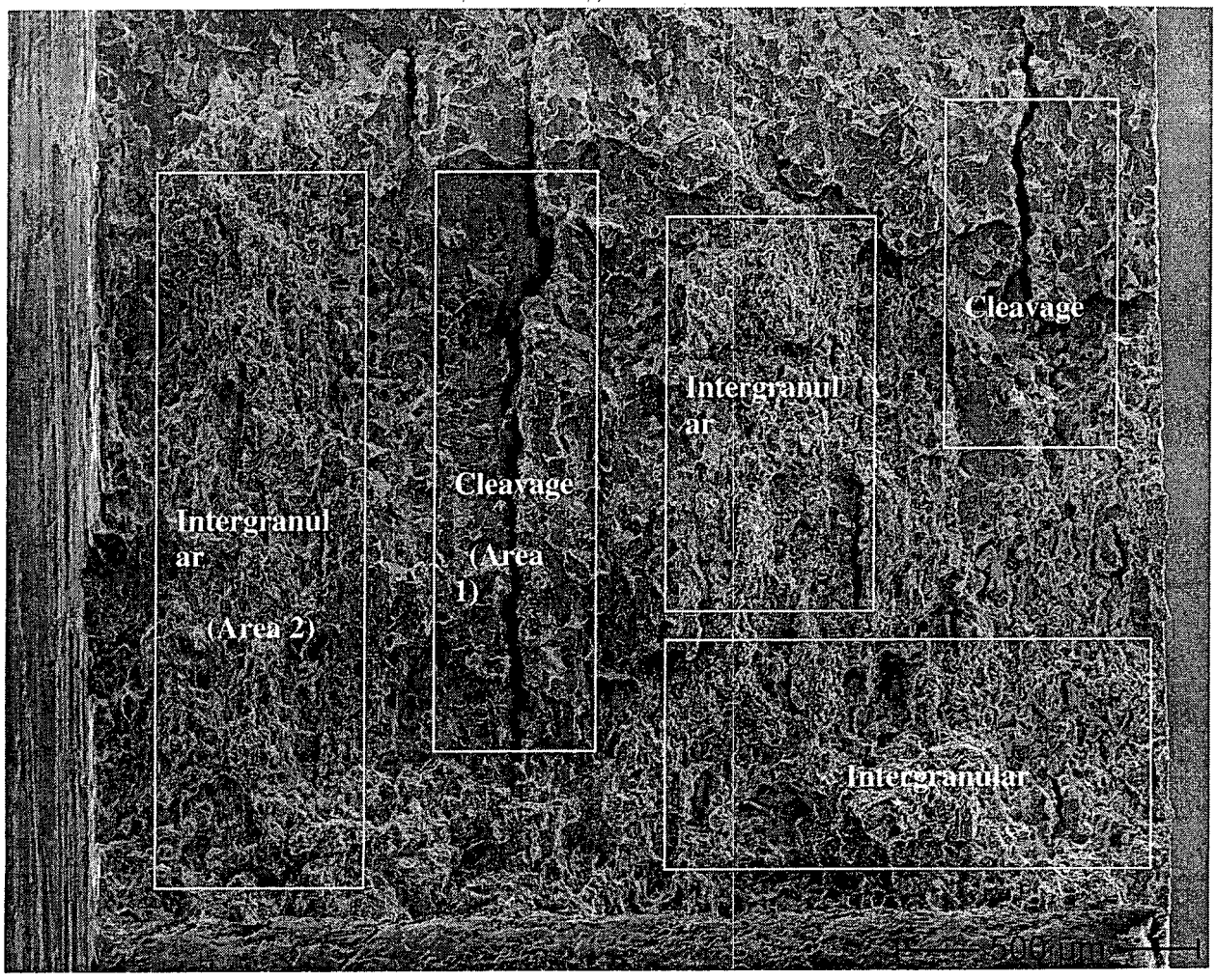

Figure E-35: Higher Magnification View of Fracture Surface Showing Discontinuous Nature of Fracture Appearance

Note: Also indicated are the two areas that are shown at higher magnification in the figures that follow

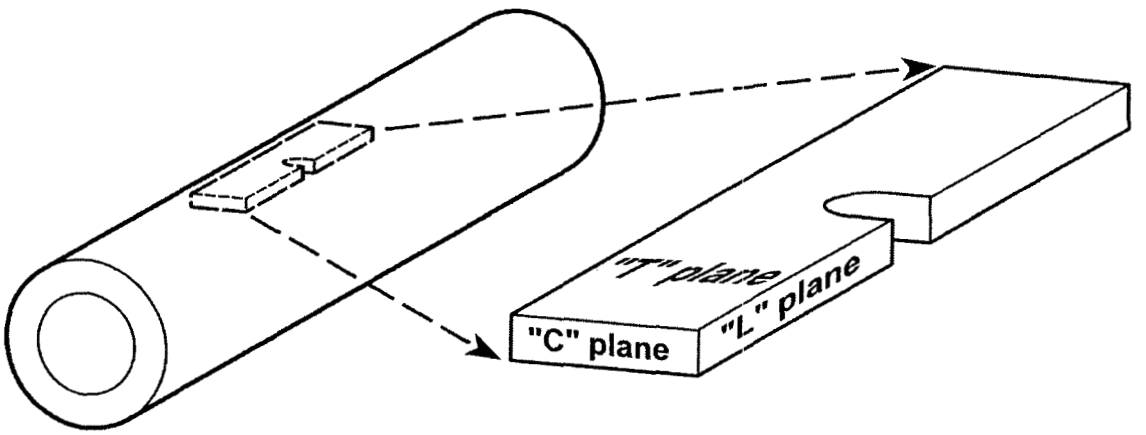

Figure E-36 Schematic Depicting the Creep Test Specimen Orientation Relative to Pipe

Note:

1. Test cracks grew along the circumferential "C" plane.
2. Service failures cracked along the longitudinal "L" plane.
3. The microstructures in Figures E-1 through E-22 were developed by polishing down on the tangential "T" plane.

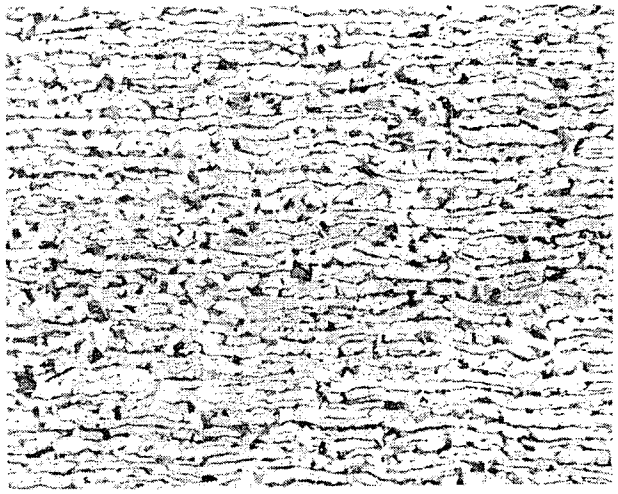

Test Cracks Follow This Plane From Left to Right

(a) Circumferential

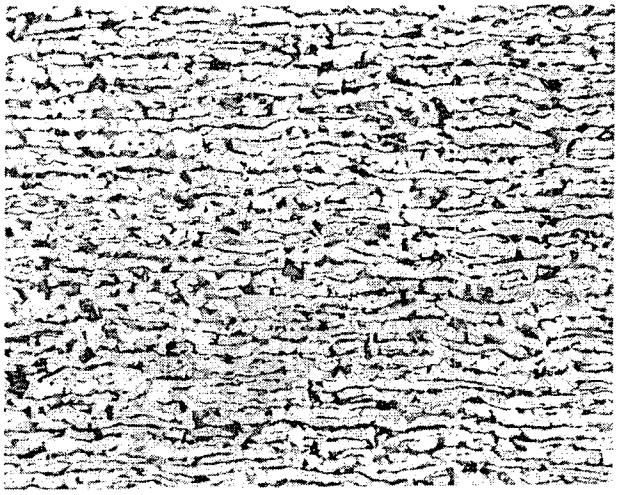

Service Failures Follow This Plane From Top to Bottom.

Test Cracks Run Perpendicular to This Plane Cutting Across Bands.

(b) Longitudinal

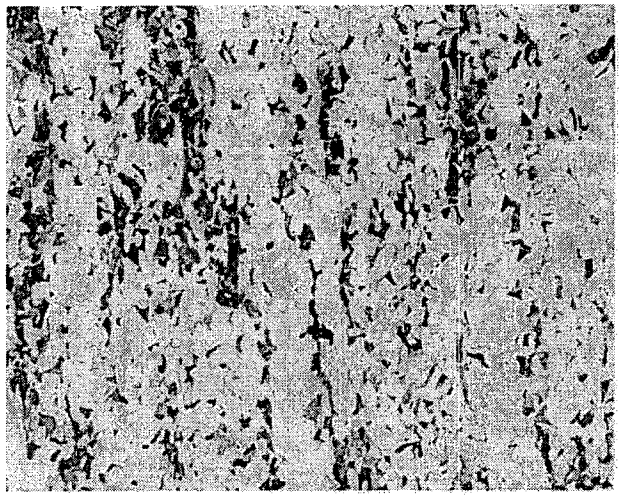

Test Cracks Grow Across This Plane From Left to Right

(c) Tangential

Figure E-37 Microstructure of As-Cold Worked Sample M-2

Test Cracks Follow This Plane From Left to Right

(a) Circumferential

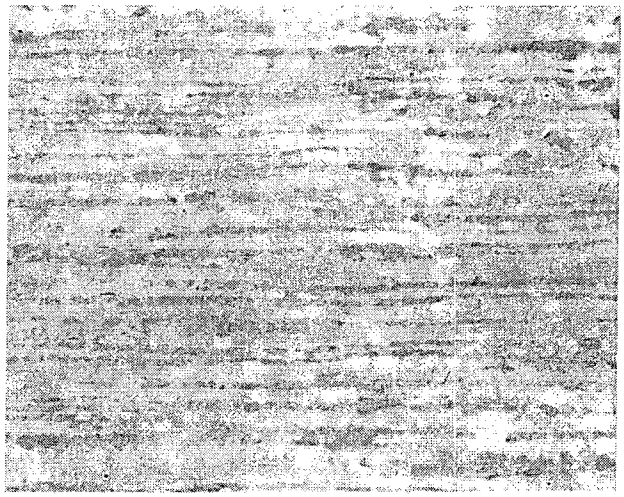

Service Failures Follow This Plane From Top to Bottom.

Test Cracks Run Perpendicular to This Plane Cutting Across Bands.

Out-Of-Plane Cracks Were Parallel to Bands

(d) Longitudinal

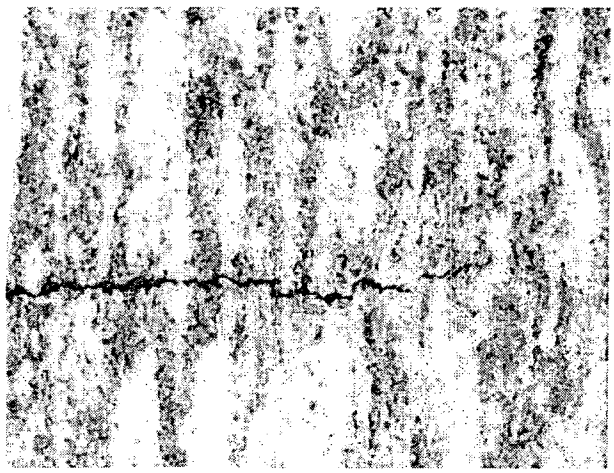

Test Cracks Grow Across This Plane From Left to Right

(e) Tangential

Figure E-38 Microstructure of As-Cold Worked Sample K-3

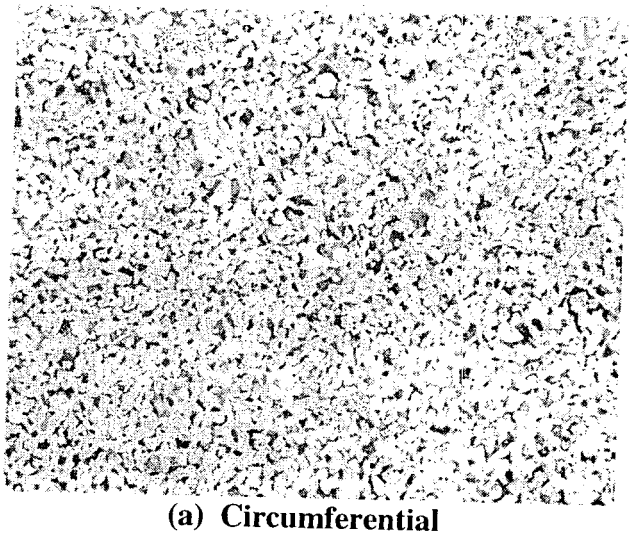

Test Cracks Follow This Plane From Left to Right

(a) Circumferential

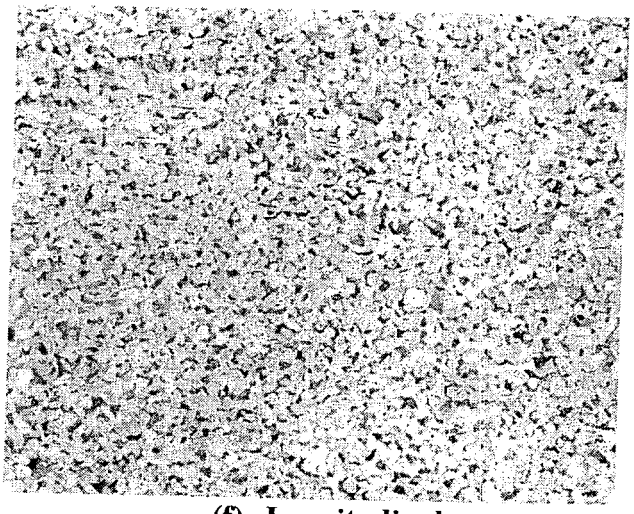

Service Failures Follow This Plane From Top to Bottom.

Test Cracks Run Perpendicular to This Plane Cutting Across Bands.

(f) Longitudinal

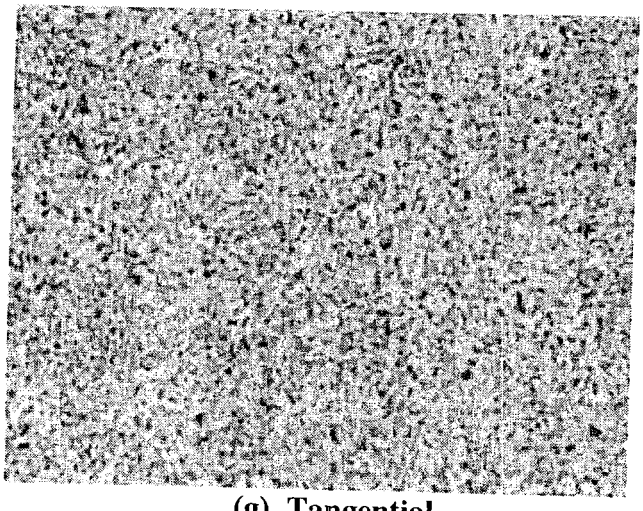

Test Cracks Grow Across This Plane From Left to Right

(g) Tangential

Figure E-39 Microstructure of As-Cold Worked Sample O-2

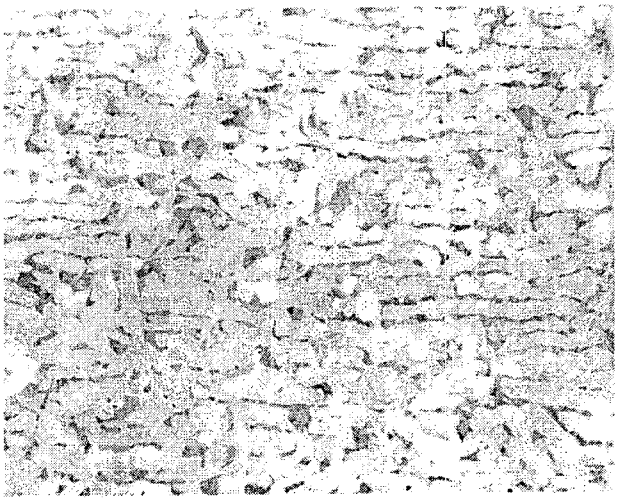

Test Cracks Follow This Plane From Left to Right

(a) Circumferential

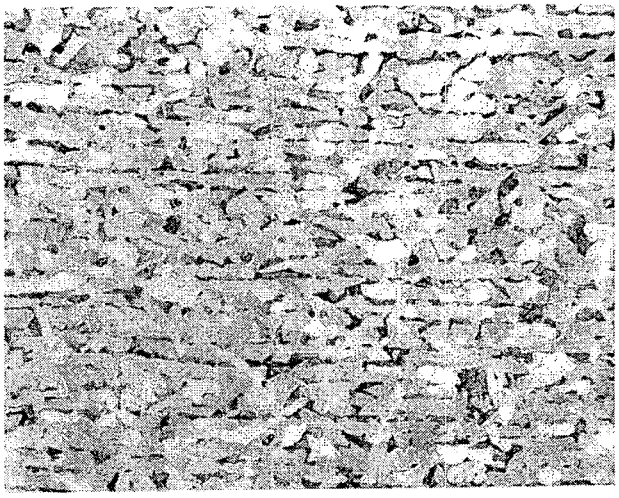

Service Failures Follow This Plane From Top to Bottom.

Test Cracks Run Perpendicular to This Plane Cutting Across Bands.

(h) Longitudinal

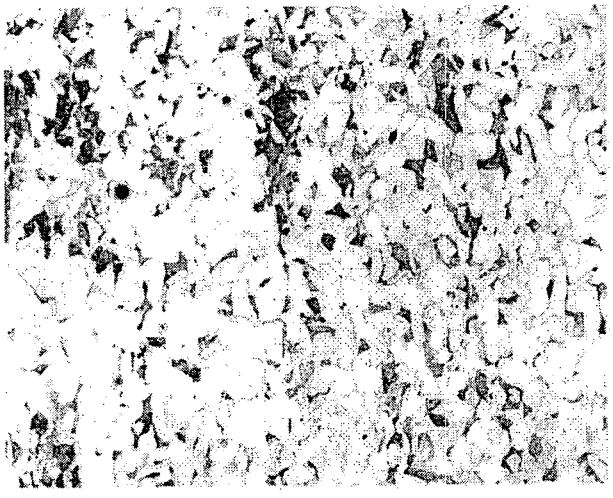

Test Cracks Grow Across This Plane From Left to Right

(i) Tangential

Figure E-40 Microstructure of As-Cold Worked Sample P-2

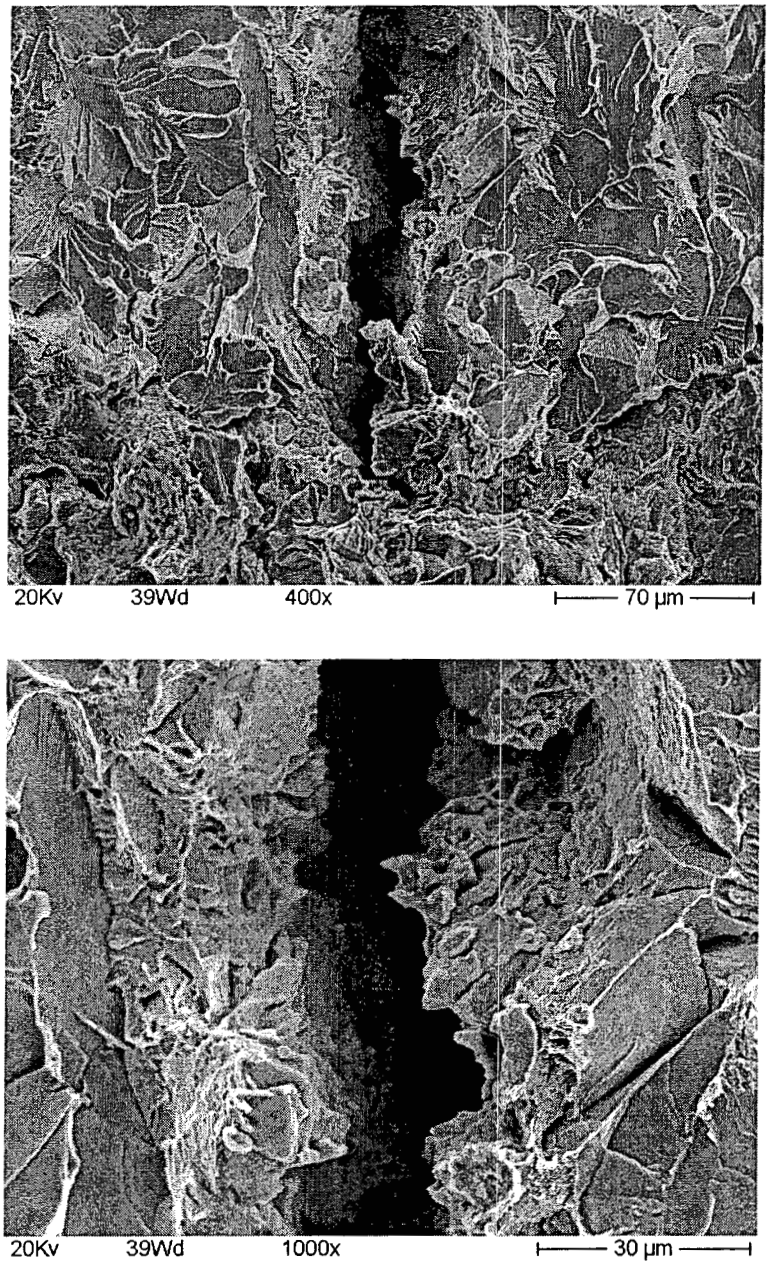

Figure E-41 Cleavage Fracture Adjacent to Out-Of-Plane Cracks, (Area 1, Figure E-35)

Note: Out-of-plane fracture surfaces appear intergranular.

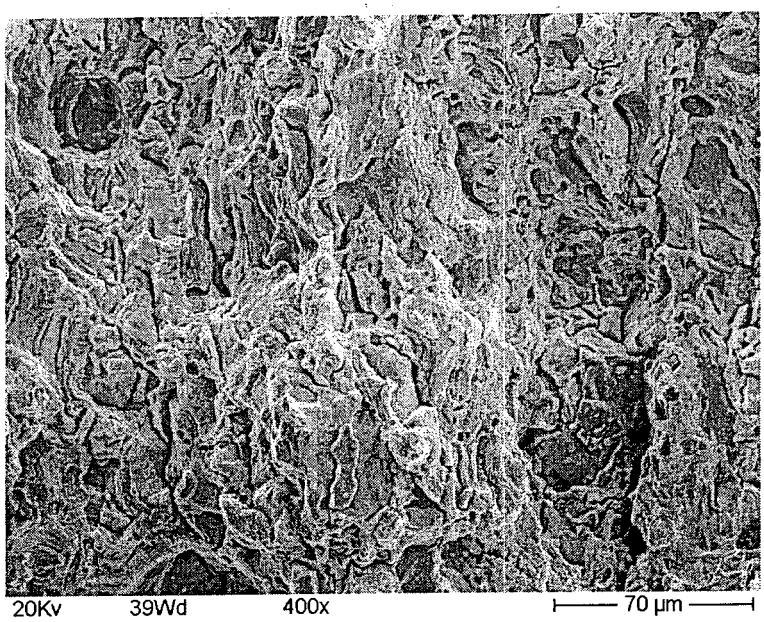

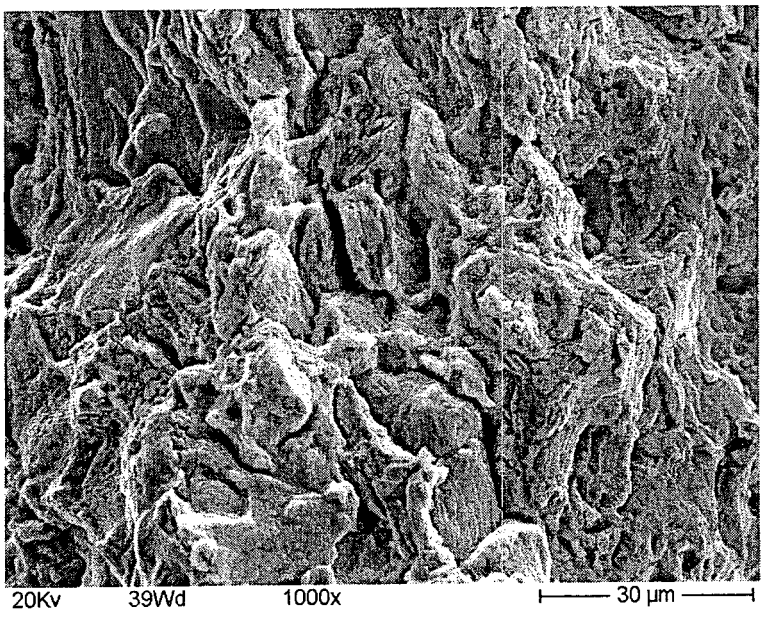

Figure E-42 Creep Mode Fracture Appearance, Area 2, Figure E-35

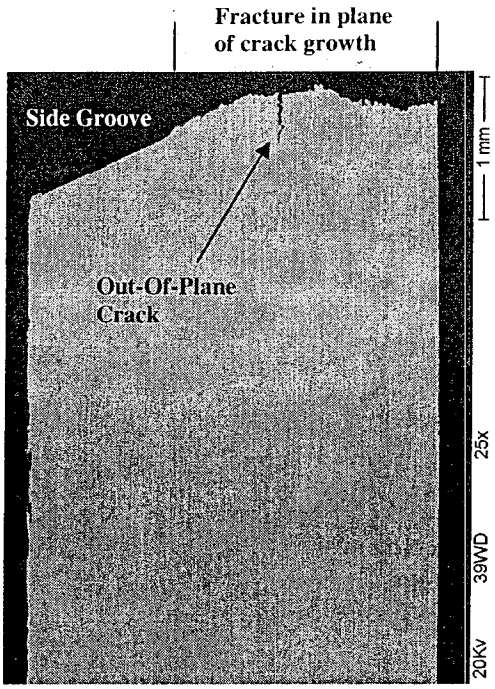

(a) Cross Section to Show Out-Of-Plane Crack

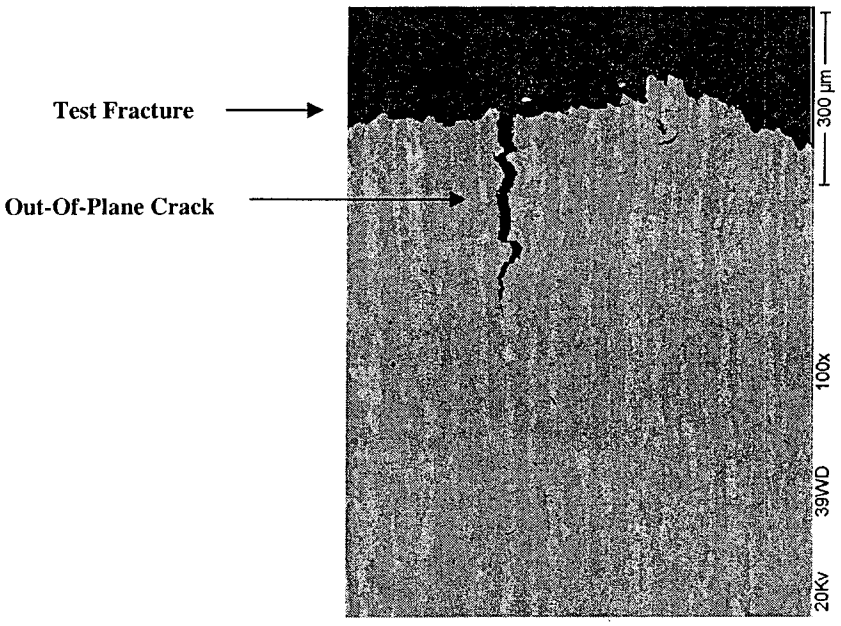

(b) Intersection of Test Fracture With Out-Of-Plane Crack

Figure E-43 SEM Micrographs of Cross Section X-X', Figure E-34

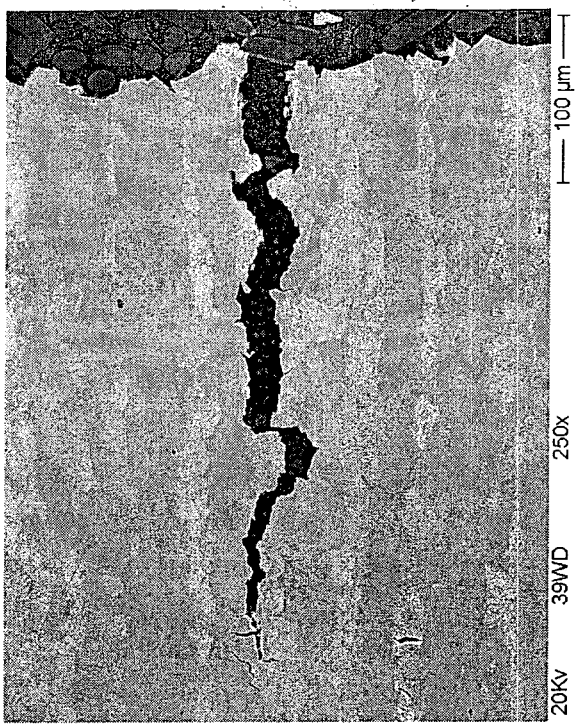

(a)

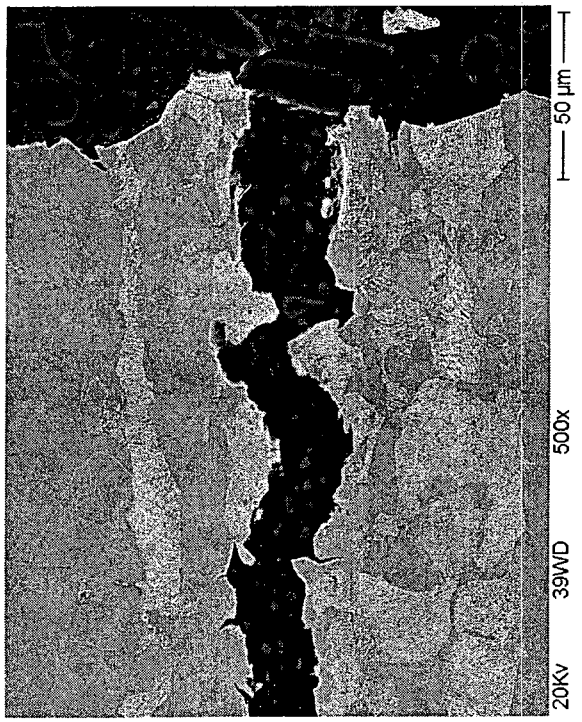

(b)

Figure E-44 Higher Magnification Views of Out-Of-Plane Crack

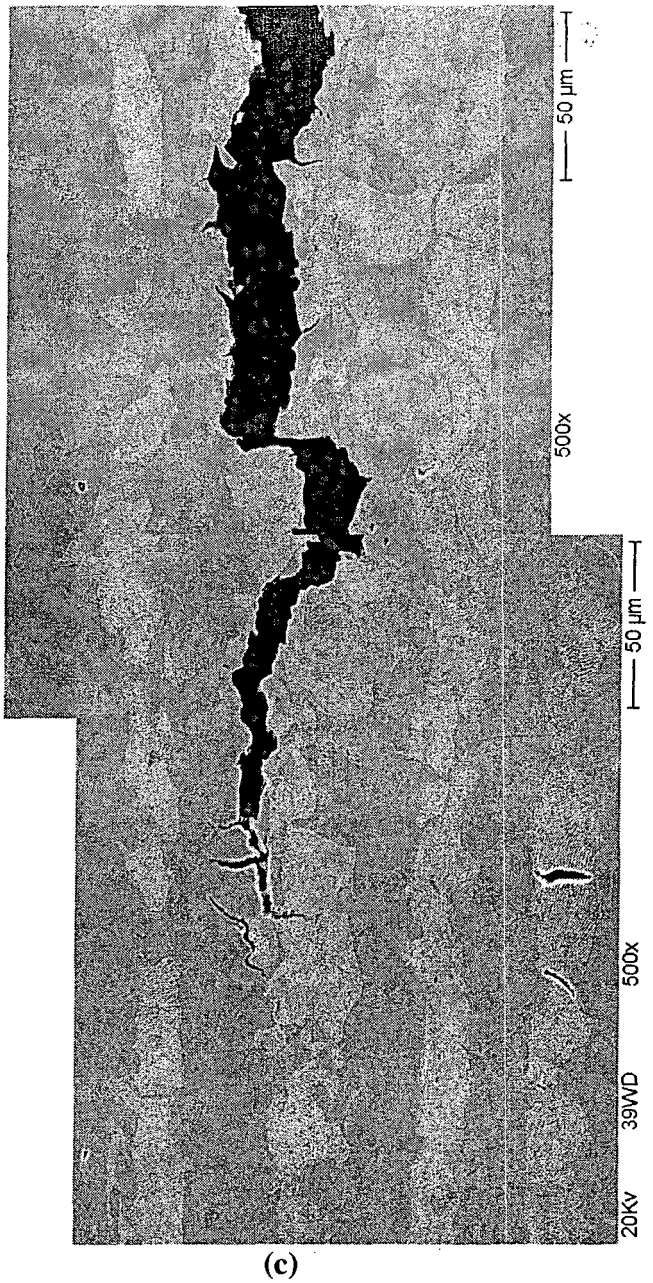

(c)

Figure E-44Cont.: Higher Magnification View of Out-Of-Plane Crack

Note: This montage is slightly skewed but it shows the full crack length.

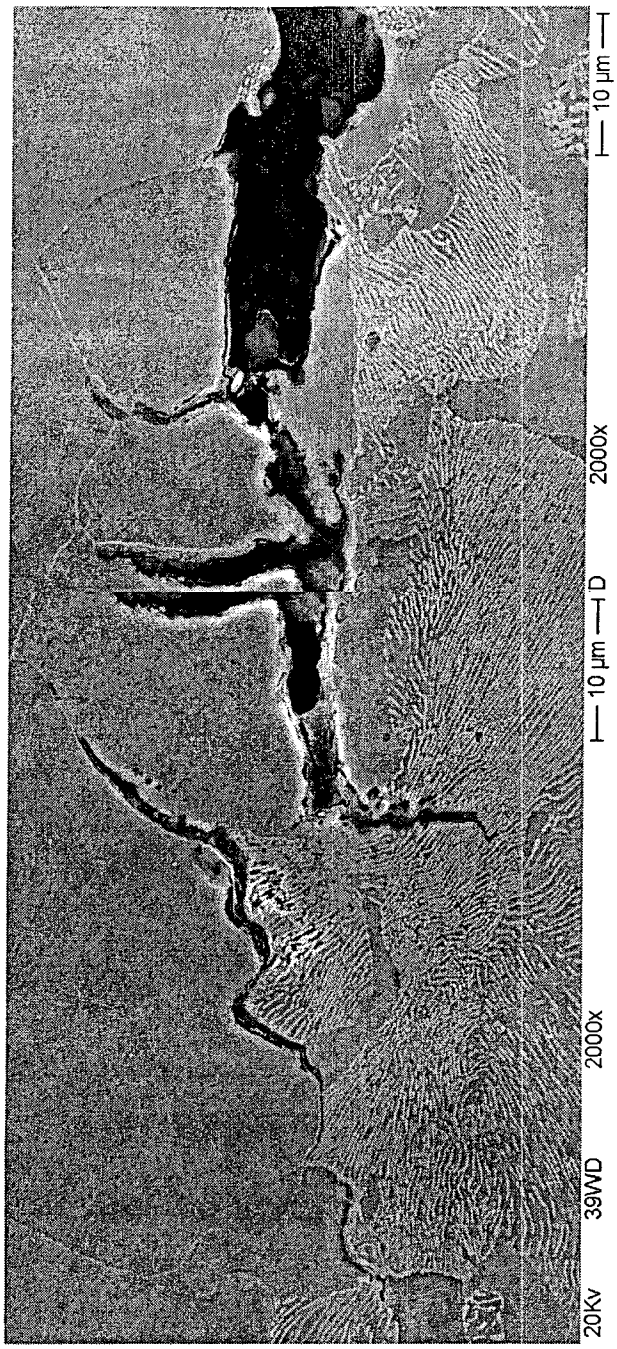

Figure E-45 Montage of Crack Tip For Out-Of-Plane Crack

Note: 1) Cracking along ferrite-ferrite and ferrite-pearlite boundaries.
2) Cracking also noted across and between pearlite lamellae

Annex F - Application of Findings

1.0 Introduction

The purpose of this Annex is to demonstrate the applicability of the creep crack growth prediction methodology to the prediction of remaining life of carbon steel riser pipe failures. The history of these failures and their causes will be briefly discussed as it relates to a remaining life prediction model based on earlier work supported by both Babcock & Wilcox and EPRI. A discussion of the important time dependent cracking parameters will be presented as they relate to the observed elbow failures. Detailed descriptions of the elbow failures will be presented as needed for the determination of the applied critical stresses, constraint (triaxiality) issues and creep crack growth models required to predict elbow lives. An example problem will be discussed wherein life expectancy is predicted for a pipe which actually failed in service for a utility. Additional calculations will be discussed relating the effects of normalization on this piping material. Lastly, a brief discussion will be provided regarding recommended follow-up work in the areas of both the importance of constraint effects and creep rate properties relevant to the piping heats obtained for this project.

2.0 History of Failures and Possible Causes

In the mid-1970's, a significant number of failures of cold-formed bends (elbows in riser pipes) occurred in the boiler integral pipework system of fossil-fueled power generating plants both in the U.S. and the U.K.[1] These failures occurred after service lives of a few years and were the result of crack growth in the axial-radial plane on the extrados of the bends. These tube bend show that extrados flattening or concavity results in a significant increase in the circumferential (hoop) stress due to pressurization. The principal factors in these failures were identified as being the presence of imperfections on the extrados of the bends and the high ovality of the bend cross-section. Work in the late 1970's and early 1980's led to improving surface quality and the setting of limits on the bend radii (reducing ovality) of these riser pipes. These changes seem to temporarily solve the problem of the riser pipe failures. However, both in the U.S. and U.K., failures started appearing again in the late 1980's and early 1990's. A plausible theory by the various British investigators[2] and Babcock & Wilcox postulated that cracks were initiating at surface imperfections at the extrados of the tight cold bends in both carbon and carbon-moly steels at temperatures lower than thought for creep conditions to occur in these type of steels. These cracks would then grow during unit operation by creep, eventually causing failure of the riser pipes.

Work sponsored by Babcock & Wilcox at Georgia Institute of Technology[3] in the early to mid 1990's used compact tension specimens to confirm that creep crack growth can occur at temperatures as low as 680°F (saturation temperature). An issue raised by this work was what correlating parameter best characterized the creep crack growth mechanism. Other issues of the effects of nitrogen, tramp elements, material conditions, and stress levels were raised but not addressed. Key issues raised were the effect of constraint or triaxiality on creep crack growth rates and which correlation parameter best characterizes creep. These issues were addressed in the current project and detailed discussions can be found in the main body of this report.

3.0 Time Dependent Fracture Mechanics Parameters

Prediction of the remaining life of fossil power plant components from creep rupture data alone is not possible. Cracks initiate and develop at critical locations in the components. These cracks propagate under creep conditions and ultimately cause leaking or possible failure of the component.

Although the low alloy steels used for fossil power plant components may begin to experience creep at temperatures of about 700°F, the allowable design stresses normally prevent creep crack growth from becoming a significant mechanism at temperatures below about 950°F in general. However as discussed earlier in this Annex and elsewhere in the final report, time-dependent cracking of carbon steel piping in the temperature range between 620°F and 680°F has been observed in the fossil power industry for the past 30 years. It will be further discussed and demonstrated in this Annex that time-dependent fracture mechanics methodology can be used to predict the observed riser pipe failures. The macroscopic crack growth observed in these riser pipes at the extrados occurs by local failure resulting from nucleation and coalescence of micro-cavities in the highly-strained region (at the extrados) ahead of the crack tip. When the fracture process zone ahead of the crack tip is small, as in the case of the cracked elbows, a detailed accounting of the fracture process zone is not needed for predicting creep crack growth. Creep crack growth can be shown to be governed by a time-dependent loading parameter that characterizes the geometry and applied loading of a flawed component. In linear elastic fracture mechanics (LEFM)-controlled fatigue crack growth, the governing parameter is the range of the stress intensity factor, ΔK. In elastic-plastic fracture mechanics (EPFM)-controlled ductile crack growth tearing, the governing parameter is the J-integral. In time-dependent fracture mechanics (TDFM), the analogous crack tip parameter is the energy release rate (power) parameter, C_t, which correlates creep crack growth rates[4] through the relationship:

$$da/dt = bC_t^q \qquad (1)$$

The remaining elevated temperature service life of a fossil power plant component, with an existing flaw, can be estimated by the numerical integration of Equation (1). In order to do this, a methodology for determining C_t, must be established.

The time-dependent fracture mechanics (TDFM) crack tip parameter, C_t, which correlates creep crack growth rates is dependent on the level of creep deformation at the crack tip. Creep crack growth occurs under small-scale creep characterized by a creep zone which is small relative to the overall dimensions of the cracked component and the crack depth. In the steady-state condition, this creep zone spreads over the entire uncracked component thickness. The transition creep conditions lie between the small-scale creep and steady-state regimes. Both these small-scale and transition creep regimes are under non-steady-state conditions because the crack tip stress varies with time. Under steady-state creep, where the crack tip stresses no longer change with time, the crack growth behavior can be characterized solely by the path independent energy rate line integral, C*.[5] Experimental studies have shown that C* characterizes the creep crack growth under large-scale (steady-state) creep conditions.

According to Saxena[4], the C_t parameter is an extension of the C* parameter into the transient regime. The connection is made through the energy rate interpretation of C_t. C_t is defined in terms of the rate of change of energy (power) with respect to crack length, a. If several pairs of cracked specimens are loaded to various load levels at elevated temperatures, the load-line deflection due to creep, V_c, as a function of time, can be recorded. At a fixed time, the load versus deflection rate, $\dot{V}_c$, can be plotted for all the cracked specimens. The area between the $P - \dot{V}_c$ curves is called ΔU_t^* (the subscript denotes that this value is at a fixed time, t) and represents the difference between the energy rates (power) supplied to the two cracked bodies. The C_t parameter is then given by:

$$C_t = \lim_{\Delta a \Rightarrow 0} \left(-\frac{1}{B} \frac{\Delta U_t^*}{\Delta a} \right) = \frac{-1}{B} \frac{\partial U_t^*}{\partial a} \tag{2}$$

where B = specimen thickness.
Note that as $t \rightarrow \infty$, $C_t \equiv C$ by definition for steady-state conditions. A significant body of experimental data[6], over a wide range of creep crack growth rates, now exists to support C_t (defined by Equation (2)) as a parameter for correlating creep crack growth behavior. The use of Equation (2) enables C_t to be determined experimentally from test specimens such as the compact tension specimen as used in fracture and fatigue testing. However, Equation (2) is not a convenient form for determining creep crack growth rates in fossil power plant components since only the applied stresses remote from the crack tip are known.

The problem of determining C_t is analogous to determining the magnitude of the J-integral under elastic-plastic conditions.[7] From Reference 8, accurate estimates of J, over a wide range of elastic-plastic conditions, can easily be made by simply adding the J values, obtained from small-scale yielding expressions in terms of K_I, to J plastic values from expressions for fully-plastic loading. Motivated by the analogous J-integral formation, Saxena[4] established a general formulation for estimating C_t based on applied loading (stress) for a wide range of creep conditions. Saxena's general formulation for C_t is:

$$C_t = \frac{4\alpha(1-\upsilon^2)}{E(n-1)} \frac{K^4}{w} (EA)^{2/(n-1)} t^{-\left(\frac{n-3}{n-1}\right)} \cdot F'/F + C^* \tag{3}$$

where

$$\alpha = \frac{1}{2\pi} \left[\frac{(n+1)^2}{2n\alpha_n^{n+1}} \right]^{(2/(n-1))} \tag{4}$$

where α_n^{n+1} = 0.69 for n between 3 and 10[4]
υ = Poisson's ratio
E = Young's modulus
K = stress intensity factor
A,n = secondary creep rate constants
W = specimen width or component thickness

F = $F(a/w) = K/PBw^{1/2}$
P = applied load
B = specimen thickness
w = specimen width
a = crack depth (length)
F' = dF/d(a/w)
t = time from the application of the initial applied load
C* = path independent integral defining the steady-state power-release rate.

The above C_t equation is based on a creep rate equation of the form

$$\dot{\varepsilon} = \dot{\sigma} / E + A\sigma^n \tag{5}$$

where primary creep is insignificant so that the total strain rate, $\dot{\varepsilon}$, is made up of the sum of an elastic part and a secondary creep rate part, $A\sigma^n$, where

E = modulus of elasticity
$\dot{\varepsilon}$ = the total strain rate
σ = the stress
$\dot{\sigma}$ = the stress rate

While the above formulation of C_t (Equation (3)) is usually quoted in the open literature, an alternate, much simpler expression for C_t originally proposed by Bassani[9] and later verified by Bloom[10] as giving similar (to within 2%) life predictions to those using Equation (3).

The alternate formulation for C_t for materials whose uniaxial creep deformations can be represented by Equation (5) is

$$C_t = C^* \left[\left(t_T / t \right)^{\frac{n-3}{n-1}} + 1 \right] \tag{6}$$

where t_T is the transition time for extensive secondary creep conditions to develop from small scale creep, and

$$t_T = \frac{\left(1 - \upsilon^2\right) K_I^2}{(n+1) E C^*} \tag{7}$$

3.1 Primary Creep

In materials that exhibit pronounced primary creep, the primary creep can have a significant impact on creep rates under sustained loading. The significance is especially important at short times and under cyclic loading conditions rather than under steady-state conditions. Primary creep is characterized by the gradual decline of the initially high creep rate to a constant strain rate characteristic of secondary creep. The high strain rate associated with primary creep contributes to rapid crack growth rates at short times. This detrimental effect of primary creep

is sustained throughout the life of a cracked component under cyclic loading conditions. The local plastic straining that occurs during start-ups and shut-downs can negate the effects of prior creep relaxation of the stresses at the creep tip so that the initially high values of C_t are reinitiated during each operating cycle. The local plasticity can similarly wash-out prior creep strain hardening so that the creep response is once again characteristic of primary creep at the start of each cycle. The significant effect of primary creep on the service life of flawed components subjected to cyclic elevated temperature service was demonstrated in Reference 10. The inclusion of primary creep in the creep crack growth driving force parameter, C_t or C(t), is important.

If the uniaxial primary creep strain rate can be represented by:

$$\dot{\varepsilon} = \frac{[B(1+p)]^{\frac{1}{(1+p)}} \sigma^m t^{-p/(p+1)}}{1+p} \tag{8}$$

then Riedel[11] demonstrated that another path-independent integral, C_h^*, can be obtained by substituting $[B(1+p)]^{1/(1+p)}$ in place of A and m in place of n in the expressions for calculating C*. Thus, C(t) for extensive primary creep can be written as

$$C^*(t) = \frac{C_h^*}{(1+p)t^{p/(1+p)}} \tag{9}$$

However, in reality, practical problems usually involve both types of creep conditions, primary and secondary creep. If steady-state, secondary creep is added to Equation (8), the combination of these two creep rates will overwhelm the elastic creep rate (represented by the first term in Equation (5)). In this case, the time and stress dependencies of strain rate will no longer be separable, and at a given time, t, the strain rate will not be a function of stress only. Therefore, C*(t) is no longer path independent. It has been shown numerically[12] that C*(t) is approximately path independent and C*(t) can be written as

$$C^*(t) \cong \left[1+(t_2/t)^{p/(1+p)}\right] C^* \tag{10}$$

where t_2 is the time of transition from extensive primary creep to extensive secondary creep expressed as

$$t_2 = \left[\frac{(n+p+1)C_h^*}{(n+1)(p+1)C^*}\right]^{(1+p)/p} \tag{11}$$

C_h^* is the value of C*(t) when only primary creep dominates, and C* is the value of C_t when secondary creep dominates. The expression for C_h^* can be evaluated in the same manner as C*.

For structural components which do not necessarily crack under extensive creep conditions, the crack tip stress fields under small-scale creep conditions must be addressed. If the uniaxial creep constitutive equation is written as

$$\dot{\varepsilon} = \dot{\sigma}/E + \frac{[B(1+p)]^{\frac{1}{(p+1)}}\,\sigma^m t^{-p/(p+1)}}{p+1} + A\sigma^n \tag{12}$$

where B,p,m, are the primary creep constants, then

$$C(t) = \left[1+(t_{TP}/t)+(t_2/t)^{p/(1+p)}\right]C^* \tag{13}$$

for materials deforming by elastic, plastic, and power law creep.[11,13] Here the above, much simpler, expression will be used as the approximate creep crack growth driving force parameter in subsequent calculations in this Annex. However, one significant disadvantage of C(t) over C_t is that C(t) cannot be measured at loading pins under small-scale creep conditions. It must instead be calculated. However, this will not cause much of a problem because under extensive creep conditions C(t) is identical to C_t which can be measured at the load line and also be calculated. The transition time, t_{TP}, in Equation (13) is the time for extensive primary creep conditions to develop from small-scale primary creep and is given by the following equation

$$t_{TP} = \left[\frac{K^2(1-\nu^2)}{EC_h^*}\right]^{(1+p)} \cdot \frac{1}{(1+m)} \tag{14}$$

This result is due to analyses by Riedel[11].

3.2 Remaining Life Predictions (Continuous Operation)

Different formulations of C_t are needed for cyclic operation than for continuous steady-state operation. The approach used for continuous operation is discussed first.

Since C_t is a function of crack depth to component thickness and time, and this dependence cannot be separated, and integration must be performed numerically. Note that C_t, as formulated in either Equations (3), (6), or (13) cannot be defined for t=0. Following the application of the load, there is a finite incubation time, t_0, during which creep crack growth is very slow. In the following discussion of cyclic crack growth, it will be shown that this time, t_0, is related to the time required for generating a creep zone within the cyclic plastic zone. For continuous or steady-state operation, an approximate, realistic approach is to set t_0 equal to one hour. This rids the C_t expression of the singularity at t=0. Equation (1) can then be rearranged for small increments of crack growth, Δa, as follows:

$$\Delta t = \frac{\Delta a}{b[C_t(t, a/b)]^q} \tag{15}$$

where Δt is the time interval during which the crack grows, Δa. If the crack grows from a_0 to a_i during the total life in equal steps of Δa, then the i-th time interval, Δt_i, can be expressed by the following:

$$\Delta t_i = \frac{\Delta a}{b[C_t(a_{i-1}/b, t_{i-1})]^q} \tag{16}$$

where

$$a_i = a_0 + i\Delta a \tag{17}$$

and

$$t_i = t_0 + \sum_{i=1}^{i} (\Delta t_i) \tag{18}$$

or

$$t_f = t_0 + \frac{\Delta a}{b} \sum_{i=1}^{s} \left[\frac{1}{C_t(a_{i-1}/b, t_{i-1})} \right]^q \tag{19}$$

where t_f is the predicted life. By choosing a crack growth interval, Δa, crack size versus time can be calculated.

3.3 Remaining Life Predictions (Cyclic Operation)

In the C_t expressions of Equations (6) and (13), instantaneous plasticity is not considered. In situations where the plastic zone around the crack tip is small, and the time scale is no longer than the time required for the creep zone to become larger than the initial plastic zone, the material can be accurately modeled without consideration of the local plasticity. For steady operation, these conditions are satisfied and the C_t parameter defined by Equations (6) and (13) is satisfactory. However, for creep-fatigue crack growth (CFCG) where hold periods are relatively short (shorter than the time required for the creep zone to surround the plastic zone), a different formulation of C_t is required.

If a cyclic plastic zone is formed on unloading and reloading and during a subsequent hold period, a creep zone starts to form within the cyclic plastic zone, then the time required for generating the creep zone of size r_{pl}^{mono} is t_{pl}. The crack tip stress field at time t, can be represented (without the explicit consideration of the plastic deformation characteristics of the material) by substituting $t+t_{pl}$ for t. The monotonic C_t behavior can be predicted by substituting $t+t_{pl}$ for t in either of Equations (6) or (13).

For cyclic behavior, K is replaced by ΔK, the applied stress intensity range, and tpl is based on the size of the cyclic plastic zone, r_{pl}^{cyclic} instead of the monotonic plastic zone, r_{pl}^{mono}.

The determination of t_{pl} is quite involved. Estimates of t_{pl} can be made depending on the selected cyclic yield strength and, creep rate exponents for the material of interest. Details of how t_{pl} is determined can be found in K. B. Yoon's Ph.D. thesis[14].

In actual plant operations, a fossil plant is shut down several times a year for a few days and then started again. Figure F-1 illustrates a plot of the pressure, temperature of a typical component during the start-up and shut-down cycle. For cyclic operation, the value of C_t decreased with time during normal operation and goes to zero at shut down. At the next start-up, the value of C_t starts from its initial value as shown in the figure. For start-up and shut-down (cyclic) operation, the crack growth rate is best estimated on a per operating cycle basis and creep-fatigue crack growth (CFCG) can be determined by portioning the crack growth into a cyclic-dependent part and a time-dependent part such that

$$\frac{da}{dN} = \left(\frac{da}{dN}\right)_{cycle} + \left(\frac{da}{dN}\right)_{time} \tag{20}$$

Figure F-1 Schematic of Pressure, Temperature, and C_t Versus Time for a Simple Start-up and Shut-down

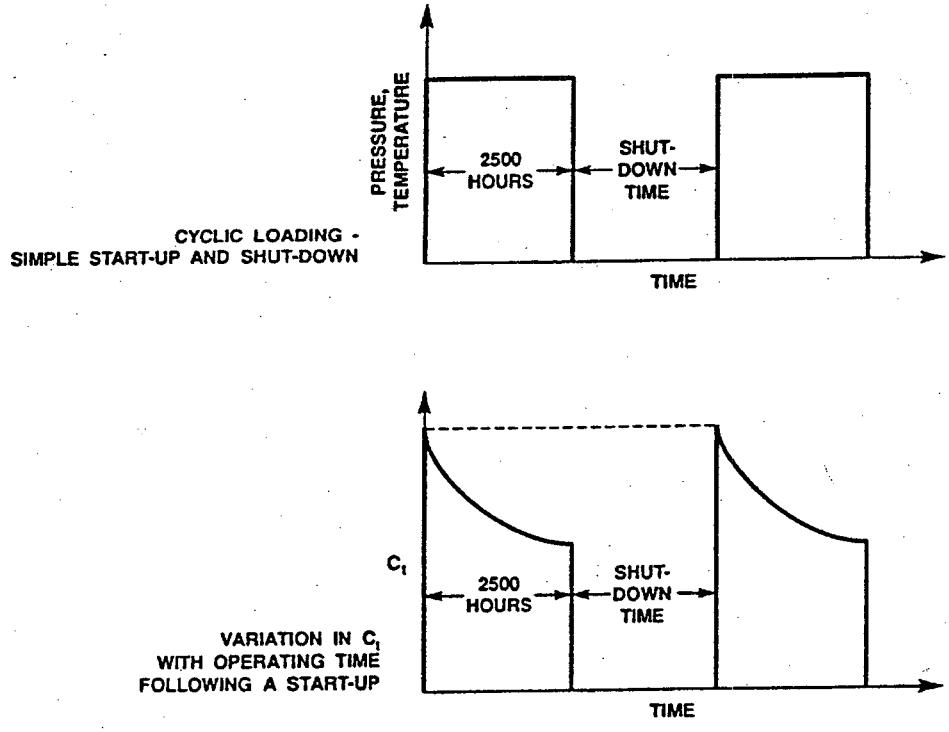

The time-dependent crack growth occurs only under constant amplitude loading during the hold period of the cycle, t_h. Thus, C* and C_t can be used in characterizing the crack growth rate during this hold period. Due to experimental limitations, it is difficult to obtain instantaneous values of da/dt and C_t during the hold period. However, average values of the crack growth rate and the C_t parameter can be accurately measured. The average da/dt and C_t can be obtained as follows:

$$\left(\frac{da}{dt}\right)_{avg} = \frac{1}{t_h}\left(\frac{da}{dN}\right)_{hold} \tag{21}$$

and

$$(C_t)_{avg} = \frac{1}{t_h}\int_0^{t_h} C_t\,dt \tag{22}$$

The $(da/dN)_{hold}$ is the crack growth rate during the hold period and is obtained by subtracting the cycle-dependent crack growth rate from the total crack growth rate. Note that using Equation (22) for cyclic loading along with Equation (6) and (13) would be a problem because of the singularity in those equations at t=0. However, allowing for instantaneous plasticity during cyclic loading using the C_t expression modified by replacing t by $t+t_{pl}$ eliminates this problem.

The cyclic term can be written as

$$\left(\frac{da}{dN}\right)_{cycle} = C(\Delta K)^n \tag{23}$$

which has the same dependency for fatigue crack growth rates under conditions where time-dependency is insignificant. Expressions for $(C_t)_{avg}$ are as follows:

For primary plus secondary creep with instantaneous plasticity,

$$(C_t)_{avg} = C^*\left[1 + t_{TP}\cdot Y + (p+1)\,t_2^{\frac{p}{(p+1)}}\cdot Z\right] \tag{24}$$

where

$$Y = \frac{\left|\ell n(t_h + t_{pl}) - \ell n(t_{pl})\right|}{t_h} \tag{25}$$

and

$$Z = \frac{\left[(t_h + t_{pl})^{\frac{1}{(1+p)}} - t_{pl}^{\frac{1}{(1+p)}}\right]}{t_h} \tag{26}$$

Also,

$$t_{TP} = \left(\frac{1}{1+m}\right) \bullet \left[\frac{(\Delta K)^2 (1-\nu^2)}{EC_h^*}\right]^{(1+p)} \tag{27}$$

and

$$t_2 = \left[\frac{(n+p+1)C_h^*}{(1+p)(n+1)C^*}\right]^{(1+p)/p} \tag{28}$$

In the above equations, t_h is the hold time between start-up and shut-down, t_{TP} is the transition time from small-scale primary creep to extensive primary creep conditions, and t_2 is the transition time from extensive primary creep to steady-state creep conditions.

The total crack growth rate is given by

$$\frac{da}{dN} = C_0 \Delta K^n + C_1 \left[(C_t)_{avg}\right]^{q_1} t_h \tag{29}$$

The significance of using Equation (1) versus Equation (29) is that experiments of creep crack growth (CCG) have been used to determine b and q of Equation (1) while creep-fatigue crack growth (CFCG) experiments have been used to determine C_1 and q_1 of Equation (29). Data from these two different type fatigue experiments[14] have shown that time-dependent crack growth behaviors under CFCG and CCG conditions can be expressed as a single trend if $(da/dt)_{avg}$ is characterized by $(C_t)_{avg}$ or da/dt is characterized by C_t. This is an important conclusion for applications because material behavior measured by CCG testing can be used to predict component life under creep-fatigue conditions or material behavior measured by CFCG testing can be used in CCG conditions. Even though C_t and $(C_t)_{avg}$ are equivalent parameters, their exact numerical values may differ in the small-scale creep regime for a given material. However, in application, this difference will not cause any significant problem, as C_t is used for steady-state continuous operation, while $(C_t)_{avg}$ is used in cyclic situations.

A last comment before leaving this discussion, creep crack growth calculations do not include the fatigue crack growth term in Equation (29). Experience has shown that at creep temperatures, this term does not significantly contribute to the crack growth under creep conditions. The second term in Equation (29) is the dominant term for crack propagation.

4.0 Modeling of Elbow Failures

As discussed earlier, a large number of carbon/carbon manganese boiler feed pipes installed in the cold-bent condition have failed over the last 30 years, both in the U.S. and in Europe. In most of these cases, failure occurred by crack propagation from the pipe outside surface along the pipe length (axis) originating at the extrados of the bend. Two types of failures occurred, either leak-before-break or violent failure where a window was blown out. The failures usually occurred after service of only 1000 – 100,000 hours after a limited number of cold and hot starts. The crack was reported to initiate from a seam or shallow defect of 40 mils (1 mm) or less at the extrados outer surface of the bend. In the power station boilers, the feed pipes

operate at approximately 680°F (360°C) with pressures of about 2400 psia (17 MPa). C* and C_t models of cracked elbows do not exist; therefore, a reasonable model of the cracked elbow is needed. For the majority of these failed elbows, a single edged cracked plate under a non-uniform hoop stress is a good approximation of the failed elbow. The hoop stress is due to change in tube cross-section at the bend due to the cold bend process and the pressure in the tube.

4.1 Resultant Stress Determinations

Studies[15] have been made on the effects of tube cross-sectional geometry on the bend's extrados stress state. Hypothetical tube bend shapes have shown that extrados flattening or concavity can result in increased hoop stresses due to pressurization of the tube bends. Finite element stress analyses have demonstrated that a stress formulation due to Rodabaugh[15] is adequate for determining pressurization stresses in tube bends of nearly flat extrados sections. The Rodabaugh formulation is a Fourier series approximation which can be used in place of finite element analyses. The Rodabaugh two-dimensional stress approximation was based on the assumption that the pipe bend cross section behaved as a closed ring and the effects of longitudinal curvature can be negated. A simpler Rodabaugh formulation only accounted for extrados hoop stresses due to changes in cross-section ovality. However in the case of a tube bend having a flat spot at its extrados (Figure F2), the Rodabaugh Fourier series expression was

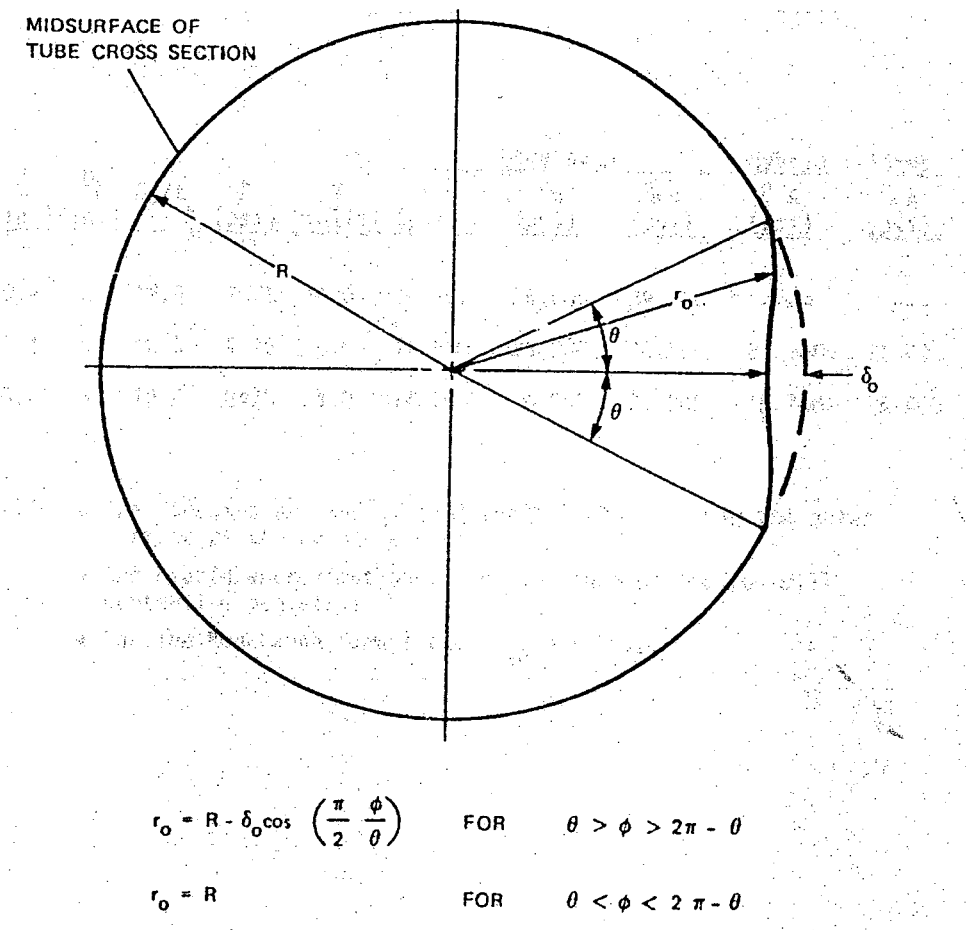

Figure F-2. Rodabaugh's Midsurface Definition of a Cross Section with a Flat Spot

shown to be accurate in predicting extrados stresses. The additional measurements of angle of the flat spot (2θ) and depth (δ_o) of the flat spot are needed. During these finite element studies, it was found that the Fourier Series expression were in more favorable agreement with most flat spot geometries. Shibli[16] in turn developed a model relating extrados hoop stress in an oval pipe as a function of cross-section ovality where the hoop stress is composed on a membrane component (σ_m) due to pressure in a straight circular pipe, plus a bending component (σ_b) due to the pressure trying to force the cross-section into a circular shape. He developed a stress concentration factor (SCF) defined as the peak stress divided by the stress in a circular pipe where

$$SCF = 1 + \sigma_b/\sigma_m \tag{30}$$

And

$$SCF = 1 + \text{constant} \times \Omega \tag{31}$$

Where Ω is the measured ovality of the tube bend. Shibli's model, however, was shown to underestimate the hoop stress at the extrados for tube bends with flat spots (θ less than 70°). In

fact, it has been shown by field measurements that a Rodabaugh 40-degree section closely matches in-field measured flat spots in failed elbows (Lon Hill model in Figure F-3). SCF of over 5 were calculated for a Rodabaugh 40-degree approximation and 6 for a Rodabough 30-degree model. A similar model, although perhaps less complicated than the Rodabaugh model, was used by Wood[17] in his paper discussing an actual service failure. The model used is due to Lees and Siverns[18]. Here SCFs up to 6.5 were calculated based on ovality measurements from service-failed pipe. Additional discussion is provided in the example problem subsection.

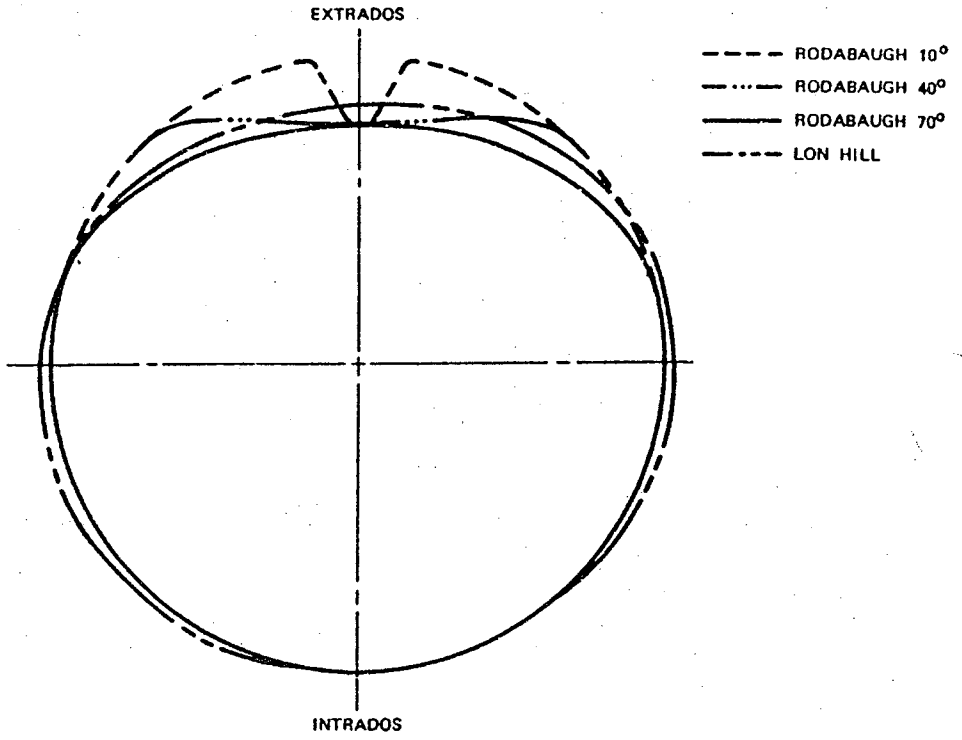

Figure F-3. Midsurface Geometries of Various Cross Sections Having Nominal 0.4-inch Wall and 5-Inch Outer (4.6-Inch Mid) Diameter and 10 Percent Ovality

4.2 Constraint Effects

Creep crack growth data has been obtained from testing mostly deeply-notched, compact specimens in the U.S. However, in Europe they have used pressurized tubes, pipes, compact tension specimens, and three-point bend test specimens. The Europeans concluded that there is a significant effect of geometry constraint on their results of creep crack growth measurements. Fracture toughness, fatigue crack growth, and more recently, creep crack growth material property data in the U.S. has been determined exclusively from deeply cracked compact tension specimens based on ASTM testing standards and validity criteria. The ASTM standards were chosen to insure plane strain behavior with high hydrostatic (triaxial) stresses at the crack tip. This leads to material property data that is independent of test specimen sizes, geometry, and crack depth. However, there is experimental evidence that fracture properties change dramatically for test specimens and structural components with shallow cracks compared to material data obtained from deeply cracked ASTM compact tension specimens.

Deeply cracked specimens are defined as specimens with crack depths to plate widths of 0.5 or greater. These specimens have high hydrostatic stresses at the crack tip leading to high constraint, while the shallow crack specimens have lower hydrostatic stresses and lower constraint. Previous testing on the SA 106, Grade C carbon steel elbow material, both aged and normalized, at Georgia Institute of Technology[3] in the early 1990's used compact specimens. Their work concluded that both the aged and normalized carbon steel material measured creep crack growth rates correlated better with the stress intensity factor K rather than C_t parameter as illustrated in Figures F-4 and F-5 taken from Reference 3. While the investigators at GIT made comparisons using the load-line deflection rate ($\dot{v}_c$) due to creep during the tests with the total load-line deflection rate ($\dot{v}$), no conclusions were drawn to theorize why correlations seem to show that K better characterized the measured creep crack growth rates. Their examinations of the ratio of $\dot{v}_c/\dot{v}$ for the various tests did not clearly confirm whether K or C_t should be the characterizing parameter.

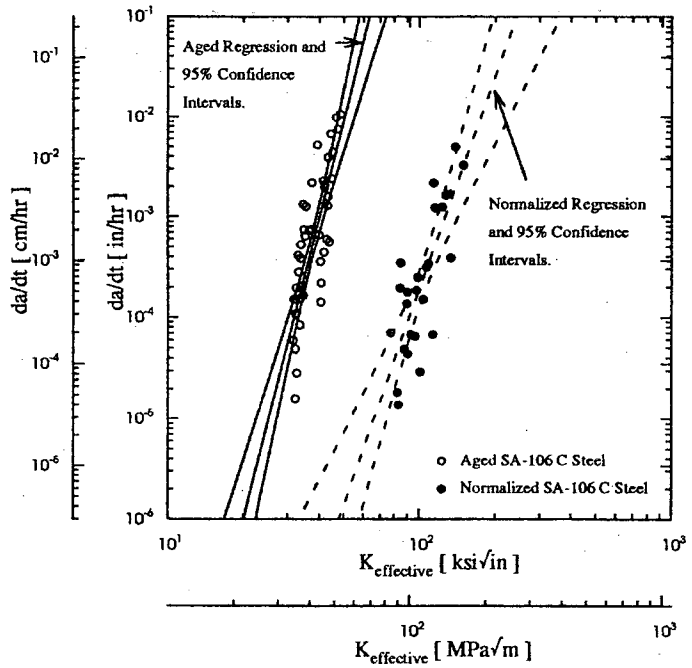

Figure F-4

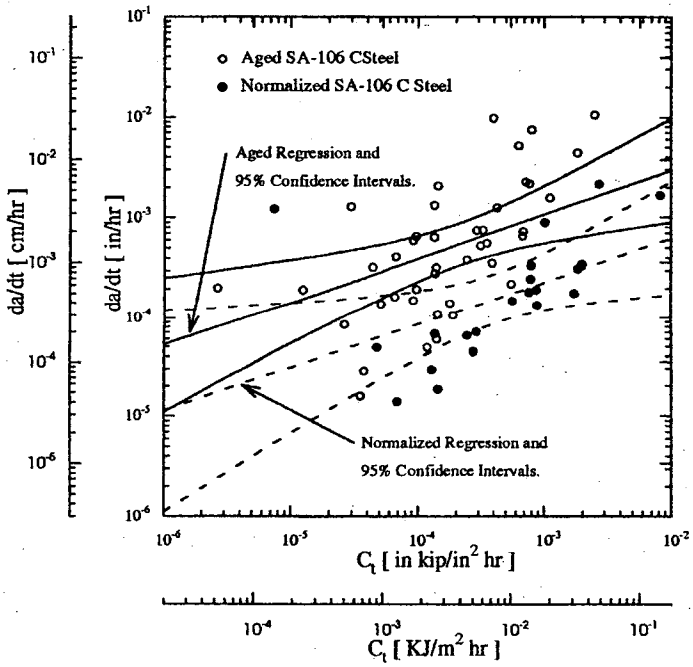

Figure F-5

Since the cracking observed at the extrados of the failed elbows was from shallow defects under a combination of bending and tension stresses, MTI investigators proposed the testing of a shallow single edge notched tension (SEN(t)) specimen. This specimen can provide test data which simulate the constraint effects seen in the cracking of the cold bent elbows. An expression for C*(t) was developed to measure the creep crack growth rates of both the aged and normalized pipe materials. Figure F-6 presents the results of tests performed at MTI using the SEN(t) specimens. It can be seen from these results that creep crack growth rates correlate with C*, and that the various heats do not show any significant trends, that is, the C* parameter seems to normalize the creep crack growth rates for the various grade C elbow materials independent of heat treatment. This is discussed in more detail elsewhere in the final report. A least square fit of this data to C* is shown in Figure F-7 fit to Equation (1) where in terms of customary U.S. units is

$$da/dt = 0.0092\, C^{*0.7124} \tag{32}$$

In addition, it is noted on comparison of the GIT data of Figure F-5 with the MTI data of Figure F-6, that the compact data gives higher rates of creep crack growth than from the SENT specimens. This is consistent with the findings of constraint effects by GIT which tested compact specimens with crack depth to specimen width of less than 0.5. The shallower crack depth specimens produced crack growth rates significantly less than those of the deeper cracked C(T) specimens. Budden and Ainsworth[19] theoretically derived an expression for da/dt as a function of C* and a measure of stress triaxiality (constraint), Q, and found that creep crack growth rates for low constraint geometries (cracked elbows) are reduced (for the same value of C*), from the data from high constraint specimens. This is consistent with the trends observed from the data shown in Figures F-5 and F-6. Therefore, it is recommended that Equation (32) be used to represent creep crack growth rate for determining the remaining life of cracked cold bent elbows.

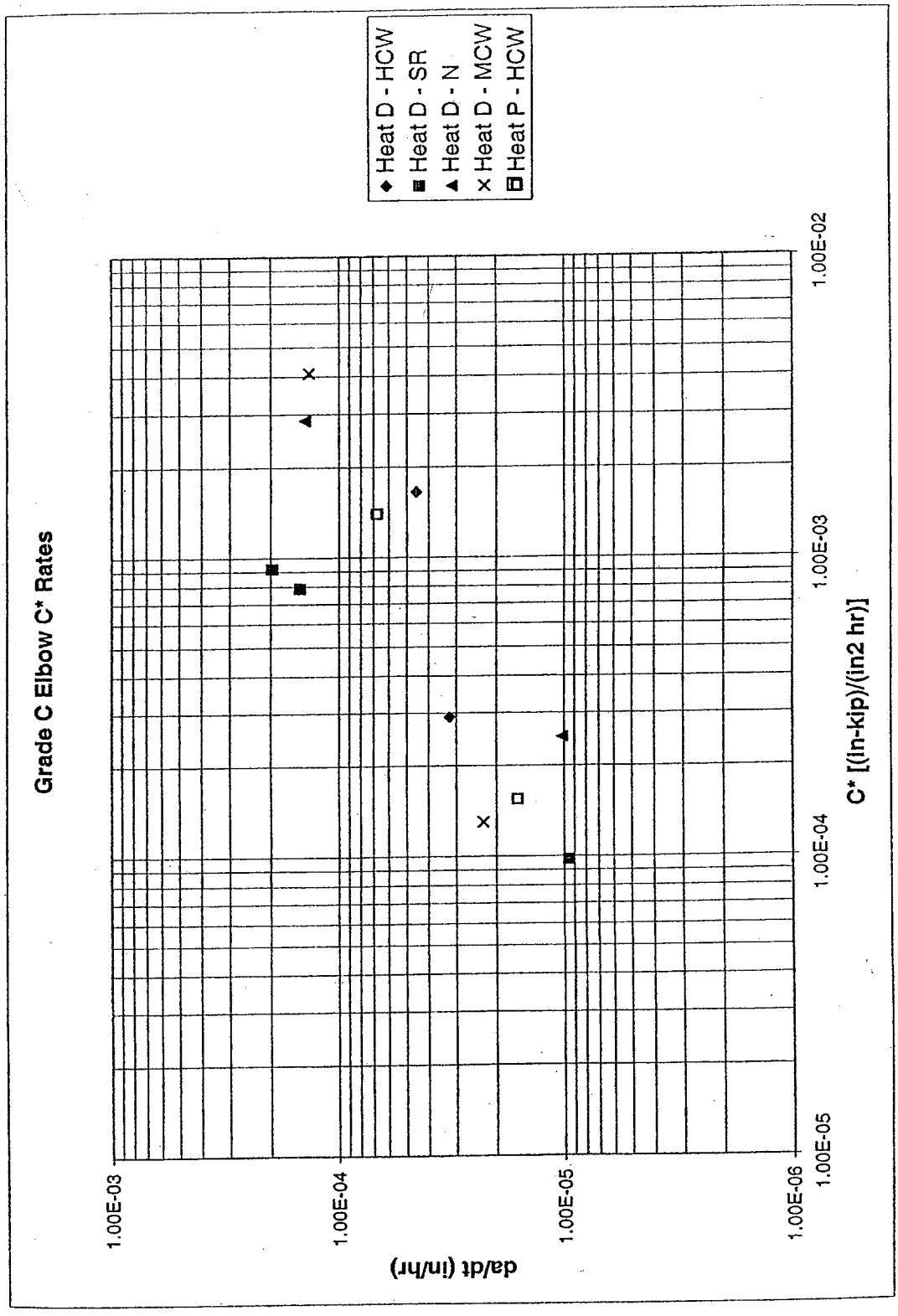
Grade C Elbow C* Rates
Heat D - HCW
Heat D - SR
Heat D - N
Heat D - MCW
Heat P - HCW
da/dt (in/hr)
1.00E-03
1.00E-04
1.00E-05
1.00E-06
C* [(in-kip)/(in2 hr)]
1.00E-02
1.00E-03
1.00E-04
1.00E-05

Figure F-6

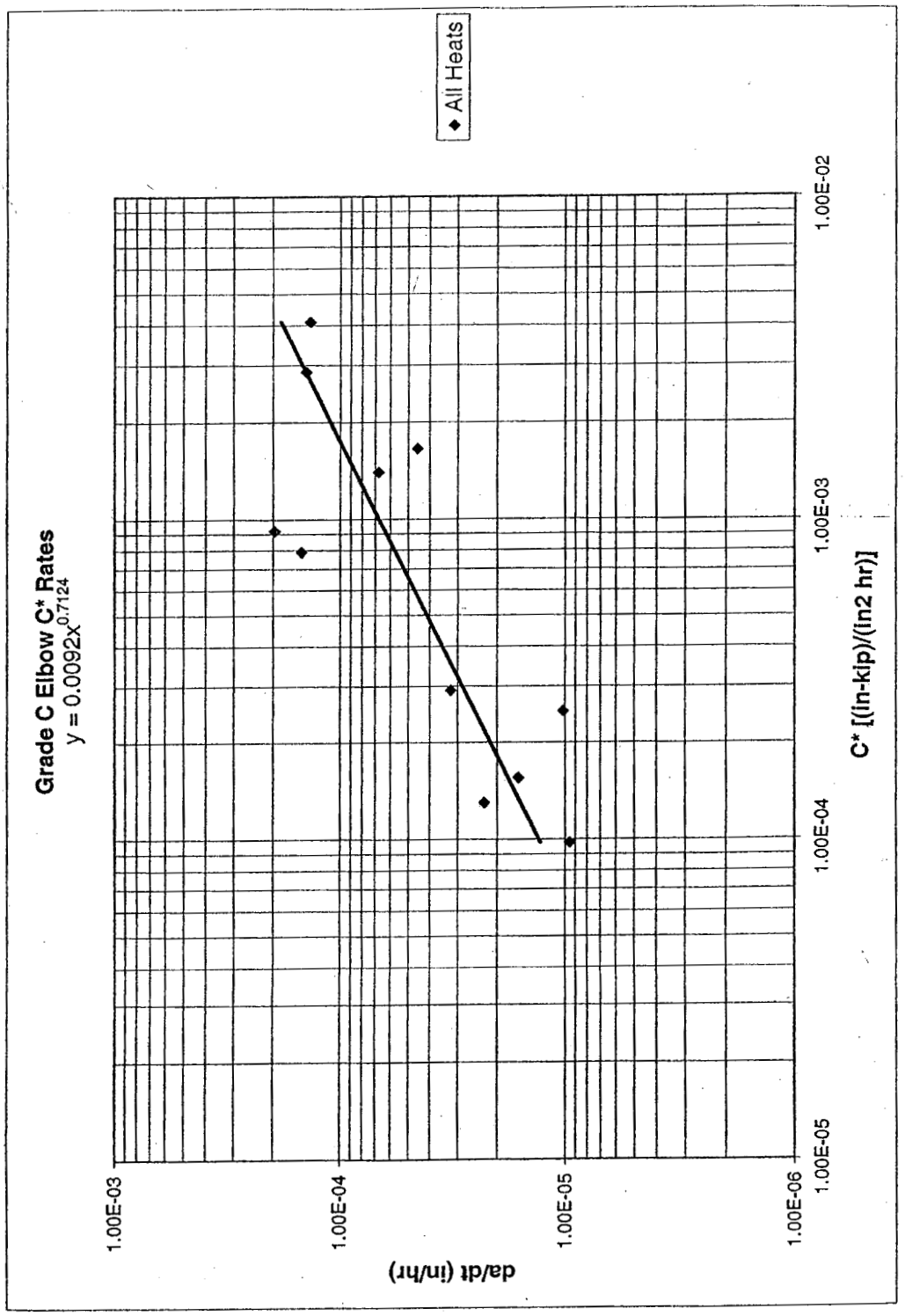
Grade C Elbow C* Rates
y = 0.0092x^0.7124
◆ All Heats
da/dt (in/hr)
C* [(in-kip)/(in2 hr)]
1.00E-03
1.00E-04
1.00E-05
1.00E-06
1.00E-02
1.00E-03
1.00E-04
1.00E-05

Figure F-7

4.3 Creep Crack Growth Modeling of Elbows

In order to calculate the remaining life of a crack component operating at creep level temperatures, a computer code is needed to do the calculations using the equations provided in the previous sections of this annex. A code developed to perform such calculations was developed in the early 1990's at MTI called PCCREEP[20]. The computer code PCCREEP determines the time for crack growth through the wall of a component operating at creep temperatures given the initial crack size, component geometry, material properties, and the operating conditions (stress, temperature, and cyclic versus continuous loading). The code has the capability to assess both circumferential and longitudinal oriented flaws in pressurized cylinders along with cracking in other type power plant components which can be represented by simple two-dimensional crack models. Material properties for specific heats can be input by the user. PCCREEP does not specifically address the geometry and operational details of specific components. The user is required to independently calculate the approximate primary stresses and metal temperatures which the component experiences. Input assumptions are directed to constant single values of pressure and/or stresses at a fixed uniform temperature. The only exception to this is for an on/off cycling (start-up/shut-down cycle) where the times between start-ups and shut-downs (cold start-ups) are specified by the user. Details of transients associated with start-up ramps and shut-down ramps (time-temperature and stress effects) are ignored.

Lastly, the program does not include the determination of critical crack sizes which are usually needed to predict rapid unstable crack propagation. Roughly 95% of the life of the component is expended in creep crack growth and in the final 5% or less of life, the creep crack growth rates are so high that these high rates control the final crack size and life process.

The inputs to PCCREEP are as follows:

- Selection of a crack geometry
- Selection of specific material properties
- Component geometry dimensions
- Size of initial crack and final crack (usually set as wall thickness or less)
- Stress or pressure
- Plant operating mode (steady-state or cyclic)
- Hours of each operating cycle for a cyclic plant

For a cracked elbow with initial crack size of less than 50% of the wall thickness of the extrados of the elbow, a reasonable approximate model is GEOMETRY 4 Surface Flaw Under Membrane Plus Bending (stresses) as shown in Figure F-8. The wall thickness, b, is selected as the extrados wall thickness and the crack depth, A_i, the initial measured defect size found from inspection of the failed elbow. The stress at point A at the extrados is the sum of the membrane component of the hoop stress in a pressurized cylinder given by

$$S = P\bar{R}/t \tag{33}$$

where

$$\overline{R} = D_N / 2 - t / 2 \tag{34}$$

where D_N is the nominal outer diameter of the tube, and t is the tube wall thickness, and a bending stress component due to the pressure trying to force the cross-section into a circular shape. This bending stress term can be calculated using the Rodabaugh Fourier Series formulation[15] or by a SCF factor times the membrane hoop stress expression given by Equation (33). The SCF factor can be found in either Shibli's paper[16] or in work by Lees and Siverns[18], both discussed earlier in this Annex. The stress at point B can be approximated as the sum of the constant membrane stress due to pressure (Eq. (33)) plus a linearized reduced outer fiber (extrados) bending stress acting at point B. This bending stress at point B is a function of the pipe (elbow radius and wall thickness). The effects of curvature of the pipe is ignored, as well as the bend curvature, since the initiating defects are long relative to the bend radius of the elbow.

GEOMETRY 4 SURFACE FLAW - MEMBRANE PLUS BENDING

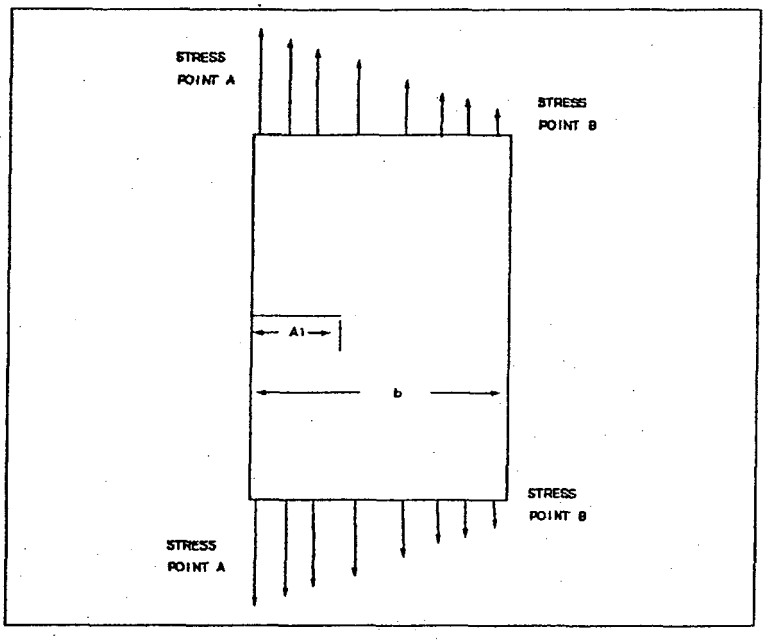

Figure F-8

4.4 Material Property Issues

Most of the mechanical testing that MTI performed under this contract related to determination of creep crack growth rates for the various heats of SA-106, Grade C grade carbon steel as reported in the main body of this final report. However, to apply the results of the findings of this work, creep rate properties are needed as well. For the purpose of demonstrating the applicability of the work performed, data generated from GIT work[3] in the early to mid-1990's will be used. As discussed in Section 3.0 of this Annex, uniaxial creep rate data is required to perform a remaining life prediction. GIT performed the majority of their testing on SA-106, Grade C carbon steel in the aged condition since it is this condition that comprises the majority of the SA-106C carbon steel in service. The material was supplied by the Fossil Power Division of Babcock & Wilcox in the form of hot finished pipe sections, 6.38 inch OD x 1.25 inch nominal wall thickness. To simulate the strains induced on the extrados of the riser pipe elbow during forming, the pipe was subjected to a 15% tensile pre-strain along the major axis. No damage in the form of cracking was observed during tensile pre-strain. Following pre-strain, the pipe was given a strain aging heat treatment of 650°F for 8 hours. The resultant heat treatment is referred to as the aged condition. Additional selected pipe sections were given an additional normalizing heat treatment of 1600°F for 1.5 hours. This heat treatment is referred to as the normalized condition. Both heat treatments were then air cooled. Tensile, creep deformation, and creep crack growth tests were then performed. Creep deformation tests at 626°F and 680°F were completed and Equation (12) was used to fit the creep data. Tensile results at 626°F and 680°F are needed for both the aged and normalized materials to determine the maximum extrados stress used in the analyses. Results of the minimum creep strain rate

versus stress for SA-106C carbon steel at 626°F and 680°F are presented in Figure F-9 taken from Reference 3. Note that the applied stress level appears to have an influence on the slope of the minimum creep rate, n. The change in slope appears to be in the range of stress between 50 ksi and 70 ksi. This is significant depending on what level of extrados stress is calculated for the particular elbow analyzed. Note also that the creep rates between the normalized and aged conditions are significantly different for stresses below 60 ksi. At 680°F where the creep data is more complete, the steady-state creep deformation rates are significantly lower for the aged condition compared to the normalized condition at stress levels less than 60 ksi. Similar trends observed by Neate[1] are shown in this figure for HFS 35 carbon steel (a steel similar in chemical composition to SA-106C carbon steel). Neate also noted the change in "n" from 16.3 to 4 at 58 ksi comparable to the stress at which the transition of "n" occurred in the SA-106, Grade C carbon steel. A change in "n" is usually associated with a change in the dominant creep mechanism. Table F-1 presents the list of primary and secondary creep regression constants determined from Reference 3. These will be used in the calculation of remaining life for the actual service-failed pipe discussed in the next section. The required creep crack growth rate that will be used in the next section is given by Equation (32) with the creep crack growth rates for the various heats tests by MTI shown in Figure F-7. This data was thought to be more representative of creep crack growth rates for the shallow defects found in cold bent elbows as discussed in Section 4.2.

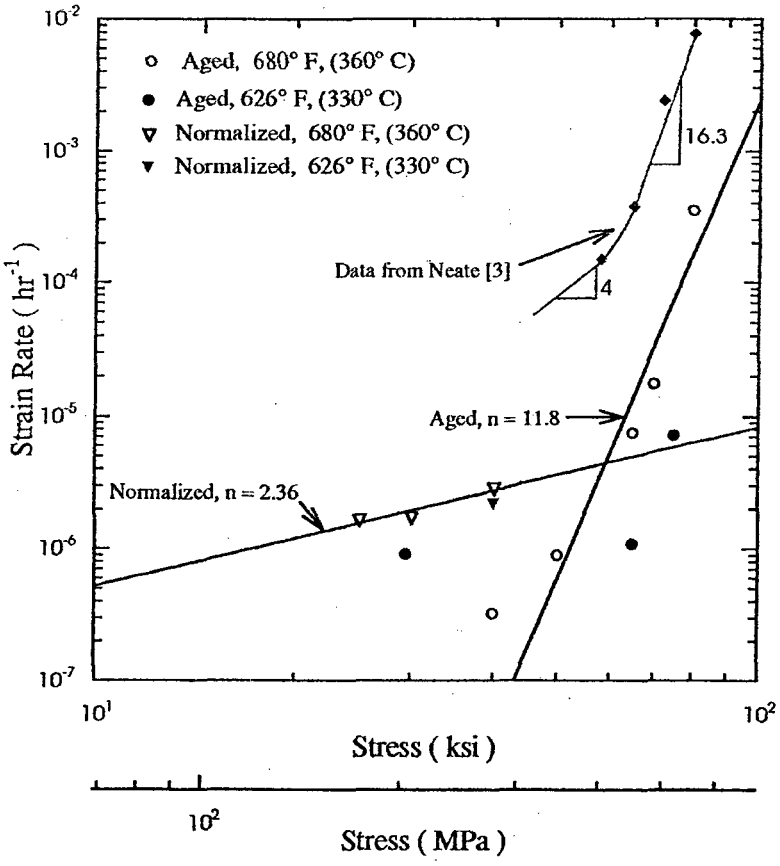

Figure F-9 The Minimum Creep Strain Rate Versus Stress for the SA-106C Carbon at 626°F and 680°F

Table F-1 List of Primary and Secondary Creep Regression Constants For the SA-106C Carbon Steel at 680°F

Creep Constants 680°F (360°C)	Aged SA-106C Carbon Steel	Normalized SA-106C Carbon Steel
A_1 $ksi^{-n(1-p)}\ hr^{-1}$ $(MPa^{-n(1-p)}hr^{-1})$	3.00×10^{-55} (5.97×10^{-75})	8.00×10^{-29} (6.26×10^{-38})
n_1	6.35	3.62
P	2.70	2.00
A $ksi^{-n}hr^{-1}$ $(MPa^{-n}hr^{-1})$	2.46×10^{-27} (3.13×10^{-37})	4.62×10^{-10} (4.85×10^{-12})
N	11.80	2.36

5.0 Example Problem

To demonstrate the applicability of the creep crack growth prediction methodology, a real life example elbow failure will be estimated.

In the early 1990's, a U.S. utility experienced a catastrophic failure in an elbow of a cyclone supply pipe. The failed pipe had a total service life of 18 months. Operating at a temperature of 662°F and a water pressure of 2400 psig, the fracture occurred in a "window opening" manner at the extrados of an SA-106, Grade C pipe bend. A piece of the pipe elbow was expelled during fracture; however, no personnel were injured. The fracture occurred at the OD of the extrados of the elbow where ratchet marks were observed at multiple crack initiation sites. Scanning electron microscopy (SEM) of the crack origin area site revealed a lap-type surface imperfection as the crack initiator.

The distortion of the pipe cross-section (ovality) of the pipe bend affects the hoop stresses at the bend. The reported measured ovality[17] was 9.8% for the pipe elbow. The degree to which the extrados stresses were elevated was estimated by the use of a SCF determined from Lees and Siverns[18], as 6.5 for an ovality measurement of 9.8%. The hoop stress for a straight pipe with 2400 psig pressure was calculated to be 11.13 ksi using Equation (33). The peak extrados stress at point A (Figure F-8) is 11.13 x 6.5 = 72.34 ksi. The point B stress was determined to be 60.42. The bend positions of the pipe were noted to be substantially harder than the straight portion of the pipe. This indicates that the cold work due to bending had not been alleviated by the post-bend heat treatment. Therefore, the material properties used were that of the aged condition. As creep data of the actual failed pipe were not available, creep properties shown in Table F-1 for the aged SA-106C carbon steel were used in the life estimation. The yield strength of the aged material was reported to be 75.6 ksi. The calculated extrados stresses are therefore in the elastic range and will be used as calculated.

Higher magnification views of the main facture showed it to be intergranular and roughly 0.5 mil in depth. This value will be used as the starting crack depth in the analysis. This defect is a lap caused by the folding of metal over the original oxidized surface. Creep crack growth rate given by Equation (32) will be used in the analysis as the best estimate of the SA-106, Grade C piping crack growth rate determined from the MTI measurements. The last piece of information needed for the analysis is the cycling history of the unit. The best estimate is approximately 5 cold starts (quarterly shutdowns) during the 18 months of service or a hold period of 2160 hours. The cyclic plastic zone, t_{pl}, is calculated based on the aged creep properties at 680°F with an upper bound value of 77 hours. The resultant predicted life is 8825 hours or a little over 12 months. Results are presented in Table F-3 along with the required inputs of geometry and material properties.

5.1 Effects of Normalization

To demonstrate the effects of normalization on the pipe elbow, the service-failed pipe was reanalyzed with the normalized creep properties given in Table F-1. The ovality measurements were taken from the unfailed pipe from the same utility where detection of linear crack-like indications in the pipe bend were reported. This prompted the removal of this pipe bend which

also had the same service exposure as the failure bend. The hardness in the unfailed bend was lower and the ovality was less, leading to the conclusion that the pipe had either been hot bent or given a post-bend heat treatment. The new analysis will assume normalized creep properties with a reduced ovality of 7.6% and a calculated SCF of 2.5 instead of 6.5, giving an extrados stress of 27.8 ksi at point A and an inside wall stress of 24.5 ksi. The yield strength of the normalized material was 29.5 ksi on normalized pipe material. This is consistent

Table F-3

Service-Failed Pipe
Case No. 4 Surface Flaw
(Combined Membrane and Bending)

Name of Files Created or Replaced = gwood4
Plane Strain Option
User Input Material Properties

E (Youngs Modulus, MSI)	26.00
Poisson Ratio	0.3000
A creep rate coefficient, 1/hr	0.2460E-26
n creep rate exponent	11.80
B primary creep rate coefficient, 1/hr	0.3000E-54
m prim. Stress creep rate expon	6.350
p prim. Strain creep rate expon	2.700
T_{pl} plastic correction time, hr	77.00
C c. c. g. const. in-kips/in^2-hr	0.9200E-02
q creep crack growth exponent	0.7124
b thickness, inch	0.4380
A_i initial crack size, inch	0.5000E-03
A_f final crack size, inch	0.4380
Sigma Point A creep-stress, ksi	72.34
Sigma Point B creep-stress, ksi	60.42

Table of Crack Size vs Cycles & Remaining Life
2160.0 Hrs/Cycle

Crack Size	Time		Remaining Life	
(in)	(hrs)	(cycles)	(hrs)	(cycles)
0.0005	77	0.00	8748	4.09
0.0057	3894	1.80	4930	4.09
0.0110	5213	2.41	3612	1.67
0.0162	6024	2.79	2800	1.30
0.0215	6590	3.05	2235	1.03
0.0267	7009	3.24	1816	0.84
0.0320	7332	3.39	1492	0.69
0.0372	7588	3.51	1236	0.57
0.0425	7798	3.61	1027	0.48
0.0477	7975	3.69	850	0.39
0.0530	8130	3.76	694	0.32
0.0582	8270	3.83	555	0.26
0.0635	8380	3.88	444	0.21
0.0687	8467	3.92	357	0.17
0.0739	8536	3.95	289	0.13
0.0792	8590	3.98	234	0.11

0.0844	8634	4.00	191	0.09
0.897	8669	4.01	156	0.07
0.949	8697	4.03	127	0.06
0.1002	8721	4.04	103	0.05
0.1054	8742	4.05	82	0.04
0.1107	8762	4.06	62	0.03
0.1159	8778	4.06	46	0.02
0.1212	8790	4.07	34	0.02
0.1264	8799	4.07	25	0.01
0.1317	8806	4.08	19	0.01
0.1369	8811	4.08	14	0.01
0.1421	8814	4.08	10	0.00
0.1474	8817	4.08	7	0.00
0.1526	8819	4.08	5	0.00
0.1579	8821	4.08	4	0.00
0.1631	8822	4.08	3	0.00
0.1684	8823	4.08	2	0.00
0.1736	8823	4.08	1	0.00
0.1789	8824	4.09	1	0.00
0.1841	8824	4.09	0	0.00
0.1946	8824	4.09	0	0.00
0.1998	8824	4.09	0	0.00
0.2051	8824	4.09	0	0.00
0.2103	8824	4.09	0	0.00
0.2156	8824	4.09	0	0.00
0.2208	8824	4.09	0	0.00
0.2261	8824	4.09	0	0.00
0.2313	8825	4.09	0	0.00
0.2366	8825	4.09	0	0.00
0.2418	8825	4.09	0	0.00
0.2523	8825	4.09	0	0.00
0.2602	8825	4.09	0	0.00

T1(0) = 51.26 hrs

T2(0) = 315.01 hrs

with measured yield strengths. The calculated extrados stress is less than the 29.5 ksi yield strength measured by testing. Note that the creep rate for the normalized material has a significantly low creep exponent (n = 2.36) for stresses 50 ksi as shown in Figure F-9. The recalculated remaining life is 87.5 months, or 7-1/3 years. The increased life is a reflection of the normalization and the reduced ovality. Figure F-10 shows the effect of normalization versus cold work in cartoon form. The first sketch shows the reduced yield strength of the normalized material and the sketch below for two stress levels, the effect of normalization on creep rate, $\dot{\varepsilon}$. The lower stress is due to the low yield strength of the normalized material, $\sigma_N < \sigma_{CW}$. The sketch on the top right-hand corner shows the relation of $\dot{\varepsilon}$ with C* (a linear relationship) and, lastly, the lower right-hand sketch of $\ln \dot{a}$ versus lnC*, shows the relationship of C* to creep crack growth rate, $\dot{a}$ which was found to be the same, independent of material condition (see Figure F-6). The result is that remaining life for the normalized material ($LIFE_N$) is greater than life for the cold worked material ($LIFE_{CW}$).

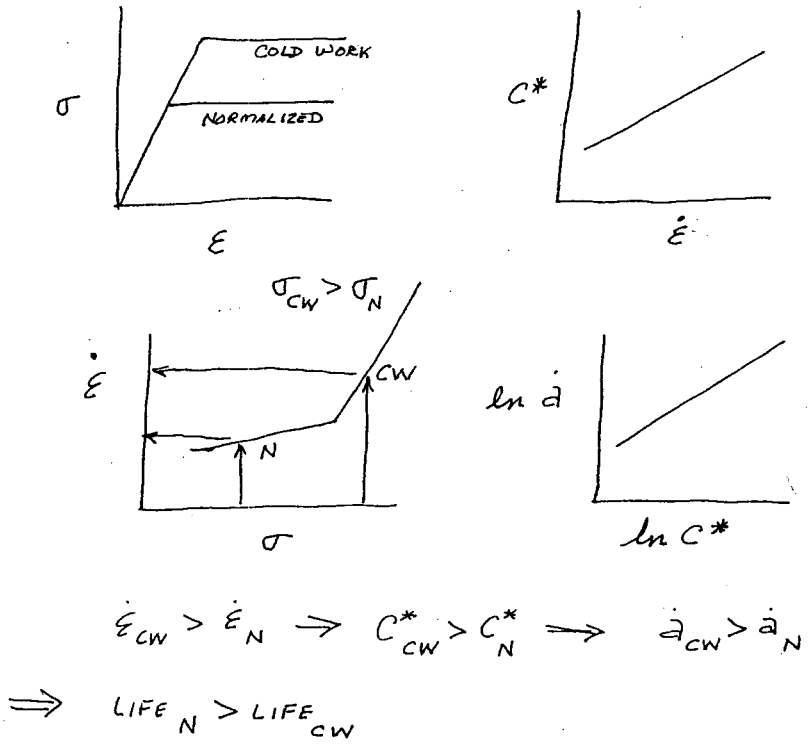

Figure F-10

6.0 Recommended Follow-Up Work

The following recommendations for follow-up work are in two areas, one in the constraint area (see Section 4.2), and the other in the determination of creep properties.

6.1 Constraint

Measurement of creep crack growth, were performed using compact specimens at GIT and SEN(t) specimens at MTI under this DOE contract. Additional tests on the same materials tested at MTI for both the compact and SEN(t) are needed to resolve the issue of the correlation of $\dot{a}$ with $C^*(C_t)$. While it was theorized that constraint may affect which parameter governs creep crack growth, no conclusive experimental data were produced. It is therefore recommended that follow-up work be performed in the measurement of $\dot{a}$ using both SEN(t) and compact specimens. The results can show conclusively that compact specimens do not necessarily produce valid data for use in predicting remaining lives of cracked elbows due to the differing constraint (stress triaxiality) of the compact to the shallow cracked elbows.

6.2 Creep Properties

Creep rate properties of actual elbow material at service temperatures are needed. The effects of cold work versus normalization and the amounts of trace elements need to be measured in terms of the creep rate parameters. The data obtained under this contract concentrated on the creep crack growth rate which was found to be independent of trace elements and/or heat treatment. However, it is strongly believed based on work at GIT[3] and in Europe[1] that creep rate properties will be strongly a function of heat treatment and trace elements. Therefore, it is strongly recommended these creep rate tests be performed in any follow-on work.

7.0 References

[1] G. J. Neate, "Creep Crack Growth in Cold-Formed C-Mn Steel at 360°C," Materials Science and Engineering, 1986, Vol. 83.

[2] D. J. Gooch, "The Effect of Cold Work on Low Temperature (0.35 Tm) Creep Crack Growth in the C-Mn Steels," Materials Science and Engineering, 1984, Vol. 64.

[3] Y. Gill, "Creep Crack Growth Characterization of SA-106C Carbon Steel," Georgia Institute of Technology, Ph.D. Thesis, March 1994.

[4] A. Saxena and P. K. Liaw, "Remaining Life Estimation of Boiler Pressure Parts – Crack Growth Studies," EPRI Report CS-4688, Electric Power Research Institute, Palo Alto, CA, July 1986.

[5] J. D. Landes and J. A. Begley, in Mechanics of Crack Growth, ASMT STP 590, American Society for Testing and Materials, 1976.

[6] A. Saxena, J. Han, and K. Banerji, "Creep Crack Growth Behavior in Power Plant Boiler and Steam Pipe Steels," Journal of Pressure Vessel Technology, Transactions of the ASME, May 1988.

[7] V. Kumar, M. D. German, and C. F. Shih, "Elastic-Plastic and Fully-Plastic Analysis of Creep Initiation, Stable Growth, and Instability in Flawed Cylinders," ASTM STP 803, 1983.

[8] V. Kumar, M. D. German, C. F. Shih, "An Engineering Approach to Elastic-Plastic Fracture Analysis," EPRI NP-1931, Electric Power Research Institute, Palo Alto, CA, July 1981.

[9] J. L. Bassani, D. E. Hawk, and A. Saxena, "Evaluation of the C_t Parameter for Characterizing Creep Crack Growth Rate in the Transition Region," Third International Symposium on Nonlinear Fracture Mechanics, ASTM STP 995, 1989.

[10] J. M. Bloom and M. L. Malito, "Using C_t to Predict Component Life," ASTM 22nd National Symposium on Fracture Mechanics presented in Atlanta, Georgia, June 27, 1990.

[11] H. Riedel, "Creep Deformation at Crack Tips in Elastic-Visoelastic Solids," Journal of Mechanics and Physics of Solids, Vol. 29, 1981.

[12] C. P. Leung, D. L. McDowell, A. Saxena, "Influence of Primary Creep in the Estimation of C_t Parameter," EPRI Topical Report, EPRI Contract 2253-10, August 1988, also International Journal of Fracture, Vol. 36, 1988.

[13] H. Riedel and F. V. Detrampel, "Creep Crack Growth in Ductile Creep-Resistant Steels," International Journal of Fracture, Vol. 33, 1987.

[14] K. B. Yoon, "Characterization of Creep Fatigue Crack Growth Behavior Using the C_t Parameter," Georgia Institute of Technology, Ph.D. Thesis, June 1990.

[15] E. C. Rodabaugh, "Stresses in Out-of-Round Pipe due to Internal Pressure," Phase Report No. 115-8, ORNL-TM-3244, Oak Ridge National Laboratory, January 1971.

[16] I. A. Shibli, "Investigation of a Failure Problem in Cold-bent Boiler Riser and Supply Pipes," International Journal of Pressure Vessel & Piping, Vol. 24, 1986.

[17] G. R. Wood, "Investigation of Failures in Carbon Steel Supply Piping," PVP-Vol. 221, Service Experience in Operating Plants, ASME 1991.

[18] D. J. Lees and M. J. Siverns, "Tolerance of Flaws in Pressurized Components," Ref. C98/78, The Institution of Mechanical Engineers, London, 1978.

[19] P. J. Budden and R. A. Ainsworth, "The Effect of Constraint on Fracture Assessments," International Journal of Fracture, Vol. 97, 1999.

[20] J. M. Bloom and D. R. Lee, "User's Guide for the Computer Program PCCREEP – Version 5," Babcock & Wilcox Letter Report RDD:94:14200-003-001:0a, March 21, 1994.